Cilt 5 Sayı 1 Haziran 2024
Volume 5 Number 1 June 2024

ISSN: 2717-8811(Online)

JOURNAL

Materials and Mechatronics:A

2024

JOURNAL

Materials

and

Mechatronics: A

e-ISSN: 2717-8811

Cilt: 5 Sayı: 1 Haziran 2024

Volume:5 Number: 1 June 2024

2024

JOURNAL

Materials

and

Mechatronics: A

Bu Sayımızı 15.03.2024 Tarihinde aramızdan ayrılan Prof. Dr. Adem KURT'un Anısına yayınlıyoruz.

Gazi Üniversitesi, Teknoloji Fakültesi, Metalürji ve Malzeme Mühendisliği Bölümü Öğretim Üyesi iken 15.03.2024 tarihinde vefat eden Prof. Dr. Adem KURT, 1958 Yılında Çorum-Alaca Dedepınar köyünde doğdu. 1977 yılında Sungurlu Endüstri Meslek Lisesinden mezun olduktan sonra 1983 yılında Gazi Üniversitesi, Teknik Eğitim Fakültesi, Metalurji Eğitimi Bölümünden Mezun oldu. 1986-1988 yılları arasında Elazığ Gazi Endüstri Melek Lisesinde Metal İşleri Bölümünde öğretmen olarak görev yaptı. 1988-1997 yılları arasında Gazi Üniversitesi, Teknik Eğitim Fakültesinde Araştırma Görevlisi olarak çalışırken 1992 yılında Yüksek lisansını, 1996 yılında da Doktorasını tamamladı. 1997 yılında Gazi Üniversitesi Teknik Eğitim Fakültesi Metal Eğitimi Bölümünde Yardımcı Doçent Doktor, 1999 yılında aynı bölümde Doçent, 2005 yılında da Profesör oldu. 1992 yılında ABD'de Purdue University ve 2003-2004 yıllarında da Florida State University de araştırmalar yaptı. Yüksek Lisansında Kendi kendini yağlayan Toz metal bronz yatakların aşınma özellikleri, Doktora tezinde Toz Metal kendi kendine yağlayan bronz yatakların çelik malzemelere difüzyon kaynağını gerçekleştirdi. 1995 yılında Türk Toz Metalürjisi Derneği kurucu üyesi oldu. 2001 yılında Kaynak Teknolojisi Derneğini kurdu. Uluslararası Kaynak Teknolojileri Konferans ve Sergisini Düzenleme Kurulu Başkanlığını yürüttü. Gazi Üniversitesinde kısa adı Gazi-KABTEM olan Gazi Üniversitesi Kaynak ve Birleştirme Teknolojileri Uygulama ve Araştırma Merkezini kurdu. Ulusal ve Uluslararası dergilerde yayınlanmış 180'nin üzerinde makalesi bulunmaktadır. Ayrıca Journal of Materials and Mechatronics: A adlı dergimizin Danışma kurulundaydı.

2024

JOURNAL of
MATERIALS and MECHATRONICS:A

JOURNAL of
MATERIALS and MECHATRONICS:A

JOURNAL of
MATERIALS and MECHATRONICS:A

İçindekiler/Contents	Sayfa/Page
Araştırma Makalesi (Research Article) Farklı Katı Malzemelerde Görgül Kip Analizi Tabanlı Foto Akustik Sinyal İşleme ile Kusur Tespiti Defect Detection with EMD-Based Photoacoustic Signal Processing on Different Solid Materials Balcı, Z., Mert, A.	1-13
Araştırma Makalesi (Research Article) Effect of Thermo-Reactive Diffusion Coatings on Microstructure and Wear Behavior of Powder Metallurgy Steel Cutting Inserts Termo-Reaktif Difüzyon Kaplamaların Toz Metalurjisi Yöntemi ile Üretilen Çelik Kesici Uçların Mikroyapısı ve Aşınma Davranışlarına Etkisi Turan, T., Günen, A., Kanca, E.	14-35
Araştırma Makalesi (Research Article) Investigation of Three Body Abrasive Wear Behavior of Micro-Nano Sized Iron Ore Pieces on Bronze Bronz Üzerindeki Mikro-Nano Boyutlu Demir Cevheri Parçalarının Üç Cisimli Aşındırıcı Aşınma Davranışının İncelenmesi Uğur, A., Erdoğdu, A.E., Demirsöz, R.	36-48
Araştırma Makalesi (Research Article) The Tensile Properties of Functionally Graded Materials in MSLA 3D Printing as a Function of Exposure Time Maruz Kalma Süresinin Fonksiyonu Olarak MSLA 3B Yazdırmada Fonksiyonel Olarak Derecelendirilmiş Malzemelerin Çekme Özellikleri Temiz, A.	49-59

JOURNAL of
MATERIALS and MECHATRONICS:A

İçindekiler/Contents	Sayfa/Page
Araştırma Makalesi (Research Article) Investigation of High-Temperature Wear Behavior of Ni-Mo Alloyed Hardfacing Coatings Applied on Hot Strip Mill Vertical Rolls by Submerged Arc Welding Sıcak şerit haddesi dikey merdanelerine tozaltı ark kaynağı ile uygulanan Ni-Mo alaşımlı sert dolgu kaplamalarının yüksek sıcaklık aşınma davranışının incelenmesi Sarsılmaz, H.G., Günen, A., Kanca, E.	60-86
Araştırma Makalesi (Research Article) Large Deflection Analysis of Functionally Graded Beam by Using Combining Method Fonksiyonel Dereceli Kirişin Bileşim Metodu Kullanılarak Büyük Sehim Analizi Demir, E., Çallıoğlu, H., Girgin, Z.	87-105
Araştırma Makalesi (Research Article) Effect of Cold Compaction Pressure on Porous NiAl Articles Produced by Using Space Holder Urea via VCS VCS ile Yer Tutucu Üre Kullanarak Üretilen Gözenekli NiAl Parçalara Soğuk Sıkıştırma Basıncının Etkisi Sarıyer, G., Çamurlu, H.E.	106-116
Araştırma Makalesi (Research Article) Low Velocity Impact Behavior of Curved Composite Panels Reinforced with Different Types of Stiffeners Used in Air Vehicle Hava Araçlarında Kullanılan Farklı Tipte Takviyelerle Güçlendirilmiş Eğri Kompozit Panellerin Düşük Hızlı Darbe Davranışı. Dağ, T., Güvenç, M.A., Uyaner, M.	117-129

JOURNAL of
MATERIALS and MECHATRONICS:A

İçindekiler/Contents	Sayfa/Page
Araştırma Makalesi (Research Article) Predicting the Corrosion Rate of Al and Mg Alloys Coated by Plasma the Spraying Method with Machine Learning Plazma Püskürtme Yöntemiyle Kaplanan Al ve Mg Alaşımlarının Korozyon Oranının Makine Öğrenmesi ile Tahmin Edilmesi Özkavak, H., Tunay, R.F.	130-142
Araştırma Makalesi (Research Article) Seçici Katalitik İndirgeme (SCR) Sisteminde Statik Karıştırıcı Kullanımının NOx Emisyonlarına Etkisinin Deneysel İncelenmesi Experimental Investigation of the Effect of Static Mixer Usage on NOx Emissions in Selective Catalytic Reduction (SCR) System Baydır, Ş.A., Erçek, E.	143-153
Araştırma Makalesi (Research Article) Investigation of Wear Behaviour of TiO_2 and Al_2O_3 Reinforced YSZ Coating TiO_2 ve Al_2O_3 Takviyeli YSZ Kaplamanın Aşınma Davranışının İncelenmesi Avcı, A., Karabaş, M.	154-167
Araştırma Makalesi (Research Article) Evaluation of The Turning Parameters of AISI 5115 Steel in Dry and MQL Cutting Environments with The Use of a Coated Carbide Cutting İnsert: An Experimental Study AISI 5115 çeliğinin kuru ve MQL kesme ortamında tornalama parametrelerinin kaplamalı karbür kesici uç kullanılarak değerlendirilmesi: Deneysel Bir Çalışma Demirpolat, H.	168-182

JOURNAL of
MATERIALS and MECHATRONICS:A

İçindekiler/Contents	Sayfa/Page
Araştırma Makalesi (Research Article) Investigation of Nickel and Chromium Ion Release from Simulated Fixed Orthodontic Appliances in Artificial Saliva Containing Fluoride Simüle Edilmiş Sabit Ortodontik Apareylerin Florür İçeren Yapay Tükürükte Nikel ve Krom İyon Salınımının Araştırılması Yurdakul, Titiz, S., Korcan, S.E., Koca, A., Hameş, E.E.	183-194
Araştırma Makalesi (Research Article) Investigation of Changing Microstructure and Mechanical Properties of FeNiMnCrCoTi0.1 High Entropy Alloy with B Addition FeNiMnCrCoTi0,1 Yüksek Entropili Alaşıma Yapılan B İlavesi ile Mikroyapı ve Mekanik Özelliklerin İncelenmesi Yalçın, M.C., Talaş, Ş.	195-213

JOURNAL of
MATERIALS and MECHATRONICS:A

e-ISSN 2717-8811
JournalMM, 2024, 5(1), 1-13
https://doi.org/10.55546/jmm.1422073

Araştırma Makalesi / Research Article

Farklı Katı Malzemelerde Görgül Kip Analizi Tabanlı Foto Akustik Sinyal İşleme ile Kusur Tespiti

Zekeriya BALCI[1]*, Ahmet MERT[2]

[1] Van Yüzüncü Yıl Üniversitesi, Çaldıran Meslek Yüksekokulu, Elektronik ve Otomasyon Bölümü, Van, Türkiye,
ORCID ID: https://orcid.org/0000-0002-1389-1784, zekeriyabalci@yyu.edu.tr
[2] Bursa Teknik Üniversitesi, Mühendislik ve Doğa Bilimleri Fakültesi, Mekatronik Mühendisliği Bölümü, Bursa, Türkiye,
ORCID ID: https://orcid.org/0000-0003-4236-3646, ahmet.mert@btu.edu.tr

Geliş/ Received: 18.01.2024**;** **Revize/Revised:** 15.02.2024 **Kabul / Accepted:** 03.03.2024

ÖZET: Bu çalışmada, görgül kip ayrışımı (GKA) ve makine öğrenimi algoritması kullanılarak malzeme kusurlarının tespiti için bir fotoakustik (FA) sinyal işleme çerçevesi önerilmiştir. Zaman ve zaman-frekans düzleminde çıkarılan özellikler ve gelişmiş sinyal işleme yöntemlerinin yardımıyla kusurların başarılı bir şekilde tespit edilmesini sağlamıştır. Lazer, mikrofon ve veri toplama kartı tabanlı bir FA sistem kullanılarak alüminyum, demir ve ahşap malzemelerden FA sinyallerinden oluşan veritabanı elde edilmiştir. Her bir malzeme grubundan toplam 240 örnek (120 sağlam örnek ve 120 kusurlu örnek) ve toplam 720 örnek, GKA uygulandıktan sonra zaman ve zaman-frekans düzlemi özelliklerini çıkarmak için kullanılmıştır. Daha sonra k-en yakın komşu sınıflandırıcısı veri tabanındaki kusurlu ve sağlam malzemelerin tespiti için çıkarılan 14 özellik kullanılarak eğitilmiş ve test edilmiştir. Materyaller özelinde ve materyaller arası sınıflandırma yapılmış ve doğruluk oranları sırasıyla %100 ve %97.77 olarak elde edilmiştir.

Anahtar Kelimeler: Fotoakustik, Görgül kip ayrışımı, Destek vektör makinesi, K-en yakın komşu, Karar ağacı, Kusur tespiti.

*Sorumlu yazar / Corresponding author: zekeriyabalci@yyu.edu.tr
Bu makaleye atıf yapmak için /To cite this article

Balcı, Z., Mert, A. (2024). Farklı Katı Malzemelerde Görgül Kip Analizi Tabanlı Foto Akustik Sinyal İşleme ile Kusur Tespiti. Journal of Materials and Mechatronics: A (JournalMM), 5(1), 1-13.

Defect Detection with EMD-Based Photoacoustic Signal Processing on Different Solid Materials

ABSTRACT: In this study, we propose a photoacoustic (PA) signal processing framework for material defect detection using empirical mode decomposition (EMD) and machine learning algorithms. The extracted time and time-frequency domain features enables to detect defects successfully with the help of the advanced processing methods. A database of the PA signals has been obtained from aluminum, iron and wood materials using a laser, microphone and data acquisition board-based PA apparatus. Within each material group, a total of 240 samples (120 intact samples and 120 defective samples), and a total of 720 samples are used to extract time and time-frequency domain features after applying the EMD. k-nearest neighbor classifier is then trained and tested using the extracted 14 features for detection of the defective and intact materials in the database. Inter-material and cross-material evaluations are performed, and the accuracy rates were 100% and 97.77% respectively.

Keywords: Photoacoustic, Empirical mode decomposition, Support vector machine, K-nearest neighbor, Decision tree, Non-destructive testing.

1. GİRİŞ

Son yıllarda giderek ilgi çeken Fotoakustik (FA) veya Optoakustik (OA), gelişmekte olan teknoloji tabanlı görüntüleme ve tahribatsız muayene yöntemidir (Chen ve Tian, 2021). Fotoakustik etkiye dayanan bu teknik Alexander Graham Bell tarafından 1880 yılında keşfedilmiştir (Bell, 1880). FA sistemin temel bileşenleri, ışık kaynağı, hedef nesne ve akustik algılayıcıdır. Lazer kaynağı, genellikle kısa darbeler halinde yollanan lazer ışığı üretir. Bu ışık, hedef nesne tarafından absorbe edildiğinde, termal enerjiye dönüşür ve enerji emiliminden ortaya çıkan termal genleşme ile ses dalgalarının oluşumuna yol açar. Akustik algılayıcı, bu ses dalgalarını algılayarak ilgili bilgileri toplar ve bu bilgiler daha sonra analiz için işlenir (Beard, 2002; Sun ve ark., 2014; Xu ve Wang, 2006).

FA biyomedikal alanında, 266nm lazer ve mikrofon ile insan nefesinden temel bileşen analizi ile astım teşhisi (V.R. ve ark., 2022), 1535 nm lazer ve odaklı ultrasonik transdüserle FA sinyaldeki lineerlik özelliğinden yararlanarak glikoz ölçümü (Yang ve ark., 2022), geniş dalga boyundaki lazerle FA sinyalin spektral özellikleri ve makine öğrenmesiyle moleküler meme kanseri tanıma (Li ve ark., 2023) ve FA veriden dalgacık dönüşümü elde edilen özellikler ve Resnet-18 ağı kullanılarak prostat kanseri teşhisi (Wu ve ark., 2022), kandaki oksijen, kandaki glukoz, lipit ve tümör takibi ile insan sağlığı görüntüleme (Jin ve ark., 2022), farklı diş örneklerinden alınan FA sinyale dayalı yeniden oluşturulan görüntüden yoğunluk analizi ile diş çürüğü tespiti (Tasmara ve ark., 2023) ve bir çok çalışmada yer bulmuştur (Nakazawa ve ark., 2022; Zhang ve ark., 2023). FA yöntem metan (Strahl ve ark., 2023), ozon (Keeratirawee ve Hauser, 2021) ve SO2F2 (Zhang ve ark., 2022) gazı ve bir çok çevresel gaz izlemede ve endüstriyel uygulamada giderek artan bir araştırma yöntemi olmuştur (Keeratirawee ve ark., 2022; Li ve ark., 2022; Liao ve ark., 2022).

Son yıllarda FA yöntem tahribatsız muayenede (NDT) (Arslan ve Toplan, 2023; Kot ve ark., 2021), malzeme kusur tespiti ve analizinde popülaritesi giderek artan bir yöntem olmuştur (Chen ve Tian, 2021). Araştırmacılar (Jeon ve ark., 2016; Setiawan ve ark., 2018; Zakrzewski ve ark., 2010), metallerdeki yüzey kusurlarını FA yöntem ile görüntülemek ve çatlak tespiti için çalışmalar yapmışlardır. Zakrzewski ve ark. (2010) lazer kaynaklı FA görüntülemeye ek olarak piezoelektrik transdüserle metal plakaya farklı frekanslarda yükleme yaparak, doğrusal olmayan çatlak görüntüleme üzerine çalışmışlardır. Doğrusal olmayan sistem etkileri sonucu oluşan karışık

frekanstaki akustik sinyal, bir ivmeölçer tarafından algılanmıştır ve çatlakların doğrusal ve doğrusal olmayan fotoakustik görüntülenmesine katkı sağlayan çeşitli fiziksel mekanizmalar incelenmiştir. Setiawan ve ark. (2018), lazer ve mikrofondan oluşan deneysel sistemleri ile elde edilen FA sinyale yazılım tabanlı Fourier dönüşümü uygulamışlardır. Sinyal genliğini ölçme yoluyla mikro çatlakları tespit etmeye çalışmışlardır. Sistemin, yüzeyinde mikro çatlakları olan bir nesnenin fotoakustik görüntüsünü üretebilecek yetenekte olduğunu belirmişlerdir. Jeon ve ark. (2016) ise metal plakadan elde edilen FA sinyaller kullanılarak oluşturulan görüntü üzerinde kenar belirleme ve ikilik resimde uzunluk ölçümü ile görüntü işleme tabanlı metal plakada çatlak tespiti yapmışlardır. Shiraishi ve ark. (2010), yaptıkları çalışmada kaynak kusurları FA yöntem ile araştırmışlardır. Wang ve ark. (2019) kompozit malzemeler için FA yöntem ile tahribatsız muayene yöntemi önermişlerdir. Piko saniye darbeli lazer, ultrasonik algılayıcı, veri işleme ve hesaplama alt sistemlerinden oluşan FA görüntüleme sisteminin CFRP kompozitlerin hasar tespiti için son derece yüksek çözünürlüklü yeni bir temaslı olmayan yaklaşım sağlayabildiğini rapor etmişlerdir.

Sun ve ark. (2014), Vangi ve ark. (2021), Yan ve ark. (2012) FA ile tren raylarındaki yüzey kusurlarının tespiti ve görüntülenmesi üzerine çalışmalar gerçekleştirmişlerdir. Sun ve ark. (2014) ultrasonik algılayıcı, 532nm ve 160mJ gücündeki lazer den oluşan sistem ile tren raylarından elde ettikleri FA sinyalleri kullanarak gerçek zamanlı FA görüntüleme sistemi önermişlerdir. FA sinyal kullanılarak yeniden oluşturulan görüntüye göre, ray kusurunun görünümü, uzanma eğilimi ve derinliği gibi hasar bilgileri etkili bir şekilde tanımlanabileceğini rapor etmişlerdir. Vangi ve ark. (2021) 20W 445nm lazer ve dar bant piezoelektrik kontak probu ile oluşturdukları çalışma düzenekleri ile FA sinyal parametrelerinin optimizasyonu üzerine çalışmışlardır. Lazer darbe sayısının, lazer darbe süresinin ve darbeler arası sürenin FA sinyal kalitesi üzerinde etkisinin olduğunu rapor etmişlerdir. Ayrıca bu çalışmada kusurlu bölgenin belli uzağında da sinyal karakteristiğinin korunduğu rapor edilmiştir. Yan ve ark. (2012) yaptıkları çalışmada 850 nm lazer ve piezo transdüser ile tren rayındaki kusurların görüntülenmesi üzerine çalışmışlardır. Ayrıca modülasyon frekansının, FA görüntü rekonstrüksiyonu kalitesi üzerinde etkisinin olduğunu rapor etmişlerdir.

Bu çalışmaya özgü 450 nm dalga boyuna sahip lazer ve mikro-elektromekanik mikrofon, veri toplama kartı ile sinyal işleme algoritması tasarlanmıştır. Alüminyum, demir ve tahta malzemeleri üzerinde tasarlanan düzenek denenerek elde edilen FA sinyalleri gelişmiş sinyal işleme teknikleri ile incelenerek, oluşan sağlam ve kusurlu sinyallerindeki ayırt edici özellikler belirlenmeye çalışılmıştır. GKA yöntemi uygulanması ile elde edilen Özgül Kip Fonksiyonu (ÖKF) kullanılarak, zaman ve zaman-frekans düzlemindeki özelliklerin çıkarılması ve bu özelliklerle eğitilen sınıflandırıcılarla tahribatsız kusur tespiti gerçekleştirilmesi amaçlanmıştır. Yukarıda verilen literatürde FA ile kusur tespiti çalışmalarında genel olarak bir malzeme özelinde ve görüntüleme üzerine çalışmaların yoğunlaştığı görülmüştür. Bu çalışmadaki amaç GKA ile FA sinyaldeki taban kaymasının elimine edilmesi ve FA sinyal işleme ile farklı malzemeler için ortak bir kusur tespiti çerçevesinin oluşturulmasıdır. Çalışmada ilk önce üç malzemeden elde edilen ham FA sinyallere GKA uygulanmıştır. Daha sonra birinci ÖKF'ler üzerinden zaman ve zaman-frekans düzleminde 14 adet özellik çıkarılmıştır. Son olarak çıkarılan özellikler ile k-NN sınıflandırıcısı eğitilerek önerilen yöntemin başarımı incelenmiştir.

2. MATERYAL VE YÖNTEM

2.1 Çalışma Düzeneği

Bu çalışmada kullanılan çalışma düzeneğinin 3B tasarımı şekil 1'de verilmiştir. Çalışma düzeneği 15W gücünde 450nm dalga boyunda ayarlanabilir odağa sahip lazer modülü, mikrofon (SparkFun Analog MEMS Mikrofon Breakout - ICS-40180), osiloskop (Analog Discovery 2: 100MS/s USB Oscilloscope, Logic Analyzer and Variable Power Supply), Stylogiannis ve ark. (2018)'deki şarj deşarj topolojisi temel alınarak KiCad ortamında tasarlanmış lazer sürücü ve lazer sabitleme tablasından oluşmaktadır. Şekil 1'de verilen çalışma düzeneğinde (10) numarası ile belirtilen bileşen (125x7.67mm içi boş silindir) ile akustik sinyalin kaynağı ile mikrofonun ses girişi arasındaki mesafe artırılmıştır. Bu sayede anahtarlamadan kaynaklanan parazit ile akustik sinyal arasında faz farkı oluşturularak, gürültünün ve malzemeden yansıyan ışımaların FA sinyal üzerindeki etkisi azaltılmaya çalışılmıştır.

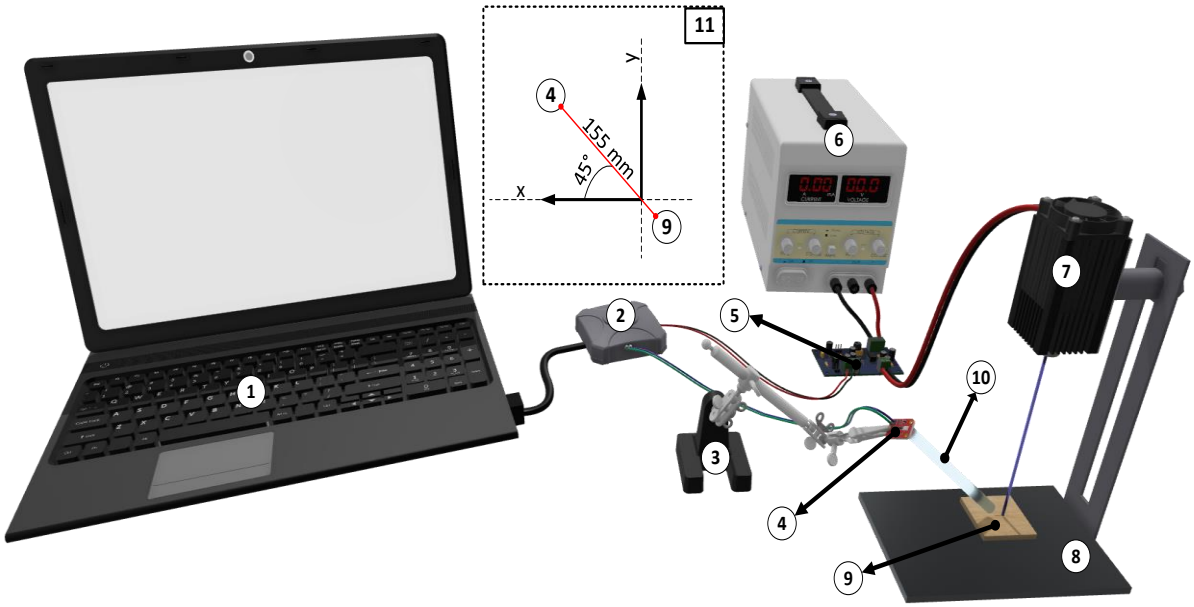

Şekil 1. Çalışma düzeneği (1- Bilgisayar, 2- Osiloskop, 3- Kıskaç, 4- Mikrofon, 5- Lazer sürücü, 6- Güç kaynağı, 7- Lazer, 8- Lazer sabitleme tablası, 9-Örnek materyal, 10- 125x7.67mm içi boş silindir, 11- Malzeme ve mikrofon arası açı ve uzaklık)

Bu çalışmada alüminyum, demir ve tahta malzemeleri denek olarak kullanılmıştır. Üç malzeme içinde kusurlu ve sağlam örnekler oluşturulmuştur. Malzeme kusurları kesik ve delik olarak malzemelerde yapay olarak üretilmiştir. Kesik kusuru için 22mmx0.8mm dairesel testere, delik kusuru için 2.30mm matkap ucu kullanılarak çeşitli derinliklerde kusurlar oluşturulmuştur. Kullanılan örnek malzemelerin yüzeyi çevreleyen kenarları 50mm olacak şekilde kare biçiminde ebatlanmıştır. Tüm malzemelerin kusurlu ve sağlam görsellerini içeren görseller şekil 2'de verilmiştir.

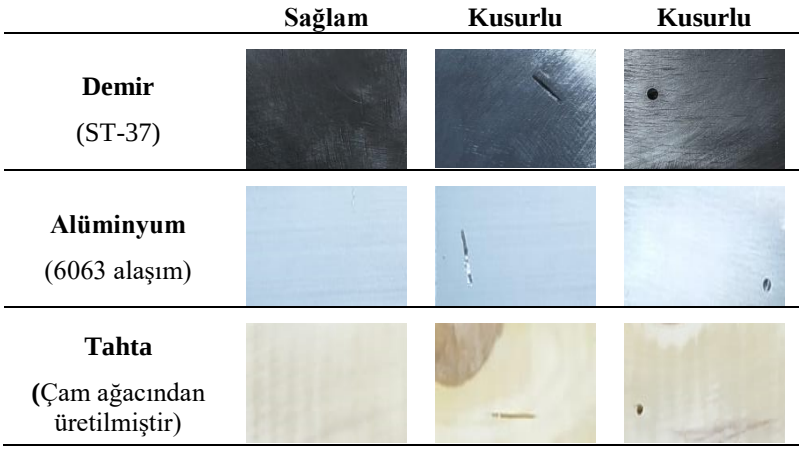

Şekil 2. Malzeme örnekleri

2.2 Veri Toplama ve Veri Artırımı

Şekil 2'de görselleri verilen üç farklı malzemeden sağlam ve kusurlu olmak üzere, her bir malzeme türünden 60 adet örnek olacak şekilde toplamda 180 adet örnek alınmıştır. Veriler kusurların bulunduğu bölgeden ve kusurdan en fazla 2mm uzaklıkta olacak şekilde alınmıştır. Bu örnekler 5µs, 10µs ve 15µs kaydırılarak orijinal örneklerden faz farkı oluşturulmuştur ve örnek gurupları kullanılarak veri artırımı yapılmıştır.

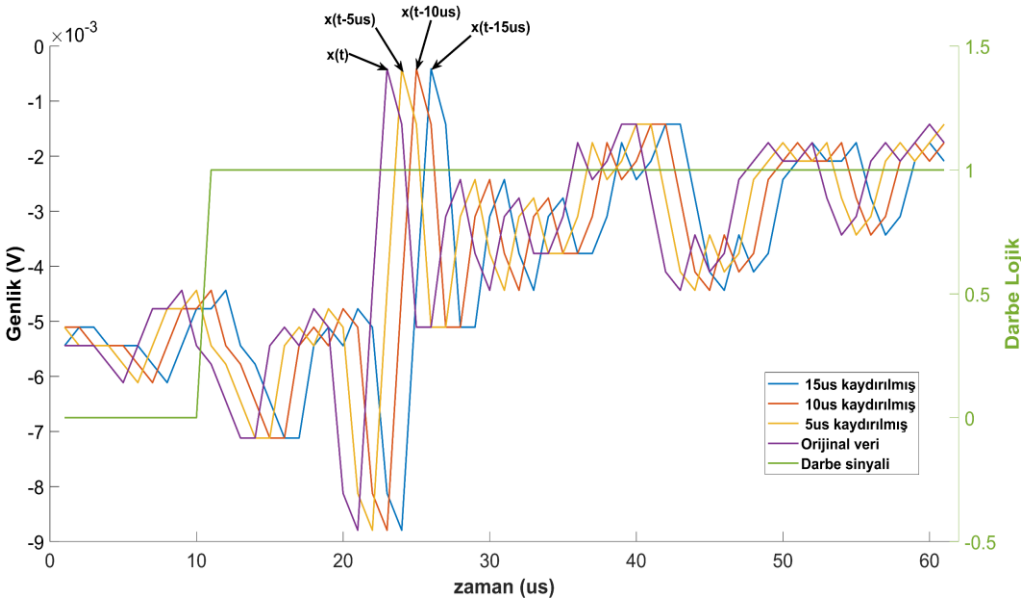

Şekil 3. Orijinal veri ve veri artırımı ile elde edilen veri grafikleri

Malzemelerden alınan örnek bir FA sinyal için veri artırımı sonucu elde edilen sinyallerin grafiği şekil 3'te verilmiştir. Burada darbe sinyali ile lazer sistemi tetiklenmektedir ve oluşan FA sinyal mikrofon aracılığıyla alınmıştır. Şekil 3'te verilen orijinal sinyalin (mor) 5µs, 10µs ve 15µs kaydırılması sonucu veri gurubu 4 kat arttırılmıştır. Orijinal ve veri artırımı sonucu elde edilen örnekleri içeren malzeme gurubu örnek sayıları çizelge 1'de verilmiştir.

Çizelge 1. Malzeme guruplarına ait örnek sayıları

	Sağlam	Kusurlu	Toplam
Demir	120	120	**240**
Alüminyum	120	120	**240**
Tahta	120	120	**240**
Toplam	**360**	**360**	**720**

Veri artırımı ile az sayıdaki orijinal veri artırılmasına ek olarak eğitim aşamasında başarımı arttırmak için bu çalışmada birini dışarıda bırak çapraz doğrulama (BDBÇD) yöntemi uygulanmıştır. Veri setinin az veya kısıtlı olduğu durumlarda etkili olan bu yöntem, bir çok çalışmada sınıflandırıcıların performans değerlendirmesinde uygulanmıştır (Wong, 2015).

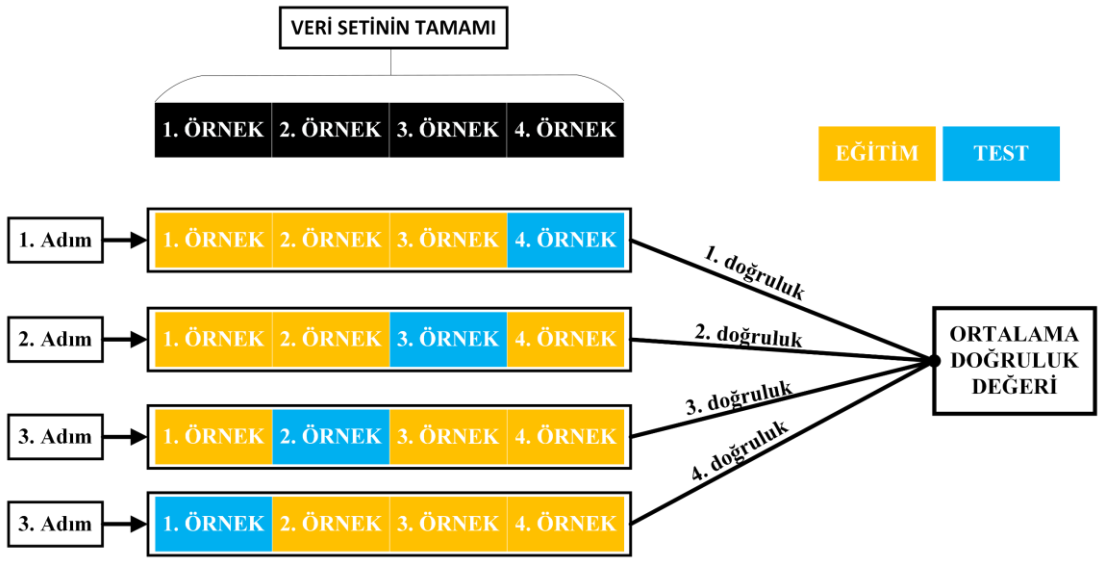

Şekil 4. Dört örnekten oluşan bir modelin birini dışarda bırak çapraz doğrulama blok şeması

Bu çapraz doğrulama yöntemi her bir iterasyonda veri setinin bir örneğini test için ayırır ve kalan örneklerle modeli eğitir, ardından ayırdığı örneği kullanarak modelin performansını değerlendirir. Dört örnekten oluşan bir modele BDBÇD yönteminin uygulanışını temsil eden şematik gösterim şekil 4'te verilmiştir. Bu çalışmada veri artırımı ve BDBÇD yönteminin uygulanması ile malzemeler başarılı bir şekilde sınıflandırılmıştır.

2.3 Görgül Kip Ayrışımı ve HD

Görgül Kip Ayrışımı, doğrusal ve durağan olamayan sinyalleri fiziksel olarak anlamlı bileşenlere ayırmak için, Huang ve arkadaşları (Huang ve ark. 1998) tarafından önerilen veri uyarlamalı sinyal işleme yöntemidir. Bu yöntem, bir sinyali farklı salınım ve çözünürlükteki Özgül Kip Fonksiyonu (ÖKF) $\varphi_k(t)$ ve kalıntı veya artık $r(t)$ adı verilen bileşenlere ayırır. Tasarım gereği, ÖKF lokal maksimum ve minimum noktalarının sıfır geçiş noktasına eşit veya farkının en fazla bir olması, lokal maksimum ve minimum zarflarının ortalamasının sıfır olması gerekmektedir. GKA'nın ana bölümü ÖKF'lerin elde edildiği eleme sürecidir. Eleme sürecinin adımları, örnek bir $x(t)$ sinyali için aşağıdaki gibidir.

i. $x(t)$ sinyalinin yerel maksimum ($M(i)$, i = 1, 2, 3, …) ve minimum ($m(j)$, j = 1, 2, 3, …) noktaları bulunur.

ii. İnterpolasyon ile yerel maksimum ve minimum noktalarını kesen zarf bulunur. $e_{min}(t)$, $e_{max}(t)$.

iii. Zarfların ortalaması hesaplanır $m(t) = (e_{min}(t) + e_{max}(t))/2$

iv. $m(t)$ ÖKF şartlarını sağlıyorsa $\varphi_k(t) = m(t)$ olarak sakla. Sağlamıyorsa $m(t)$, $x(t)$'den çıkarılır, $x(t) = x(t) - m(t)$.

v. Durdurma kriteri (Mert ve Akan, 2018) $x(t)$ için sağlanıyorsa $r(t) = m(t)$ olarak atanır.

GKA'da eleme süreci $r(t)$ artık fonksiyonu elde edilene kadar özyinelemeli olarak uygulanır. Orijinal sinyal ÖKF'lerin ve artık sinyalin toplamına eşittir ve eşitliği aşağıda verilmiştir.

$$x(t) = r(t) + \sum_{k} \varphi_k(t) \tag{1}$$

Bu şekilde elde edilen ÖKF'lere, Hilbert dönüşümü (HD)(Huang ve ark. 1998) uygulanması sonucu ÖKF'lerden anlık frekans ve genlik bilgileri elde edilir. Bu sayede ÖKF'ler üzerinde zaman-frekans düzleminde analiz gerçekleştirilir.

Bir $x(t)$ sinyaline HD uygulanırsa eşitlik (2)'deki gibi analitik bir sinyal elde edilir (Huang ve ark. 1998);

$$y(t) = \alpha(t) + j\beta(t) = A(t)e^{j\phi(t)} \tag{2}$$

burada $\alpha(t)$ ve $\beta(t)$ HD çiftini, $A(t)$, $y(t)$'nin genliğini ve $\phi(t)$ ise fazını ifade eder ve (3) numaralı eşitlik ile hesaplanır.

$$\phi(t) = arctan\big(\beta(t) \,/\, \alpha(t)\big) \tag{3}$$

Anlık frekans $\omega(t)$ ise, anlık faz $\phi(t)$'nin türevi alınarak elde edilir.

$$\omega(t) = \frac{d\phi(t)}{dt} \tag{4}$$

Böylece sinyalin barındırdığı $\omega(t)$ ve $A(t)$ bileşenleri ile zaman-frekans düzleminde analiz gerçekleştirilir. GKA ve anlık frekans kombinasyonu bu yöntemi, zaman-frekans analizi için güçlü bir sinyal işleme çerçevesi kılmaktadır.

2.3 Özellik Çıkarımı

Alüminyum, demir ve tahta örneklerine ait tüm veri setine GKA uygulanarak ÖKF'ler her bir örnek için elde edilmiştir. Zaman ve zaman-frekans düzleminde çıkarılan özellikler çizelge 2'de verilmiştir. Zaman düzlemindeki özellikler ÖKF 1'den, zaman-frekans düzlemindeki özellikler ise ÖKF 1'in HD'si alındıktan sonra elde edilen anlık genlik $A(t)$ ve anlık frekans $\omega(t)$ kullanılarak elde edilmiştir.

Çizelge 2. Öznitelikler

Zaman Düzlemi	**Zaman-frekans Düzlemi**
ÖKF 1'den çıkarılan özellikler	*A(t)* ve ω*(t)* 'den çıkarılan özellikler
Tepe genlik Tepeden tepeye genlik Form faktör (a) Hjorth parametreleri (etkinlik (b), hareketlilik (c), karmaşıklık (d)) Entropi (e)	Tepe genlik Eğim Standart sapma Ortalama genlik Aktif sinyal süresi Tepe frekans Ortalama frekans
$\sigma^2(x) = \frac{1}{N}\sum_{n=1}^{N}(x_n - \bar{x})^2$	$x' = f'(n) = \frac{dx}{dn}$ $x'' = f''(n) = \frac{d^2x}{dn^2}$
$a = \sqrt{\frac{\sigma^2\left(\frac{x''}{x'}\right)}{\sigma^2\left(\frac{x'}{x}\right)}}$ $b = \sigma^2(x)$ $c = \sqrt{\frac{\sigma^2(x')}{\sigma^2(x)}}$ $d = \frac{\text{hareketlilik}(x')}{\text{hareketlilik}(x)}$ $e = -\sum x_i \log x_i$	

3. BULGULAR VE TARTIŞMA

Öznitelikler alüminyum, demir ve tahta malzemelerinden alınan FA verilerine GKA ve HD uygulanarak elde edilen ÖKF'ler üzerinden elde edilmiştir. Bir örneğe ait ham FA sinyali ve ÖKF bileşenleri şekil 5'te verilmiştir. Şekildeki grafikler malzemeye ait FA sinyalin farklı frekanslardaki salınımlarını ifade etmektedir. Şekillerde ilk ÖKF'lerin yüksek frekans bileşenlerini barındırdığı, son ÖKF'ye doğru gidildikçe bileşenlerin periyotunda artma eğilimi olduğu görülmüştür.

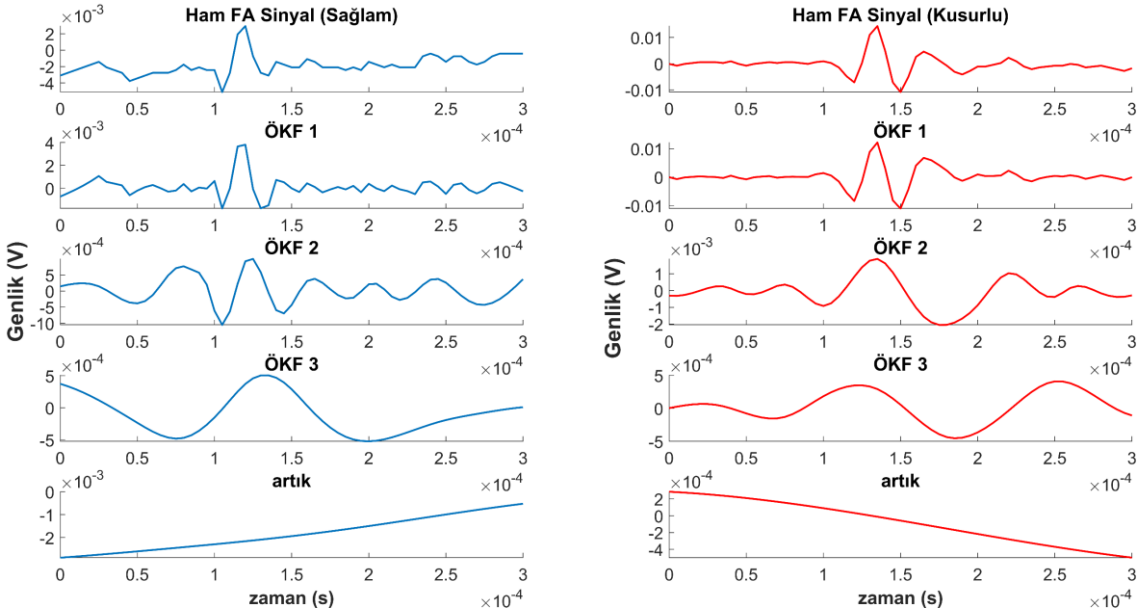

Şekil 5. Ham sinyal ve GKA bileşenleri

Şekil 6'da bir örnekten alınan ham FA sinyal ve GKA uygulanması sonucu elde edilen ÖKF grafikleri verilmiştir. Şekilde ham veriye ait grafikte sağlam ve kusurlu sinyaller arasında taban kayması olduğu görülmektedir. GKA uygulandıktan sonra elde edilen ÖKF sinyallerinde, ham sinyalde bulunan taban kayması önemli ölçüde kusurlu ve sağlam sinyaller arasında azaldığı şekildeki grafiklerde gözükmektedir. Özellikle ilk ÖKF'lerin ham sinyalde bulunan taban kaymasına, azaltıcı yönde etkisi daha baskın olduğu görülmüştür.

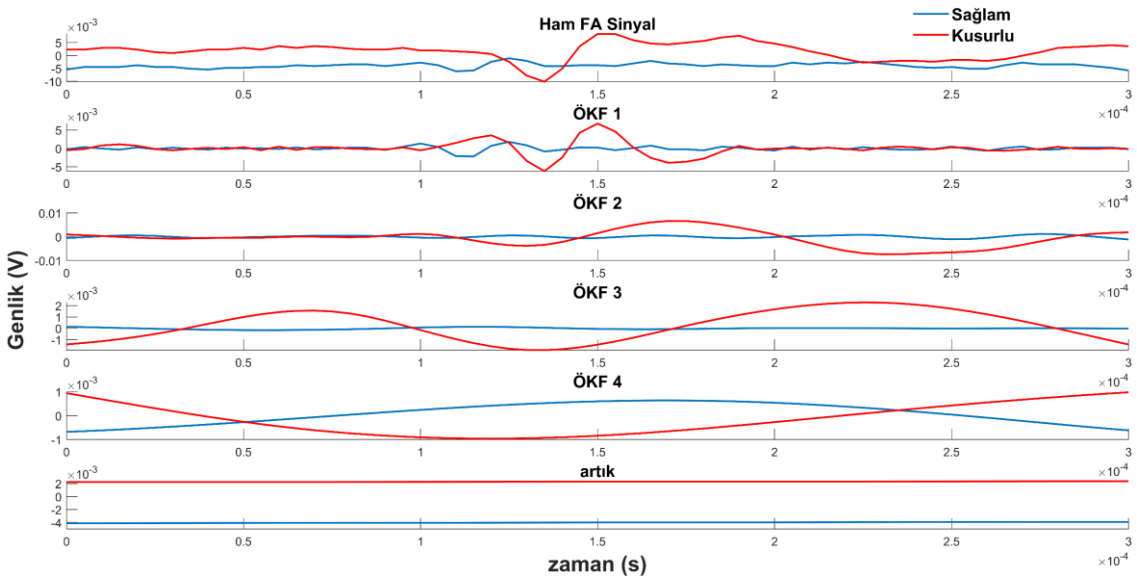

Şekil 6. GKA'nın FA sinyal üzerindeki taban kayması etkisi

Her bir malzeme ve sinyal için farklı sayıda ÖKF üretilmektedir. Ham sinyal birçok bileşen barındırabileceğinden bu sinyali temsil eden ÖKF veya orijinal sinyale en yakın ÖKF'nin belirlenmesi amacıyla ham sinyal ile ÖKF'ler arasındaki korelasyon katsayıları (Fisher, 1915) hesaplanmıştır. Korelasyon katsayıları çizelge 3'te verilmiştir. Ham sinyal ile birinci ÖKF arasındaki korelasyon katsayısı tüm örneklerde bire yakın çıkmıştır. Bu sonuçlar birinci ÖKF'nin sinyal analizi için daha uygun olduğunu göstermiştir ve özellik çıkarımı için ÖKF 1 kullanılmıştır.

Çizelge 3. Ham sinyal ve ÖKF'ler arası korelasyon katsayısı değerleri

	Korelasyon Katsayısı		
	ÖKF 1	**ÖKF 2**	**ÖKF 3**
Alüminyum	0.5949	0.5667	-
Demir	0.9617	0.1718	0.0815
Tahta	0.9274	0.5079	0.2841

GKA ile elde edilen birinci ÖKF'lere HD uygulanarak ÖKF'lere ait anlık frekans $\omega(t)$ ve anlık genlik $A(t)$ izgeleri elde edilmiştir. Alüminyum, demir ve tahta örneklerine ait anlık genlik ve anlık frekans grafikleri şekil 7'de verilmiştir.

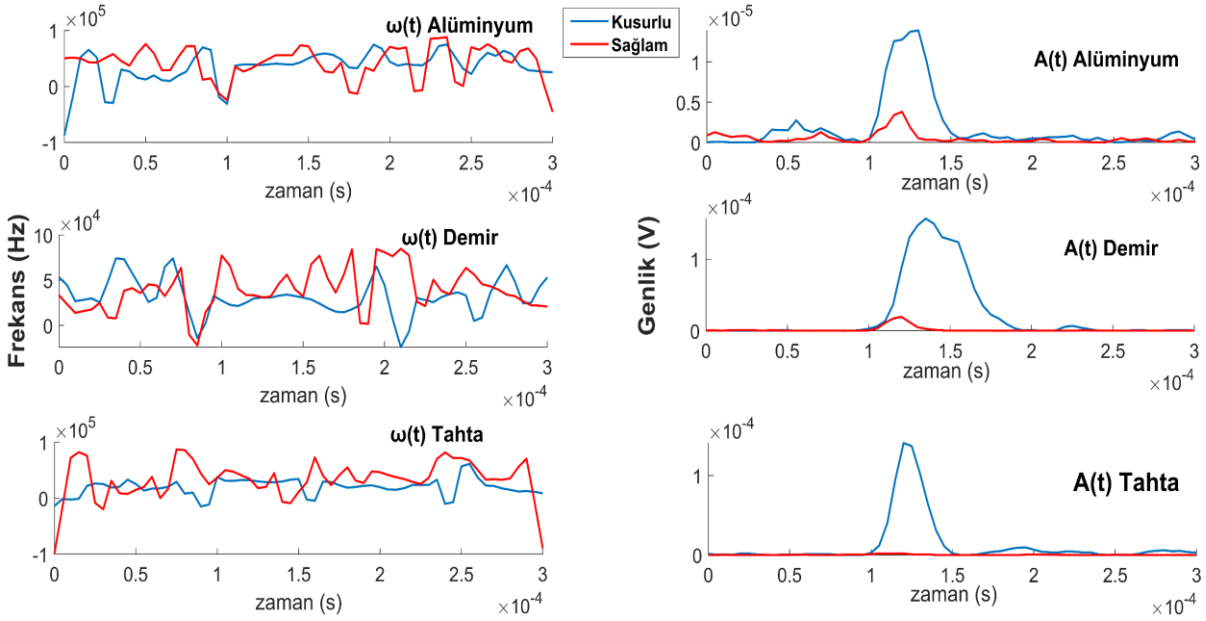

Şekil 7. Materyallerin *A(t)* ve *ω(t)* grafikleri

Şekil 7'de verilen grafikler ışığında malzeme sınıflarının anlık genlik izgesinin, anlık frekans izgesine göre sağlam ve kusurlu örnekler üzerinde ayırt ediciliğinin daha yüksek olduğu görülmüştür.

Malzemelere ait özelliklerin çıkarılmasının ardından, sınıflandırıcı eğitimlerine geçilmiştir. Bu çalışmada, diğer bazı sınıflandırma algoritmalarına kıyasla daha az karmaşık bir yapıya sahip olduğu, bu nedenle daha hızlı eğitildiği ve daha az kaynak tüketiminden dolayı (Kumar ve Sowmya, 2021), k-En Yakın Komşu (k-NN) (Zhang ve ark., 2018) sınıflandırıcı olarak belirlenmiştir ve çıkarılan bu 14 adet özellikle eğitilmiştir. k-NN için 1 komşuluk parametre olarak girilmiştir. Sınıflandırıcı eğitimi için çapraz doğrulama yöntemi olarak birini dışarıda bırak çapraz doğrulama yöntemi uygulanmıştır.

Çizelge 4. Sınıflandırıcı için kusurlu örnekleri tespit etme doğruluk değerleri

	Materyal	**Kusurlu Materyal Tespit Etme Doğruluk Değeri (%)**
Sınıf içi	Alüminyum	100
	Demir	100
	Tahta	100
Tüm materyallerin dahil olduğu durum	(Alüminyum + Demir + Tahta)	97.77

k-NN için eğitim sonucu doğruluk değerleri çizelge 4'te verilmiştir. Tablodaki değerler ışığında her bir malzeme gurubu için sınıf içi eğitim sonucu sınıflandırma doğruluk değerlerinin, tüm malzemelerin dahil olduğu sınıf içi eğitim sonucu doğruluk değerlerinden daha yüksek başarımda bir doğrulukla sınıflandırma yaptığı görülmüştür. Sınıf içi doğruluk değeri üç farklı materyalin de kendi özelinde kusurlu örneklerinin tespitini, tüm materyallerin dahil olduğu durum ise üç farklı materyalin de dahil olduğu, materyal türü farketmeksizin kusurlu örneğin tespit edildiği durumu ifade etmektedir.

Bu çalışmada uyguladığımız yöntem ile hem ham sinyal üzerindeki gürültü giderilerek faydalı sinyalin salınımı elde edilmiştir, hem de sinyalden özellik çıkarımı yapılmıştır. Literatürde bir malzeme özelinde yapılan çalışmaların aksine, uygulanan yöntem ile şekil 2'de verilen farklı kusurların bulunduğu ve farklı malzemeler için ortak bir sınıflandırma çerçevesi geliştirilmiştir (Jeon ve ark., 2016; Setiawan ve ark., 2018; Sun ve ark., 2014; Vangi ve ark., 2021; Yan ve ark., 2012;

Zakrzewski ve ark., 2010). Çizelge 4'te verilen sınıflandırıcı doğruluk değerleri uyguladığımız yöntemin başarımını desteklemektedir.

4. SONUÇ

Bu çalışmada, FA yöntemi kullanarak malzemelerde kusur tespiti için bir yöntem önerilmiştir. Kusurlu malzeme sinyal değişimlerini zaman ve zaman-frekans düzleminde analiz etmek için düşük maliyetli FA sistem geliştirilmiştir. Malzemelerden elde edilen FA sinyallere GKA analizi uygulanarak, sinyalin bilgilendirici salınımlarını ifade eden ÖKF'ler elde edilmiştir. Böylece, makine öğrenimi algoritmaları yardımıyla malzeme sınıf içi ve malzemeler arası, FA tabanlı kusur tespiti başarıyla gerçekleştirilmiştir.14 adet özellik, sinyallerin en bilgilendirici ÖKF'lerinden çıkarılmış ve k-en yakın komşu algoritması bu özelliklerle eğitilmiştir. Önerilen yöntem alüminyum, demir ve tahta malzemeleri üzerinde test edilmiş, tek bir malzeme için sınıf içi ve tüm malzemelerin dahil olduğu sınıf içi sınıflandırma doğruluk değerleri sırasıyla %100 ve %97.77 doğruluk değeriyle gerçekleşmiştir.

5. TEŞEKKÜR

Bu çalışma, Bursa Teknik Üniversitesi Bilimsel Araştırma Projeleri Koordinatörlüğü Birimi tarafından "210D003" kodlu proje ile desteklenmiştir.

6. ÇIKAR ÇATIŞMASI

Yazarlar, bilinen herhangi bir çıkar çatışması veya herhangi bir kurum/kuruluş ya da kişi ile ortak çıkar bulunmadığını onaylamaktadırlar.

7. YAZAR KATKISI

Ahmet MERT çalışmanın kavramsal ve tasarım süreçlerinin belirlenmesi ve yönetimi, Zekeriya BALCI veri toplama, veri analizi, tasarım süreçlerinin geliştirilmesi ve yorumlama süreçlerinde çalışmaya katkı sağlamışlardır.

8. KAYNAKLAR

Arslan, M., Toplan, N., AA6061 Serisi Alüminyum Plakalarına Yapılan MIG ve TIG Kaynak Tamirlerinin Tahribatlı ve Tahribatsız Testlerle İncelenmesi. J. Mater. Mechat. A 4, 333–354, 2023.

Beard P.C., Photoacoustic imaging of blood vessel equivalent phantoms. Biomedical Optoacoustics III 4618, 54–62, 2002.

Bell A.G., On the production and reproduction of sound by light. American Journal of Science 3(20), 305–324, 1880.

Chen S.L., Tian C., Recent developments in photoacoustic imaging and sensing for nondestructive testing and evaluation. Visual Computing for Industry, Biomedicine, and Art 4, 6, 2021.

Fisher R.A., Frequency Distribution of the Values of the Correlation Coefficient in Samples from an Indefinitely Large Population. Biometrika 10, 507–521, 1915.

Huang N.E., Shen Z., Long S.R., Wu M.C., Shih H.H., Zheng Q., Yen N.C., Tung C.C., Liu H.H., The empirical mode decomposition and the Hilbert spectrum for nonlinear and non-stationary time series analysis. Proceedings of the Royal Society of London Series A 454, 903–998, 1998.

Jeon S., Kim J., Yun J.P., Kim C., Non-destructive photoacoustic imaging of metal surface defects. J. Opt. 18, 114001, 2016.

Jin Y., Yin Y., Li C., Liu H., Shi J., Non-Invasive Monitoring of Human Health by Photoacoustic Spectroscopy. Sensors 22, 1155, 2022.

Keeratirawee K., Furter J.S., Hauser P.C., Low-cost electronic circuitry for photoacoustic gas sensing. HardwareX 11, e00280, 2022.

Keeratirawee K., Hauser P.C., Photoacoustic detection of ozone with a red laser diode. Talanta 223, 121890, 2021.

Kot P., Muradov M., Gkantou M., Kamaris G.S., Hashim K., Yeboah D., Recent Advancements in Non-Destructive Testing Techniques for Structural Health Monitoring. Applied Sciences 11, 2750, 2021.

Kumar V.P., Sowmya I., A review on pros and cons of machine learning algorithms. Journal of Engineering Sciences 12, 272–276, 2021.

Li C., Qi H., Zhao X., Guo M., An R., Chen K., Multi-pass absorption enhanced photoacoustic spectrometer based on combined light sources for dissolved gas analysis in oil. Optics and Lasers in Engineering 159, 107221, 2022.

Li J., Chen Y., Ye W., Zhang M., Zhu J., Zhi W., Cheng Q., Molecular breast cancer subtype identification using photoacoustic spectral analysis and machine learning at the biomacromolecular level. Photoacoustics 30, 100483, 2023.

Liao Z., Zhang J., Gan Z., Wang Y., Zhao J., Chen T., Zhang G., Thermal runaway warning of lithium-ion batteries based on photoacoustic spectroscopy gas sensing technology. International Journal of Energy Research 46, 21694–21702, 2022.

Mert A., Akan A., Emotion recognition from EEG signals by using multivariate empirical mode decomposition. Pattern. Anal. Applic. 21, 81–89, 2013.

Nakazawa H., Tokumine J., Lefor A.K., Yamamoto K., Karasawa H., Shimazu K., Yorozu T., Use of a photoacoustic needle improves needle tip recognition in a video recording of simulated ultrasound-guided vascular access: A pilot study. J. Vasc. Access 0, 11297298221122137, 2022.

Setiawan A., Suparta G.B., Mitrayana M., Nugroho W., Surface Crack Detection with Low-cost Photoacoustic Imaging System. IJTech 9, 159, 2018.

Shiraishi D., Kato R., Endoh H., Hoshimiya T., Destructive Inspection of Weld Defect and its Nondestructive Evaluation by Photoacoustic Microscopy. Jpn. J. Appl. Phys. 49, 07HB13, 2010.

Strahl T., Steinebrunner J., Weber C., Wöllenstein J., Schmitt K., Photoacoustic methane detection inside a MEMS microphone. Photoacoustics 29, 100428, 2023.

Stylogiannis A., Prade L., Buehler A., Aguirre J., Sergiadis G., Ntziachristos V., Continuous wave laser diodes enable fast optoacoustic imaging. Photoacoustics 9, 31–38, 2018.

Sun M., Lin X., Wu Z., Liu Y., Shen Y., Feng N., Non-destructive photoacoustic detecting method for high-speed rail surface defects. IEEE International Instrumentation and Measurement Technology Conference (I2MTC), 12-15 Mayıs, 2014, Montevideo.

Tasmara F.A., Widyaningrum R., Setiawan A., Mitrayana M., Photoacoustic imaging of hidden dental caries using visible–light diode laser. Journal of Applied Clinical Medical Physics 24, e13935, 2023.

Vangi D., Banelli L., Gulino M.S., Interference-based amplification for CW laser-induced photoacoustic signals. Ultrasonics 110, 106270, 2021.

V.R. N., Mohapatra A.K., Nayak R., V.K. U., Kartha V.B., Chidangil S., UV laser-based photoacoustic breath analysis for the diagnosis of respiratory diseases: Detection of Asthma. Sensors and Actuators B: Chemical 370, 132367, 2022.

Wang S., Tran T., Xiang L., Liu Y., 2019. Non-Destructive Evaluation of Composite and Metallic Structures using Photo-Acoustic Method. AIAA Scitech 2019 Forum. 7-11 Ocak, 2019, San Diego.

Wong T.T., Performance evaluation of classification algorithms by k-fold and leave-one-out cross validation. Pattern Recognition 48, 2839–2846, 2015.

Wu S., Liu Y., Chen Y., Xu C., Chen P., Zhang M., Ye W., Wu D., Huang S., Cheng Q., Quick identification of prostate cancer by wavelet transform-based photoacoustic power spectrum analysis. Photoacoustics 25, 100327, 2022.

Xu M., Wang L.V., Photoacoustic imaging in biomedicine. Review of Scientific Instruments 77, 041101, 2006.

Yan L., Gao C., Zhao B., Ma X., Zhuang N., Duan H., Non-destructive Imaging of Standard Cracks of Railway by Photoacoustic Piezoelectric Technology. Int. J. Thermophys. 33, 2001–2005, 2012.

Yang L., Chen C., Zhang Z., Wei X., Glucose Determination by a Single 1535 nm Pulsed Photoacoustic Technique: A Multiple Calibration for the External Factors. J Healthc Eng 2022, 9593843, 2022.

Zakrzewski J., Chigarev N., Tournat V., Gusev V., Combined Photoacoustic–Acoustic Technique for Crack Imaging. Int. J. Thermophys. 31, 199–207, 2010.

Zhang S., Li X., Zong M., Zhu X., Wang R., Efficient kNN Classification With Different Numbers of Nearest Neighbors. IEEE Transactions on Neural Networks and Learning Systems 29, 1774–1785, 2018.

Zhang Y., Wang M., Yu P., Liu Z., Optical gas sensing of sub-ppm SO2F2 and SOF2 from SF6 decomposition based on photoacoustic spectroscopy. IET Optoelectronics 16, 277–282, 2022.

Zhang Z., Jin H., Zhang W., Lu W., Zheng Z., Sharma A., Pramanik M., Zheng Y., Adaptive enhancement of acoustic resolution photoacoustic microscopy imaging via deep CNN prior. Photoacoustics 30, 100484, 2023.

JOURNAL of
MATERIALS and MECHATRONICS:A

e-ISSN 2717-8811
JournalMM, 2024, 5(1), 14-35
https://doi.org/10.55546/jmm.1447858

Araştırma Makalesi / Research Article

Effect of Thermo-Reactive Diffusion Coatings on Microstructure and Wear Behavior of Powder Metallurgy Steel Cutting Inserts

Talat TURAN[1], Ali GÜNEN[2], Erdoğan KANCA[3*]

[1]Iskenderun Technical University, Faculty of Engineering and Natural Sciences, Department of Mechanical Engineering, Hatay, Turkey,
ORCID ID: https://orcid.org/0009-0000-4693-7163, turantalat46@gmail.com
[2] Iskenderun Technical University, Faculty of Engineering and Natural Sciences, Department of Mechanical Engineering, Hatay, Turkey,
ORCID ID: https://orcid.org/0000-0002-4101-9520, ali.gunen@iste.edu.tr
[3*]Iskenderun Technical University, Faculty of Engineering and Natural Sciences, Department of Mechanical Engineering, Hatay, Turkey,
ORCID ID: https://orcid.org/0000-0002-7997-9631, erdogan.kanca@iste.edu.tr

Geliş/ Received: 07.03.2024**;** **Revize/Revised:** 05.04.2024 **Kabul / Accepted:** 13.04.2024

ABSTRACT: In this study, powder metallurgy-produced 1.337 steel (PMS 1.3377) was subjected to boronizing, titanizing, and vanadinizing processes at 950 °C for 2 hours. The influence of boride and carbide coatings formed on the surface of PMS 1.3377 on the microstructure of these steels and their wear behaviors at room temperature and 500 °C were investigated. Characterization of the formed coating layers was carried out through Scanning Electron Microscopy (SEM-EDS), X-ray Diffraction (XRD), microhardness, and wear testing. Wear tests considering the cutting tool turning, milling, and drilling applications of PMS 1.3377 were conducted at room temperature and 500 °C in ambient air with a 10 N load and a 250 m sliding distance against an Al_2O_3 ball. Metallographic studies showed that coating layers with thicknesses of 98±2.1, 11±0.5, 13.5±0.6 µm and hardness of 2566±125 HV0.1, 2037±104 HV0.1, and 1800±197 were obtained by boronizing, titanizing and vanadinizing processes, respectively. The dominant phase structures in the obtained coatings were determined to be FeB, TiC, and VC for boronizing, titanizing, and vanadinizing, respectively. Due to the high hardness of boride and carbide phases and their ability to form more stable oxide layers during wear, the coated samples exhibited lower friction coefficients and lower wear volume losses. While untreated PMS 1.3377 experienced delamination and oxidation wear mechanisms at room temperature, the wear mechanism at 500 °C transformed into adhesive and oxidation wear. On the other hand, in the coated samples, the wear mechanism was found to occur as adhesive, oxidative, and delamination at both room temperature and 500 °C.

Keywords: Powder metallurgy, Thermo-reactive diffusion technique, Hardness, Friction, Wear.

*Sorumlu yazar / Corresponding author: erdogan.kanca@iste.edu.tr
Bu makaleye atıf yapmak için /To cite this article

Turan, T., Günen, A., Kanca, E. (2024). Effect of Thermo-Reactive Diffusion Coatings on Microstructure and Wear Behavior of Powder Metallurgy Steel Cutting Inserts. Journal of Materials and Mechatronics: A (JournalMM), 5(1), 14-35.

1. INTRODUCTION

Cutting inserts are essential components in various machining operations like turning, milling, and drilling, where they are used to shape workpieces accurately and efficiently (König et al., 1984; Gürbüz et al., 2020; Hasçelik and Aslantaş 2021). Powder metallurgy (PM) is a versatile and cost-effective method for producing cutting edges with tailored properties for various machining applications (Angelo et al., 2022; Aras et al. 2022). By utilizing metal powders, PM offers a wide range of material composition choices that may not be achievable through conventional methods (Erden et al., 2021). The production of cutting tools using the PM technique involves the development of composite materials through the consolidation of metal powders (Rizzo et al., 2020). This process allows for the creation of cutting edges with enhanced properties such as wear resistance, hardness, and dimensional stability. Studies have shown that PM is energetically efficient and economically feasible for producing both simple and complex cutting edge designs to meet specific dimensional requirements (Şap et al., 2021; Nayak et al. 2022; Gökmen, 2023).

Furthermore, advancements in PM technology have enabled the production of cutting tools with improved machinability, microstructural properties, and corrosion resistance. By optimizing sintering parameters and material compositions, PM offers a viable route for fabricating cutting tools with superior mechanical and corrosion properties (Nayak et al., 2022; Sathish et al., 2021). The unique advantages of PM, such as near-net shape forming capabilities and freedom in material composition selection, make it an attractive method for producing cutting edges with tailored properties (Angelo et al., 2022; Somunkıran et al., 2022). Researchers have also explored the impact of PM on the tribological behavior and machinability of cutting edges, highlighting the potential for enhancing cutting performance through PM-synthesized materials (Aras et al., 2022; Liu et al., 2023).

Although cutting inserts produced by powder metallurgy are used in many machinability applications, the corrosive working conditions to which these inserts are exposed have revealed the need for studies to increase the lifespan of these inserts. For this purpose, alloying these metal tips or making surface modifications as a secondary process are among the main topics studied (Rizzo et al., 2020; Erden et al., 2021; Vijaya Kumar and Velmurugan 2022). Although these methods have advantages and disadvantages compared to each other, the fact that cutting inserts end their useful life due to surface damage has made the improvement of these materials with surface modifications often a cost-effective method. Recent advancements in cutting edge coatings have been focused on improving tool performance and sustainability. Strategies such as applying advanced coatings like TiAlN, AlCrN, and TiCN on cutting inserts have been explored to enhance tool wear resistance, reduce cutting forces, and improve surface quality during machining processes (Daicu et al., 2017; Mathivanan et al., 2021). These coatings have demonstrated potential in extending tool life and enhancing machining efficiency, particularly when working with challenging materials such as super duplex stainless steels and nickel-based superalloys (Khan & Gupta, 2020).

The utilization of 1.3377 cutting tools produced by the powder metallurgy method offers a promising approach for developing cutting edges with enhanced properties tailored to meet the demands of modern machining processes. Powder metallurgy enables the production of cutting tools with superior wear resistance, hardness, and dimensional stability through the consolidation of metal powders. This method allows for the creation of cutting tools with improved mechanical properties and corrosion resistance, contributing to enhanced machining efficiency and prolonged tool longevity (Fang et al., 2017; Gevorkyan et al., 2021).

Boronizing, titanizing, and vanadinizing coatings produced by thermo-reactive methods offer significant advantages when applied to materials produced by the powder metallurgy and casting methods (Arai 2015; Kayalı and Yalçın 2020; Ghadi et al., 2023; Turgut and Günen 2020; Günen et al., 2023). Boriding coatings enhance wear resistance and hardness, crucial for materials used in cutting tools, thereby extending tool life and improving machining efficiency (Günen et al. 2016). Titanizing coatings provide enhanced mechanical properties and corrosion resistance, ideal for materials requiring durability and protection against environmental factors (Pashechko et al., 2020). Vanadinizing coatings improve adhesion properties, making them valuable for applications where strong bonding is essential (Dement et al., 2018).

The thermo-chemical methods used to produce these coatings allow for precise control over the coating process, ensuring that the coatings are tailored to the specific properties required for materials produced by powder metallurgy. Boriding, titanizing, and vanadinizing coatings offer advantages such as improved wear resistance, enhanced mechanical properties, and increased corrosion resistance, making them valuable for enhancing the performance and longevity of materials produced by powder metallurgy (Duran et al., 2021; Calik et al., 2021; Pashechko et al., 2020; Dement et al., 2018). Additionally, the ability to combine these coatings with powder metallurgy materials further enhances their benefits, offering a comprehensive solution for improving material properties and performance (Çaligülü et al., 2021).

In this study, it was aimed to improve the surface hardness and wear resistance of PMS 1.3377 cutting tools produced by the powder metallurgy method by applying boriding, titanizing and vanadinizing. In this context, PMS 1.3377 was subjected to boriding, titanizing and vanadinizing processes at 950 °C for 2 hours, creating boride or carbide phases on the surface. The influence of boride and carbide coatings formed on the surface of PMS 1.3377 on the microstructure of these steels and their wear behaviors at room temperature and 500 °C were investigated.

2. MATERIALS AND METHODS

2.1 Materials

The powder metallurgy-produced 1.3377 steel (1.3377 PMS) used in this study was purchased from KORKMAZ ÇELİK AŞ (Istanbul, Turkey). This powder metallurgy steel is widely used in turning, milling, CNC cutting and drilling applications. The chemical composition of the 1.3377 powder metallurgy steel, obtained from the technical documentation provided by the supplier company, is presented in Table 1.

Table 1. Chemical composition of 1.3377PMS.

Material	C	Cr	Mo	W	Co	V	Fe and impurities
1.3377	1.50	4.0	2.5	2.5	-	4.0	Balance

2.2 Determination of Used Powders and Coating Methods

Based on the satisfactory results obtained in TRD studies in the literature in improving the wear resistance of high carbon content steels, it was decided to use B_4C, Fe-Ti and Fe-V powders as coating powders (Kurt et al., 2018; Turgut and Günen 2020; Günen et al., 2020). $NaBF_4$ was used as an activator for boronizing, while NH_4CI activator was used for titanizing and vanadinizing. Ferro vanadium powder consists of 82% V, 1.5% Al, 0.25% C, 0.03% P, and 0.03% S, with a density of 6.4 g/cm³ and particle size <91 μm. B_4C powder is composed of 95% B_4C, with a density of 2.52

g/cm³ and a particle size <25 μm. Ferro titanium powder contains 73% Ti, 4% Al, 0.5% C, 0.25% Si, 0.02% S, and the balance is Fe, with a density of 3.95 g/cm³ and a particle size <43 μm. The weight percentages of the powders used in the coating processes were determined based on previous studies in the literature (Kurt et al., 2018; Turgut and Günen, 2020; Günen et al., 2020). Due to the necessity for a more economical industrial-scale coating process, a decision was made to use a cost-effective and high-quality ferroalloy instead of pure powders. Table 2 presents the powders used for the three coatings and their weight ratios.

Table 2. Weight percentages of powders used in the coating processes.

TRD processing	B_4C	$NaBF_4$	Fe-Ti	Fe-V	Al_2O_3	NH_4Cl
Boronizing	90	10	-	-	-	-
Titanizing	-	-	45	-	45	10
Vanadinizing	-	-	-	45	45	10

2.3 Preparation of Samples for Coating Process

Prior to the coating process, samples obtained from the company were acquired with rough dimensions of 20 × 30 × 1000 mm³. Precise machining techniques were employed on the sample to bring it to its final dimensions. Machining processes included milling, drilling, and cutting techniques. The surface of the sample was gradually polished using 1200-grit SiC sand paper through precision sanding. Considering that three different coating processes would be applied to samples measuring 19 × 19 × 8 mm³, three samples were manufactured for each type of coating. For optical, SEM, EDS, XRD tests, and analyses, samples measuring 10 × 10 × 10 mm³ were prepared from these larger samples. The prepared sample for the coating process is illustrated in Figure 1.

Due to the high temperatures involved in the coating process, and considering the affinity of the ferro powder components used to oxygen, a 20 mm-thick layer of Al_2O_3 powder was applied to the top surface of the powders. This layer was sealed with an airtight cover to prevent contact with oxygen. The coating steps are shown in Figure 1. Coating processes were carried out by placing the samples embedded in coating powders within air-tight steel crucibles in an atmosphere-controlled furnace at 950 ºC for 2 hours. Subsequently, the crucibles were left to cool in an open-air environment as stated in the previous study (Günen et al. 2022b).

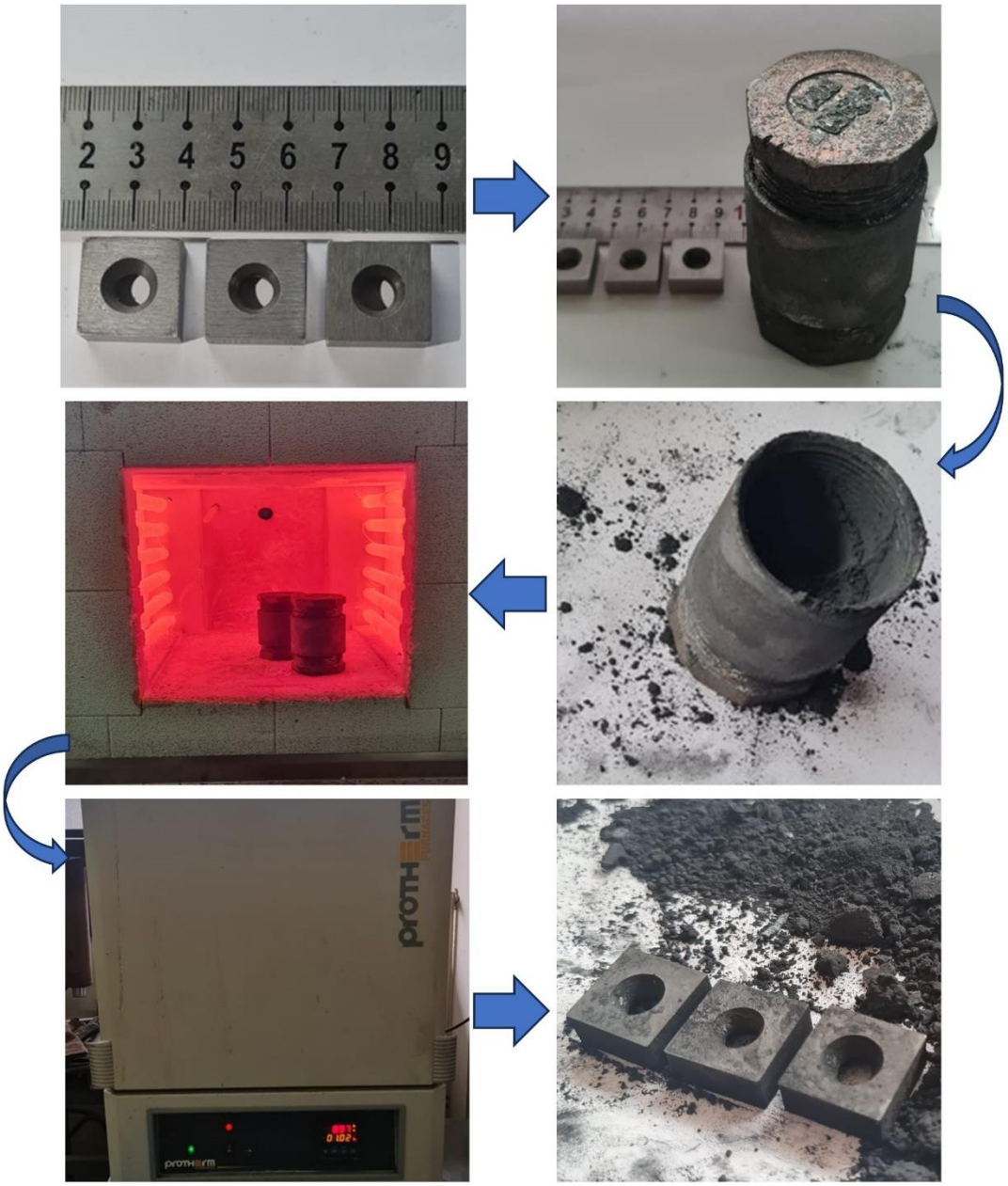

Figure 1. Representation of coating process steps.

2.4 Metallographic Studies

The coated specimens were precision-cut into dimensions of 10×10×5 mm³ using a precision cutter for microstructural analysis, hardness testing, corrosion analysis, wear testing, and XRD analysis. Following the cutting process, the specimens designated for microstructure examinations were embedded in hot bakelite, and subsequent polishing steps with SiC sandpaper ranging from 320 to 2500 grit were performed. Subsequently, precise polishing was achieved using 3 and 1-micron diamond solutions to obtain a mirror-like smooth surface. For a clearer observation of grain boundaries, the specimens were etched with a 3% nital solution for 3-6 seconds.

The Thermo Fisher Scientific Apreo S SEM device was employed for SEM analysis. In addition to SEM examinations, EDS and X-ray methods were utilized to identify carbides and phases formed in coating layers and intermediate regions. For XRD analysis, a Malvern Panalytical EMPYREAN device was used, applying 30mA and 40kV current and voltage values with Cu-K-α radiation at room

temperature. Diffraction patterns were recorded in the angular range of 10 to 90° at a fixed grazing angle (0.8°), obtaining a strong signal at a speed of 2°/minute and a step size of 0.02°.

Following the acquisition of X-ray diffraction patterns, the corresponding phases were determined through library scanning using the PDXL (Integrated Powder X-ray Diffraction Software) software. Microhardness measurements were performed using an EMCOTEST DuraScan 70 G5 device, employing the Vickers hardness method with a diamond pyramid tip under 50 gf load and 15 s dwell times. Hardness measurements of coating layers were conducted by moving from the cross-sectional surface towards the interior, leaving a minimum distance of twice the indentation size between traces. At least 5 hardness values were obtained for each coating layer, and their averages were considered as the hardness value for that specific layer.

2.5 Wear Test

Untreated 1.337 PMS and samples coated with three different methods were subjected to wear tests using a ball-on-disk type adhesive wear testing machine. The wear tests were performed at room temperature and 500 °C, applying a 10 N load, 250 mm/s speed, and against a 6.3 mm diameter Al_2O_3 ball. In a study evaluating the wear behavior of hardfacing alloys, Al_2O_3 balls with a hardness value of 2720 HV0.05 were used in experiments, highlighting their robustness (Kılınc et al., 2022). All Wear Test parameters are given in Table 3. To ensure the accuracy of the results, each test was repeated three times, and volume and friction coefficients were measured. The data obtained from these tests were organized in Excel, taking the arithmetic average of the results. After the wear tests, the width and depth of the circular wear tracks were measured at 0°, 90°, 270°, and 360° for each sample using an optical microscope and a 2D profilometer. The shape of the resulting wear track was observed to be semi-elliptical and was calculated in Excel using the formula below, based on previous studies (Gunen et al., 2022b; Gunen ve Ergin 2023).

Table 3. Wear test parameters

Wear Test Parameters	
Temperature	24ºC, 500 ºC
Load	10 N
Speed	250 mm/s
Test ball	6.3 mm diameter Al_2O_3

$$L = 2\pi r \quad (1)$$

$$V = 0.25\pi WD \quad (2)$$

$$Wr = V/FS \quad (3)$$

Where, L represents the length of the wear track (mm), V stands for the wear track volume (mm^3), r denotes the radius of the wear track (mm), W is the average width of the wear track (μm), D represents the average depth of the wear track (μm), F corresponds to the applied load (N), S is the sliding distance (m), and Wr is the wear rate (mm^3/Nm) (Günen et al., 2022a).

3. RESULTS AND DISCUSSION

3.1 XRD Analyses and Microstructure

XRD analyses were conducted to determine the phase structure of the untreated PMS 1.337 sample and coated samples. The obtained XRD patterns are presented in Figure 2.

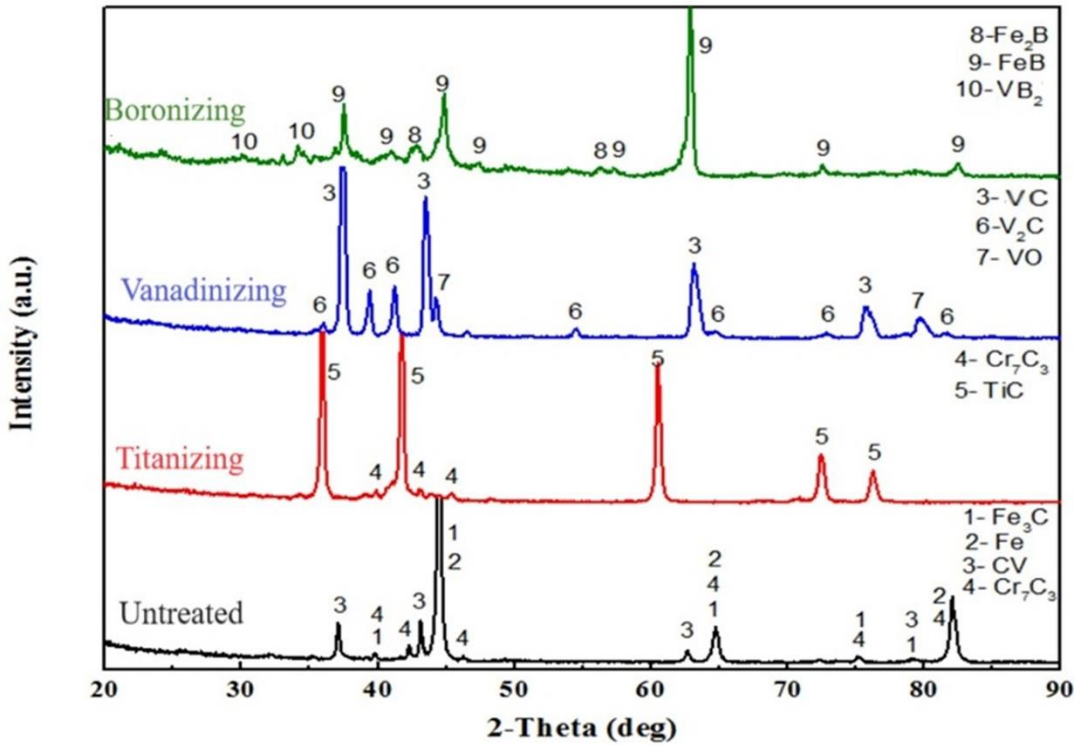

Figure 2. XRD patterns of untreated PMS 1.337 and coated samples.

As seen in Figure 2, the untreated PMS 1.3377 sample exhibits a dominant austenite peak at 44.80°, along with low levels of Fe_3C, VC, and Cr_7C_3 peaks, in accordance with the chemical composition of the PMS 1.337. In the boronized sample, the dominant phase is identified as FeB at 36.74°, 44.8°, and 63.33°, accompanied by a lower presence of Fe_2B and V_2B phases. The vanadinized sample reveals the dominance of the VC phase at 37.5°, 43.5°, 63.5°, and 76.0° along with the emergence of V_2C and VO phases. For the titanized sample, the presence of TiC phases is evident at 36°, 42.5°, 60°, 72.5°, and 76.5° degrees, alongside the detection of Cr_7C_3 phases. The obtained phase structures align with previous studies on boronizing, titanizing, and vanadinizing on steels, as reported in the literature (Şen 2004; Kurt et al. 2018; Karakaş 2020; Çakır 2022).

To validate the accuracy of the obtained phases in XRD analyses, the samples were examined using SEM, and EDS line analyses were conducted along the coating layers. SEM images taken from the cross-sectional surfaces of the coatings and EDS line analyses are presented in the range of Figure 3 to Figure 5.

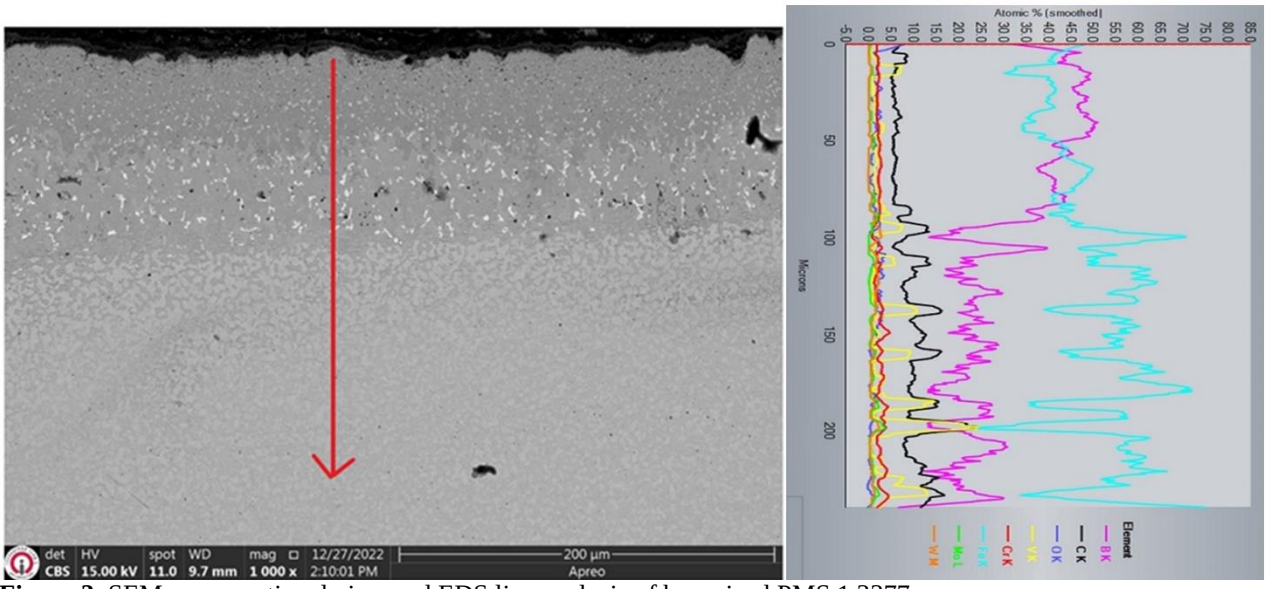

Figure 3. SEM cross-sectional view and EDS line analysis of boronized PMS 1.3377.

Upon examining the SEM microstructure image of the boride layer formed at 950°C for 2 hours using the TRD method (Figure 3), a continuous coating layer of approximately 100 µm along the surface, free from issues such as cracks and porosity, is observed. The EDS line analysis confirms that this layer is composed of Fe and B, validating its identification as a boride layer, as indicated in XRD analyses. Further analysis of the boron layer reveals a slight difference in boron content between the 0-50 µm range and the 50-100 µm range. The boron and iron ratios in the 0-50 µm range, around 50%, suggest the formation of the FeB phase in this region, consistent with XRD analyses. As the boron ratio decreases to approximately 35-40% and the iron ratio increases to around 60% in the 50-100 µm range, it indicates a decrease in diffusion from the surface towards the interior, and this region corresponds to the formation of the Fe2B phase, in accordance with XRD analyses. A transition region of approximately 20-25 µm is clearly observed both in the microstructure image and EDS line analysis beneath the 100 µm coating layer. The presence of a transition region between the coating layer and the substrate is a consequence of thermo-reactive coatings being diffusional coatings, resulting in higher adhesion between the coating and the substrate compared to coatings such as non-diffusional coatings and thermal spray coatings (Kara et al., 2016; Kurt et al., 2020; Campos-Silva et al., 2023)

Upon examining the SEM microstructure image of the sample treated with titanizing at 950°C for 2 hours using the TRD method (Figure 4), it is observed that a coating layer of approximately 10 µm has formed on the surface. This coating layer exhibits a dense and continuous uniform coating. EDS line analysis reveals that the atomic ratio of Ti in the coating layer is in the range of 60-65%, while the C content decreases from 40% to 30%. The very low presence of elements other than Ti and C in the coating layer indicates that the Cr_7C_3 phase determined in XRD analyses originates from the substrate material rather than the coating layer, and the coating layer consists solely of TiC. EDS line analysis shows that an extremely thin (~2 µm) transition region has formed between the coating layer and the matrix (Zakharov et al., 1989; Kasprzycka, E. 2015), and beneath this region, it exhibits a chemical composition consistent with the chemical composition of the 1.3377 powder metallurgy steel.

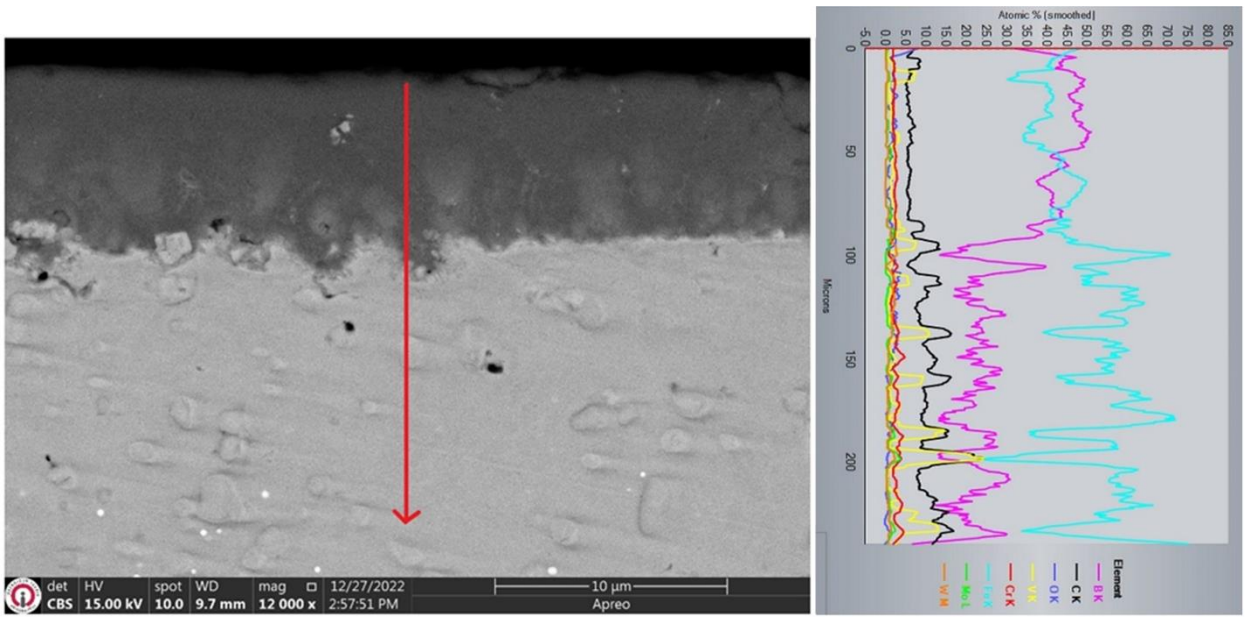

Figure 4. SEM cross-sectional view and EDS line analysis of titanized PMS 1.3377.

Considering the SEM microstructure image of the sample treated with vanadinizing at 950°C for 2 hours using the TRD method (Figure 5), it is observed that the coating layer is thicker compared to nitriding but thinner compared to boronizing, with a thickness of approximately 14-15 µm. Analysis of the coating layer through SEM microstructure images and EDS line profile indicates the presence of non-homogeneous regions, unlike boronizing and titanizing. In EDS line analyses, it is determined that these non-homogeneous regions consist of V and C, in addition to Fe and O_2. This may be attributed to insufficient oxidation prevention measures for vanadium nitriding due to the implementation of the coating process in an open-air environment (Çakır 2022).

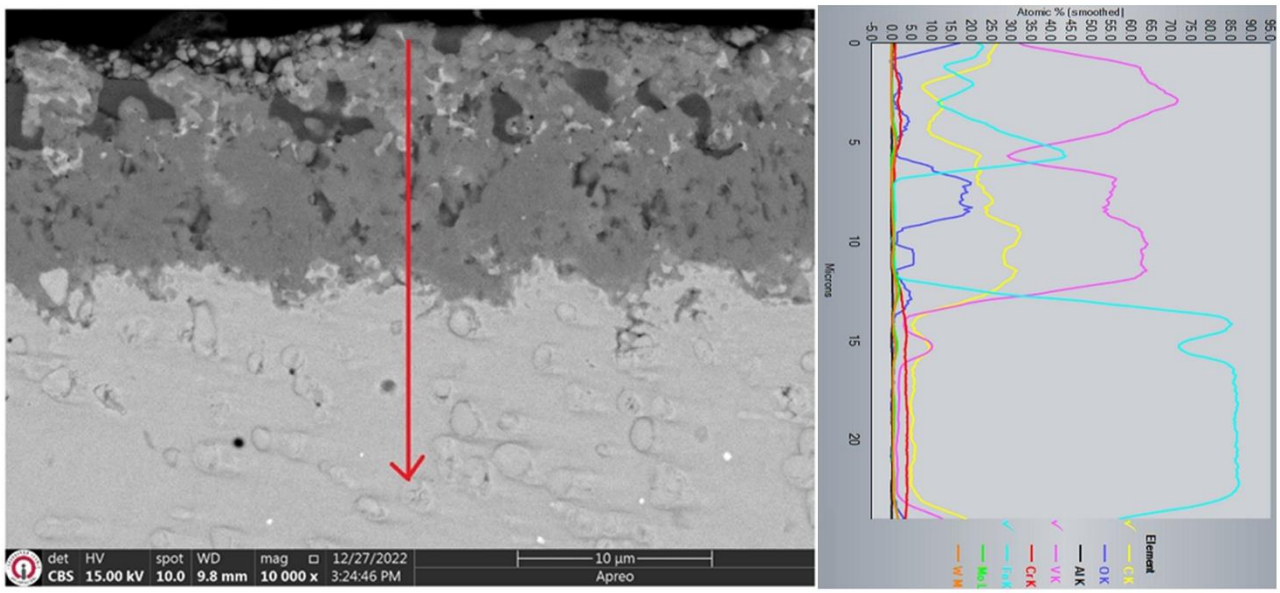

Figure 5. SEM cross-sectional view and EDS line analysis of vanadinized PMS 1.3377.

The coatings applied to PMS 1.3377 are aimed at enhancing wear resistance by improving the surface hardness of this alloy. The microhardness values of the coatings were determined using the Vickers method, and the obtained data are presented in Table 4.

Table 4. Microhardness values obtained based on TRD methods.

Sample	Coating thickness (µm)	Micro-hardness ($HV_{0.1}$)
Boronizing	98 ± 2.1	2566± 125
Titanizing	11 ±0.5	2037± 104
Vanadinizing	13.5 ±0.6	1800± 197
PMS 1.3377	-	334±30

Upon examining Table 3, it is observed that the coating layer thicknesses are approximately 98±2.1 µm for boronizing, 11±0.5 µm for tetanizing and finally, 13.5±0.5 µm for vanadinizing coating. Analyzing the microhardness values reveals measurements of 2566 HV0.1 for boronizing, 2037 HV0.1 for TiC layer, and 1800 HV0.1 for VC. When evaluating the microhardness values, it is noted that the hardness value of 2566 HV identified in boronizing is higher than the literature-specified hardness values for FeB 1900-2100 HV and Fe_2B 1650-1850 HV (Kayali et al., 2010; Campos-silva et al., 2023). This may be attributed to the V_2B phase formed within the two boride layers. On the other hand, the detection of TiC phase, specified as 3200 HV in the literature (Kurt et al. 2018), and VC phase, specified as 2950 HV (Günen et al. 2020), at lower hardness values in titanium coating can be attributed to the formation of Cr7C3 in titanium coating and V2C and VO phases in vanadium coating, which are present in low amounts in the coating content.

3.2 Wear Behaviors

In order to gain insights into the behavior of the friction coefficient during the wear test, the friction coefficient was measured. The obtained data was processed using Excel, and graphs for room temperature and 500 °C were prepared, as presented in Figure 6.

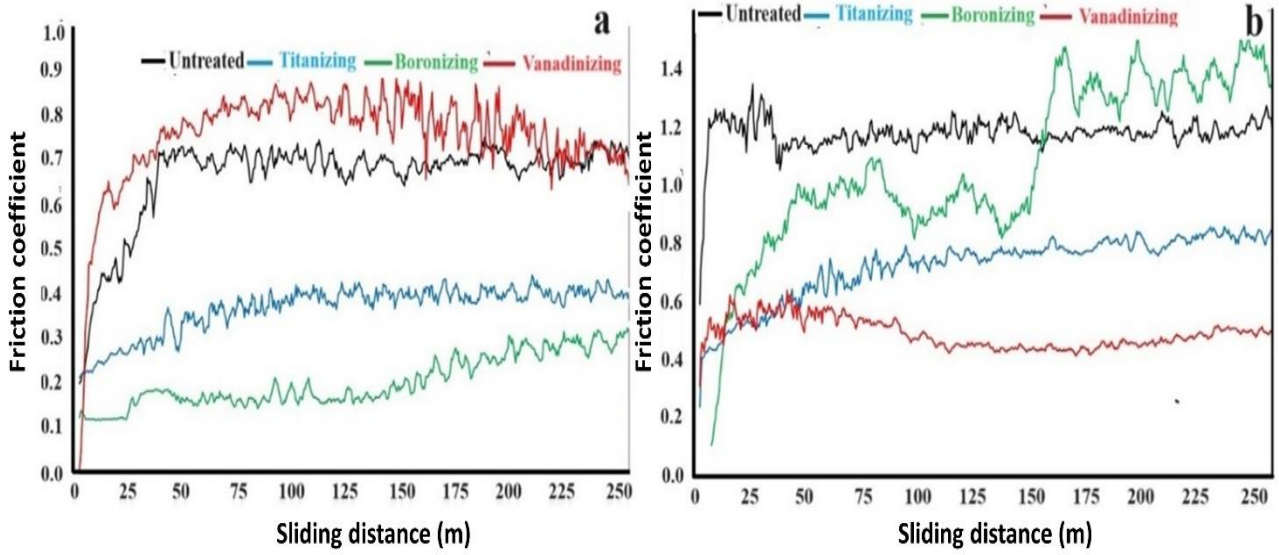

Figure 6. Friction coefficient of untreated PMS 1.337 and coated specimens at a) room temperature b) 500 °C.

Considering Figure 6a, it is observed that the 1.3377 PMS specimen exhibits a rapid increase to the level of 0.7 within the first 20 m, followed by a zigzag trend in the range of 0.65-0.75 until the end of the test. In Figure 6a, the titanized specimen shows a slight increase in the friction coefficient, starting from 0.2 and ending at the level of 0.35 at the end of the test. Therefore, it can be stated that the titanized specimen exhibits a significantly lower friction coefficient compared to the untreated specimen. Similarly, the boronized specimen shows a lower friction trend compared to the titanium-

coated specimen. However, when examining the friction coefficient graph of the vanadinized specimen, it is observed that there are periods (25-200 m) where the friction coefficient is higher than the untreated specimen, and it eventually concludes at the same level as the untreated specimen at the end of the test. Considering the overall friction coefficients of room temperature wear testing, it can be concluded that boride and titanium coatings exhibit lower friction coefficients compared to the untreated specimen. However, the higher friction coefficient observed in vanadium coating suggests that hardness values have a positive effect on reducing friction (Kato 200; Gutierrez-Noda et al., 2019; Türkmen and Yalamaç 2021). Nevertheless, in the case of coating layer inhomogeneity, some regions may wear out more quickly, leading to an increase in friction coefficients due to the abrasive effect of the worn surfaces.

From the wear tests conducted at 500 °C, the friction coefficient graphs (Figure 6b) reveal that the friction coefficient of untreated PMS 1.3377 rapidly increases in the 0-25 m range, slightly decreases in the 25-50 m range, and shows a fluctuating pattern of increase and decrease between 50-160 m, continuing with horizontal zigzag movements until the completion of the test. The friction coefficient of untreated PMS 1.3377 starts at 0.6 and peaks and reach to 1.38. Analyzing the friction coefficient graph of the titanized sample at 500 °C shows a slight increase similar to room temperature but with the friction coefficient approximately doubling. In this case, the friction coefficient starts at 0.2 and reaches maximum levels around 0.8. For the boronized sample, a continuous increase is observed in the 0-75 m range, followed by a decrease up to 150 m, a rapid increase between 150-175 m, and subsequent fluctuations of increases and decreases until the end of the test. Examining the entire test, the friction coefficient starts at 0.1 and reaches up to 1.5. This is believed to result from the sintered hard boride layer undergoing oxidation at high temperatures, acting as an abrasive between the abrasive ball and the substrate material (Zhang et al., 2023). Finally, for the vanadinized sample, the friction coefficient starts at 0-25 m, reaches around 0.5 in the 25-50 m range, experiences a slight increase from 75-125 m, and exhibits a mild increase from 175 m until the end of the test. Therefore, in high-temperature wear tests, the coatings undergo faster oxidation compared to room temperature, leading to the abrasive function of broken particles in hard coatings. This complex behavior is attributed to the formation, breakage, and regeneration of oxide layers by the complex boride and carbide phases within the structure. As long as the formed oxide layer remains unbroken, it acts as a lubricating effect, reducing friction coefficients. However, when the oxide layer breaks, the hard oxides act as abrasives, resulting in an increase in friction coefficient values (Taktak et al., 2008; Carlos et al., 2017; Günen ve Ergin 2023).

An increase in friction coefficients generally implies an escalation in wear volume losses. The wear volume losses of the samples subjected to wear tests at room temperature and 500 °C are illustrated in Figure 7.

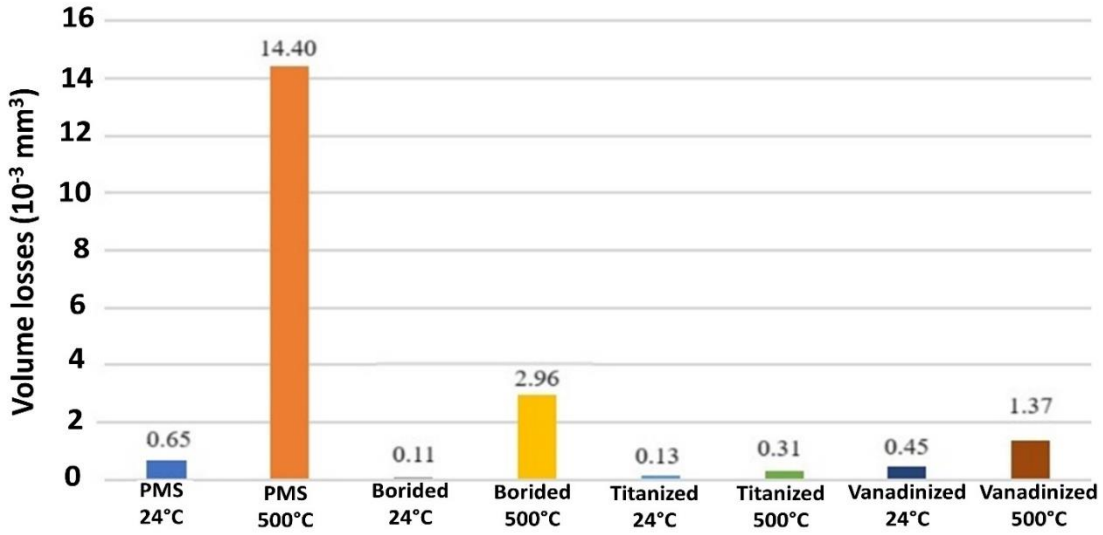

Figure 7. Wear volume losses of untreated PMS 1.337 and coatings at room temperature and 500 °C.

When examining Figure 7, it is evident that both temperature and coating methods have a significant impact on wear volume losses. Specifically, the untreated sample exhibited a wear volume loss of 0.653 × 10-3 mm³ at room temperature. However, at 500 °C, this sample experienced a 22.05-fold increase in wear compared to room temperature, resulting in a wear volume loss of 14.40 × 10-3 mm³. Furthermore, all of the coatings demonstrated lower wear volume losses compared to the untreated sample. In descending order of wear resistance relative to the untreated sample, these are ranked as boride coatings (5.88 times), TiC coating (5.14 times), and VC (1.44 times). The correlation between the wear resistance of the samples at room temperature and their surface hardness values, as observed in the literature, underscores the relationship between wear resistance and hardness. A harder surface requires higher force for plastic deformation. Examining the wear volume losses at high temperatures, a notable observation is that all coating samples experienced lower wear volume losses compared to the untreated sample, mirroring the trend observed at room temperature. However, upon closer examination of the wear volume losses at 500 °C of coatings, it is observed that the highest wear volume loss occurred in the boronized sample, which had the lowest wear volume loss at room temperature. This phenomenon may be attributed to the dual-layered coating structure of the boride layer, as depicted in the SEM image in Figure 2. The different thermal expansion coefficients of FeB and Fe_2B within the boride layer could lead to varied responses to temperature effects, resulting in distinct reactions of the phases during high-temperature wear (Kulka et al., 2017; Hamamcı et al., 2024). On the other hand, considering the volume losses in 500 °C wear tests, it is determined that the TiC coated sample exhibited the best wear resistance.

In order to identify wear mechanisms, SEM images of wear tracks were taken, and EDS analyses were conducted at relevant locations. In pictures 8 to 15, SEM images numbered I should be magnified at X40, images numbered II should be magnified at X200, and images numbered III should be magnified at X2000.

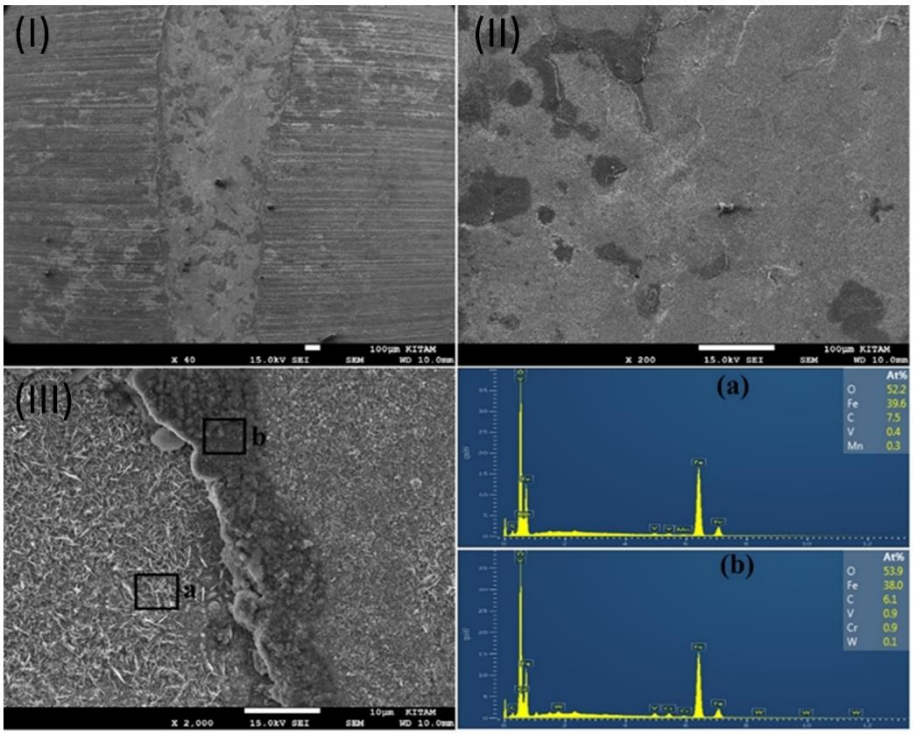

Figure 8. SEM view and EDS analysis taken from the wear scar of the untreated 1.3377 PMS worn at room temperature.

When Figure 8 is examined, it can be seen that delamination and oxidation type wear mechanisms are the dominant wear mechanisms in the sample. Delamination wear mechanism is defined as the formation of cracks beneath the surface as a result of the stresses generated under the surface by the load applied to a material exceeding the tensile strength of the material (Zhao et al. 2010; Wang et al. 2010; Demir et al. 2020), and these cracks progress towards the surface and peeling off the surface particles from the surface, causing an appearance similar to casing. In these regions where the flaking occurs, oxide layers often form in the areas of the flacked. As a matter of fact, the fact that around 50% oxygen was detected in the EDS analyzes taken from the black areas on the surface of this material (Figure 8c b region) supports this point. Indeed, the EDS analyses conducted on the areas appearing black on the material's surface (Figure 8c, region b) revealed an atomic concentration of approximately 50% oxygen, supporting this observation.

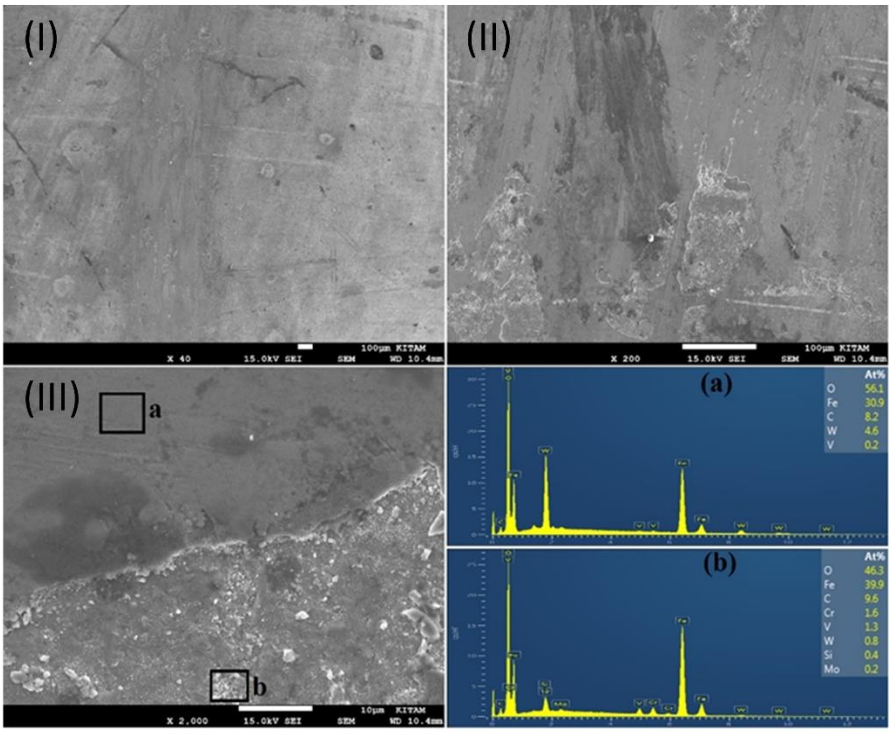

Figure 9. SEM view and EDS analysis taken from the wear scar of the untreated 1.3377 PMS worn at 500 °C.

Upon examining Figure 9, it is observed that a smoother surface has formed compared to room temperature; however, Figure 9c reveals that a portion of this surface has fractured. This condition is attributed to particles detached from the softened surface at 500 °C adhering to the surface, undergoing oxidation during the wear process due to the combined influence of temperature and ambient air, and subsequently breaking due to repeated loads. EDS analyses, detecting an oxygen concentration above 50% in this region, indicate the presence of oxidation. Therefore, the wear mechanism in this specimen is identified as adhesive-supported oxidation wear.

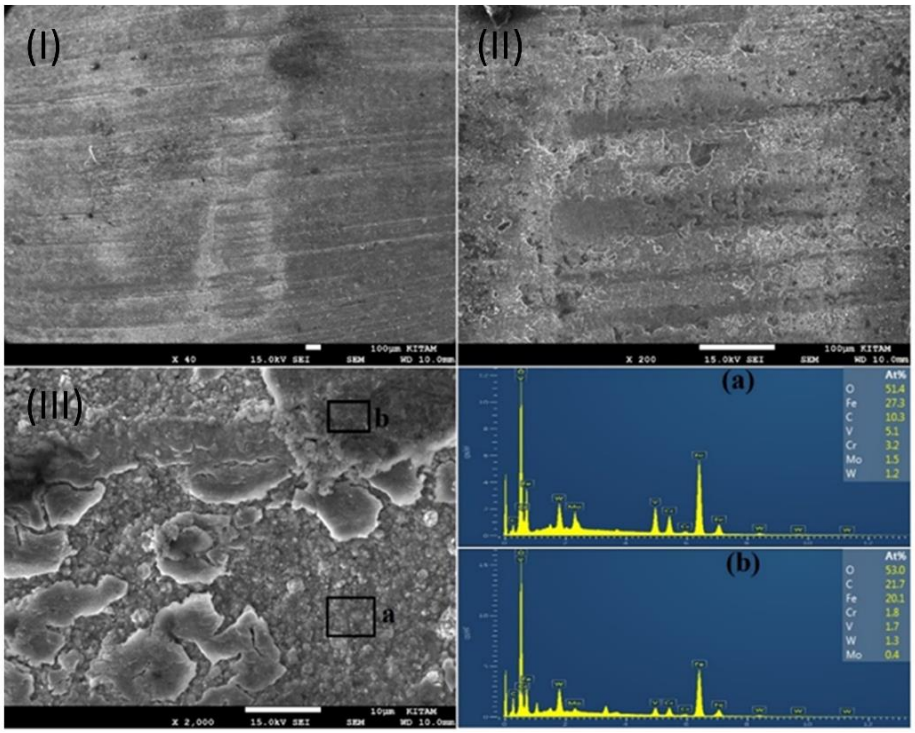

Figure 10. SEM view and EDS analysis taken from the wear scar of the borided PMS worn at room temperature.

Considering the SEM images of the worn surface of the boronized specimen at room temperature, it has been observed that the visibility of wear features on the surface is minimal. This finding supports the evidence presented in Figure 7, indicating the least wear volume losses occurring in this specimen. Upon closer inspection of the 2000X magnification image, it is understood that the wear event occurred as a result of the fracture of the boride layer due to the merging of microcracks. EDS analyses conducted on these regions revealed an atomic oxygen concentration above 50%, a consequence of the oxidation process occurring due to the wear tests being conducted in an open-air environment.

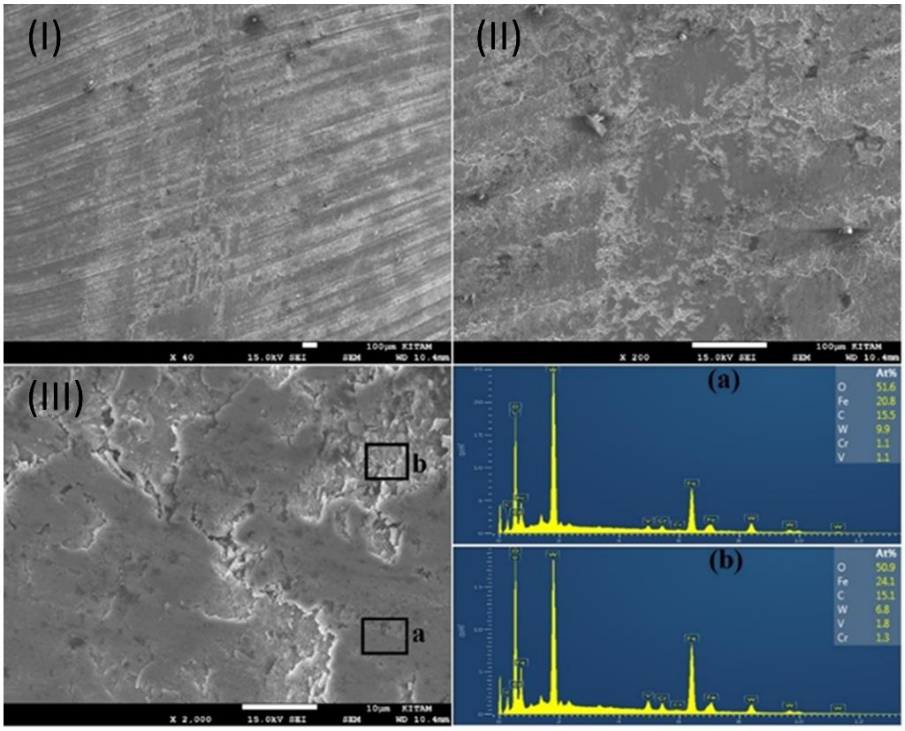

Figure 11. SEM view and EDS analysis taken from the wear scar of the borided PMS worn at 500 °C.

When examining of the SEM image of the worn surface of the boronized specimen at 500 °C, it is observed that, unlike at room temperature, there are smooth areas where material has adhered to the surface and deep delamination regions between these areas. The flat surfaces in these regions indicate that wear debris adhered (sintered) to the surface due to the 500 °C temperature and applied load, and the delamination zones suggest that these adhered debris are worn again due to repeated loads. In regions taken from the surface, an oxygen concentration above 50% is detected, indicating the occurrence of adhesion, oxidation, and delamination mechanisms in the boronized specimen during high-temperature wear testing.

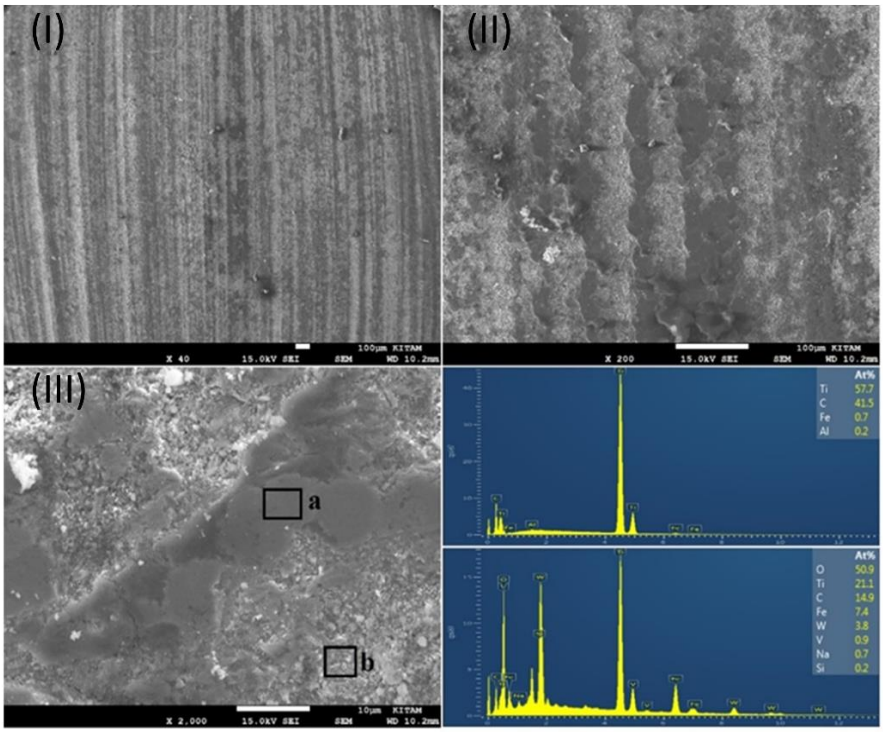

Figure 12. SEM view and EDS analysis taken from the wear scar of the titanized PMS worn at room temperature.

When examining the SEM images of the room temperature wear tracks on the titanium-coated specimen, abrasive wear marks on the surface are clearly visible. In the 200X SEM image of the specimen, these abrasive marks are observed to form channels (grooving), and according to EDS analyses of the dark areas marked as (a), they consist of unworn TiC layers. On the other hand, the white, fractured areas marked as (b) are concluded to be composed of the damaged TiC coating and the substrate material. Based on these observations, it was concluded that the oxidatively supported abrasive wear mechanism was dominant in this sample.

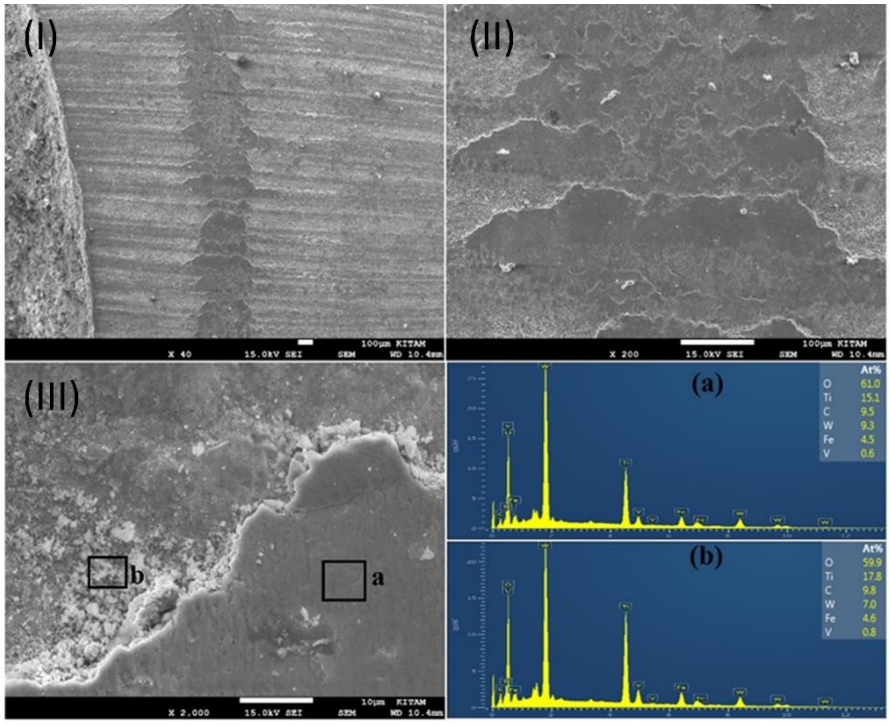

Figure 13. SEM view and EDS analysis taken from the wear scar of the titanized PMS worn at 500 °C.

Considering the SEM images of the wear tracks on the titanium-coated specimen at 500 °C, it is observed that the wear process resulted in the particles detached from the surface during wear adhering (sintering) to the surface (Günen et al. 2022b), forming a vertically oriented stripe on the horizontal specimen surface, similar to TiC coatings. In the 2000X SEM image of the specimen, it is clearly visible that these adhered regions experience fractures due to the progression of micro-cracks on the surface (Mohan et al. 2012). EDS analyses from both intact (a) and fractured (b) regions, where elements such as Ti, C, Fe, and O are closely located, strengthen the claim that the surface is composed of adhered wear debris, as mentioned above. This situation indicates that the wear mechanism at elevated temperatures occurs as an oxidative-supported adhesive wear mechanism.

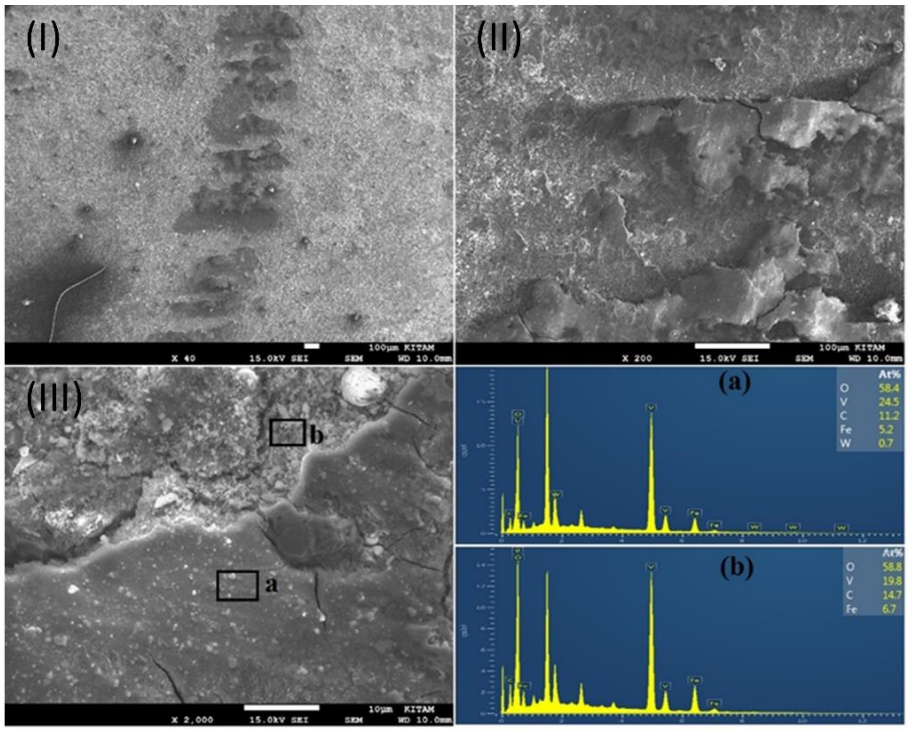

Figure 14. SEM view and EDS analysis taken from the wear scar of the vanadinized PMS worn at room temperature.

When examining Figure 14, it is observed that particles adhered to the surface, similar to the 500 °C-abraded TiC sample, also occur on the surface of the vanadium-coated specimen. This phenomenon is a consequence of the sample's susceptibility to wear due to the mentioned heterogeneity in its microstructure, making it more prone to wear and causing the wear particles to adhere to the surface due to the compression between the abrasive ball and the material. Upon closer inspection of the 2000X SEM images of the specimen, it is evident that these adhered regions harbor numerous micro-cracks, with some areas breaking due to the progression of these micro-cracks. EDS analyses from both intact (a) and fractured (b) regions, where elements such as V, C, Fe, and O are closely located, support the claim that the surface is composed of sintered wear debris, as mentioned above. Therefore, the similarity in the wear volume loss between the vanadium-coated specimen at room temperature and the titanium-coated specimen at 500 °C strengthens the aforementioned observations.

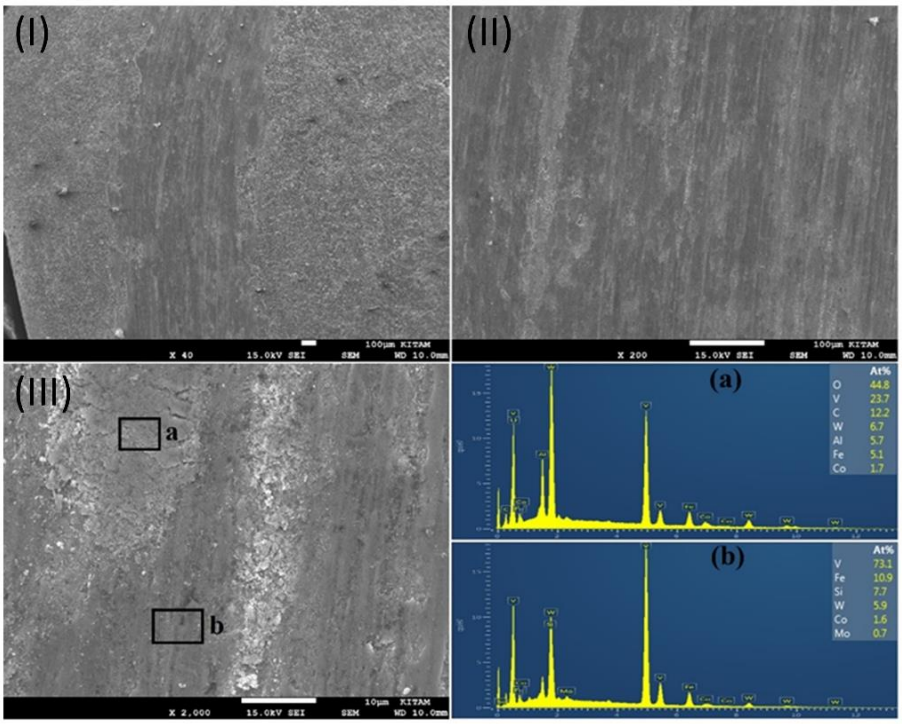

Figure 15. SEM view and EDS analysis taken from the wear scar of the vanadinized PMS worn at 500 °C.

When the wear trace SEM images of the vanadinized sample at 500 °C are examined, a much smoother wear surface is seen compared to room temperature. When the 2000X image of the sample is examined, it is seen that the flat surface actually consists of sintered wear debris and that these areas consist of gaps and cracks within themselves. EDS analyzes show that a similar wear mechanism occurs in these samples at room temperature.

4. CONCLUSION

In this study, the effects of boride and carbide coatings formed with TRD coatings on the surface of cutting edge 13377 PMS, produced by powder metallurgy method, on the microstructure and wear behavior of this alloy were studied. After the coating process, characterization studies were carried out by SEM, EDS, XRD, microhardness test, room temperature and high temperature wear tests. The results obtained are summarized below.

1- Dense, continuous and homogeneous coatings were obtained on the surface by boronizing and titanizing processes while in vanadinizing oxide formation and unhomogeneity in the coating layer detected.

2- XRD analyzes showed that the dominant phase in the coated samples was FeB for boronizing, TiC for titanizing and VC for vanadinizing. Additionally, apart from these phases, phases such as Cr_7C_3, VO, V_2B were formed in low amounts depending on the chemical composition and the applied coating method.

3- PMS 1.3377 steel, whose hardness was determined as 334 HV, was improved up to 2566 HV by boronizing, 2034 HV by titanizing and 1800 HV by vanadinizing, with the boride and carbide coatings formed by the applied coating processes.

4- The thickness of the coating layers obtained was determined as 98±2.1, 11±0.5, 13±0.6 for boronizing, titanizing and vanadinizing, respectively.

5- All coated samples showed lower mean friction coefficient values than the untreated sample at room temperature and 500 °C. This can be attributed to the high hardness values of borides and carbides and the fact that the oxides they form, such as B_2O_3, TiO_2, VO, are more stable than Fe_2O_3 and Fe_3O_4.

7- Coated samples exhibited up to 20 times higher wear resistance than untreated samples at both room temperature and 500 °C. While room temperature wear resistance is mostly related to the increase in hardness values, high temperature wear resistance is mostly related to the stability of the phase structure at high temperatures.

8- While the untreated sample was exposed to delamination and oxidation wear mechanisms at room temperature, the wear mechanism turned into adhesive and oxidation at 500 °C. On the other hand, it was determined that the wear mechanism in coated samples occurred in the form of adhesive, oxidation and delamination at both room temperature and 500 °C.

9- While the best wear resistance at room temperature was obtained in the boronized sample, the best wear resistance at 500 °C was obtained in the titanized sample. The fact that boriding shows the lowest wear resistance among samples coated at high temperatures can be attributed to the fact that the layers are exposed to different thermal expansions since they are dual-layered (FeB+Fe_2B).

10- The study demostrated that the wear resistance of PMS 1.3377, which is used in applications such as cutting tool turning, milling and drilling, can be improved by 3 different coating methods from room temperature to 500°C, but the most suitable method for this steel is titanizing.

5. ACKNOWLEDGEMENTS

This study did not benefit from any support.

6. CONFLICT OF INTEREST

Authors approve that to the best of their knowledge, there is not any conflict of interest or common interest with an institution/organization or a person that may affect the review process of the paper.

7. AUTHOR CONTRIBUTION

Erdoğan Kanca determined and managed the concept and design process of the research. Talat TURAN collected the data of the experiments related to the study and made the necessary graphic drawings. Ali Günen analyzed the SEM, EDS, XRD and microhardness data for the study and interpreted the results. All authors prepared and critically analyzed the manuscript.

8. REFERENCES

Angelo, P. C., Subramanian, R., & Ravisankar, B., Powder metallurgy: science, technology and applications. PHI Learning Pvt. Ltd., 2022.

Arai, T., The thermo-reactive deposition and diffusion process for coating steels to improve wear resistance. In Thermochemical surface engineering of steels (pp. 703-735). Woodhead Publishing, 2015.

Aras, M., Şahin, M., & Gündoğdu, Ö., Effects of sintering temperature on microstructural properties of ni1-xznxfe2o4 synthesized by powder metallurgy. Materials Science/Medziagotyra, , 28(4), 487-495, 2022. https://doi.org/10.5755/j02.ms.30204

Campos Silva, I. E., Günen, A., Serdar Karakaş, M., & Delgado Brito, A. M., The Boriding Process for Enhancing the Surface Properties of High-Temperature Metallic Materials. Coatings for High-Temperature Environments: Anti-Corrosion and Anti-Wear Applications, 221-259, 2023.

Claros, J. M., do Nascimento, E. M., & D Oliveira, A. S. C. M., Effect of the oxide film on the sliding wear behavior of a CoCrMoSi alloy hard facing coating. In 24th ABCM International Congress of Mechanical Engineering: pp. 3-8, 2017.

Çakir, M. V., A Comparative Study on Tribocorrosion Wear Behavior of Boride and Vanadium Carbide Coatings Produced by TRD on AISI D2 Steel. Protection of Metals and Physical Chemistry of Surfaces, 58(3), 562-573, 2022.

Çalıgülü, U., Durmuş, H., Akkaş, M., & Sahin, B., Microstructure and mechanical properties of ni matrix b4c reinforced functionally graded composites. Science of Sintering, 53(4), 475-484, 2021. https://doi.org/10.2298/sos2104475c

Çalık, A., Karakaş, M. S., Uçar, N., & Ünüvar, F., Boriding kinetics of pure cobalt. Metallic Materials, 52(02), 107-112, 2021. https://doi.org/10.4149/km_2014_2_107

Daicu, R., Chivu, C., & Oancea, G., A case study about acquisition of mechanically fixed cutting inserts. MATEC Web of Conferences, 137, 03004, 2017. https://doi.org/10.1051/matecconf/201713703004

Dement, T. V., Kurzina, I., Калашников, М. П., Попова, Н. А., & Karakchieva, N., Structure and phase composition of material based on vanadium alloy v-4.9ti-4.8cr and ferrite steel 17cr-12ni-fe. MATEC Web of Conferences, 243, 00019, 2018. https://doi.org/10.1051/matecconf/201824300019

Demir, M., Kanca, E., & Karahan, I. H., Characterization of electrodeposited Ni–Cr/hBN composite coatings. Journal of Alloys and Compounds, 844, 155511, 2020.

Duran, H., Özkan, D., Karaoğlanli, C., Borlama işlemi uygulanmış Inconel 718 süperalaşımın mikroyapı, aşınma ve mekanik özelliklerinin incelenmesi. Karaelmas Fen ve Mühendislik Dergisi, 11(1), 61-72, 2021. DOI:10.7212/ karaelmasfen.811408

Erden, M. A., Yaşar, N., Korkmaz, M. E., Ayvacı, B., Nimel Sworna Ross, K., & Mia, M., Investigation of microstructure, mechanical and machinability properties of Mo-added steel produced by powder metallurgy method. The International Journal of Advanced Manufacturing Technology, 114, 2811-2827, 2021.

Fang, Z. Z., Paramore, J. D., Sun, P., Chandran, K. R., Zhang, Y., Yang, X., … & Free, M. L., Powder metallurgy of titanium – past, present, and future. International Materials Reviews, 63(7), 407-459, 2017. https://doi.org/10.1080/09506608.2017.1366003

Hamamcı, M., Nair, F., Cerit, A. A., & Güneş, R., Thermal shock effects on the microstructure and mechanical properties of iron-based composites reinforced by in-situ Fe2B/FeB ceramic phases. Ceramics International, 43(1), 1584-1587.2024.

Hasçelik, A., & Aslantaş, K., Mikro Tornalama İşleminde Kesici Takım Burun Yarıçapının Kesme Kuvvetlerine Etkisi. Journal of Materials and Mechatronics: A, 2(1), 13-25, 2012.

Gevorkyan, E., Rucki, M., Sałaciński, T., Siemiątkowski, Z., Nerubatskyi, V., Kucharczyk, W., … & Nejman, M., Feasibility of cobalt-free nanostructured wc cutting inserts for machining of a tic/fe composite. Materials, 14(12), 3432, 2021. https://doi.org/10.3390/ma14123432

Ghadi, A., Ebrahimnezhad-Khaljiri, H., & Gholizadeh, R., A comprehensive review on the carbide-base coatings produced by thermo-reactive diffusion: microstructure and properties viewpoints. Journal of Alloys and Compounds, 171839, 2023.

Gökmen, U., Eslam Jamal Golzari, L., Gürgen Avşar, S., Özkan, Z., & Bilge Ocak, S., Microstructural and radioactive shielding analyses of alumix-231 and alumix-231 reinforced with b4c/sic/al2o3 particles produced through hot pressing. ACS Omega, 8(39), 35755-35767, 2023. https://doi.org/10.1021/acsomega.3c03132

Gutierrez-Noda, L., Cuao-Moreu, C. A., Perez-Acosta, O., Lorenzo-Bonet, E., Zambrano-Robledo, P., & Hernandez-Rodriguez, M. A. L., The effect of a boride diffusion layer on the tribological properties of AISI M2 steel. Wear, 426, 1667-1671, 2019.

Günen, A., Kanca, E., Demir, M., Er, Y., Sağlam, G., & Gök, M. S., Microabrasion wear behavior of fast-borided steel tooth drill bits. Tribology Transactions, 60(2), 267-275, 2016. https://doi.org/10.1080/10402004.2016.1159359

Günen, A., Kalkandelen, M., Karahan, İ. H., Kurt, B., Kanca, E., Gök, M. S., & Serdar Karakaş, M., Properties and corrosion behavior of chromium and vanadium carbide composite coatings produced on ductile cast iron by thermoreactive diffusion technique. Journal of Engineering Materials and Technology, 142(4), 041008, 2020.

Günen, A., Lindner, T., Karakaş, M. S., Kanca, E., Töberling, G., Vogt, S., ... & Lampke, T., Effect of the boriding environment on the wear response of laser-clad AlCoCrFeNi high entropy alloy coatings. Surface and Coatings Technology, 447, 128830, 2022.

Günen, A., Soylu, B., & Karakaş, Ö., Titanium carbide coating to improve surface characteristic, wear and corrosion resistance of spheroidal graphite cast irons. Surface and Coatings Technology, 437, 128280, 2022.

Günen, A., Bölükbaşı, Ö. S., Özgürlük, Y., Özkan, D., Odabaş, O., & Somunkıran, İ., Effect of cr addition on properties and tribological behavior at elevated temperature of boride layers grown on borosintered powder metallurgy alloys. Metals and Materials International, 29(3), 748-766, 2023.

Günen, A., & Ergin, Ö., A comparative study on characterization and high-temperature wear behaviors of thermochemical coatings applied to cobalt-based Haynes 25 superalloys. Coatings, 13(7), 1272, 2023.

Gürbüz, H., Şeker, U., & Kafkas, F., Effects of cutting tool forms on the surface integrity in turning of AISI 316L stainless steel. Journal of the Faculty of Engineering and Architecture of Gazi University, 35(1), 225-240, 2020.

Kara, R., Çolak, F., & Kayali, Y., Investigation of wear and adhesion behaviors of borided steels. Transactions of the Indian Institute of Metals, 69, 1169-1177, 2016.

Karakaş, M. S., Tribocorrosion behavior of surface-modified AISI D2 steel. Surface and Coatings Technology, 394, 125884, 2020.

Kasprzycka, E., Corrosion resistant layers produced in vacuum titanizing process on a low carbon steel surface coated electrolytically with cobalt. Solid State Phenomena, 223, 110-118, 2015.

Kato, K., Wear in relation to friction—a review. wear, 241(2), 151-157, 2000.

Kayali, Y., Taktak, S., Ulu, S., & Yalcin, Y., Investigation of mechanical properties of boro-tempered ductile iron. Materials & Design, 31(4), 1799-1803, 2010.

Kayalı, Y., & Yalçın, Y., Borlanmış AISI 316 L Paslanmaz Çeliğin Difüzyon Kinetiğinin İncelenmesi. Journal of Materials and Mechatronics: A, 1(1), 12-21, 2020.

Khan, M. A. and Gupta, K., A study on machinability of nickel based superalloy using micro-textured tungsten carbide cutting tools. Materials Research Express, 7(1), 016537, 2020. https://doi.org/10.1088/2053-1591/ab61bf.

Kılınç, B., Kocaman, E., Şen, Ş., & Şen, U., Effect of titanium content on the microstructure and wear behavior of fe(13-x)tixb7 (x=0-5) hardfacing alloy. Journal of Mining and Metallurgy, Section B: Metallurgy, 58(1), 29-41, 2022. https://doi.org/10.2298/jmmb210430047k

König, W., Komanduri, R., Toenshoff, H. K., & Ackershott, G., Machining of hard materials. CIRP annals, 33(2), 417-427, 1984.

Kulka, M., Makuch, N., & Piasecki, A., Nanomechanical characterization and fracture toughness of FeB and Fe2B iron borides produced by gas boriding of Armco iron. Surface and Coatings Technology, 325, 515-532, 2017.

Kurt, B., Günen, A., Kanca, Y., Koç, V., Gök, M. S., Kırar, E., & Askerov, K., Properties and tribologic behavior of titanium carbide coatings on AISI D2 steel deposited by thermoreactive diffusion. Jom, 70, 2650-2659, 2018.

Kurt, B., Özdoğan, L., Güney, B., Bölükbaşı, Ö. S., & Günen, A., Characterization and wear behavior of TiBC coatings formed by thermo-reactive diffusion technique on AISI D6 steel. Surface and Coatings Technology, 385, 125332, 2020.

Liu, S., Huang, P., Sun, X., Zeng, W., Zhang, J., & Zu, G., Fatigue of an aluminum foam sandwich formed by powder metallurgy. Materials, 16(3), 1226, 2023. https://doi.org/10.3390/ma16031226

Mathivanan, A., Sudeshkumar, M. P., Radhika, R., Ezilarasan, C., Raju, G. U., & Jayaseelan, V., Finite element simulation and regression modeling of machining attributes on turning aisi 304 stainless steel. Manufacturing Review, 8, 24, 2021. https://doi.org/10.1051/mfreview/2021022

Mohan, N., Natarajan, S., & KumareshBabu, S. P., The role of synthetic and natural fillers on three-body abrasive wear behaviour of glass fabric–epoxy hybrid composites. Journal of applied polymer science, 124(1), 484-494, 2012.

Nayak, K. C., Rane, K., Date, P. P., & Srivatsan, T. S., Synthesis of an aluminum alloy metal matrix composite using powder metallurgy: role of sintering parameters. Applied Sciences, 12(17), 8843, 2022. https://doi.org/10.3390/app12178843

Pashechko, M. I., Dziedzic, K., & Jóźwik, J., Analysis of wear resistance of borided steel c45. Materials, 13(23), 5529, 2020. https://doi.org/10.3390/ma13235529

Rizzo, A., Goel, S., Luisa Grilli, M., Iglesias, R., Jaworska, L., Lapkovskis, V., ... & Valerini, D., The critical raw materials in cutting tools for machining applications: A review. Materials, 13(6), 1377, 2020.

Sathish, T., Mohanavel, V., Karthick, A., Arunkumar, M., Ravichandran, M., & Rajkumar, S., Study on compaction and machinability of silicon nitride (si3n4) reinforced copper alloy composite through p/m route. International Journal of Polymer Science, 1-10, 2021. https://doi.org/10.1155/2021/7491679

Somunkıran, İ., Çelik, E., Tunç., B & Güneş, Ç., Toz Metalurjisi Yöntemiyle Üretilen Fe Esaslı Fe-Ni-Cu Elmas Kesici Takımında Co'ın Etkisi. Journal of Materials and Mechatronics: A, 3(2), 194-205, 2022.

Şap, E., Usca, Ü. A., Gupta, M. K., Kuntoğlu, M., Sarıkaya, M., Pimenov, D. Y., … & Mia, M., Parametric optimization for improving the machining process of cu/mo-sicp composites produced by powder metallurgy. Materials, 14(8), 1921, 2021. https://doi.org/10.3390/ma14081921

Şen, U., Thermo-reactive diffusion vanadium nitride coatings on AISI 1020 steel. Key Engineering Materials, 264, 577-580, 2004.

Taktak, S., Ulker, S., & Gunes, I., High temperature wear and friction properties of duplex surface treated bearing steels. Surface and Coatings Technology, 202(14), 3367-3377, 2008.

Turgut, S., & Günen, A., Mechanical properties and corrosion resistance of borosintered distaloy steels. Journal of Materials Engineering and Performance, 29, 6997-7010, 2020.

Türkmen, İ., & Yalamaç, E., Effect of alternative boronizing mixtures on boride layer and tribological behaviour of boronized SAE 1020 steel. Metals and Materials International, 1-15, 2021.

Vijaya Kumar, P., & Velmurugan, C., Surface Treatments and Surface Modification Techniques for 3D Built Materials. Cham: Springer International Publishing. In Innovations in Additive Manufacturing: pp. 189-220, 2022.

Wang, S. Q., Wei, M. X., Wang, F., & Zhao, Y. T., Transition of elevated-temperature wear mechanisms and the oxidative delamination wear in hot-working die steels. Tribology International, 43(3), 577-584, 2010.

Zakharov, B. V., Minkevich, A. N., Pikunov, D. V., Toné, É. R., & Argasova, E. D., Role of the phase composition of tungsten containing hard alloys in the formation of a layer of titanium carbide in gas titanizing. Soviet Powder Metallurgy and Metal Ceramics, 28(7), 574-578, 1989.

Zhao, Y. T., Wang, S. Q., Yang, Z. R., & Wei, M. X., A new delamination pattern in elevated-temperature oxidative wear. Journal of materials science, 45, 227-232, 2010.

JOURNAL of
MATERIALS and MECHATRONICS:A

e-ISSN 2717-8811
JournalMM, 2024, 5(1), 36-48
https://doi.org/10.55546/jmm.1445220

Araştırma Makalesi / Research Article

Investigation of Three Body Abrasive Wear Behavior of Micro-Nano Sized Iron Ore Pieces on Bronze

Abdullah UĞUR[1*], Ahmet Emrah ERDOĞDU[2], Recep DEMİRSÖZ[3]

[1*]Karabük University, Faculty of Engineering, Department of Mechanical Engineering, Karabük, Turkey,
ORCID ID: https://orcid.org/0000-0002-3495-529X, augur@karabuk.edu.tr
[2] Karabük University, Faculty of Engineering, Department of Mechanical Engineering, Karabük, Turkey,
ORCID ID: https://orcid.org/ 0000-0003-1831-3972, aemraherdogdu@karabuk.edu.tr
[3] Karabük University, Faculty of Engineering, Department of Mechanical Engineering, Karabük, Turkey,
ORCID ID: https://orcid.org/ 0000-0003-0674-4572 , recepdemirsoz@karabuk.edu.tr

Geliş/ Received: 01.03.2024**;** **Revize/Revised:** 12.04.2024 **Kabul / Accepted:** 16.04.2024

ABSTRACT: In In this work, the three-body abrasive wear of bronze (C86200) in pig cart transmissions was examined. Micro-nano-sized ore particles were introduced to the lubricating media during the Ball-on-flat test to represent three-body abrasive wear. Load shear rate and lubricating medium were useful research inputs. Outputs included examining sample surfaces, mass loss, friction coefficient, and trace depth. Taguchi, ANOVA, and RSM were used to analyze experimental data. The most effective parameter for all outputs was the load value, with a rate of 55.76 percent, while the speed had the lowest influence on mass loss, at 9.74 percent. The regression model fits these results well.

Keywords: Three-Body Abrasive Wear, Ore Particle, Lubricated Environment, Bronze.

1. INTRODUCTION

Wear is a very common fundamental problem, especially in systems with movement and contact (Bozkurt et al., 2021; Huang et al., 2019; Sardar et al., 2018). To solve and understand this problem, which is encountered in a wide variety of fields, many different solution methods and situation analyzes are carried out by considering the effects of the problem (cost, time, comfort, safety, etc.) (Kusumoto et al., 2019). Wear mechanisms are affected and diversified by many similar variables, especially mechanical properties (force, speed, etc.), material-related factors (hardness, surface roughness, etc.) and environmental factors (PH, lubrication, chemical concentrations, etc.)(Akram et al., 2021; Cetin and Korkmaz, 2020; Radhika and Sai Charan, 2017) . One of the wear types is abrasive wear. In the case of abrasive wear, the wear mechanism can be two-body (Singh et al., 2022) or three-body (Varol et al., 2018). During three-body abrasive wear, there are also abrasive

*Sorumlu yazar / Corresponding author: augur@karabuk.edu.tr
Bu makaleye atıf yapmak için /To cite this article

Uğur, A., Erdoğdu, A. E, Demirsöz, R. (2024). Investigation of Three Body Abrasive Wear Behavior of Micro-Nano Sized Iron Ore Pieces on Bronze. Journal of Materials and Mechatronics: A (JournalMM), 5(1), 36-48.

particles, which can be considered as a third body, between two surfaces moving relative to each other (R.A. García-León et al., 2021; Liu et al., 2018). During three-body abrasive wear, the type, properties (size, hardness, etc.) and mechanical behavior of the abrasive particles are additional factors affecting wear (Gheisari and Polycarpou, 2018; Lan et al., 2017; Lan and Polycarpou, 2018). Although the three-body abrasive wear phenomenon is complex, it offers a more realistic wear approach, especially for dust and particulate media applications. Charging facilities, which are a part of the blast furnace process, can be given as an example to the raw material loading areas of the production facilities. The elements of the mechanical structures in these facilities that come into contact with each other are exposed to three-body abrasive wear from time to time due to the particles coming from the external environment (Manoharan et al., 2019). In addition, two-body wear mechanisms can also turn into three-body wear mechanisms. This event occurs when particles break off from one or both elements that make up the structure (Radhika, 2017). Today, it is seen that there are not enough studies on the three-body wear mechanism of bronze materials and the abrasive effect of ore particles as the third body (R. A. García-León et al., 2021a).

Purba et al. In their study, they examined the yield strength and tribological properties of the material they developed. For this, they carried out rubber wheel abrasive machine tests in different particle sizes in accordance with the ASTM G65 standard. As a result, they stated that the microstructure and abrasive size should be known in order to know the wear properties of alloys (Purba et al., 2023).

Xin et al. evaluated friction and wear of amorphous-nanocrystalline plasma-sprayed coatings with oil lubrication. The coating holds up effectively under modest strains and resists abrasive particles even at higher loads (Xin et al., 2022). Zhao et al. employed molecular dynamics simulations to study heterostructure films' tribological characteristics. This study found that self-rotating abrasives reduced friction and wear. This work revealed the molecular tribological characteristics of graphene/h-BN sheets (Zhao et al., 2022).

Studies on the three-body wear mechanisms of bronze materials and the abrasive effect of ore particles acting as the third body, particularly in micro-nano sized particles, are currently lacking. (Bharatish et al., 2018; Yin et al., 2020) . To fill this gap in the literature, this paper aims to contribute with the better understanding of the three-body abrasive behavior on bronze C86200 alloy materials. This study is about the effects of load and sliding speed on mass loss (ML), friction coefficient (CoF) and trace depth (TD) in different oil environments containing micro and nano (min.50 nm – max.2 μm) ore particles.

2. MATERIALS AND METHODS

Wear tests were carried out in Karabük University Engineering Faculty laboratories. The bronze material using as the test specimen was carried out with the help of a ball-on-flat type original test installation, in an environment containing only lubricant and in a lubricant environment in which micro-nano ore particle was added at two different rates. Experimental design and parameters are given in Table 1.

Table 1. Parameters and experimental design.

Factor levels	Factors			Distance (m)	Stroke length (mm)
	Load (N)	Ore Particle mass ration (%)	Sliding speed (mm/s)		
1	20	-	17.3	100	14
2	40	0.3	30.3		
3	60	0.6	43.3		

2.1 Material

In the study, special casting C86200 bronze material used in raw material manipulation systems was selected. The chemical composition of the bronze material is given in Table 2. The hardness, yield strength and surface roughness values of the C86200 material used are given in Table 3.

Table 2. Chemical composition of the brass specimen

Cu	Zn	Ni	Fe	Al	Si	S	Mn	Sn	Others
70.28	21.78	3.65	0.68	1.9	0.11	0.07	0.48	0.6	0.45

Table 3. Average hardness, yield strength and surface roughness values of the specimen

Average Hardness [HV]	Yield Stress [MPa]	Ra [µm]
212,3 (±4.92)	621	0.086-0.096

2.2 Abrasive Particles & Lubricant

The abrasive particles to be used in the three-body abrasion test were first taken from the ore heap to remain under the 25 µm sieve. Then, abrasive particle size was reduced by using the Fristch Pulverisette 7 Classic Line micro mill device. The milling process was obtained for each 14 g of abrasive ore particle, after a net 20-hour milling at 700 rpm for 5 minutes and 2 minutes of pause (Bailon-Poujol et al., 2011; Lakshmikanthan et al., 2019; Madhusudan et al., 2020). After the milling process, size measurements were made with the SEM device. The images and particle size measurements taken from the SEM device are given in Figure 1. In SEM imaging, abrasive particle sizes were found to be less than 2 µm. The chemical composition of the abrasive particles used is given in Table 4.

In the study, a lubricant with a viscosity of 320 according to ISO 348 and a density of 895 kg/m3 at 15 °C was used. In the experiments, different environments were created by mixing the ore particle with the lubricant at 0.3 wt. % and 0.6 wt. %.

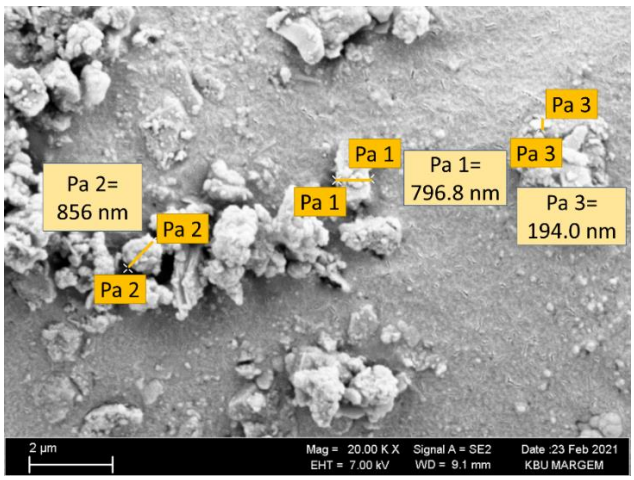

Figure 1. SEM image of abrasive ore particle and dimensional measurements

Table 4. Chemical composition of the abrasive particles

O	Fe	Si	Ca	Sb	Al	Others
63.49	19.25	5.99	4.72	2.69	1.71	2.15

2.3 Abrasive Test

Karabuk University Laboratories created the ball-on-flat wear test arrangement. The device can handle loads between 5 N and 65 N at 0 to 43.3 mm/s. During tests, a dynamometer measured force levels to calculate the friction coefficient. Figure 2 shows the device and technique schematics. Preliminary tests and literature reviews were used to determine the 20 - 40 - 60 N loads (Table 1), 17.3 – 30.3 – 43.3 mm/s sliding speeds, and sliding distance. Preliminary test traces were emphasized. After each experiment, MLs were measured with a 10-4 g balance. In the experiments, a 6 mm diameter ball made of 100Cr6 (AISI52100) material was selected and used as abrasive (Demirsoz et al., 2023).

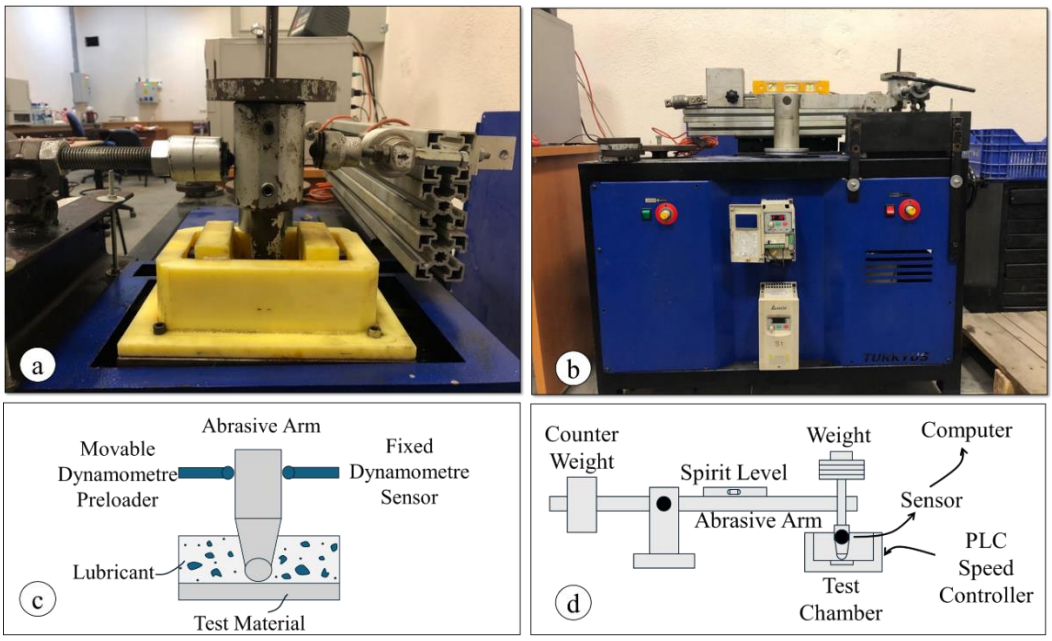

Figure 2. Photographs and schematic representations of the experimental device and the applied method a) abrasive arm and chamber, b) test setup, c) schematic representation of abrasive medium, d) schematic representation of test setup.

2.4 Experimental Design

TAGUCHI method is generally used in engineering experimental design. Performing full-variable experiments that will cover all parameters in multi-parameter test systems causes losses in terms of time and cost. For this reason, L9 (3x3) experimental design was created by Minitab program using TAGUCHI method (Rahiman et al., 2020; Sasidharan et al., 2018).

Load (N), rotational speed (rpm) and ore mass ratio in the lubricant were determined as independent variables for the test. Therefore, type of design is 3 level and number of factors is 3 (33) and the objective function were chosen as ,Smaller is Best,. Table 5 provides the TAGUCHI L9 orthogonal array control parameters.

Table 5. L9 Orthogonal array.

No	Load [N]	Sliding Speed [mm/s]	Concentration [wt. %]
1	20	17.3	0.0
2	20	30.3	0.3
3	20	43.3	0.6
4	40	17.3	0.3
5	40	30.3	0.6
6	40	43.3	0.0
7	60	17.3	0.6
8	60	30.3	0.0
9	60	43.3	0.3

3. RESULTS AND DISCUSSION

The ML values, CoF values, wear profiles and their signal to noise ratios obtained because of the work done with the C86200 material are given in the following section. The data obtained as a result of the experiments are given in Table 6.

Table 6. Ml, Cof and Td values obtained from the experiments.

No	L [N]	S [rpm]	C [%]	EML [mg]	ECoF	ETD [μm]
1	20	17.3	0.0	0.4 ±0.17	0.0888 ±0.0023	0.948 ±0.34
2	20	30.3	0.3	2.2 ±0.26	0.0933 ±0.0015	2.735 ±0.12
3	20	43.3	0.6	3.4 ±0.34	0.1299 ±0.0012	4.968 ±0.24
4	40	17.3	0.3	3.5 ±0.3	0.1222 ±0.0016	2.519 ±0.17
5	40	30.3	0.6	4.3 ±0.1	0.1396 ±0.0016	3.019 ±0.16
6	40	43.3	0.0	3 ±0.17	0.0804 ±0.0009	2.455 ±0.14
7	60	17.3	0.6	4.1 ±0.36	0.1447 ±0.0015	6.719 ±0.14
8	60	30.3	0.0	4.2 ±0.34	0.1005 ±0.0014	3.761 ±0.34
9	60	43.3	0.3	4.4 ±0.26	0.1181 ±0.0016	9.038 ±0.16

L: Load, S: Speed, C: Concentration, EML: Experimental Mass Loss, ECoF: Experimental Friction Coefficient, ETD: Experimental Trace Depth

In order to check the accuracy of the data, confirmation experiments were carried out with the optimum variables obtained from the Taguchi experimental design. Optimum variables for ML and TD outputs are 20 N at load, 50 rpm at slip velocity, and 0.3 wt. % at concentration. The ideal variables in the CoF outputs were found to be the load value of 40 N, the sliding speed value of 50 rpm, the concentration value, and the environment with only lubricant. The anticipated values and

the outcomes of the confirmation experiments are provided in Table 7. A confirmation experiment with a load value of 40 N, a sliding speed value of 50 rpm, and a lubricant-free environment free of abrasive particles is recommended by the Taguchi experimental design. These variable values presented for control purposes are one of the 9 experiments requested by Taguchi. For this reason, it was not necessary to conduct a control experiment for these values. When Table 7 is examined, the predicted result for the ML and CoF variables is 11.11% and 8.61% lower, respectively, then the value obtained as a result of the experiment. When the TD variable was examined, the predicted result value was 5.11% more than the experimental result value.

Table 7. Confirmation test result and predicted values.

No	L[N]	S[mn/s]	C %	EML [mg]	PML [mg]	ECoF	PCoF	ETD [μm]	PPD [μm]
6	40.0	43.3	0.0	3.0	3.2	0.0804	0.0873	2.455	2.503
15	20.0	43.3	0.3	2.7	2.4	0.0937	0.0986	4.851	5.099

L: Load, S: Speed, C: Concentration, EML: Experimental Mass Loss, PML: Predicted Mass Loss, ECoF: Experimental Friction Coefficient, PCoF: Predicted Friction Coefficient, ETD: Experimental Trace Depth PPD: Predicted Trace Depth.

The average values and probabilities of the ML, CoF and TD measurements obtained after the completion of the tests are given in Table 8. An analysis of variance was performed to determine what effect the load, sliding speed and environment parameters had on outputs such as ML, CoF and TD. The results from the wear test were used for statistical analysis. During this process, load (L), speed (S), concentration (C) were used as the variable source, while LxL, SxS and CxC were used as their relations. Significant and unimportant model terms were stated to be significant or insignificant according to the P index value being $P<0.05$ [(R. A. García-León et al., 2021b; Nas and Oztürk, 2018)].

Table 8. Anova values and contribution rates of load, speed and environment.

SoV	DF	ML	P Value	CoF	P Value	TD	P Value
Repetitions	3						
Test	27						
L	3	7.48167	0.05	0.000439	0.111	19.6819	0.013
S	3	1.30667	0.214	0.000124	0.367	6.5626	0.038
C	3	2.94	0.114	0.00348	0.019	9.4803	0.027
L x L	3	0.46722	0.395	0.000005	0.843	8.2459	0.03
S x S	3	0.37556	0.437	0.000017	0.698	3.2233	0.073
C x C	3	0.04957	0.76	0.000008	0.564	2.5137	0.09
Error	6	0.40444		0.000222		0.2625	
R^2		93.97%		94.84%		98.95%	
R^2(adj)		75.88%		79.37%		95.82%	
Contribution to wear test							
L		55.76%		10.20%		39.18%	
S		9.740%		2.88%		13.06%	
C		21.91%		80.91%		18.87%	
Error		6.02%		5.16%		1.05%	

SoV: Source of Variance, DF: Degrees of Freedom L: Load, S: Speed, C: Concentration, ML: Mass Loss, CoF: Friction Coefficient, TD: Trace Depth

Upon examining the R2(adj) values presented in Table 8, it is evident that the variables L, S, and C exert a significant influence on the ML, CoF, and TD outputs. When the P values obtained after the analysis are examined, it can be said that the P value for TD is significant. When the ML

and CoF columns are examined in the same table, P=0.05 is obtained only for the load variable in the ML column, and the result is significant (Cetin and Korkmaz, 2020) . The difficulty to entirely remove the oil that is still on the specimen surface and the embedding of the particles on the specimen surface are assumed to be the reasons why the P value is greater than 0.05.

It can be seen that some of the p values in the ML and CoF columns are greater than 0.05. The reasons for the high p value are thought to be very difficult to control events such as heating of the samples and abrasive, wear of the abrasive ball, and the inclusion of irregularly sized particles in the three-body wear mechanism.

3.1 Mass Loss (ML)

Specimen 9 yielded the largest ML when the MLs measured during the wear tests were analyzed (Table 6). The ML was determined to be 4.4 mg in this experiment with a 60 N load, a 43.3 mm/s sliding speed, and 0.3 weight percent ore. In specimen number 1, with a 20 N load, a 17.3 mm/s sliding speed, and a lubricating medium free of abrasive particles, the lowest ML was measured at 0.4 mg. It is evident that there are similarities between the actions of ML and TD. This condition may be related to increased load and speed as well as increased chip removal from the specimen surface by the abrasive particle plowing process, similar to what Mahajan and Peshwe found in their investigation. (Mahajan and Peshwe, 2018) .

When the ANOVA analysis were examined, it was concluded that the load parameter was effective on the ML at the rate of 55.76% and the lowest effect value on the ML was caused by the speed with a rate of 9.74%. Temperature change, vibration and material microstructure defects, etc., which are not included in the test variables and may affect ML. It can be said that the factors that are not included in the test variables constitute 6.02% error value. In the study, it was concluded that there is a strong interaction between ML and independent variables (R2(adj)=0.758). According to the results obtained, the ML changes significantly with the increase of the force. This situation can be associated with the increase in load and the removal of more material from the specimen surface by the plow mechanism of the abrasive particles.

S/N ratios were computed using the ‚Smaller is better, function in the study (Nas and Altan Özbek, 2020) . Figure 3a displays the plots that were obtained for experimental ML and S/N ratios. Additionally, Figure 3b displays the graph that illustrates the correlation between the experimental outcomes and the anticipated outcomes derived from the regression analysis of the ML values.

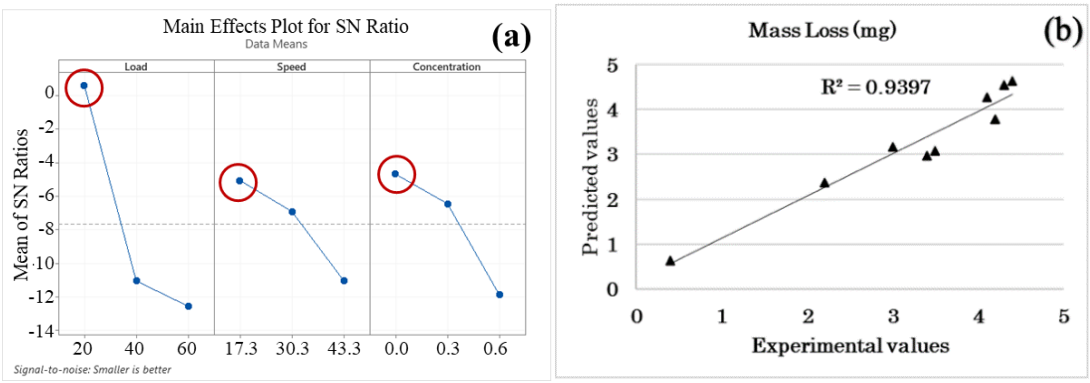

Figure 3. a) SN ratios for ML, b) the relationship between the experimental results and the predicted results of the ML values from the regression analysis

3.2 Friction Coefficient (CoF)

When the friction coefficients obtained after the wear tests were examined, the maximum CoF was obtained from the specimen number 7 (Table 6). In this experiment with a 60 N load, a 17.3 mm/s sliding speed, and 0.6 weight percent ore particles, the CoF was determined to be 0.1447. Specimen 6 had the lowest coefficient of friction, measuring 0.0804 at 43.3 mm/s sliding speed, 40 N load, and a lubricating liquid free of abrasive particles. Upon examination of the CoF data from the ANOVA analysis, it was determined that the concentration parameter had the highest effectiveness rate (80.91%) on CoF, while speed had the lowest effect value (2.88%) on CoF. Figure 4a displays the plots that were obtained for experimental CoF and S/N ratios. Figure 4b displays the graphs illustrating the correspondence between the experimental outcomes and the anticipated outcomes about the coefficient of determination (CoF) as derived from the regression analysis.

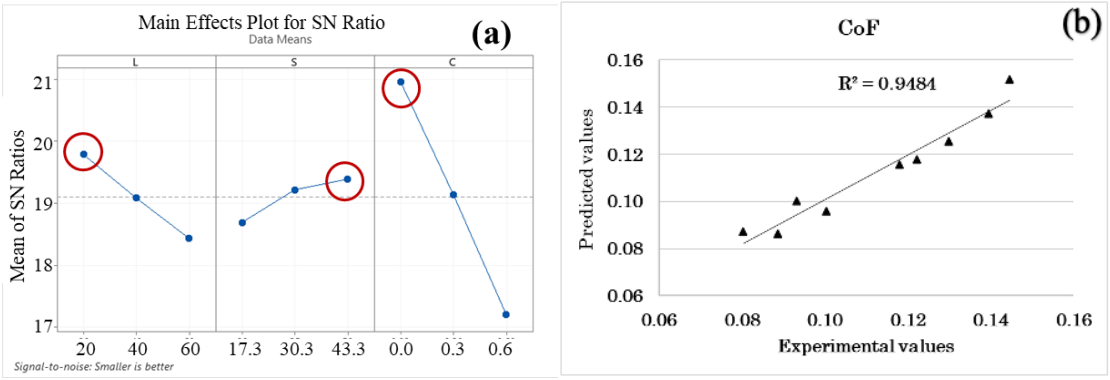

Figure 4. a) S/N ratios for CoF, b) the correlation between the outcomes of the experiment and the CoF values anticipated by the regression analysis

3.3 Trace Depth (TD)

When the TDs observed on the specimen surface after the abrasion tests were examined, the maximum TD was obtained from the specimen number 9 (Table 6). In this experiment, which had a 60 N load, a 43.3 mm/s sliding speed, and 0.3 weight percent ore particles, the minimum TD was measured at 9.038 µm. On specimen number 1, with a load of 20 N, a sliding speed of 117.3 mm/s, and a lubricating medium free of abrasive particles, the lowest TD was measured at 0.948 µm. The study's findings indicate that TD and independent variables have a significant interaction (R2(adj)=0.9582). Figure 5a displays the plots that were obtained for experimental TD and S/N ratios. Figure 5b displays the graphs that illustrate the correlation between the TD experimental findings and the anticipated outcomes derived from the regression analysis.

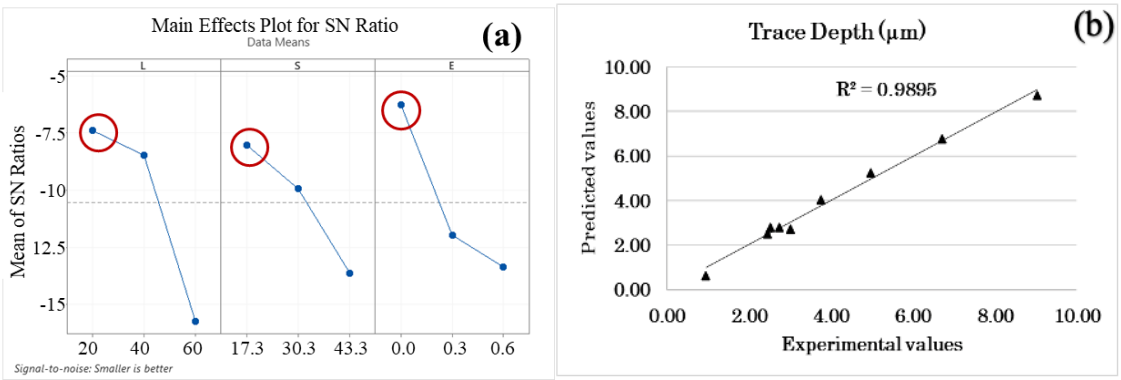

Figure 5. a) S/N ratios for TD, b) The relationship between experimental results and predicted results of the PD values from the regression analysis

3.4 Surface Observation

The wear profiles obtained by using a profilometer and the worn surface images obtained with the FESEM device are brought together in Figure 6, and the wear depth values are given in order from largest to smallest.

Examining the wear markings, it is clear that the specimens' wear marks—which were tested in a lubricating media containing 0.6% weight percent ore particles—are visible. Test specimens 9 with a 60 N load, 443.3 mm/s sliding speed, and 0.3% weight percentage of ore particles by weight were used to measure the maximum wear depth, which came out to be 9.038 µm. Conversely, test specimen No. 1 with a 20 N load, a 17.3 mm/s sliding speed, and an ore-free lubricating media yielded the lowest wear depth value, which was recorded at 0.948 µm.

Examining the wear surface profiles reveals that as the amount of particles increases, so do the wear surfaces' fluctuation and roughness. The wear profile fluctuates due to pegging and plowing mechanisms on the specimen surface, which can be explained by the rise in particle count in the environment (R. A. García-León et al., 2021b). Additionally, Bhoi et al. demonstrated that cutting lines on the degraded surface indicate ductile failure at high impact velocities (Bhoi et al., 2021). An example of a typical micro-ploughing process is seen in the worn debris, which suggests ductile failure.

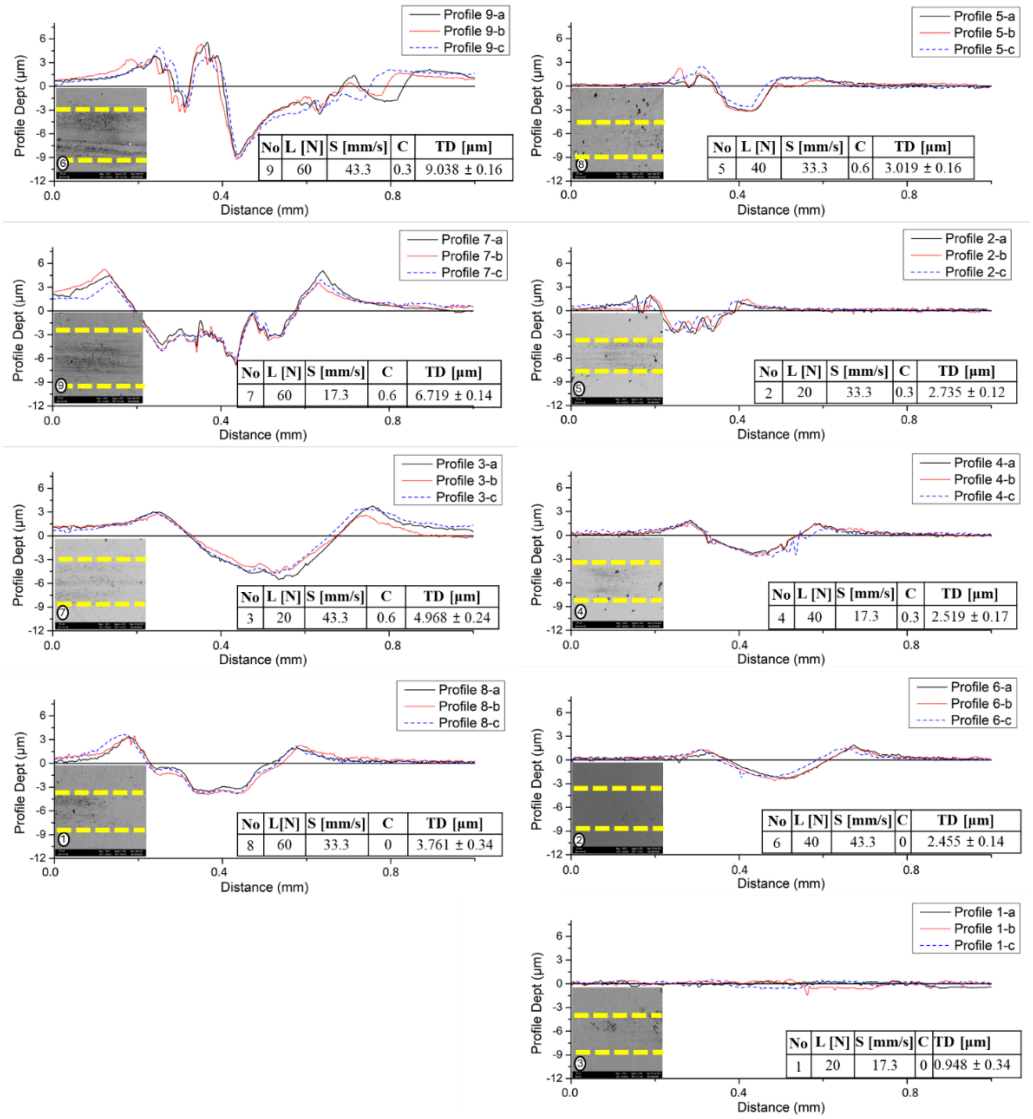

Figure 6. Wear trace profiles and worn surface images obtained from the SEM device

To observe the abrasive wear, 300X and 3kX magnified worn surface SEM images of specimen 7 are given in Figure 7. Upon analyzing the photos of the degraded surface, it was discovered that the ore particles were stuck to the surface. Abrasive ball chip particles of ore particles and bronze chip particles plow traces and related side extrude, and material agglomerations are observed. EDX analysis was performed to determine the components on the surface of the samples obtained, and EDX analyzes for some points and areas are given in Figure 8. In figure 8, EDX analysis was performed to determine what the bodies detected in the SEM images belonged to. In Figure 7, point P1 is thought to belong to the iron ore. Point P2 belongs to the sample. It is observed that in areas A1 and A2, iron ore, abrasive ball and elements belonging to the sample are mixed.

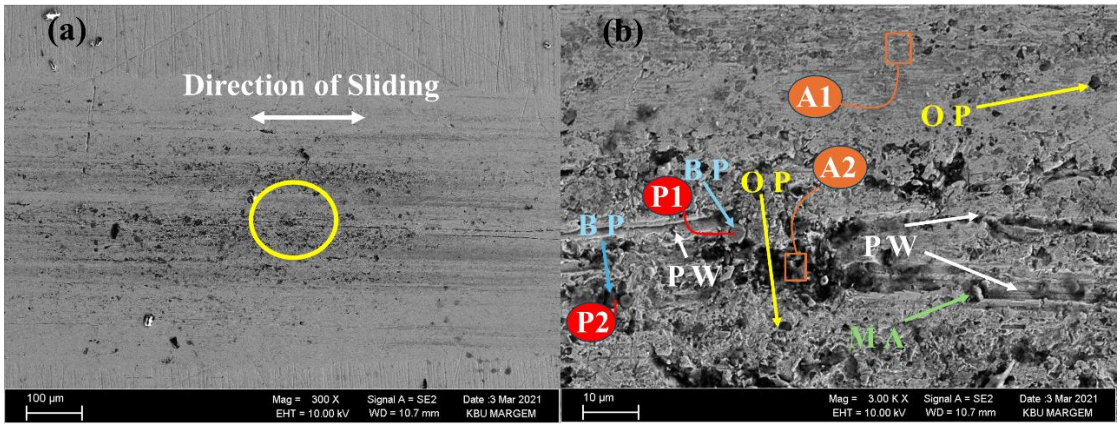

Figure 7. Wear mechanisms on the specimen surface a) 300X zoom, b) 3kX zoom. (OP: Ore Particle, PW: Plowing Wear, MA: Material Agglomeration, BP: Ball Particle)

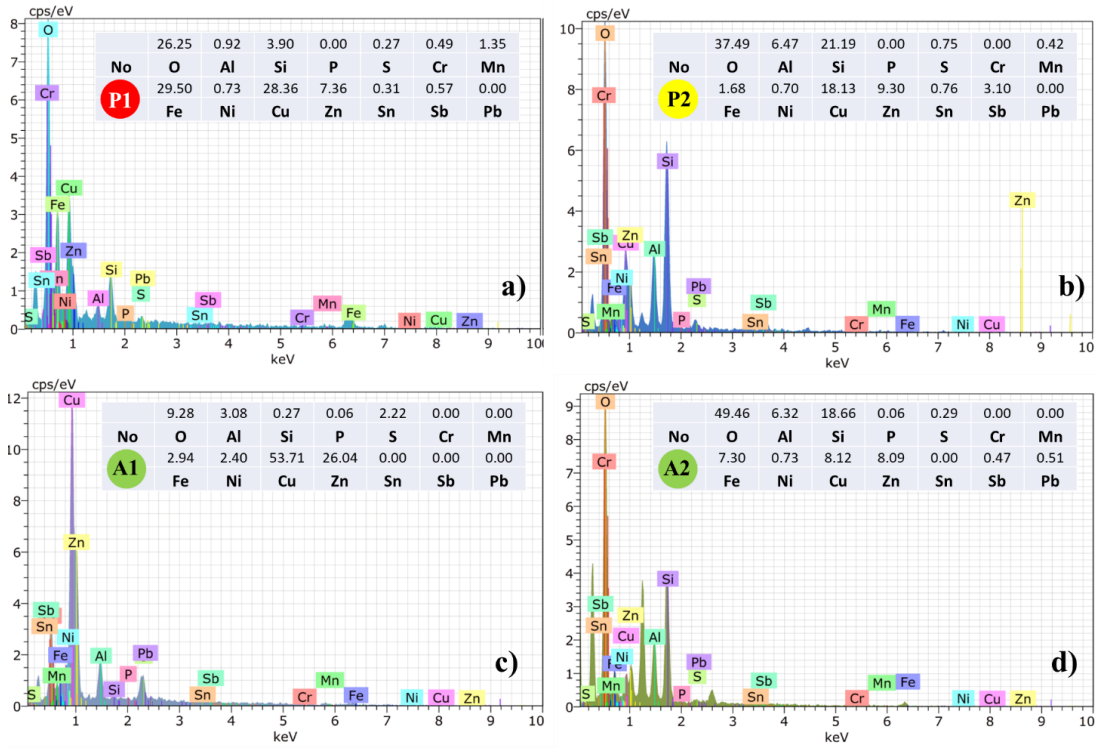

Figure 8. EDX analysis results of the points and areas on Figure 7 a) P1 point, b) P2 point, c) A1 area, d) A2 area.

4. CONCLUSION

This study investigated the effects of the three-body abrasive wear event on ML, coefficient of friction, and TD on the C86200 bronze material when micro-nano abrasive particles enter the lubricant using a ball-on-flat experiment design. The agreement between the predicted and experimental findings was assessed using the Response Surface Method. Furthermore, surface wear mechanisms were assessed based on EDX findings and SEM pictures.

The maximum ML was 4.4 mg (4.64 mg according to the predicted results) in the environment containing 60 N load, 43.3 mm/s sliding speed and 0.3 wt. % ore particles. Considering the predicted results, the highest wear value was obtained from the experiment with a 60 N load of 5.21 mg, a sliding speed of 43.3 mm/s and a medium containing 0.6 wt. % ore particles.

The highest CoF value was 0.1147 (0.1516 according to the predicted results) and 60 N load, 117.3 mm/s sliding speed and 0.6 wt. % ore particles were found in the environment. Considering the predicted results, the highest CoF value belongs to the experiment using the same parameters as the experimental parameters.

The highest TD value was 9.038 μm (8.721 μm according to the predicted results) with 60 N load, 43.3 mm/s sliding speed and 0.3 wt. % ore particles. Considering the predicted results, the highest value is 8.859 μm with 60 N load, 43.3 mm/s sliding speed and 0.6 % by weight of ore particles in the experiment.

5. ACKNOWLEDGEMENTS

The authors gratefully acknowledge Professor Hayrettin AHLATCI for his support in using the test device. The authors gratefully thank KARDOKMAK A.Ş. For their support in sample supply.

6. CONFLICT OF INTEREST

Author(s) approve that to the best of their knowledge, there is not any conflict of interest or common interest with an institution/organization or a person that may affect the review process of the paper.

7. AUTHOR CONTRIBUTION

Abdullah UĞUR contributed to the experiment design, data collection, and manuscript writing. Ahmet Emrah ERDOĞDU contributed to the execution of the experiments, the statistical analysis of the data, and manuscript editing. Recep DEMİRSÖZ contributed to the determination of the research concept, research management, interpretation of the findings, and manuscript editing.

8. REFERENCES

Akram, S, Babutskyi, A, Chrysanthou, A, Montalvão, D, Whiting, MJ, Pizurova, N: Improvement of the wear resistance of nickel-aluminium bronze and 2014-T6 aluminium alloy by application of alternating magnetic field treatment. Wear, 480–481: 2021.

Bailon-Poujol, I, Bailon, JP, L'Espérance, G: Ball-mill grinding kinetics of master alloys for steel powder metallurgy applications. Powder Technol, 210: 267–272, 2011.

Bharatish, A, Harish, V, Bathe, RN, Senthilselvan, J, Soundarapandian, S: Effect of scanning speed and tin content on the tribological behavior of femtosecond laser textured tin-bronze alloy. Opt Laser Technol, 108: 17–25, 2018.

Bhoi, S, Singh, RB, Harsha, AP, Manna, R: Effect of Grain Refinement on Tribological Study of Low Carbon Steel. Transactions of the Indian Institute of Metals, 74: 1489–1499, 2021.

Bozkurt, F, Çakir, Investigation of the Tribological and Mechanical Properties of Boron Steels in Terms of Potential Usage in Agricultural Applications. Politeknik Dergisi, 24: 431–438, 2021.

Cetin, M.H, Korkmaz, S: Investigation of the concentration rate and aggregation behaviour of nano-silver added colloidal suspensions on wear behaviour of metallic materials by using ANOVA method. Tribol Int, 147: 2020.

Demirsoz, R, Uğur, A, Erdoğdu, AE, Korkmaz, ME, Gupta, MK: Abrasive Wear Behavior of Nano-Sized Steel Scale on Soft CuZn35Ni2 Material. J Mater Eng Perform, 32: 8858–8869, 2023.

García-León, RA, Martínez-Trinidad, J, Campos-Silva, I, Figueroa-López, U, Guevara-Morales, A: Wear maps of borided AISI 316L steel under ball-on-flat dry sliding conditions. Mater Lett, 282: 17–18, 2021.

García-León, RA, Martínez-Trinidad, J, Zepeda-Bautista, R, Campos-Silva, I, Guevara-Morales, A, Martínez-Londoño, J, Barbosa-Saldaña, J: Dry sliding wear test on borided AISI 316L stainless steel under ball-on-flat configuration: A statistical analysis. Tribol Int, 157: 2021.

Gheisari, R, Polycarpou, AA: Three-body abrasive wear of hard coatings: Effects of hardness and roughness. Thin Solid Films, 666: 66–75, 2018.

Huang, L, Deng, X, Li, C, Jia, Y, Wang, Q, Wang, Z: Effect of TiC particles on three-body abrasive wear behaviour of low alloy abrasion-resistant steel. Wear, 434–435: 202971, 2019.

Kusumoto, K, Shimizu, K, Efremenko, VG, Hara, H, Shirai, M, ito, J, Hatate, M, gaqi, Y, Purba, RH: Three body type abrasive wear characteristics of multi-component white cast irons. Wear, 426–427: 122–127, 2019.

Lakshmikanthan, A, Bontha, S, Krishna, M, Koppad, PG, Ramprabhu, T: Microstructure, mechanical and wear properties of the A357 composites reinforced with dual sized SiC particles. J Alloys Compd, 786: 570–580, 2019.

Lan, P, Polycarpou, AA: High temperature and high pressure tribological experiments of advanced polymeric coatings in the presence of drilling mud for oil & gas applications. Tribol Int, 120: 218–225, 2018.

Lan, P, Polychronopoulou, K, Zhang, Y, Polycarpou, AA: Three-body abrasive wear by (silica) sand of advanced polymeric coatings for tilting pad bearings. Wear, 382–383: 40–50, 2017.

Liu, Q, Qi, F, Wang, Q, Ding, H, Chu, K, Liu, Y, Li, C: The influence of particles size and its distribution on the degree of stress concentration in particulate reinforced metal matrix composites. Materials Science and Engineering A, 731: 351–359, 2018.

Madhusudan, BM, Ghanaraja, S, Sudhakar, GN: Synthesis and development of size hybrid nano SiC-Al7075 composites by advanced stir casting. In: Materials Today: Proceedings. Elsevier Ltd, 2020, pp 3804–3809.

Mahajan, Y, Peshwe, DR: Effect of Temper Conditions on Abrasive Wear Behavior of AA7010 Alloy. Transactions of the Indian Institute of Metals, 71: 1025–1032, 2018.

Manoharan, S, Vijay, R, Lenin Singaravelu, D, Kchaou, M: Experimental Investigation on the Tribo-Thermal Properties of Brake Friction Materials Containing Various Forms of Graphite: A Comparative Study. Arab J Sci Eng, 44: 1459–1473, 2019.

Nas, E, Altan Özbek, N: Optimization of The Machining Parameters in Turning of Hardened Hot Work Tool Steel Using Cryogenically Treated Tools. Surface Review and Letters, 27: 1–14, 2020.

Nas, E, Oztürk, B: Optimization of surface roughness via the Taguchi method and investigation of energy consumption when milling spheroidal graphite cast iron materials. Materialpruefung/Materials Testing, 60: 519–525, 2018.

Purba, R. H., Shimizu, K., & Kusumoto, K: Three-Body Abrasive Wear-Resistance Characteristics of a 27Cr-Based 3V-3Mo-3W-3Co Multicomponent White Cast Iron with Different Ti Additions. Journal of Manufacturing and Materials Processing, 7(1), 21, 2023

Radhika, N, Sai Charan, K: Experimental Analysis on Three Body Abrasive Wear Behaviour of Stir Cast Al LM 25/TiC Metal Matrix Composite. Transactions of the Indian Institute of Metals, 70: 2233–2240, 2017.

Radhika, N: Mechanical Properties and Abrasive Wear Behaviour of Functionally Graded Al-Si12Cu/Al2O3 Metal Matrix Composite. Transactions of the Indian Institute of Metals, 70: 145–157, 2017.

Rahiman, AHS, Smart, DSR, Wilson, B, Ebrahim, I, Eldhose, B, Mathew, B, Murickan, RT: Dry sliding wear analysis OF Al5083/CNT/Ni/MoB hybrid composite using DOE Taguchi method. Wear, 460–461: 2020.

Sardar, S, Karmakar, SK, Das, D: Evaluation of Abrasive Wear Resistance of Al2O3/7075 Composite by Taguchi Experimental Design Technique. Transactions of the Indian Institute of Metals, 71: 1847–1858, 2018.

Sasidharan, S, Puthucode, R, Radhika, N, Shivashankar, A: Investigation of three body abrasive wear behaviour of centrifugally cast Cu-Sn/SiC functionally graded composite using Design of Experiment Approach. 2018.

Singh, RK, Telang, A, Das, S: The influence of abrasive size and applied load on abrasive wear of Al-Si–SiCp composite. Arab J Sci Eng, 47: 8617–8628, 2022.

Varol, T, Canakci, A, Ozsahin, S: Prediction of effect of reinforcement content, flake size and flake time on the density and hardness of flake AA2024-SiC nanocomposites using neural networks. J Alloys Compd, 739: 1005–1014, 2018.

Xin, W, Wang, YJ, Wei, SC, Liang, Y, Xia, XC, Chen, X, Wang, B, Xu, BS: Friction and wear behavior under oil lubrication conditions of amorphous-nanocrystalline composite coatings deposited via HVAS. Surf Coat Technol, 429: 2022.

Yin, YL, Yu, HL, Wang, HM, Song, ZY, Zhang, Z, Ji, XC, Cui, TH, Wei, M, Zhang, W: Friction and wear behaviors of steel/ bronze tribopairs lubricated by oil with serpentine natural mineral additive. Wear, 456–457: 2020.

Zhao, B, Zhang, Y, Fan, Y, Yu, X, Zhang, Z, Zhang, B: The three-body abrasive tribological characteristics of the Graphene/h-BN heterostructure film considering defects. Tribol Int, 171: 2022.

JOURNAL of
MATERIALS and MECHATRONICS:A

e-ISSN 2717-8811
JournalMM, 2024, 5(1), 49-59
https://doi.org/10.55546/jmm.1413577

Araştırma Makalesi / Research Article

The Tensile Properties of Functionally Graded Materials in MSLA 3D Printing as a Function of Exposure Time

Abdurrahim TEMİZ[1*]

[1*]Karabük University, Department of Industrial Design Engineering, Karabük, Turkey,
ORCID ID: https://orcid.org/0000-0001-6885-1475, abdurrahimtemiz@karabuk.edu.tr

Geliş/ Received: 03.01.2024**;** **Revize/Revised:** 13.03.2024 **Kabul / Accepted:** 19.04.2024

ABSTRACT: Functionally graded additive manufacturing (FGAM) emerged from the combination of Functionally Graded Materials into additive manufacturing. This work involved the production of FGAM specimens to alter the characteristics of both the outer and inner zones of tensile specimens. This was achieved by adjusting the exposure time without additional costs or equipment. During the assessment, the tensile specimen was separated into three zones. The exterior layers were initially created with a 3-second exposure time, followed by the interior layers with a 15-second exposure time. Then, the process was reversed, with the outer layers exposed for 15 seconds and the inner layers exposed for 3 seconds. Subsequently, all layers were generated using exposure durations of 3 seconds and 15 seconds, respectively, without any alterations, resulting in a total of 4 distinct samples. The hardness and tensile tests were conducted on all specimens, both with and without post-curing, in order to assess the impact of post-curing. The outcomes indicate that the levels of hardness and maximum tensile strength rise as the final curing process progresses, but the elongation capability diminishes. The highest ultimate tensile strength, achieved after 15 seconds of exposure time with post cure, was measured at 46.46 ± 0.9 MPa. The green FGAM specimens have a greater ultimate tensile strength (35.85 ± 0.4 MPa) when created with an exposure time of 15-3-15 s. However, the specimen produced with an exposure time of 3-15-3 s demonstrates a higher ultimate tensile strength (38.77 ± 0.7 MPa) following post curing.

Keywords: MSLA printer, 3D printing, functionally graded material, additive manufacturing.

1. INTRODUCTION

Functionally Graded Materials (FGMs) are a specific category of composite materials that are particularly suitable for situations when one component must contain conflicting characteristics. FGMs are a category of substances distinguished by the existence of property fluctuations across their entirety (Hisham et al., 2022). The quick fabrication of 3D parts for diverse purposes has led to

*Sorumlu yazar / Corresponding author: abdurrahimtemiz@karabuk.edu.tr
Bu makaleye atıf yapmak için /To cite this article

Temiz, A. (2024). The Tensile Properties of Functionally Graded Materials in MSLA 3D Printing as a Function of Exposure Time. Journal of Materials and Mechatronics: A (JournalMM), 5(1), 49-59.

increased interest in additive manufacturing (AM) (Bayraklilar et al., 2023; Güdür et al., 2023; Kaya et al., 2023). Additive manufacturing (AM) has revolutionized modern manufacturing by enabling the creation of complex and customized structures (Demir et al., n.d.; Güdür et al., 2023). FGMs have attracted significant interest in the field of additive manufacturing (AM) due to their potential to provide tailored material properties within a single component (Loh et al., 2018; Ren et al., 2018). The advantages of AM techniques, including the capacity to fabricate intricate things, the minimal generation of waste, the low energy consumption, and the flexibility in design, render them highly appealing for the production of functionally graded materials (FGMs), heterogeneous multi-materials, as well as homogenous single-materials (Bazyar et al., 2023). The capability of AM to manufacture FGMs has been demonstrated, enabling the production of parts with discrete or continuous variations in their attributes and compositions throughout their volume (Nohut and Schwentenwein, 2022; Schneck et al., 2021). Briefly, functionally graded additive manufacturing (FGAM) is the process of deliberately altering the material arrangement within a component in order to produce a certain function (Hisham et al., 2022). This technology offers the potential for novel industrial applications and has been applied in various fields such as orthopedics, automobile, energy, aerospace, ceramics, and dentistry (Alshaikh et al., 2022; Bazyar et al., 2023; González et al., 2019; Rouf et al., 2022). Furthermore, the use of FGMs in AM has extended to the development of composite materials with heterogeneous microstructures, allowing specific physical and mechanical properties to change continuously in the thickness direction (Torabian and Khalili, 2020). This capability has opened up opportunities for the design and production of components with tailored performance characteristics, such as enhanced mechanical properties and improved functionality (Carraturo et al., 2019; Clarke-Hicks et al., 2022). The research on FGMs and AM has also delved into the mechanical performance and properties of additively manufactured materials. Studies have investigated the strength, cyclic properties, and impact toughness of additively manufactured components, providing insights into their structural integrity and suitability for various applications (Chmelko et al., 2023; Lucon and Hrabe, 2018). Additionally, the development of FGMs has led to the exploration of new materials, such as continuous fiber-reinforced thermosetting polymer composites, which offer high-performance characteristics and mechanical compatibility with specific applications (Rahman et al., 2023; Yao et al., 2019). The integration of FGMs with AM processes, particularly in the context of Stereolithography (SLA) grey resin, presents a promising avenue for the production of parts with customized material properties. In this context, the exposure time during the additive manufacturing process plays a critical role in influencing the material characteristics and attributes of the finished component. The photocuring conversion rate is dependent upon the exposure duration and exerts a substantial impact on material properties, including density, shrinkage, and elastic modulus (Bonada et al., 2017). SLA 3D printing involves the laser scanning and curing of the photopolymer resin point by point, while in DLP systems, UV light can cure an entire layer of the resin at once (Xiao et al., 2019). Additionally, there are many studies in the literature considering exposure time as a parameter to optimize the SLA printed parts (Borra and Neigapula, 2022; Seprianto et al., 2020; Temiz, 2023). The final characteristics of 3D printed materials are dependent upon the configuration and potential fluctuations of all manufacturing factors (Riccio et al., 2021). In summary, the integration of functionally graded materials with additive manufacturing processes, particularly in the context of SLA grey resin, presents a promising avenue for the production of parts with tailored material properties. The exposure time during the additive manufacturing process, along with the ability to achieve gradationally varying material organization, offers opportunities for the development of components with enhanced performance and functionality.

This investigation involved the production of FGAM dog bone tensile samples by controlling the exposure time using a Masked Stereolithography (MSLA). FGAM was created employing two distinct exposure times and samples without FGAM were likewise generated and analyzed under these exposure times. All dog bone tensile test specimens were created using the ASTM D638 standard test protocol (Anonymous, 2022) for evaluating the tensile characteristics of polymers.

2. MATERIALS AND METHODS

2.1 Material

This study utilized an Anycubic Photon M3 MSLA machine equipped with a light-source emitting at a wavelength of 405 nm. The Anycubic Photon Mono M3 printing machines has a build volume of 180 x 163 x 102 mm. The printers employ a 405 nm Para LED matrix as a UV light source, along with an LCD screen to exhibit a masked image of each sliced data. This study specifically examined the mechanical properties of the standard UV resin used in the Anycubic printer, despite the fact that it can also accommodate other resins like as UV tough resin, dental resin, UV resin for casting, and acrylonitrile butadiene styrene (ABS). The Standard UV Resin is a UV-curable resin with high precision. It cures when exposed to a UV curing wavelength ranging from 365 to 410 nm, often within 5 to 15 seconds (Temiz, 2023). The composition comprises acrylate oligomer, acrylate monomer, and a photoinitiator. The material utilised was a conventional UV resin, with specific characteristics outlined in Table 1.

Table 1. Characteristics of conventional UV resin.

Properties	Value
Viscosity, cP or mPa·s	150-200
Density, g/cm^3	1.05-1.25
Molding shrinkage, %	3.72-4.24
Tensile strength, MPa	36-52
Flexural strength, MPa	50-70
Surface hardness, HD	84
Flexural modulus, MPa	1200-1600

The Anycubic wash and cure plus post printing washing and curing machine was used to do the final curing and washing operation. The dimensions of this equipment for washing are 192*120*290 mm, while the dimensions for curing are 190*245 mm.

2.2 Sample Production

The development of a dog bone tensile test specimen involved following the ASTM D638 standard test technique for evaluating the tensile characteristics of polymers. Specimen dimensions were derived from an ASTM D638 Type 4 model, and Solidworks was used to build the specimen's computer-aided design (CAD) (Anonymous, 2022). The created samples were saved in STL format and subsequently sliced using Anycubic Photon Workshop 3D Slicer Software. The layer thickness in the slicing parameters remained consistent at 50μm for all samples. All settings, except for the exposure time, are predetermined by default. The samples were generated using 4 distinct parameters, which varied based on the time of exposure. Initially, all layers were generated using a 3-second exposure time, followed by the generation of all layers using a 15-second exposure time.

Subsequently, the sample was divided into three sections, with the bottom and top layers being generated using a 3-second exposure time, while the layers in the middle were generated using a 15-second exposure time. At last, both the top and bottom levels were created with a 15-second exposure period, while the middle layers were formed with a 3-second exposure time. The three distinct zones were obtained by adjusting the exposure period on the MSLA screen during printing, leading to differing levels of exposure. In order to finalize the polymerization process, it is advisable to cleanse 3D printed items using a solvent to eliminate any unpolymerized resin, and subsequently transfer them to a gentle polymerization chamber (Wada et al., 2022). In order to fully evaluate the impact of post curing, the samples were individually analyzed both prior to and after to the post curing process. Following the printing procedure, the printed parts were extracted from the build platform and cleaned of excess resin through rinsing with isopropyl alcohol (IPA). Each sample used for the tensile and hardness tests was washed in an Anycubic wash & cure 2.0 machine with IPA for two minutes. After washing the samples with IPA, the MSLA 3D printer samples were divided into two groups. Half of the cleaned samples were then placed in the curing chamber of the Anycubic wash & cure 2.0 machine and underwent a 5-second final curing process to investigate the impact of this final step. This post curing protocol is similar to those used in dental and medical applications, however, it allows for constant light intensity and adjustable time. This technology is also widely used in the dental industry for manufacturing components using resins like dental temp and surgical guide, which are subsequently subjected to post-curing. Figure 1 displays the schematic depiction of the generated samples.

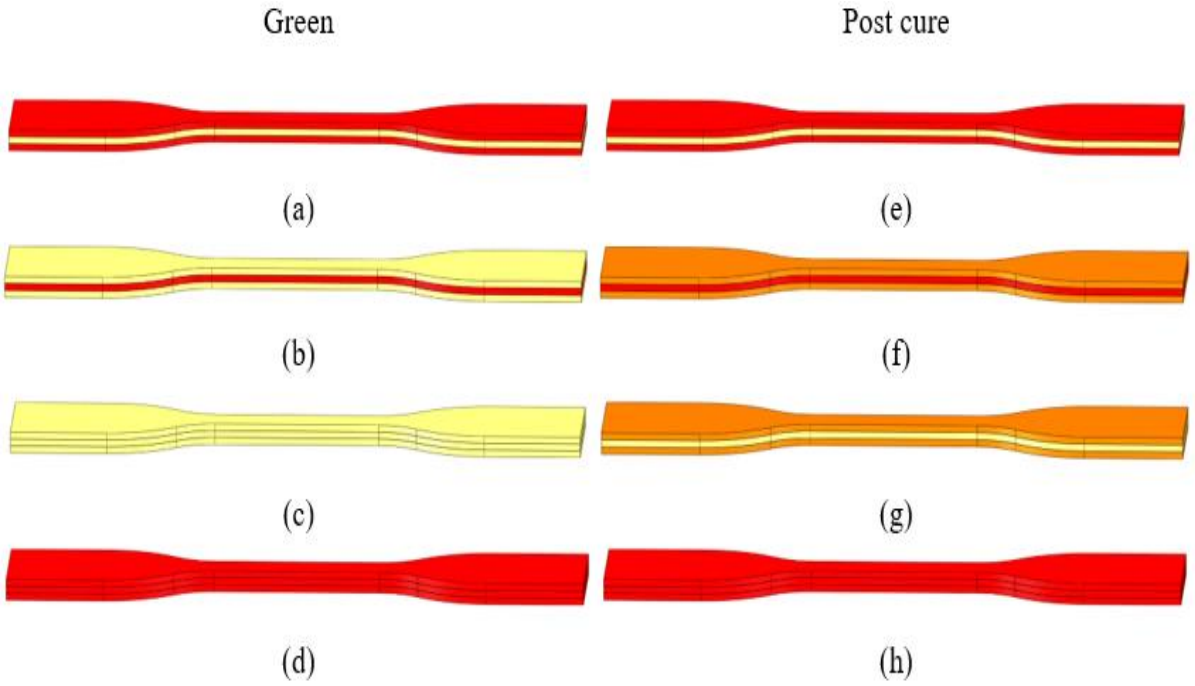

Figure 1. Layers in (a) and (e) were exposed for 15 s, while layers in the middle were exposed for 3 s, layers in (b) and (f) were exposed for 3 s, while layers in the middle were exposed for 15 s, layers in (c) and (g) were exposed for 3 s, and layers in (d) and (h) were exposed for 15 s

2.3 Mechanical Testing

The application of several criteria resulted in the production of a total of eight samples. A tensile test was conducted using the AG-50 kN Shimadzu Autograph under controlled settings, maintaining a constant crosshead speed of 5 mm/min and operating at room temperature. Tensile testing was

performed using the parameters specified in ASTM D638 (Anonymous, 2022). The specimens were subjected to tensile testing until they reached the point of fracture. To reduce the influence of fluctuations and unpredictable errors, each recorded value in the dataset corresponds to a minimum of three valid tests. No instances of further peaks in strength were seen in the samples. The UTS was identified as the maximum stress measurement ever recorded. In addition, for the purpose of measuring hardness (Shore D), two distinct samples were created, each with dimensions of 20 mm x 20 mm x 10 mm, with an exposure time of 3 seconds and 15 seconds, respectively. Hardness values of these samples were measured separately before and after post curing.

3. RESULTS AND DISCUSSION

Each sample was manufactured successfully in accordance with the given parameters. Although not a significant constraint identified during the investigation, minor concerns emerged regarding the adherency of the printed samples to the build tray, particularly when distinct exposure periods were employed for each layer. In particular, when using a shorter exposure time (3 seconds) for the outer layers and a longer exposure time (15 seconds) for the middle layers, cases were observed where the sample did not always stick to the tray during printing. However, it is important to mention that samples could also be effectively generated with a first layer exposure period of 3 seconds. The stress-strain curves for each of the chosen exposure times are depicted in Figure 2. The tensile test results demonstrate that increasing exposure time leads to an increase in the elastic modulus. According to the literature (Bazyar et al., 2023), it is typical for the elastic modulus to rise as the time of exposure increases. Equation (1) confirms that the primary cause for this phenomenon.

$$\phi\,(z,t) = 1 - \exp(-KI_0 \exp(-\mu z)t) \quad (1)$$

The variables in the equation are defined as follows: ϕ represents the ratio of monomer-to-polymer conversion, t represents the exposure duration, K represents the effective reaction conversion rate of the material, μ represents the attenuation coefficient, and z represents the direction of the manufacturing process (Bonada et al., 2017). As the exposure time increases, more monomers undergo polymerization, as indicated by Equation (1). Therefore, the increase in exposure time leads to a rise in Young's modulus and other mechanical properties (Ambrosio et al., 2020; Temiz, 2023). This is confirmed by the tensile results in Figure 1 (a) in the absence of final curing. However, a negative correlation was observed between exposure time and elongation. The post-curing process enhanced the tensile strength and Young's modulus values, as illustrated in Figure 2. Prior research findings indicate that the tensile strength of various resins exhibited a rise ranging from 29% to 215%, while Young's modulus showed an increase ranging from 33% to 172% (Riccio et al., 2021). These results validate the alteration observed in the stress-strain curve depicted in Figure 2 after the post-curing process.

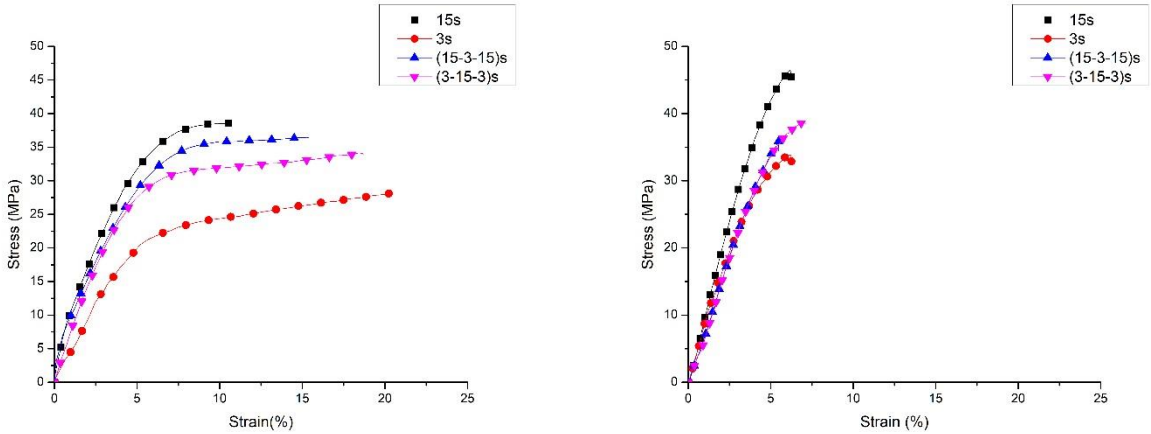

(a) (b)

Figure 2. Curves of stress and strain for exposure durations of 3s, 15s, 15-3-15s, and 3-15-3s are presented a) green and b) following post cure

The data for ultimate tensile strength and elongation are displayed in Figure 3. The elongation and ultimate tensile strength values of all specimens have been determined using the tensile test. Figure 3 (a) indicates that the ultimate tensile strength of green specimens, which were produced for 3 seconds exposure time, was measured to be 28.08 ± 0.4 MPa. By extending the time spent of the exposure to 15 seconds, there was a significant increase in the ultimate tensile strength, which reached a value of 38.59 + 0.4 MPa. The post cure specimens, produced with an exposure time of 3 seconds, exhibited an ultimate tensile strength of 33.87 ± 1.04 MPa. By increasing the duration of exposure to 15 seconds, there was also a notable rise in the ultimate tensile strength, which reached a value of 46.46 ± 0.9 MPa. Two distinct materials were generated as FGMs. Designated as (15-3-15), these objects have the central area exposed for a duration of 3 seconds, while the edges are exposed for 15 seconds. Similarly, designated as (3-15-3), these objects have the central area exposed for 15 seconds, while the edges are exposed for 3 seconds. The green specimens produced during 15-3-15 s exposure time had an ultimate tensile strength of 35.85 ± 0.4 MPa. After post curing, the ultimate tensile strength was measured as 36.45 ± 1.1 MPa. The green specimens, which were exposed for 3-15-3 seconds, exhibited an ultimate tensile strength of 34.15 ± 0.8 MPa. After the post curing process, the ultimate tensile strength was determined to be 38.77 ± 0.7 MPa.

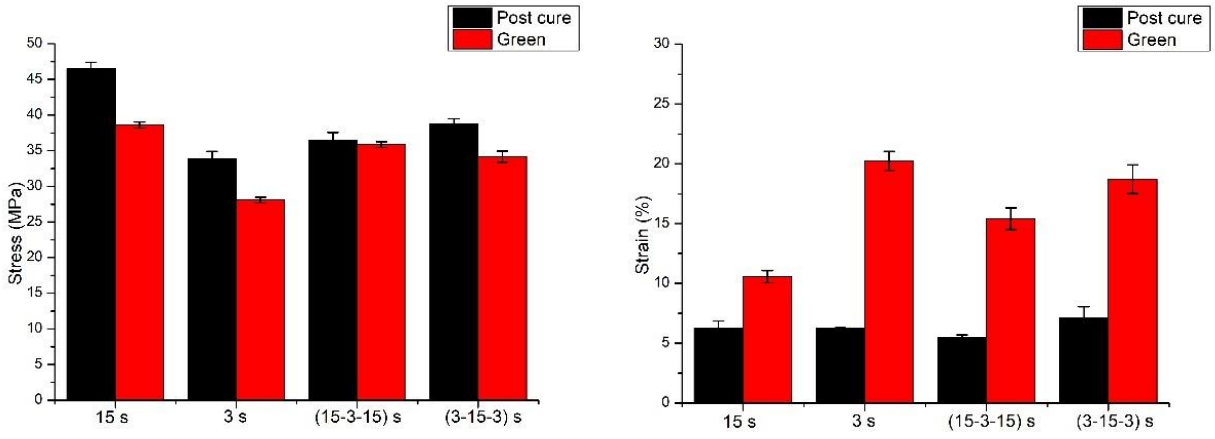

(a) (b)

Figure 3. Depending on the exposure time, (a) ultimate tensile strength and (b) elongation

Furthermore, Figure 3 (b) displays the maximum strain values. The graph clearly illustrates a decrease in strain levels following the final curing process. The reduction in amount is more

pronounced for a low curing value (3 seconds exposure time), but comparatively less significant at a high curing value (15 seconds exposure time). Understanding the hardness values of each material in FGM design is a crucial component for optimizing material performance, durability, and life. This can be utilized to attain more precise and efficient material designs in a multitude of industrial and technical applications. Hardness is a significant mechanical property of resins, since it determines their ability to withstand wear and deformation (Vasques et al., 2019). Figure 4 displays the Shore D hardness values of samples obtained at various exposure durations, both before and after post curing.

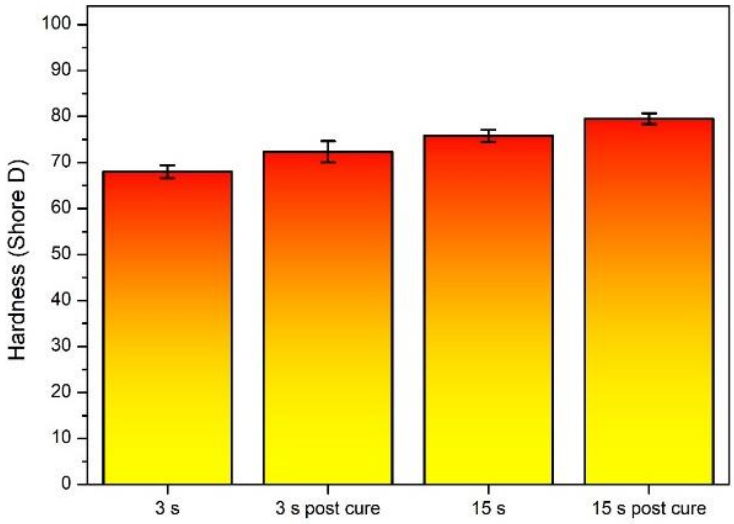

Figure 4. Hardness value of the specimens

Increasing the time of exposure enables a more comprehensive polymerization process of the resin, resulting in a greater degree of conversion of monomers into polymer chains. In addition, post-curing enhances the progress of the curing reaction, eliminating any remaining uncured monomers and enhancing the overall uniformity of the material. The improved curing efficiency leads to the observed enhancement in mechanical characteristics, as the material becomes more homogeneous and structurally resilient. Figure 4 illustrates a direct correlation between the exposure time and the hardness value of the material, indicating that as the exposure time rose, the hardness value also increased. Furthermore, post curing results in a heightened level of material hardness. The hardness of the sample, which was initially 68, increased to 72.33 after post curing, following a 3-second exposure duration. The hardness of the sample, obtained with a 15-second exposure time, was 75.8 prior to post-curing and increased to 79.5 after post-curing. The increase in hardness of the material with longer exposure time and post-curing aligns with findings in the literature. A study on 3D-printed orthodontic aligner material reported that longer curing times resulted in increased surface hardness of the printed objects (Wada et al., 2022). Additionally, post-curing has been shown to enhance the mechanical properties of 3D-printed materials. For instance, a study on the influence of post-processing methods on the Knoop hardness of photosensitive resins used in dentistry found that post-curing significantly increased the hardness of the materials (Vasques et al., 2019). These findings support the observed increase in hardness with post-curing in the samples. It is important to note that the choice of 3D printing technology can impact the mechanical properties of the printed objects. For instance, a study comparing different 3D printing technologies found that SLA printers provided higher surface hardness compared to DLP printers (Wada et al., 2022). The layers and graded transitions were also studied by examining microscopic photographs of the samples. Microscopic images of the materials are depicted in Figure 5.

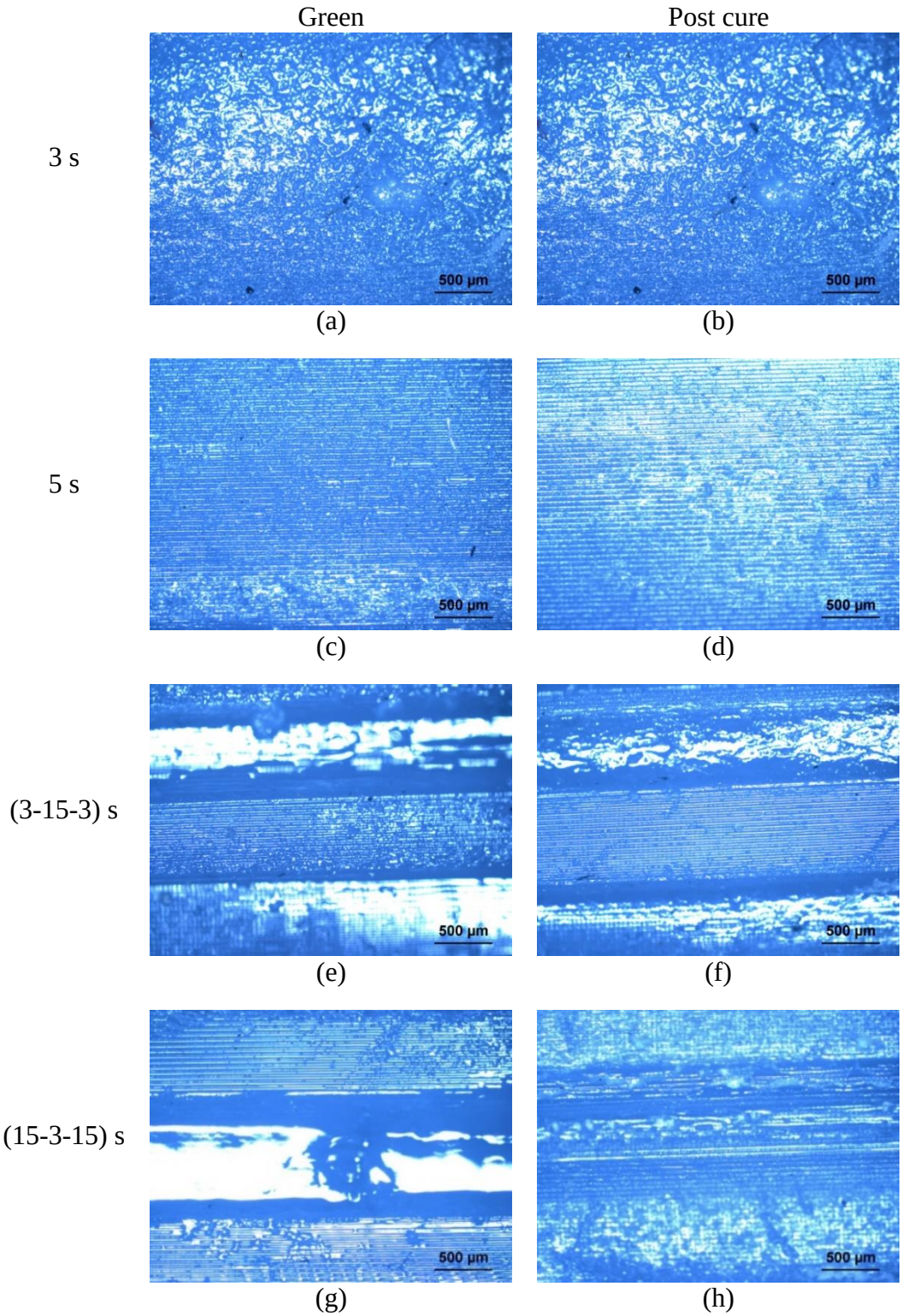

Figure 5. Microscopic images of the different exposre time sambles (a) 3 s, (b) 3s with post cure, (c) 15 s, (d) 15 s with post cure, (e) (3-15-3) s, (f) (3-15-3) s with post cure, (g) (15-3-15) s, and (h) (15-3-15) s with post cure

Upon analyzing Figure 5, it is evident that the layer transitions in the samples created with a 15-second exposure time are more distinct, whereas the layer transitions are not observable in the samples produced with a 3-second exposure period. Furthermore, the transitions in grades of FGAM specimens are more distinctly visible, particularly in specimens with a green coloration.

In conclusion, the elastic section is typically more susceptible to deformation. Thus, in the process of conducting tensile testing, a significant portion of the deformation is likely to take place in the more elastic section. Given its inherent rigidity and resistance, the hard section frequently serves as the site where cracking or fracture initiates. Cracks frequently initiate and spread in the boundary zones of materials due to the contrasting mechanical characteristics of hard and soft materials. Instead of sudden variations in mechanical characteristics across different areas of the printed part, a smooth transition can be incorporated. This can be accomplished by incrementally modifying the exposure time throughout each layer, facilitating a more seamless transition between materials that have distinct properties. This method has the potential to reduce stress concentration at the borders, which in turn can assist prevent the beginning and spread of cracks.

4. CONCLUSION

This study introduced an easy and useful technique for printing polymer materials with distinct characteristics in each layer using MSLA printers. The tensile test samples were printed with different characteristics in their inner and exterior regions, and their mechanical properties were examined. In addition, an investigation was conducted to evaluate the alterations in the mechanical characteristics of these graded printed samples subsequent to the post curing process. It has been noted that materials manufactured with longer exposure times exhibit higher hardness, and the post curing process further enhances the material's hardness. Increasing exposure time polymerizes the resin more thoroughly, converting monomers into polymer chains. Post-curing also accelerates the curing procedure, eliminates uncured monomers, and improves material consistency. Improved curing efficiency makes the material more uniform and structurally resilient, improving mechanical properties. The samples, when manufactured with a more rigid interior and a more flexible outside, exhibited a decreased ultimate tensile strength compared to those made with a flexible interior and a rigid exterior. However, this trend was reversed after undergoing post curing. This approach has the capability to selectively generate specific regions of the material with increased elasticity or rigidity, depending on the desired qualities. Structural engineering applications in industries like aerospace or automotive often necessitate components that possess a blend of rigidity and flexibility. Structures that require both internal support and outward stress absorption, such as composite panels for aircraft or automobile body panels, could benefit from components that have a rigid inner and a flexible exterior. When it comes to protective gear and sportswear, such as helmets, padding, or athletic footwear, it is crucial to have materials that provide both impact resistance and flexibility. Utilizing samples that have an inflexible core and adaptable exterior could offer improved defense against impacts while simultaneously preserving the wearer's comfort and mobility. Biomedical engineering frequently necessitates the use of materials that imitate the mechanical characteristics of natural tissues for implants, prostheses, and medical devices. Implants or surgical instruments that have a hard core and a flexible outer layer offer advantages by providing stability during insertion and minimizing tissue stress.

5. ACKNOWLEDGEMENTS

This study was supported by Karabuk University Scientific Research Coordinatorship with Project number of KBÜBAP-23-ABP-069.

6. CONFLICT OF INTEREST

The author confirms that, to the best of their knowledge, there are no common interests or conflicts of interest with any organization, institution, or individual that could potentially impact the review process of the paper.

7. AUTHOR CONTRIBUTION

Abdurrahim TEMİZ contributed determining the concept of the research and research management, design process of the research and research management, data analysis and interpretation of the results, critical analysis of the intellectual content, preparation of the manuscript, and final approval and full responsibility.

8. REFERENCES

Alshaikh, A. A., Khattar, A., Almindil, I. A., Alsaif, M. H., Akhtar, S., Khan, S. Q., Gad, M. M., 3d-Printed Nanocomposite Denture-Base Resins: Effect of ZrO2 Nanoparticles on the Mechanical and Surface Properties in Vitro. Nanomaterials 12(14), 2451, 2022.

Ambrosio, D., Gabrion, X., Malécot, P., Amiot, F., Thibaud, S., Influence of manufacturing parameters on the mechanical properties of projection stereolithography–manufactured specimens. The International Journal of Advanced Manufacturing Technology 106(1), 265–277, 2020.

Anonymous, 2022. ASTM, I. Standard Test Method for Tensile Properties of Plastics. https://doi.org/10.1520/D0638-14.

Bayraklilar, M. S., Kuncan, M., Buldu, A., Koçak, M. T., Ülkir, O., Comparison of Mechanical Properties of Samples Fabricated by Stereolithography and Fused Deposition Modelling. Journal of Materials and Mechatronics: A 4(2), 4(2), 475-491, 2023.

Bazyar, M. M., Tabary, S. A. A. B., Rahmatabdi, D., Mohammadi, K., Hashemi, R. A novel practical method for the production of Functionally Graded Materials by varying exposure time via photo-curing 3D printing. Journal of Manufacturing Processes 103, 136–143, 2023.

Bonada, J., Muguruza, A., Fernández-Francos, X., Ramis, X. Influence of exposure time on mechanical properties and photocuring conversion ratios for photosensitive materials used in Additive Manufacturing. Procedia Manufacturing 13, 762–769, 2017.

Borra, N. D., & Neigapula, V. S. N. (2022). Parametric optimization for dimensional correctness of 3D printed part using masked stereolithography: Taguchi method. Rapid Prototyping Journal 29(1), 166–184, 2022.

Carraturo, M., Rocca, E., Bonetti, E., Hömberg, D., Reali, A., Auricchio, F. Graded-Material Design Based on Phase-Field and Topology Optimization. Computational Mechanics 64, 1589-1600, 2019.

Chmelko, V., Šulko, M., Škriniarová, J., Margetin, M., Gašparík, M., Koščo, T., Semeš, M. Strength and Cyclic Properties of Additive vs. Conventionally Produced Material AlSi10Mg. Materials 16(7), 2598, 2023.

Clarke-Hicks, J., Ochoa, I., Correa, D. Harnessing Plastic Deformation in Porous 3D Printed Ceramic Light Screens. Architecture Structures and Construction 3(2), 193-204, 2022.

Demir, S., Temiz, A., Pehlivan, F.. The investigation of printing parameters effect on tensile characteristics for triply periodic minimal surface designs by Taguchi. Polymer Engineering & Science, 2023.

González, P., Schwarzer, E., Scheithauer, U., Kooijmans, N., Moritz, T. Additive Manufacturing of Functionally Graded Ceramic Materials by Stereolithography. Journal of Visualized Experiments (143), e57943, 2019.

Güdür, C., Türkoğlu, T., & Eren, İ. (2023). Effect of Lattice Design and Process Parameters on the Properties of PLA, ABS AND PETG Polymers Produced by Fused Deposition Modelling. Journal of Materials and Mechatronics: A 4(2), 561-570, 2023.

Hisham, M., Saravana Kumar, G., Deshpande, A. P. Process optimization and optimal tolerancing to improve dimensional accuracy of vat-photopolymerized functionally graded hydrogels. Results in Engineering 14, 100442, 2022.

Kaya, Z., Aksoy, B., Özsoy, K. Eklemeli İmalat Yöntemiyle Üretilen Altı Eksenli Robot Kol ile Görüntü İşleme ve Yapay Zeka Tabanlı Ürünlerin Tasniflemesi. Journal of Materials and Mechatronics: A 4(1), 4(1), 193-210, 2023.

Loh, G. H., Pei, E., Harrison, D., Monzón, M. An Overview of Functionally Graded Additive Manufacturing. Additive Manufacturing 23, 34-44, 2018.

Lucon, E., Hrabe, N. Instrumented Impact Testing of Miniaturized Charpy Specimens of AM Ti-6Al-4v. Materials Performance and Characterization 7, 2018.

Nohut, S., Schwentenwein, M. Vat Photopolymerization Additive Manufacturing of Functionally Graded Materials: A Review. Journal of Manufacturing and Materials Processing 6(1), 17, 2022.

Rahman, A., Hall, E., Gibbon, L., Islam, Md. Z., Ulven, C. A., La Scala, J. J. A Mechanical Performance Study of Dual Cured Thermoset Resin Systems 3d-Printed With Continuous Carbon Fiber Reinforcement. Polymers 15(6), 1384, 2023.

Ren, L., Song, Z., Liu, H., Han, Q., Zhao, C., Derby, B., Liu, Q., Ren, L. 3D Printing of Materials With Spatially Non-Linearly Varying Properties. Materials & Design. 156, 470-479, 2018.

Riccio, C., Civera, M., Grimaldo Ruiz, O., Pedullà, P., Rodriguez Reinoso, M., Tommasi, G., Vollaro, M., Burgio, V., Surace, C. Effects of Curing on Photosensitive Resins in SLA Additive Manufacturing. Applied Mechanics 2(4), 2021.

Rouf, S., Malik, A., Raina, A., Ul Haq, M. I., Naveed, N., Zolfagharian, A., Bodaghi, M. Functionally Graded Additive Manufacturing for Orthopedic Applications. Journal of Orthopaedics 33, 70-80, 2022.

Schneck, M., Horn, M., Schindler, M., Seidel, C. Capability of Multi-Material Laser-Based Powder Bed Fusion—Development and Analysis of a Prototype Large Bore Engine Component. Metals 12(1), 44, 2021.

Seprianto, D., Sugiantoro, R., Siproni, Yahya, Erwin, M. The Effect of Rectangular Parallel Key Manufacturing Process Parameters Made with Stereolithography DLP 3D Printer Technology Against Impact Strength. Journal of Physics: Conference Series 1500(1), 012028, 2020.

Temiz, A. The Effects of Process Parameters on Tensile Characteristics and Printing Time for Masked Stereolithography Components, Analyzed Using the Response Surface Method. Journal of Materials Engineering and Performance 1-10, 2023.

Torabian, M., Khalili, S. M. R. Numerical and Experimental Analysis of Cu–Fe Functionally Graded Beam Subjected to Tensile Loading. Proceedings of the Institution of Mechanical Engineers Part C Journal of Mechanical Engineering Science 234(19), 3837-3845, 2020.

Vasques, M. T., Mulder, J. N., Machado, D. S., Lagana, D. C. The influence of the post-processing method on knoop hardness of photosensitive resins for 3D SLA printer used in Dentistry. Clinical and Laboratorial Research in Dentistry 2019.

Wada, J., Wada, K., Gibreel, M., Wakabayashi, N., Iwamoto, T., Vallittu, P. K., Lassila, L. Effect of Nitrogen Gas Post-Curing and Printer Type on the Mechanical Properties of 3D-Printed Hard Occlusal Splint Material. Polymers 14(19), 2022.

Xiao, K., Wu, J., Chen, K., Zhao, Z., Ding, Z., Hu, F., Fang, D., Hu, Q. Grayscale Digital Light Processing 3D Printing for Highly Functionally Graded Materials. Science Advances 5(5), eaav5790, 2019.

Yao, M., Duan, Y., Wang, B., Hong, X., Zhang, X.-H. A Novel Route to Fabricate High-Performance 3D Printed Continuous Fiber-Reinforced Thermosetting Polymer Composites. Materials 12(9), 1369, 2019.

JOURNAL of
MATERIALS and MECHATRONICS:A

e-ISSN 2717-8811
JournalMM, 2024, 5(1), 60-86
https://doi.org/10.55546/jmm.1455324

Araştırma Makalesi / Research Article

Investigation of High-Temperature Wear Behavior of Ni-Mo Alloyed Hardfacing Coatings Applied on Hot Strip Mill Vertical Rolls by Submerged Arc Welding

Hikmet Gizem SARSILMAZ[1], Ali GÜNEN[2], Erdoğan KANCA[3*]

[1]Iskenderun Technical University, Faculty of Engineering and Natural Sciences, Department of Mechanical Engineering, Hatay, Turkey,
ORCID ID: https://orcid.org/0000-0002-2733-8242, sarsilmazhikmet@gmail.com
[2] Iskenderun Technical University, Faculty of Engineering and Natural Sciences, Department of Mechanical Engineering, Hatay, Turkey,
ORCID ID: https://orcid.org/0000-0002-4101-9520, ali.gunen@iste.edu.tr
[3*]Iskenderun Technical University, Faculty of Engineering and Natural Sciences, Department of Mechanical Engineering, Hatay, Turkey,
ORCID ID: https://orcid.org/0000-0002-7997-9631, erdogan.kanca@iste.edu.tr

Geliş/ Received: 20.03.2024**;** **Revize/Revised:** 29.04.2024 **Kabul / Accepted:** 04.05.2024

ABSTRACT: In this study, hot strip mill vertical rolls made of AISI 4140 steel, commonly used in the iron and steel industry's hot rolling section, were coated with ER430 and E430+EC410NiMo using the submerged arc welding (SAW) method. The coatings were characterized through scanning electron microscopy (SEM), energy dispersive spectroscopy (EDS), microhardness, and wear testing (room 24 °C, 300 °C, and 600 °C). XRD analysis showed that in the ER430 sample, the dominant phase was α-ferrite phase and a small amount of γ (austenite) phase observed, while in the ER 430+EC410NiMo sample, the α-ferrite phase was the dominant phase, but the γ (austenite) phase in the structure was more severe and additionally M_6C carbide phase was formed. Coating thicknesses and microhardness values of ER430 and ER430+EC410NiMo coatings were measured as 1.5 mm and 3.75 mm thicknesses, and 533±42 $HV_{0.1}$ and 473±35 $HV_{0.1}$ respectively. The increase in hardness on the surface of coated specimens resulted in higher wear resistance compared to the uncoated specimens under all conditions. Regarding average friction coefficient values, coated specimens generally exhibited lower values, although in some cases, the average friction coefficient was higher. In the wear tests, the lowest wear volume losses occurred in the tests conducted at 300°C, while the highest wear volume losses were observed in the tests at 600°C. Upon evaluating the wear mechanisms, it was determined that adhesive and oxidative wear mechanisms were generally dominant in the coated specimens. At higher temperatures, oxidative wear mechanisms became more prominent. ER430+EC410NiMo coatings exhibited better wear resistance compared to ER430, which

*Sorumlu yazar / Corresponding author: erdogan.kanca@iste.edu.tr
Bu makaleye atıf yapmak için /To cite this article

Sarsılmaz H. G., Günen, A., Kanca, E. (2024). Investigation of High-Temperature Wear Behavior of Ni-Mo Alloyed Hardfacing Coatings Applied on Hot Strip Mill Vertical Rolls by Submerged Arc Welding. Journal of Materials and Mechatronics: A (JournalMM), 5(1), 60-86.

can be attributed to the toughness effect of γ (austenite) and M6C phases in these coatings. Consequently, it was concluded that applying powder deposition coatings onto hot strip mill vertical rolls made of AISI 4140 steel could enhance their wear resistance, thereby increasing productivity in manufacturing processes.

Keywords: Submerged arc welding, Hardfacing; Characterization, Friction, Wear

1. INTRODUCTION

The iron and steel sector globally holds strategic importance, pivotal for industrial, infrastructural, and economic advancement. It shapes nations' industrial prowess, crafting resilient steel products vital across diverse sectors like construction, energy, automotive, and defense, fostering industrial diversity and competitiveness (URL-1). In steel manufacturing plants, rolling occupies a significant position due to advantages such as production speed, continuity, and ease of process application. The rollers performing rolling need to possess high heat resistance, high toughness, good surface quality, suitable hardness, good wear resistance, and resistance to thermal shocks. Producing rollers that encompass all of these properties would be challenging and consequently expensive. Since most damage mechanisms in rollers are surface-related, coating their surfaces with materials possessing these properties often presents a more economical and practical approach. Therefore, the development of roller surfaces with hard coatings has been utilized in the iron and steel sector for a long time, and this sector is gaining importance day by day. In the iron and steel sector, various coatings are applied to rollers, ranging from thin film coatings (<1 μm) to thick fill coatings up to 5 mm. These coatings are applied using methods such as chemical vapor deposition (CVD), physical vapor deposition (PVD), thermal spray (TS), thermochemical coatings (TKK), and hard facing (SD) welding coatings (Çürük, 2017; Günen et al., 2018). While these methods have their respective advantages and disadvantages, the ability of hardfacing coatings to be applied in thicker layers, to be repeatedly applied to worn rollers, and to be more cost-effective compared to other methods have positioned this method ahead of others (Garbade and Dhokey b, 2021).

Hard facing coating processes involve depositing cobalt, chromium, nickel-based alloys etc. onto steel surfaces to improve wear, corrosion, and impact resistance (Podgornik et al., 2000; Hamada et al., 2015; Jiang and Kovacevic, 2007). Combined with surface hardening techniques, these methods prolong the lifespan and enhance performance in various industries (Brühl et al., 2016). Despite their advantages, careful application and consideration of associated characteristics are necessary for effective use (Khan et al., 2004; Padilla et al., 2018). For example, hypereutectic high chromium white iron alloys, are extensively utilized in diverse applications like grinding, milling, and pumping devices, providing cost-effective solutions and superior wear resistance (Kazemipour et al., 2010). They are also favored in challenging environments like nuclear reactors for their robustness and corrosion resistance (Bowden et al., 2018). These coatings significantly enhance wear resistance, hardness, and durability in sectors such as mining, forging, and thermal power plants (Saklakoğlu et al., 2018). However, challenges arise in controlling welding processes to minimize dilution effects and understanding stress-induced phase transformations during hard facing (Rovatti et al., 2015; Yang et al., 2016).

Some of the hard facing coatings include: Jilleh et al. (2021) investigated the effect of Nb and Mo additions on microstructure and wear resistance of eutectic high Cr content white cast iron (WCI) hard facing coatings applied on carbon steel by the cored wire method. XRD analyses revealed that the dominant phase in the coatings was M_7C_3 (M=Cr and Fe), and MC structures were also formed.

The researchers stated that the addition of alloying elements led to grain refinement of the eutectic M_7C_3 carbide phase and formation of MC structures. Particularly, coatings prepared using a filler containing 5.5 Mo, 6 Nb, 2 W, and 1 V showed the highest wear resistance due to grain refinement, MC carbide formation, and solid solution strengthening by W and V. Suraj (2021) investigated the effect of hard facing coatings applied by TIG welding with ER 70S-2 wire on the wear and corrosion resistance of medium carbon steels EN-8, EN-9, and EN-24. The author reported that the microhardness values obtained on the surface of EN24 were higher than those of EN 8 and EN 9, resulting in better performance in both wear and corrosion resistance for EN24 alloy. Moreover, it was reported that the hard facing layers on the surface of all three alloys exhibited stable behavior in friction regimes. Ardigo-Besnard et al. (2021) evaluated hard facing coatings obtained by using a Fe-based hardening powder named Norem 02 with Plasma Transferred Arc (PTA) and Hot Isostatic Pressing (HIP) methods against WC-Co balls. The study found that coatings obtained by HIP had a finer grain structure and superior mechanical properties in terms of yield, tensile, elastic modulus, and hardness values compared to those obtained by PTA. Coatings obtained by HIP generally exhibited dominant oxidative and adhesive wear, while also offering higher wear resistance and approximately 5.5 times lower wear rate under a 10 N load. This was attributed to the better resistance of fine microstructure and well-dispersed small globular carbides to mechanical stresses, reducing surface damage. Bembenek et al. (2022) recommended the use of tungsten-free hard facing alloys based on the Fe-Mo-B-C system due to the cost limitation of tungsten carbide electrodes. Researchers who developed the chemical composition of the Fe-Mo-B-C system examined the microstructure and mechanical properties of the obtained hard facing alloys. The study showed that the addition of Ti and Mn to the Fe-Mo-B-C system resulted in the formation of wear-resistant Fe $(Mo, B)_2$ phase during FCAW. The findings indicate that the addition of Ti and Mn led to significant increases (1.2 and 1.3 times, respectively) in wear and impact-wear resistance.

Therefore, the use of Fe, Cr, Ni, Mo coatings produced at lower costs compared to tungsten-free coatings may be more cost-effective (Kiryukhantsev-Korneev et al 2018; Ortner et al. 2014). Within hard facing coatings, submerged arc welding (SAW) hard facing coatings, which allow the production of particularly thick coatings, have a wide range of applications (Singh and Kumar Shukla 2018). Introducing submerged arc welding (SAW) prior to hard facing coatings can be beneficial. Submerged arc welding (SAW) is a widely used method for joining, filling, or coating metal parts (Davis, 1993). This process involves the formation of a welding arc underneath a granular flux layer consisting of elements such as silicate, lime, magnesite, and oxide. The granular flux not only protects the welding arc but also affects the mechanical properties and crack resistance of the weld deposit. The electrode used in SAW is a copper-coated wire wound on a spool that can be continuously fed into the welding area. The copper coating on the electrode wire plays a significant role in affecting the electrical resistance and heat input of the welding method. The copper-coated electrode wire used in submerged arc welding is essential to ensure the efficiency and quality of the welding process. Additionally, crucial parameters such as heat input, welding current, arc voltage, welding speed, and arc efficiency affect the welding process in submerged arc welding. These parameters directly influence the penetration, width, and reinforcement of the weld, thereby affecting the overall weld shape (Davis, 1993).

Additionally, optimization of welding parameters such as welding current, arc voltage, welding speed, and electrode extension has been the subject of comprehensive research to improve weld geometry and overall welding performance. Furthermore, the temperature field during surface coating

with submerged arc welding has been modeled to understand heat distribution and its effect on the welded material. Moreover, time-frequency entropy analysis of the arc signal in non-stationary submerged arc welding has been utilized to assess and validate the welding process effectiveness (Davis, 1993.

It has been observed in the literature that the number of submerged arc welding hardfacing coatings is relatively limited compared to other methods. Some of these studies include: Turunç (2015) investigated the effect of complex chemical compositions of hardfacing coatings obtained by submerged arc welding method using solid wire and a powder blend containing Fe-Cr-C with Si and Mn on abrasive wear behavior. The author attributed the positive effect on abrasive wear resistance to the hardness values of C and the formation of primary carbides. According to the study, the hardfacing coatings exhibited significantly higher wear resistance compared to S235JR and Hardox samples according to ASTM G65 abrasive wear test. Furthermore, it was reported that coatings with a wide range of chemical compositions could be used in various sectors. In another study, Kaptanoğlu and Eroğlu (2017) investigated the effect of different levels of ferro-niobium and ferroboron alloying on the microstructure, hardness, and wear resistance of hardfacing coatings produced on SAE 1020 steel surface by submerged arc welding method using Fe-based welding wires containing 0.5 Mn, 0.07C, and 0.05 Si. According to the results, the highest hardness value was determined as 48 HRC in the coating obtained with 12% ferro-niobium and 10% ferroboron, while the lowest hardness value was found as 41 HRC in the coating obtained with 3% ferro-niobium and 2.5% ferroboron. The authors reported that the increased addition of ferro-niobium and ferroboron increased the percentage of borides in the coating microstructure and hardness values, leading to a decrease in the wear volume loss values of the coatings.

Literature reviews have shown that although there have been numerous studies on hardfacing coatings, there is a limited number of studies focusing on hardfacing coatings produced with the cost-effective submerged arc welding method, which is considered to be ahead of other welding methods in terms of cost-effectiveness. Furthermore, the fact that the wear resistance of the obtained hardfacing coatings has generally been studied only at room temperatures has triggered the need for this study. This is because the hot rolling process is of great importance in the iron and steel industry, which seeks cost-effective production. Many rolling tools are exposed to temperatures ranging from room temperature to 600°C within the rolling process.

Considering the studies in the literature, it was determined that although hardfacing coatings were used in high temperature applications, the published studies examined the wear behavior of these coatings at room temperature. For this reason, this study is dedicated to the gap of in the literature high temperature wear behavior of hard facing coatings. In this context, in this study, hardfacing coatings were applied to hot rolling vertical rollers using the submerged arc welding method with Er430 and 41NiMo alloy buffer and buffer+hardfacing coatings. Subsequently, the microstructure, phase formations, and hardness of these coatings were examined, and their effects on the wear behavior of hot rolling vertical rollers at working conditions (24, 300 and 600°C) were compared with untreated AISI 4140 steel.

2. MATERIALS AND METHODS

2.1 Materials

The material chosen for the application of hardfacing coatings on its surface is AISI 4140 steel (42CrMo4/1.7225), a medium carbon low alloy steel containing Chromium (Cr) and Molybdenum (Mo). AISI 4140 steel was selected due to its high strength and resistance, making it suitable for

working under stress and heavy loads (Şen, 1993). The chemical composition provided by the supplier is presented in Table 1, while the mechanical properties are detailed in Table 2.

Table 1. Chemical composition of AISI 4140 (wt.%).

Material	C	Si	Mn	Cr	Mo	P	S	Fe and impurities
4140	0.42	0.25	0.83	1.01	0.18	0.011	0.004	Balance

Table 2. Mechanical properties of AISI 4140 (wt.%).

Material	Yield strengh (N/mm^2)	Tensile strengh (N/mm^2)	Elongation (%)	Reduction rate (%)	Hardness (HRC)
4140	1080	1160	15.5	57.0	187

2.2 Determination of Used Wires and Powder

In the experiments, two types of wires were utilized: Buffer and Hardfacing welding wires. ER430 wire was used for the buffer application, while 41NiMo welding wire was employed for hardfacing welding applications. The chemical compositions of wires are provided in Table 3. As a welding flux powder, GEKA ELIFLUX BSS brand powder was chosen, and its chemical composition, supplied by the manufacturer given as 50 wt.% CaF_2, 38 wt.% Al_2O_3, 10 wt.% SiO_2, and 2 wt.% K_2O+Na_2O. The chemical composition are given in Table 3.

Table 3. Chemical composition of the used welding wire (wt.%)

Wire	C	Si	Mn	Cr	Ni	Mo	Fe and impurities
ER430	0.06	0.94	1.43	18.6	0.06	0.02	Balance
41NiMo	0.05	0.6	0.9	13.8	4.3	1.1	Balance

2.3 Preparation of Hardfacing Coating

Prior to the submerged arc welding hardfacing coatings process, samples obtained from the company were acquired with rough dimensions of 320×100×30 mm^3. Milling machining technique was applied on the sample to bring it to its final dimensions. The surfaces were soaked in 5% H2SO4 for 5 minutes and then rinsed in distilled water. AISI 4140 steel samples with dimensions of 320×100×30 mm were used in hardfacing welding processes. The thickness of ER430 and 41NiMo welding wires used in the studies are 3.2 mm and 2.4 mm, respectively. Submerged arc welding applications were carried out based on the parameters obtained as a result of the optimization studies of Kahraman Sarsılmaz Makina İskenderun, which provides services regarding the coating of hot rolled parts to the iron and steel industry. In creating the hardfacing coatings of the samples, the welding speed was 300 mm/min and the distance between the weld piece and the torch was 25 mm. Based on preliminary studies, ER430 and 41NiMo hardfacing welding applications were carried out at 130 A and 100 A, respectively.

2.4 Metallographic Studies

The hardfacing coatings produced by submerged arc welding were precision-cut into dimensions of 20×20×5 mm^3 using a precision cutter for microstructural optic and SEM (scanning electron microscopy), EDS (energy dispersion spectroscopy) analysis, hardness testing, XRD (X-ray diffraction), and wear testing. After the cutting process, specimens designated for microstructure examinations were embedded in hot bakelite, and subsequent polishing steps with SiC sandpaper ranging from 320 to 2500 grit were performed. Precise polishing was then achieved using 3 and 1-

micron diamond solutions to obtain a mirror-like smooth surface. For a clearer observation of grain boundaries, the specimens were etched with a 3% nital solution for 3-6 seconds.

Optical images of the specimens were obtained using an Olympus BX41M-LED microscope. SEM and EDS analyses were conducted using a Jeol JSM 6060 SEM device and an IXRF EDS system, respectively. EDS examinations were carried out to determine the chemical composition of the coatings and the substrate material. Microhardness measurements of untreated AISI 4140 and coated samples were conducted using the EMCOTEST DuraScan 70 G5 microhardness device. Measurements were performed with a diamond pyramid tip, 100 gf load, and a 15 s dwell time, starting from 50 μm below the surface and at 100 μm intervals up to 5.0 mm. At least 5 measurements were taken for each region, and the averages of these measurements were provided, considering the thicknesses of the coating layers for ER430 (1.5 mm) and E430+EC 410Ni coatings (3.75 mm).

2.5 Wear Test

The working conditions of hot strip mill vertical rolls were learned from the iron and steel producers operating in the Iskenderun region and the average values of these conditions were determined. Depending on these conditions, the wear tests were conducted at room temperature, 300°C, and 600°C, with sliding speeds of 500 mm/s and 1000 mm/s, using a 6 mm diameter 52100 bearing steel ball against a 1000 m sliding distance and 10 N load. In the wear test at 600°C and 500 mm/s, due to excessive deformation of the 52100 bearing steel, the tests were incomplete, and WC ball was used instead of the bearing steel ball. During the wear test, the data collected by the load cell were automatically recorded in the computer program.

Following the wear test, the width and depth of the circular wear track were measured at 0, 90, 270, and 360 degrees for each sample, using an optical microscope and 2D profilometer. The resulting wear track shape was observed to be semi-elliptical. Based on previous studies, the wear volume losses were calculated using the following formula, and the formulas were written into an Excel program for calculation as stated in the previous studies (Günen et al., 2014; Kayalı et al., 2022).

$$L = 2\pi r \quad (1)$$

$$V = 0.25\pi WD \quad (2)$$

$$Wr = V/FS \quad (3)$$

Where, L: Length of the wear track (mm), V: Wear track volume (mm^3), r: Radius of the wear track (mm), W: Average wear track width (μm), D: Average wear track depth (μm), F: Applied load (N), S: Sliding distance (m), and Wr: Wear rate (mm^3/Nm).

3. RESULTS AND DISCUSSION

3.1 XRD Analyses and Microstructure

XRD analyses were conducted to determine the phase structure of the untreated AISI 4140 and submerged hardfacing coating (SHC)samples. The obtained XRD patterns are presented in Fig. 1. DB card numbers of the phases indicated in XRD analyses have been added on the figure.

α- Ferrite Fe (03-065-4899)

γ- Austenite Fe,Ni,Cr (00-047-1417)

β- Cementite Fe_3C (96-901-2189)

ε- M_6C (01-080-0338)

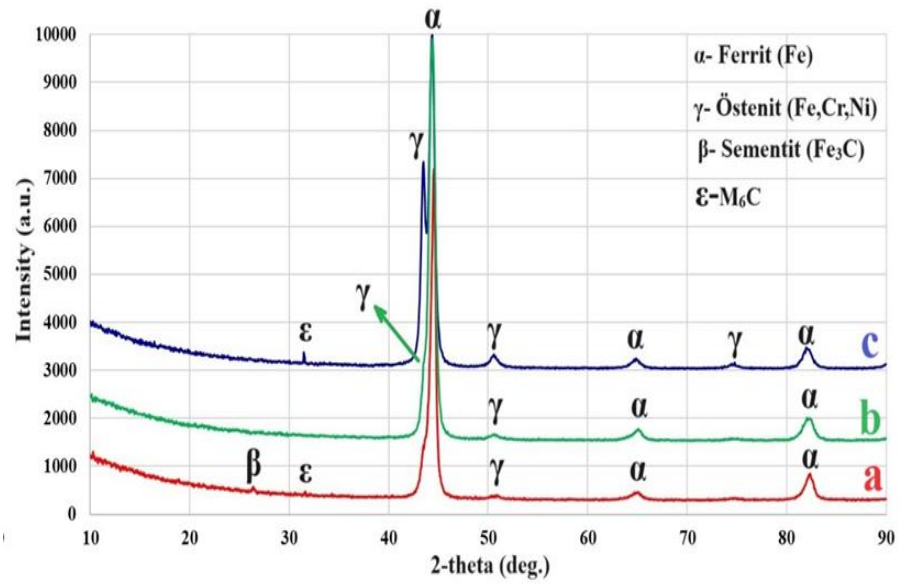

Figure 1. XRD patterns of a) untreated AISI 4140 b)ER430 c)ER430+41NiMo SHC samples.

As seen in Figure 1, the most intense peak at 44.53° in AISI 4140 steel is attributed to the α-ferrite phase, with additional α-ferrite peaks detected at 65.07° and 82.35°. In untreated AISI 4140 steel, peaks for the γ (austenite) phase at 50.84°, M_6C carbide at 31.61°, and cementite (Fe_3C) at 27.88° were also observed at low intensities in the untreated AISI 4140. In the ER430 sample (Fig. 1.b), the most intense peak at 44.38° is related to the α-ferrite phase, and γ (austenite) peaks were additionally detected at 50.52°, with low-intensity α-ferrite peaks at 65.07° and 82.03°. On the other hand an the X-ray patterns of EC 410NiMo sample revealed that the most intense peak at 44.38° is associated with the α-ferrite phase, followed by a prominent γ (austenite) peak at 43.48°. In addition to these two intense peaks, low-intensity γ (austenite) peaks at 50.52°, α-ferrite peaks at 65.07° and 82.03°, and an M_6C peak at 31.46° were observed, similar to the other samples.

The optical microstructure images taken from the cross-sections of AISI 4140 steel, ER 430, and 410NiMo coated samples are shown in Figure 2- Figure 4.

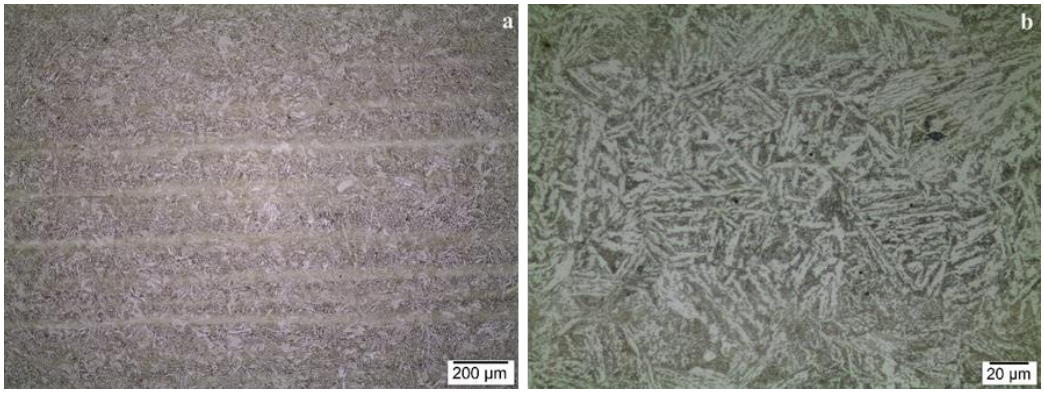

Figure 2. Optical microstructure view of AISI 4140 steel a) 50x b)500X

As seen in Figure 2a, the microstructure of AISI 4140 steel consists predominantly of ferrite and pearlite (ferrite + cementite) phases, in accordance with XRD analysis. In addition, very low amounts of retained austenite and M6C carbides, appearing as black spots in the structure were observed (Figure 2b).

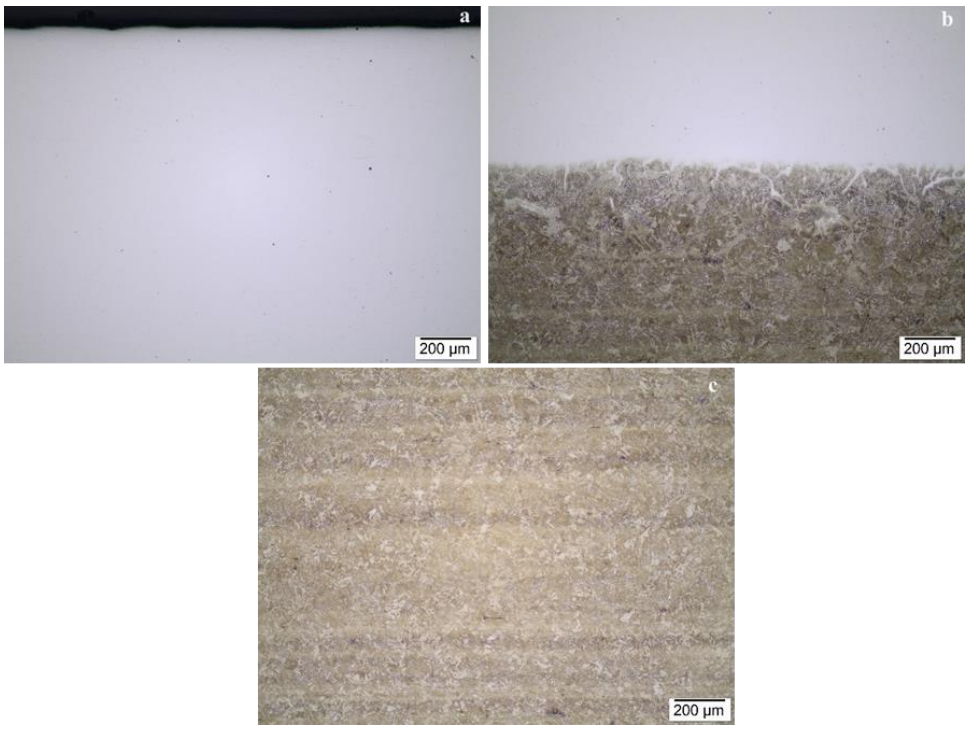

Figure 3. 50X optical microstructure views of a) coating region b) diffusion region c) matrix portions of the ER430 buffer coating formed on the surface of AISI 4140 steel.

As seen in Figure 3, the optical microstructure image taken from the polished cross-section surface of the ER430 coating formed on the surface of AISI 4140 steel reveals that the coating layer exhibits continuity along the section without any adverse issues such as cracks or porosity. It can be observed that a coating free from negative aspects has been formed. When the diffusion region between the coating and the substrate AISI 4140 steel is examined (Figure 3b), it is noted that a diffusion zone has formed due to melting during the welding process, and the coating and substrate regions are completely bonded to each other. The presence of the diffusion region positively affects the adhesion forces between the coatings, making it difficult for them to separate from the surface when external force is applied (Zahiri et al., 2014; Lemke et al., 2016). Upon examining Figure 3c, it can be observed that the AISI 4140 steel exhibits a similar microstructure to that shown in Figure 1, indicating that it largely maintains its microstructure after the coating process.

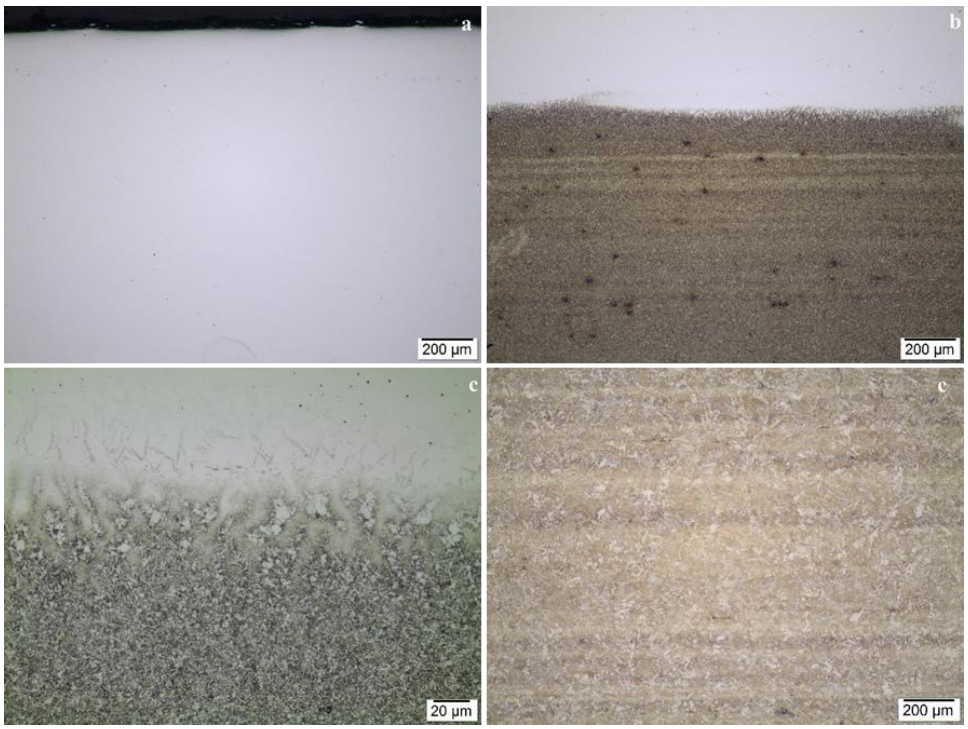

Figure 4. Optical microstructure views of a) coating region b) coating and diffusion 50X c) coating and diffusion region 500X d) matrix portions of the ER430+410NiMo duplex coating formed on the surface of AISI 4140 steel.

As seen in Figure 4, on the polished surface of the ER430+410NiMo coating formed on the surface of AISI 4140 steel, similar to the coating layer in Figure 3, it was observed that the coating on the cross-sectional surface exhibited continuity, forming a surface free from any adverse factors such as cracks or porosity. Additionally, it was noted that there were no optical indications of the two different coating layers of ER430+410NiMo. When the diffusion zone between the coating layer and the substrate AISI 4140 steel was examined (Figure 4b), it was observed that the diffusion zone formed due to the melting process during welding was less distinct compared to the area where ER430 was applied. However, at 500X magnification in Figure 4c, the formation of this diffusion zone and diffusion towards the substrate AISI 4140 steel was clearly identified. This indicates that both the buffer and duplex coating applied are diffusion-bonded to the substrate AISI 4140. Upon closer examination of Figure 4d, a typical microstructure of AISI 4140 steel similar to that in Figure 2 and Figure 3 is observed. SEM and EDS analyses were conducted for a more detailed examination of the coating layers and to determine the chemical compositions of the coating layers (Figures 5 and 6).

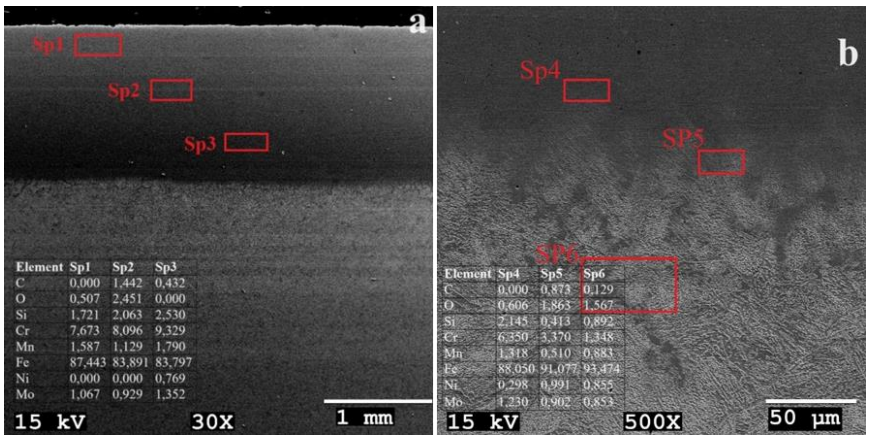

Figure 5. SEM view of the ER 430 coating formed on the surface of AISI 4140 steel: a) coating layer, b) transition zone.

As seen in Figure 5, the ER 430 coating layer has a thickness of approximately 1.5 mm and exhibits continuity along the surface. EDS analysis from regions Sp1, Sp2, and Sp3 taken from the coating layer indicates that it is nearly homogeneous, and in contrast to the chemical composition of ER 430, it contains Ni and Mo from the AISI 4140 steel composition (especially in the lower part of the coating), suggesting a material transfer between the substrate and the wire during the submerged arc welding process. Examination of the transition zone reveals regions with varying color concentrations, indicating differences in composition between the coating and the substrate. Cruz-Crespo et al (2016) reported similar phase structures and EDS analysis results as a result of their studies using Self-shielded Flux Cored Arc Welding and ER430 wire to improve the abrasive wear resistance of AISI 1020 steel. The authors reported that hardfacing coatings obtained using ER430 wire consisted of smaller primary NbC carbides surrounded by a eutectic matrix composed of austenite and fine M7C3 carbides. Moreover, they reported that the chemical composition of the eutectic structure determined by EDS consists of wt.% 0.8C, 10.5Cr, 87.1 Fe, 1.6Si, while the M_7C_3 carbide structures consist of 7.3C, 46.8Cr, and 45.9Fe. As understood from both our study and Cruz-Crespo et al.'s study, the chemical composition of the coatings differs slightly from the wire composition. This indicates that some burning occurs in the alloying elements due to the very high temperatures of the welding methods in which the coatings are applied.

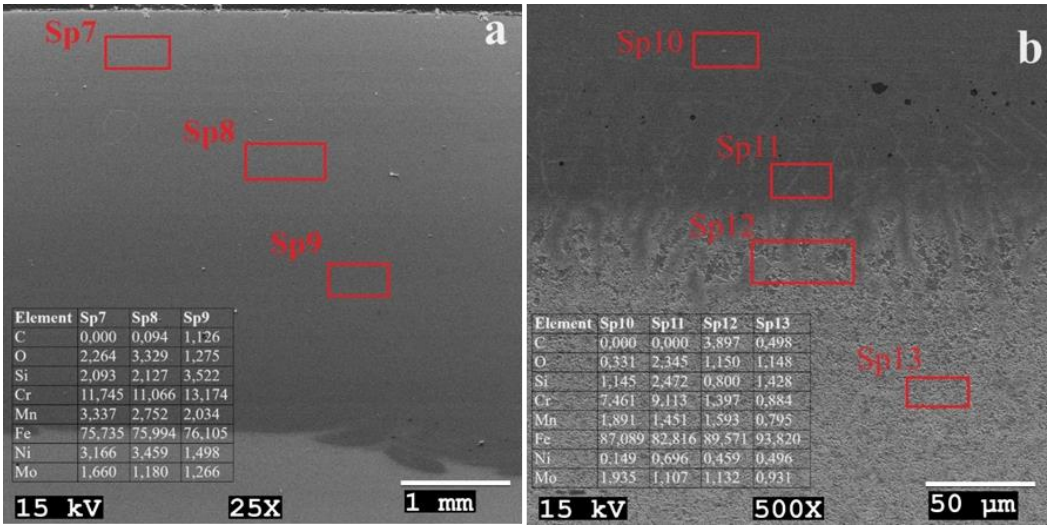

Figure 6. SEM view of the ER430+EC410Ni duplex coating formed on the surface of AISI 4140 steel: a) coating layer, b) transition zone.

As depicted in Figure 6, it is observed that the duplex coating layer of ER 430 + EC 410Ni is approximately 3.75 mm thick, indicating the application of a 2.25 mm hardfacing coating layer over the 1.5 mm ER 430 coating layer. In Figure 6a, the SEM image presented shows no distinct separation line between these two coating layers, appearing as if they were a single coating layer. However, in Figure 6b, a clear formation of a diffusion zone between the coating layer and the substrate material is evident in the transition zone of this sample. Regions Sp10 and Sp11, with higher alloy content according to EDS analysis, are identified as the coating layer, whereas region Sp12 is identified as the transition zone, containing both the chemical composition of the coating wires and the substrate AISI 4140 steel. The region designated as SP13 is close to the chemical composition of AISI 4140 steel. The microhardness values from the surface to the substrate material for untreated AISI 4140 steel and hardfacing coatings are shown in Figure 7.

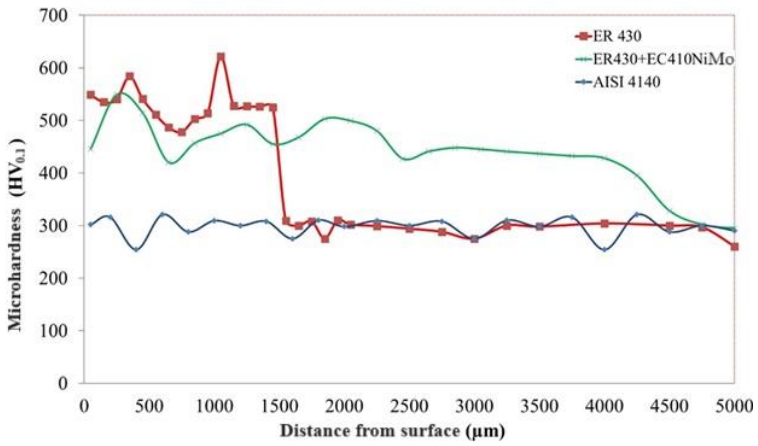

Figure 7. Microhardness distributions from the surface to the inner 5 mm of AISI 4140 steel, ER 430, and ER 430+EC 410Ni coatings.

As seen in Figure 7, the hardness value of the ER430 coated sample fluctuates in the range of 478-672 HV0.1 within the 0-1500 µm range, showing fluctuations in terms of homogeneity, and reaches ~ 300 HV0.1 hardness value after 1500 µm, corresponding to the hardness of AISI 4140 steel. In contrast, the hardness distribution of the ER430+410NiMo duplex coating is more homogeneous, generally showing a slight decrease trend towards 4000 µm from the surface, with hardness values of the coating layer ranging from 427-549 HV0.1, and after the coating layer, the hardness value decreases to ~ 300 HV similarly with the other coating layer. The calculated average and standard deviation values of the obtained hardness values using an Excel program are as follows: the microhardness value of AISI 4140 steel is 296±27 HV0.1, while the average hardness value of the coating layer formed with ER 430 is 533±42 HV0.1, and the average hardness value of the ER430+ 410NiMo coating layer is determined as 473±35 HV0.1. Therefore, the improvement in surface hardness values of AISI 4140 steel due to the hardfacing coatings is determined to be 80% and 60% with ER430 and ER430+410NiMo coatings, respectively. The hardness value of ER430 is approximately 60 HV higher than ER430+410NiMo, and this is due to a more homogeneous distribution on the surface, resulting in a lower hardfacing coating thickness in ER430. This is because ER430 is performed in a single pass, whereas ER430+410NiMo hardfacing coating is done in two passes. In a two-pass coating process, the first pass results in a less homogeneous coating due to the presence of carbide and eutectic zones. This lack of homogeneity will further increase in the second pass. Additionally, the increased exposure to heat during the second pass and slower cooling under post-welding atmospheric conditions have led to lower hardness levels in hardfacing coatings.

3.2 Wear Behaviors

Wear tests were conducted considering the operating conditions of hot rolling vertical rollers in steel production. The tests were performed at room temperature, 300°C, and 600°C, with speeds of 500 mm/s and 1000 mm/s, using a 6 mm diameter 52100 bearing steel ball against which a sliding distance of 1000 m was applied. The average coefficient of friction values and wear volume losses obtained from the wear tests are presented in Table 4.

Table 4. The average COF values and wear volume losses of samples depending wear conditions.

Sample	Wear temperature (°C)	Sliding speed (mm/s)	Average COF	Average wear track width (µm)	Average wear deep width (µm)	Wear volume losses $10^{-5}mm^3$
AISI 4140	24	500	0.64±0.14	1766±26	32.27±0.35	28.17±0.72
ER430			0.69±0.22	1621±29	23.44±0.20	18.66±0.52
41NiMo			0.60±0.16	1543±24	23.33±0.12	17.75±0.33
AISI 4140	24	1000	0.83±0.19	806±3.5	9.0±0.2	7.16±0.35
ER430			0.62±0.24	1197±3.8	6.0±0.15	7.09±0.26
41NiMo			0.62±0.20	1021±2.5	6.33±0.18	6.38±0.23
AISI 4140	300	500	0.78±0.09	1374±24	12.0±0.12	8.36±0.65
ER430			0.63±0.16	1346±26	6.33±0.11	4.21±0.35
41NiMo			0.53±0.18	1330±25	6.00±0.13	3.94±0.27
AISI 4140	300	1000	0.58±0.11	1783±38	7.3±0.20	12.90±0.45
ER430			0.30±0.07	900±27	9.5±0.28	8.43±0.30
41NiMo			0.45±0.12	1033±22	8.0±0.32	8.15±0.27
AISI 4140	600	500	0.39±0.06	2294±79	38.33±0.34	43.37±1.03
ER430			0.61±0.10	1866±58	35.0±0.25	32.22±0.95
41NiMo			0.37±0.10	1218 ±35	13.33±0.15	8.01±0.26
AISI 4140	600	1000	0.27±0.08	2230±85	53.33±0.06	120.99±2.57
ER430			0.60±0.27	2235±82	27.67±0.06	60.98±1.25
41NiMo			0.24±0.15	1928±67	29.33±0.06	55.78±1.33

When examining Table 4, it can be observed that the ER430+41NiMo coated sample exhibited lower friction coefficients and consequently lower wear volume losses compared to ER430 and AISI 4140 steel in all wear tests. However, although the friction coefficients of the ER430 sample varied depending on the test environment, its wear volume losses were lower. It is believed that the fluctuations in the friction coefficients of the ER430 sample are attributed to the fluctuations in the hardness values observed in this coating layer. Despite fluctuations in the friction coefficients, the increase in hardness in the coated samples significantly enhanced their wear resistance, as evident from Table 4. Notably, among the coated samples, only the ER430 sample exhibited higher friction coefficient values at room temperature and 600°C during wear at 500 mm/s compared to the untreated AISI 4140 sample, both at 500 mm/s and 1000 mm/s. This finding explains the high wear volume losses of the coated sample under these conditions. Another observation from Table 4 is that the friction coefficient values at 500 mm/s were generally higher than those at 1000 mm/s, except at room temperature. This phenomenon can be attributed to the increased centrifugal force with increasing sliding speed, resulting in less effect of the 10 N force applied to the specimen. Similar observations were reported by Grützmacher et al. (2017), who stated that larger sliding radii would have a significant impact on friction forces due to the decrease in centrifugal forces in rotational wear. Considering the friction coefficient and wear volume losses depending on temperature, it is generally observed that friction coefficients decrease with increasing temperature, while wear volume losses increase. This can be explained by the formation of a lubricating oxide layer on the surface due to increased temperature, resulting in a decrease in friction coefficients. However, the softening of surfaces due to temperature facilitates easier material removal from the surface, leading to increased wear volume losses. Particularly, as mentioned earlier, the increase in sliding speed, along with the increase in centrifugal force, reduces the force exerted on the abraded specimen, resulting in a decrease in friction coefficient values. Grützmacher et al. (2017) explained this phenomenon by

stating that there could be a significant decrease in friction coefficient values in solid-solid contact until the lubricating layer formed during the wear process is broken. The most striking point in the table is that the lowest volume loss in all samples occurred at 300 C. The occurrence of wear volume losses lower than room temperature has also been reported by researchers in previous literature studies on the high temperature wear resistance of AISI41410 steel and ductile iron. Koçyiğit et al. (2020) reported that AISI 4140 steel exhibited the best wear resistance at 300 C, as in our study, and its wear resistance at 600 C was higher than room temperature. The authors attributed this situation to the glazed layer formed at 300 C. Çelik et al. (2005) reported that the highest wear resistance in ductile cast iron was achieved between 50-100 C, and that the wear resistance decreased after 200 C. The authors attributed this to the increase in the mechanical properties of the uptake due to dynamic strain aging at these temperatures.

SEM images and EDS line analyses were performed on the worn surfaces of the abraded samples to justify the friction coefficient and wear volume loss values. SEM views and EDS line analyses obtained from the worn traces formed under the wear conditions of room temperature (24°C) and 600°C at 500 mm/s and 1000 mm/s sliding speeds for untreated AISI 4140 steel and AISI 4140 steel coated with ER 430 and ER 430+EC410NiMo powder overlay coatings are shown in Figures 8 to 17.

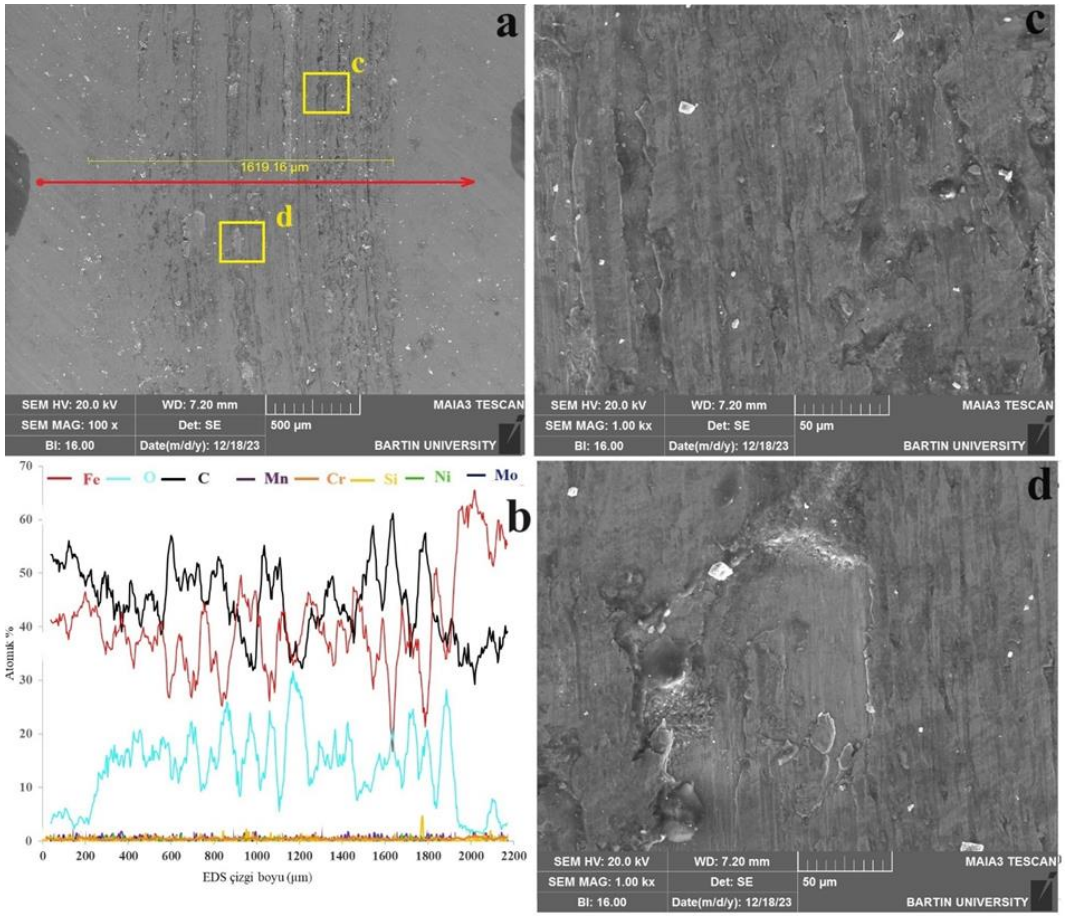

Figure 8. SEM images of the wear track on AISI 4140 steel worn at 500 mm/s at room temperature: a) overall view, b) EDS line analysis, c) magnified view of region c at 1000X, d) magnified view of region d at 1000X.

Upon examining Figure 8a, the wear track appears to be 1619.16 µm wide, consisting of micro-scratches and smeared regions regionally. The EDS line analysis of the worn area reveals the localized formation of oxides in the region where the abrasion process occurred. When the 1000X magnified

image of the micro-scratches is examined (Figure 8c), it is observed that these scratches are not deep channels; instead, particles are smeared on the surface mainly at the edges of the channels, as seen in Figure 8d. Therefore, it can be concluded that micro-scratching and adhesion wear are the dominant wear mechanisms in this sample.

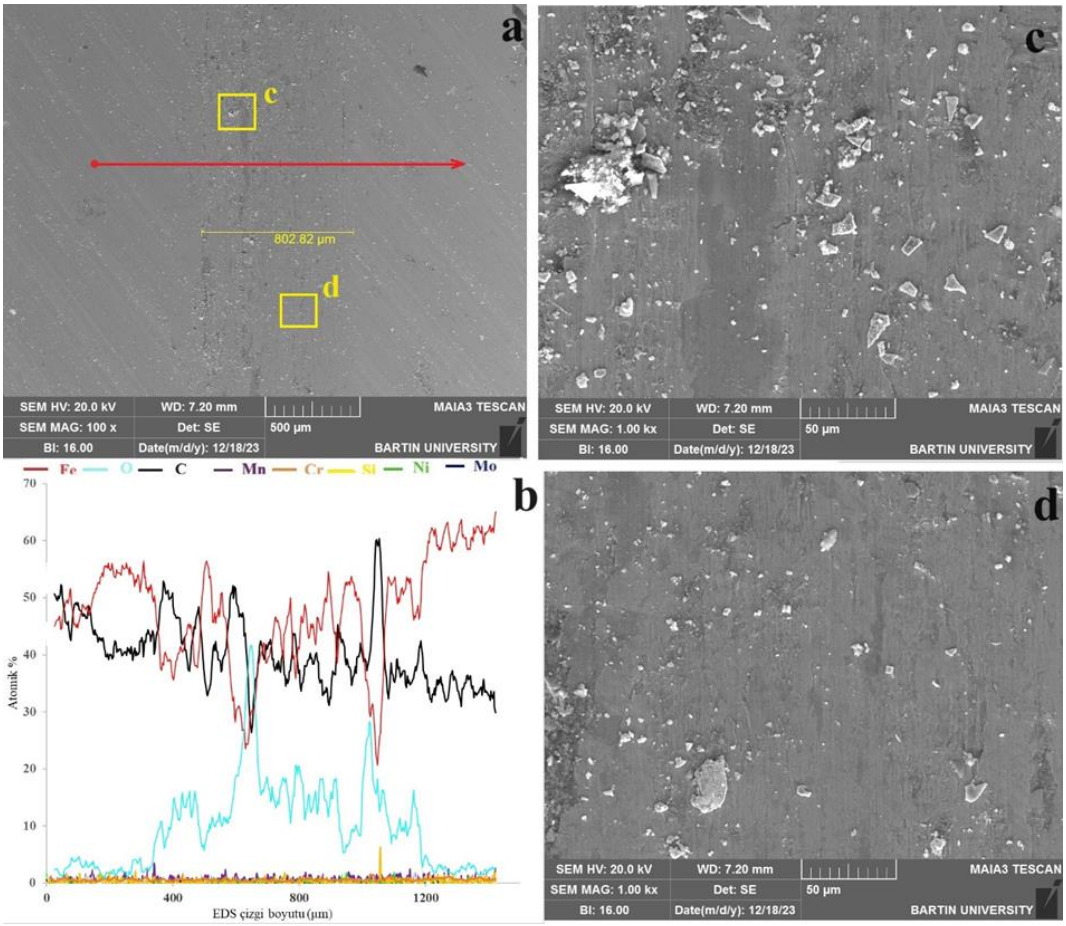

Figure 9. SEM images of the wear track on AISI 4140 steel worn at 1000 mm/s at room temperature: a) overall view, b) EDS line analysis, c) magnified view of region c at 1000X, d) magnified view of region d at 1000X.

Upon examining Figure 9a, it is noteworthy that the wear track width is approximately 50% smaller (802.82 µm) compared to the speed of 500 mm/s. This is attributed to the increase in wear rate due to the increased centrifugal force of the rotating 52100 abrasive ball with increasing speed, resulting in reduced contact surface with the worn sample. The increased speed has led to shallow micro-scratches on the sample surface, and the wear debris (Figures 9c-9d) has remained on the surface due to the increased centrifugal force without adhering sufficiently. However, the locally black regions indicating oxidation appear to be higher in the areas than in the sample tested at 500 mm/s. This is supported by the EDS line analysis (Figure 9b), which shows that the O2 ratio reaches up to 30-40% in some atomic regions, supporting the aforementioned claim. Therefore, it can be concluded that micro-scratching, smearing, and oxidation wear occurred in this sample.

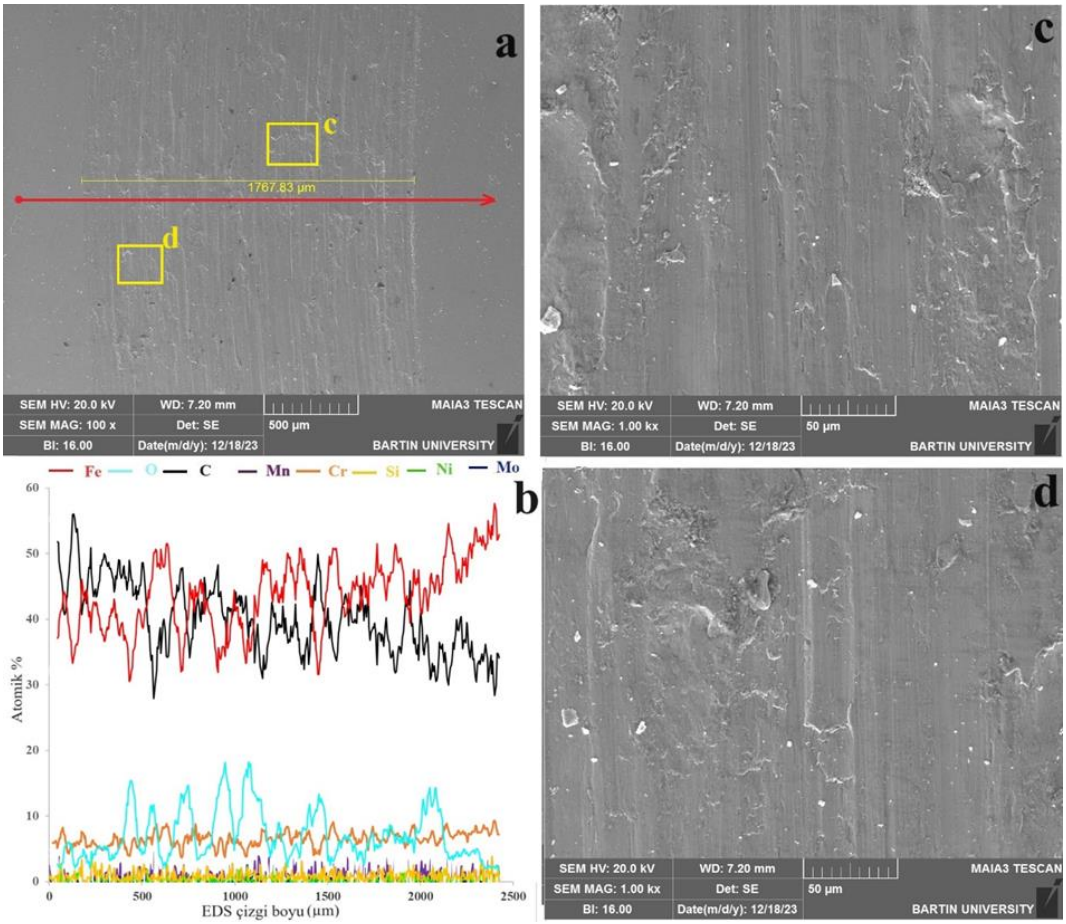

Figure 10. SEM images of the wear track on ER430 worn at 500 mm/s at room temperature: a) overall view, b) EDS line analysis, c) magnified view of region c at 1000X, d) magnified view of region d at 1000X.

Considering the general view of the wear track SEM image of the ER430 sample (Figure 10a), it is observed that the track width is 1767.83 µm, consisting of superficial micro-scratches and smeared areas on the surface. Upon analyzing the EDS line analysis of the worn area, the presence of Fe, C, O2, and Cr is observed on the surface. While O2 fluctuates within the wear track, the Cr content in the coating shows a more stable trend. When examining the images at 1000X magnification, it is observed that the micro-scratches are shallower compared to the untreated AISI 4140 steel under the same conditions, but localized fractures occur in some areas. This can be attributed to the increased hardness of the surfaces due to the applied coating. Specifically, the harder coated sample may have exhibited more resistant scratching behavior against the 52100 bearing steel ball, while the increased hardness may have led to fractures under applied load and 1000 m of repeated stress. Therefore, it can be concluded that micro-scratching wear mechanism is the dominant wear mechanism in this sample.

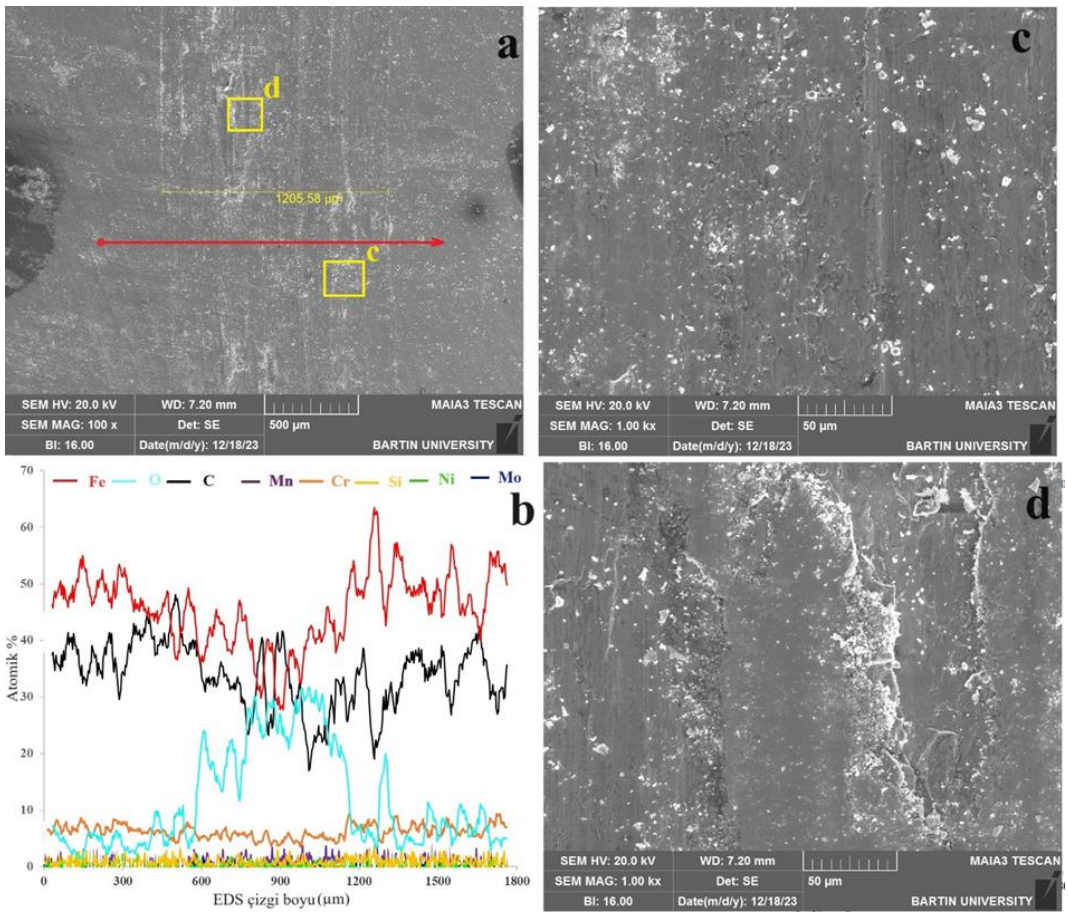

Figure 11. SEM images of the wear track on ER430 worn at 1000 mm/s at room temperature: a) overall view, b) EDS line analysis, c) magnified view of region c at 1000X, d) magnified view of region d at 1000X.

Upon examining the general view of the wear track SEM image of the ER430 sample at 1000 mm/s speed (Figure 11a), it is observed that the track width is 1205.58 µm, indicating that, similar to the untreated sample, the width of the wear track decreased with increased speed in this sample as well. When the wear track SEM image is examined in terms of microstructure, it is observed that there are more localized micro-scratches on the surface compared to 500 mm/s, along with wear debris (white spots) on the surface. In Figure 11c, the depth of micro-scratches and the distribution of wear debris are more clearly visible. In the image taken from the region where micro-scratching is observed in the general view (Figure 11d), it is seen that the fractures occur as the oxide layer smeared on the surface breaks rather than as micro-scratches. The EDS line analysis showing oxygen atomic ratios reaching the 30s along the line supports this observation. Therefore, the increase in wear speed from 500 mm/s to 1000 mm/s in the ER430 coated sample has led to a change in the wear mechanism from micro-scratching to oxidative wear.

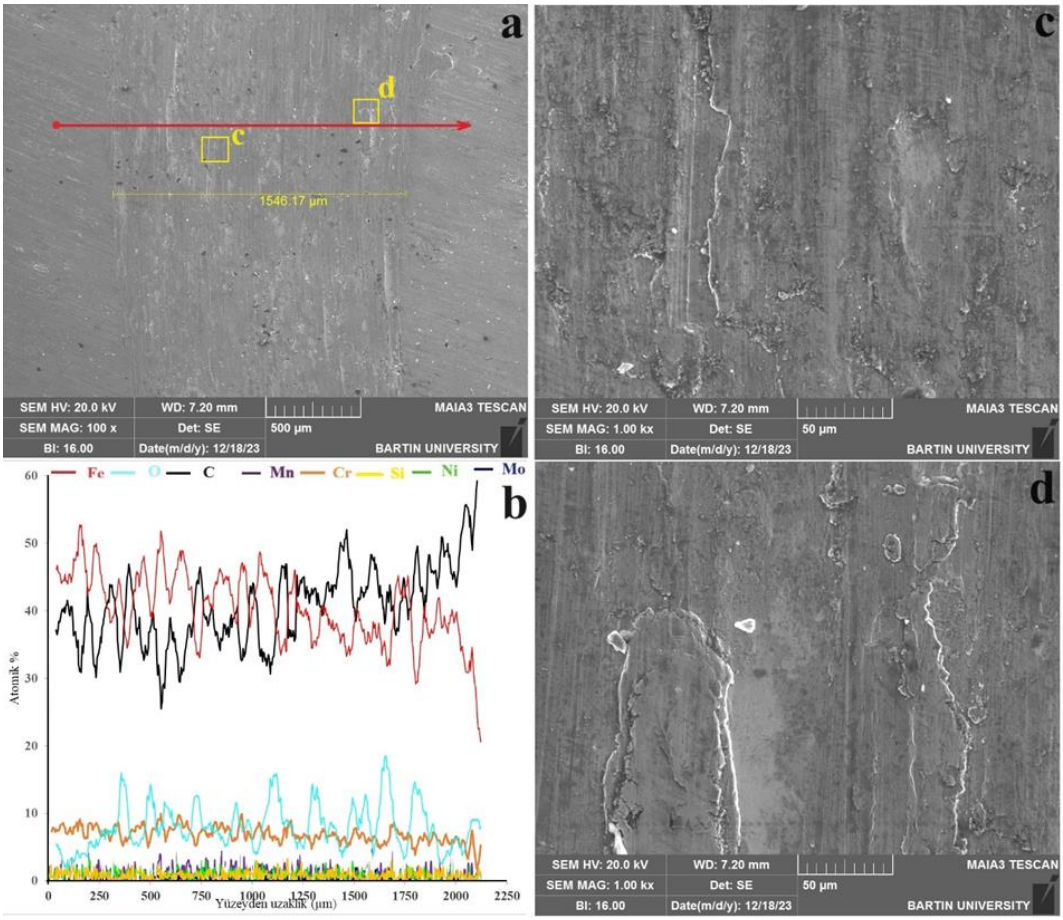

Figure 12. SEM images of the wear track on ER430+410NiMo worn at 500 mm/s at room temperature: a) overall view, b) EDS line analysis, c) magnified view of region c at 1000X, d) magnified view of region d at 1000X.

Upon examining the general view of the wear track SEM image of the ER430+410NiMo sample (Figure 12a), it is observed that the track width is 1546.17 µm, and the surface exhibits superficial micro-scratches, occasional black spots, and smeared areas. When the EDS line analysis of the worn area is examined, it is determined that the oxide layer on the surface is regional, with Fe and O2 peaks showing parallelism. Upon examining the 1000X magnification images in Figure 12b, it is seen that black areas are scratched in the areas where scratches are present. In Figure 12c, at 1000X magnification, it is clearly observed that wear debris is smeared on the surface in some parts. It is concluded that the micro-scratches in this sample, similar to the ER430 sample, are shallower than those on untreated AISI 4140 steel under the same conditions, but the presence of regional oxide zones is more pronounced. The presence of shallower micro-scratches and more oxide-rich regions can be attributed to the ball attempting particle abrasion on a more resistant surface, resulting in higher surface heating and increased oxidation, and less penetration into the substrate material. Therefore, it is concluded that micro-scratching, adhesion, and oxidation wear mechanisms occur in this sample, similar to the ER430-coated sample.

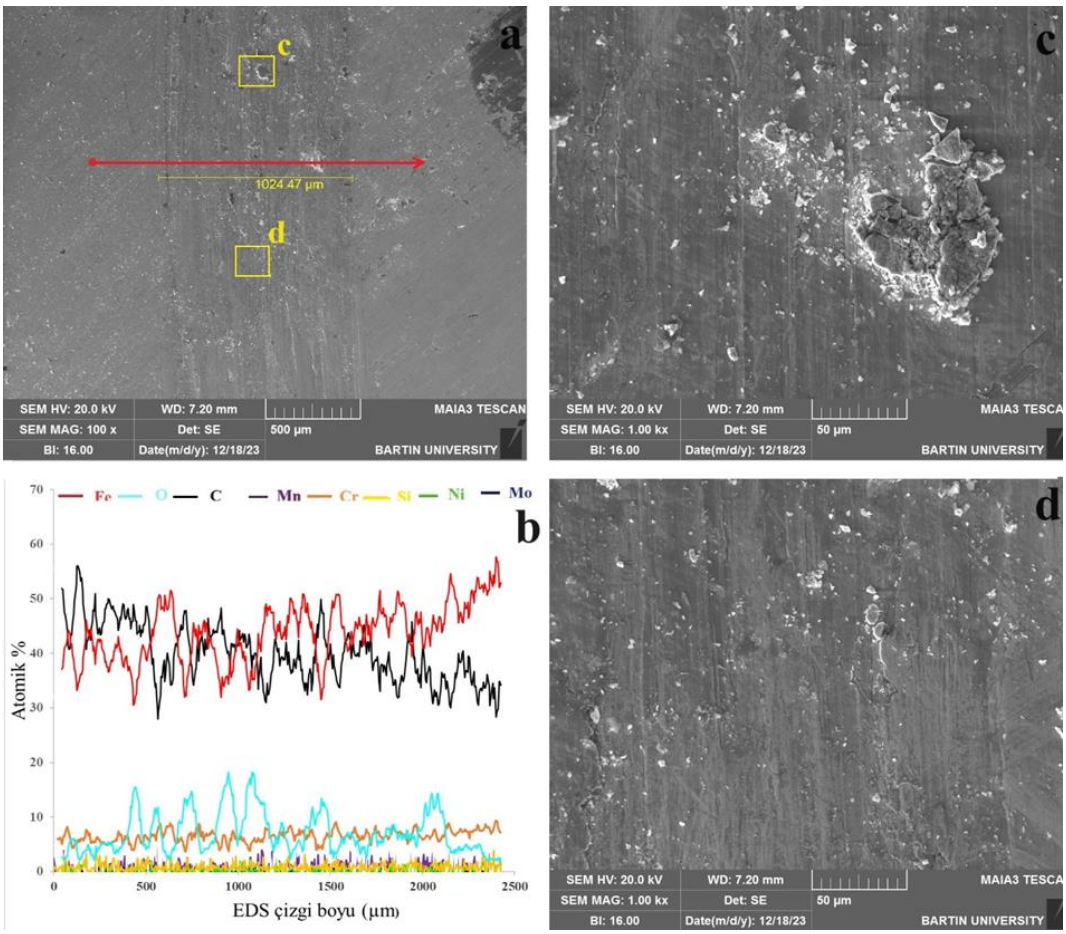

Figure 13. SEM images of the wear track on ER430+410NiMo worn at 1000 mm/s at room temperature: a) overall view, b) EDS line analysis, c) magnified view of region c at 1000X, d) magnified view of region d at 1000X.

Upon examining the general view of the wear track SEM image of the ER430+410NiMo sample at 1000 mm/s speed (Figure 13a), it is determined that the track width is 1024.47 µm, indicating a decrease in the width of the wear track with increasing speed, as observed in the untreated sample. When the SEM image of the wear track is examined in terms of microstructure, it is observed that the micro-scratches are shallower compared to 500 mm/s, but there are more wear debris on the surface. In Figure 13c, the appearance of the worn debris from the surface is clearly visible. In Figure 13d, it is observed that the cracks in the oxidation zones, which were detected in the ER430 sample (Figure 12), are not present in this sample. This can be attributed to the slightly lower hardness value of the ER430+410NiMo sample compared to the ER430 sample, resulting in a better fracture toughness value. When evaluated in terms of wear mechanisms, it is concluded that the wear mechanism in this sample occurs in the form of micro-scratching and oxidation wear.

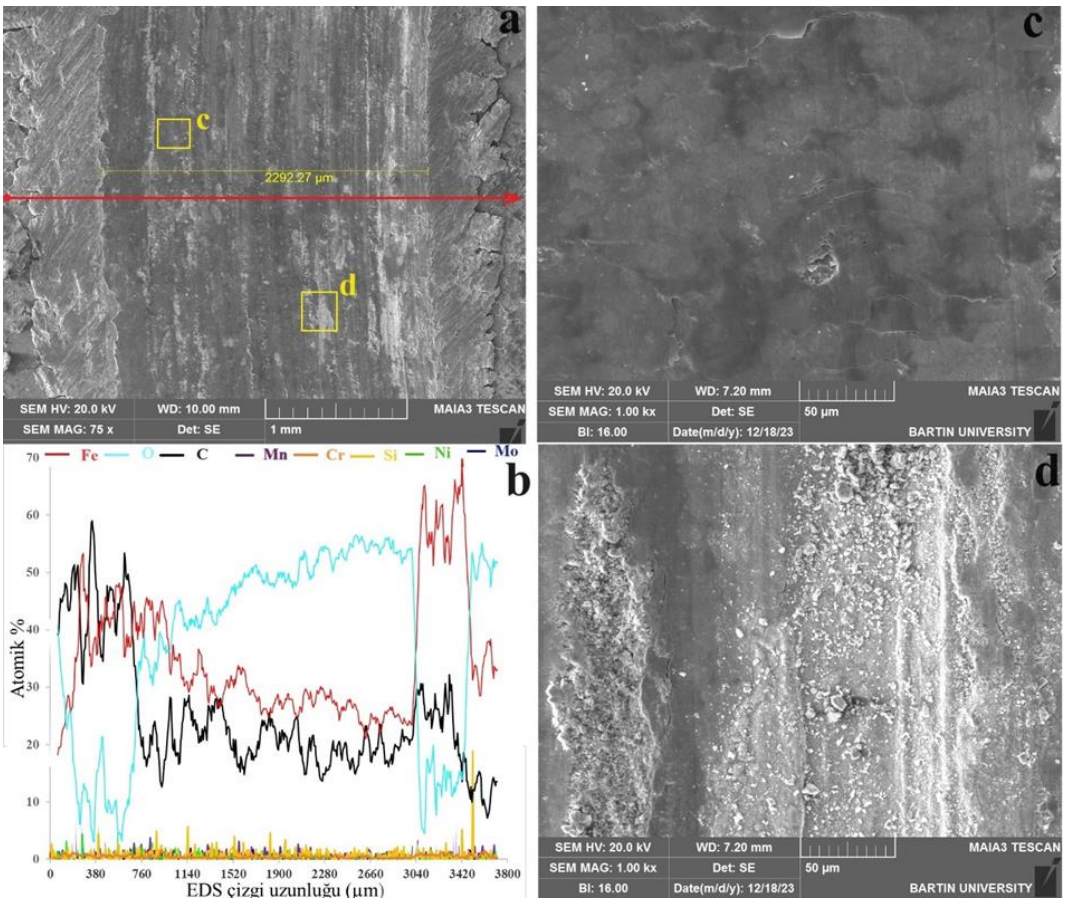

Figure 14. SEM images of the wear track on AISI 4140 steel worn at 500 mm/s at 600°C: a) overall view, b) EDS line analysis, c) magnified view of region c at 1000X, d) magnified view of region d at 1000X (Note: Since the 52100 ball was worn out, WC ball was used).

Since the 52100 ball was worn out under these wear test conditions and could not complete the test, WC ball, resistant to high temperatures, was used. When Figure 14a is examined, a plastered wear trace with a width of 2292.27 µm and an irregular debris around 200-250 µm on both sides of it can be seen, where the wear waste is pushed out by the ball. When the EDS line analysis is examined, the O2 content of these wear wastes is quite low compared to the wear trace, which shows that these wastes are not exposed to any load after being pushed out by the ball during the wear process, and therefore do not sinter on the surface because there is no heating or cooling. It was determined that the presence of O2 in the wear trace was significantly higher than in the samples at room temperature and was atomically higher than Fe and C. Dark and gray areas on the wear scar are striking. When the 1000X image of the dark area (Figure 14c) is examined, it is seen that the black areas are plastered flat surfaces, but micro cracks and fracture ruptures occur in some places. It is thought that as a result of the increase of these micro-cracks in the oxide layer due to repeated loads, the oxide layer broke and oxide layers scattered on the surface were formed as in Figure 14c. Therefore, it was determined that oxidatively supported fatigue type wear occurred in this sample.

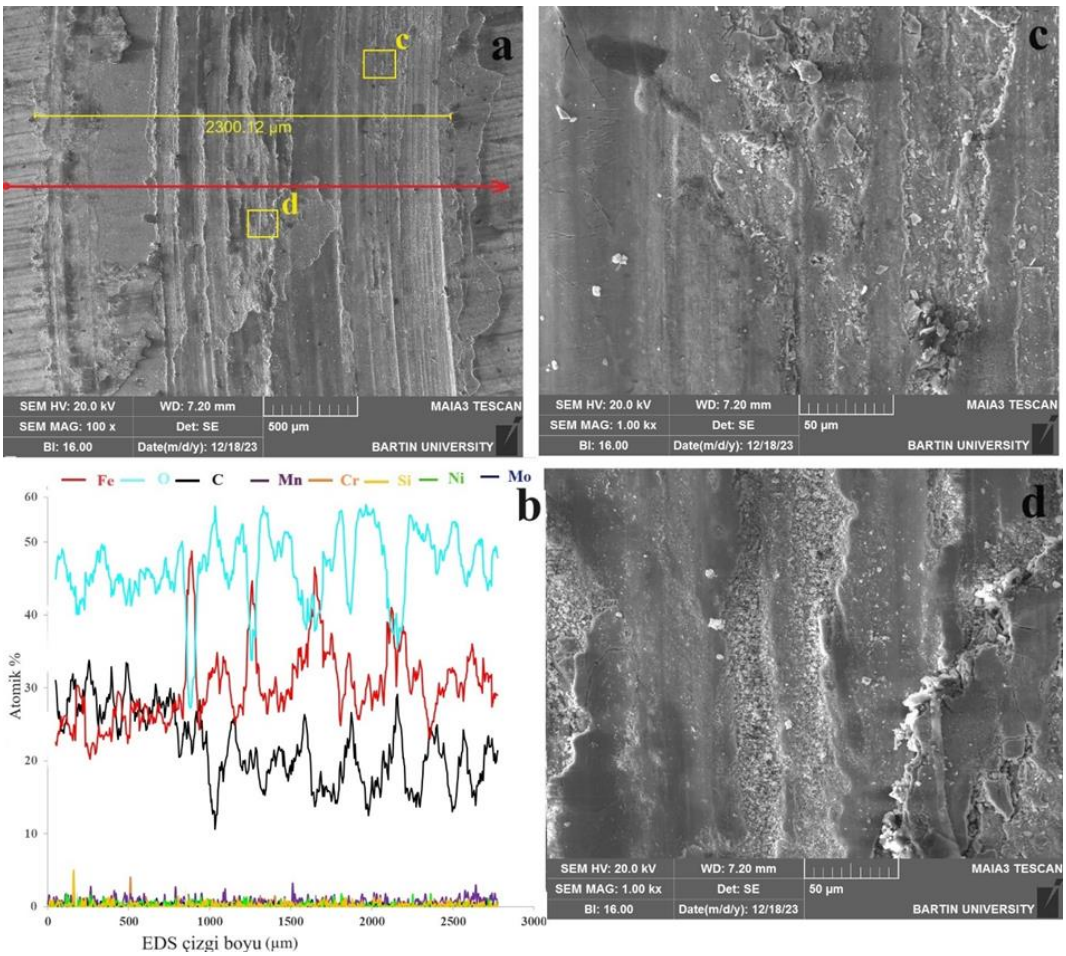

Figure 15. SEM images of the wear track on AISI 4140 steel worn at 1000 mm/s at 600°C: a) overall view, b) EDS line analysis, c) magnified view of region c at 1000X, d) magnified view of region d at 1000X.

Since the contact between the ball and the substrate material decreased by increasing the speed from 500 mm/s to 1000 mm/s during the abrasion process of untreated AISI 4140 steel at 600 °C, the 52100 steel ball completed the test under these test conditions. When Figure 15a is examined, a wear scar with locally plastered areas on abrasive wear scars with a width of 2312.12 µm can be seen. When the EDS line analysis was examined, it was concluded that in this sample, as in the 500 mm/s sample, the O2 ratios were above 50 atm.%, but the stability of the oxide layer was lower. This shows that oxidation occurred independently of the wear test conditions, since the wear tests were carried out at a high temperature of 600 °C. It is seen that the dark areas and occasionally broken gray areas on the wear trace have a lower thickness than the 500 mm/s sample. When the 1000X image of the dark region (Figure 15c) is examined, it shows that the microcracks and fracture ruptures of the plastered black regions are more severe than the 500 mm/s sample, and the formed oxide layer has a lower thickness and therefore a lower resistance. As a matter of fact, wear volume losses were higher at 1000 mm/s than at 500 mm/s. Since the oxide layer in this sample is lower, the ball scratches the soft surface, indicating that an abrasive wear mechanism occurs in addition to oxidatively supported fatigue type wear.

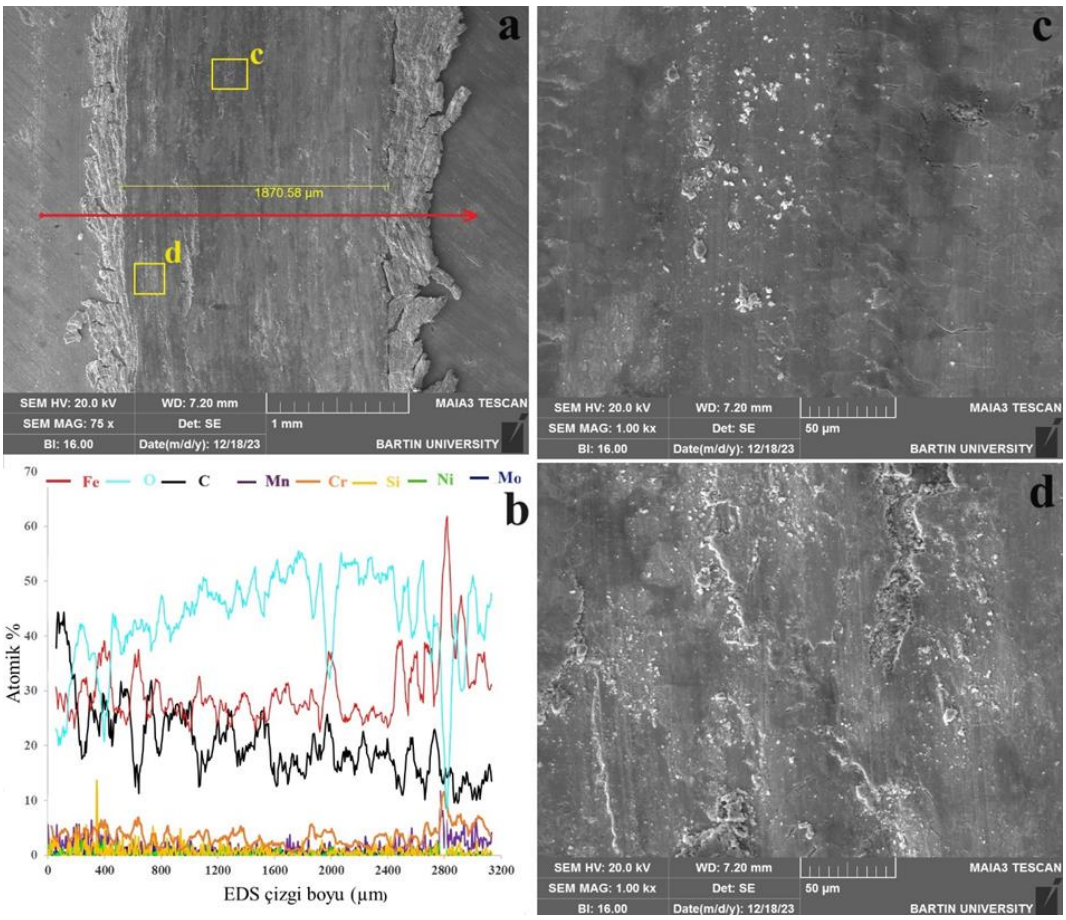

Figure 16. SEM images of the wear track on ER430 worn at 500 mm/s at 600°C: a) overall view, b) EDS line analysis, c) magnified view of region c at 1000X, d) magnified view of region d at 1000X (Note: Since the 52100 ball was worn out, WC ball was used).

Upon examination of Figure 16a, it is evident that the wear track and wear debris next to it exhibit similar wear phenomena as seen in the untreated AISI 4140 steel. The only difference between this sample (ER430) and the untreated AISI 4140 steel is that the wear track is narrower (1870.58 µm). This difference can be attributed to the higher hardness value of the ER430 sample (533±42 HV0.1) compared to the hardness value of untreated AISI 4140 steel (296±27 HV0.1). During the wear process, the abrasive ball can more easily remove material from softer surfaces, allowing it to penetrate deeper, resulting in a wider and deeper wear track. Conversely, in harder materials, resistance to plastic deformation is higher, making it more difficult for the ball to penetrate and deform the material, resulting in a narrower wear track. It is widely reported in literature that an increase in material hardness generally leads to an increase in wear resistance.

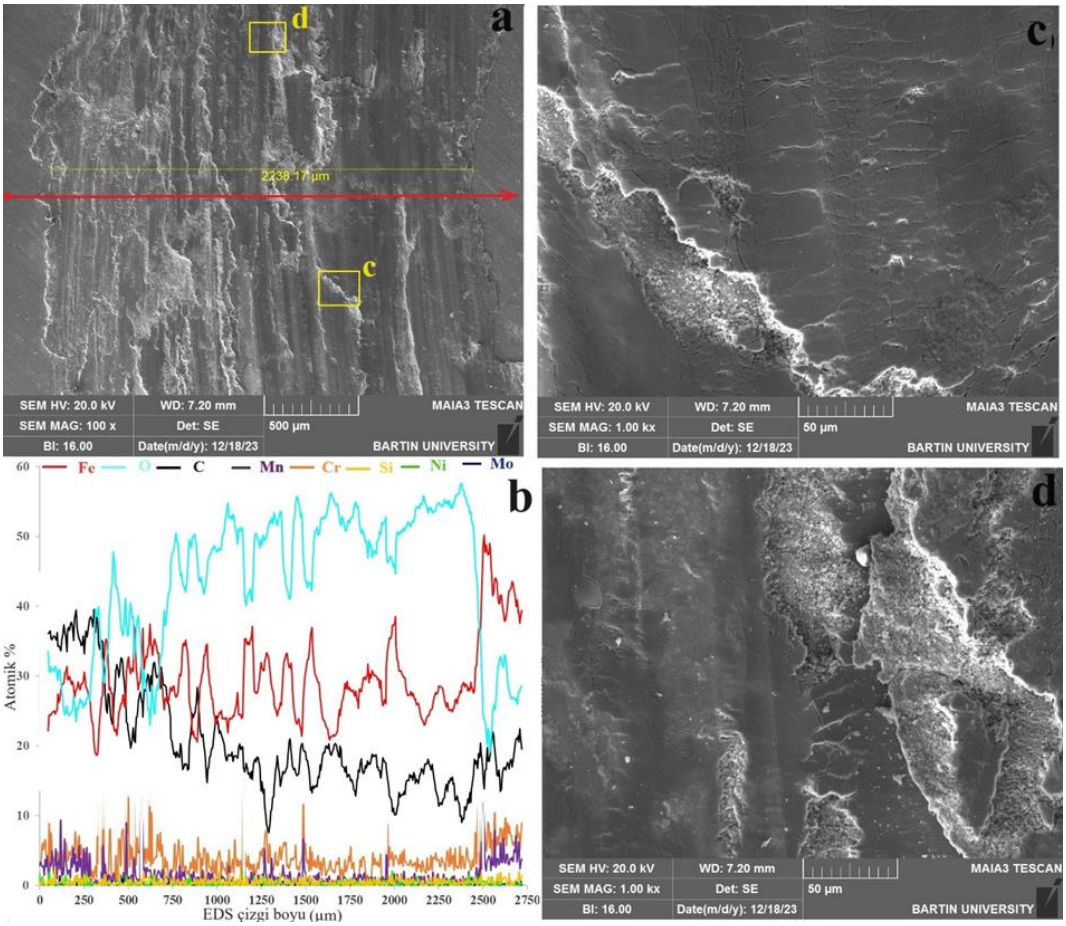

Figure 17. SEM images of the wear track on ER430 worn at 1000 mm/s at 600°C: a) overall view, b) EDS line analysis, c) magnified view of region c at 1000X, d) magnified view of region d at 1000X

As can be seen in Figure 17a, a black layer with an extruded appearance is observed on the right side, while on the left side, there are gray-toned wear debris resembling plastic deformation. Upon analysis of the EDS line, it is observed that as O2 increases from the left (gray areas) to the right (dark areas), reaching levels of around 60%. This indicates that due to the rotational nature of the wear process, with increasing pressure towards the inner part, the wear debris has been sintered into these areas. In Figures 17c and 17d, at 1000X magnification, the wear mechanism is found to occur similarly to other samples, where repeated loading leads to the formation of microcracks in the oxide layer, ultimately resulting in fracture.

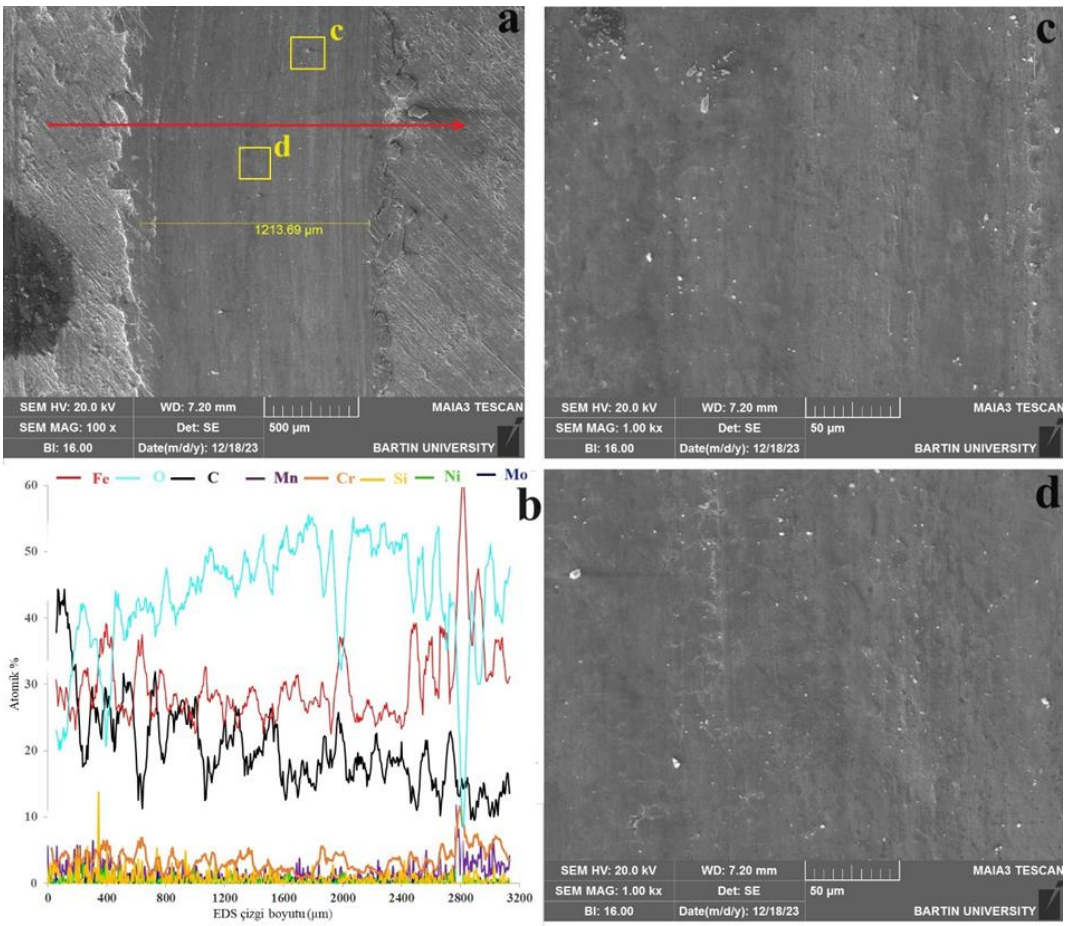

Figure 18. SEM images of the wear track on ER430+410NiMo worn at 500 mm/s at 600°C: a) overall view, b) EDS line analysis, c) magnified view of region c at 1000X, d) magnified view of region d at 1000X (Note: Since the 52100 ball was worn out, WC ball was used).

Looking at Figure 18a, it can be seen that the wear scar is narrower (1213.69 µm) compared to the AISI 4140 (2294 µm) and ER430 (1866 µm) samples worn under the same conditions, and the wastes formed in AISI 4140 and ER430 are not visible on the side edges of the wear scar ohvthis sample. This indicates that this sample suffered less wear volume loss. As a matter of fact, as can be seen from the wear volume loss graph, the ER430+410NiMo sample wears 5.38 times and 4 times less, respectively, than the AISI 4140 steel and ER430 samples worn under the same conditions (Table 4). Although the ER430+410NiMo (473±35 HV0.1) sample has a lower hardness value than the other coated ER430 (533±42 HV0.1) sample, it showed better wear resistance and the hardness distribution in this sample is more regular, thus it performs better during the wear process. It can be attributed to the fact that it provides a hardness-toughness relationship.

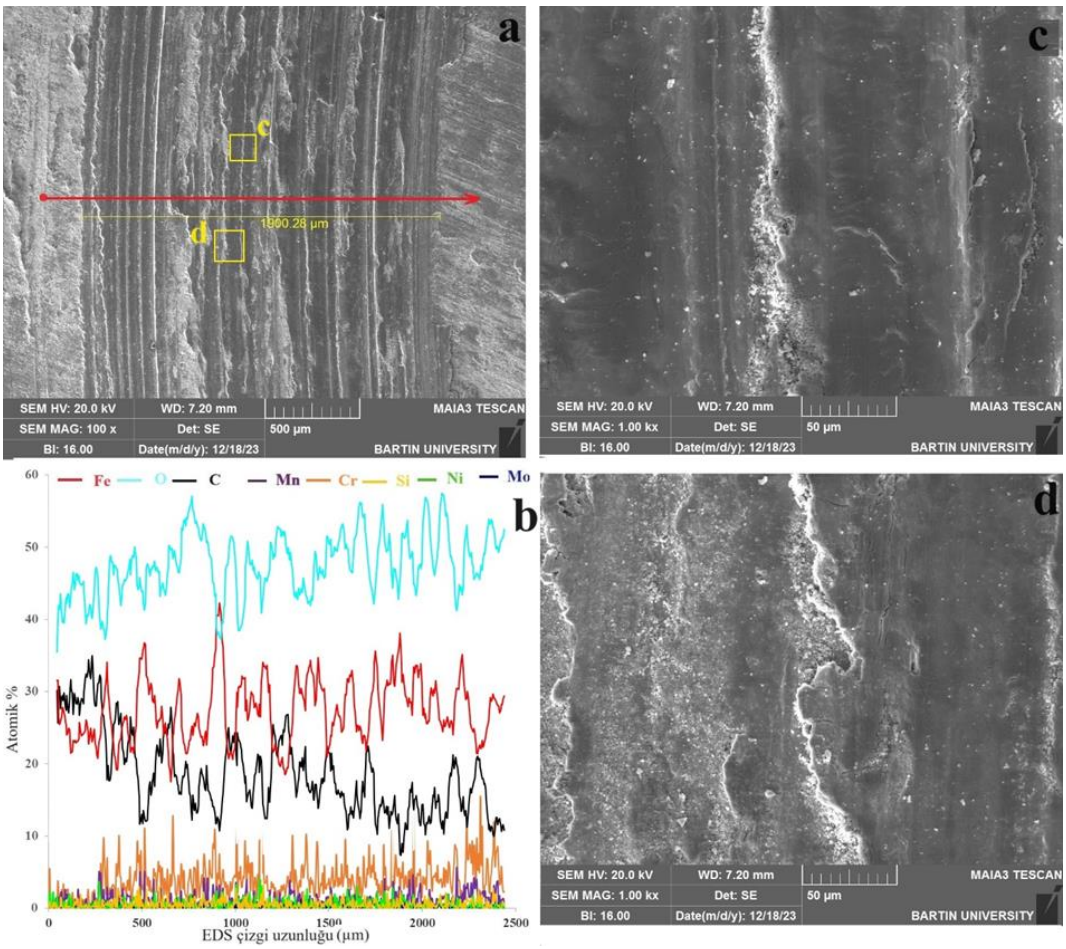

Figure 19. SEM images of the wear track on ER430+410NiMo worn at 1000 mm/s at 600°C: a) overall view, b) EDS line analysis, c) magnified view of region c at 1000X, d) magnified view of region d at 1000X (Note: Since the 52100 ball was worn out, WC ball was used).

In the wear testing of the ER430+410NiMo hardfacing coating at 600°C (Figure 19), increasing the speed from 500 mm/s to 1000 mm/s reveals an abrasion trace with sintered areas among abrasive wear tracks, measuring 1900.28 µm in width. Upon examination of the EDS line analysis, it is observed that, similar to the 500 mm/s sample, oxygen levels are above 50 atm.%, yet the oxide layer is seen to have fractured along the white lines due to repetitive loading in the sintered regions. Upon closer inspection of the dark region in the 1000X magnification (Figure 19b), it is noted that unlike in other samples, there are no micro-cracks present; instead, there are formations resembling channels and occasional fractures. Additionally, in Figure 19c, it is evident that the oxide layer has detached from the surface intermittently in the form of separations. Hence, it is concluded that the abrasion mechanism in this sample is an oxidative-supported abrasive wear.

4. CONCLUSION

In this study, the application of ER430 and ER430+EC410NiMo coatings on hot rolling vertical rolls made from AISI 4140 steel, which are used in the iron and steel industry's hot rolling section, through the powder under welding method, their characterization, and their abrasion behaviors (at room temperature, 300°C, 600°C) were investigated. The obtained results and recommendations can be summarized as follows:

1. Microstructure examinations revealed that the coatings are homogeneous along the surface, exhibit continuity, and do not contain any negative aspects such as porosity, cracks, or segregation throughout the coating layer. A diffusion layer between the coating layer and the substrate was observed.
2. XRD analyses of the obtained coating layers showed that the predominant phase in the ER430 sample is the α-ferrite phase, accompanied by the formation of γ (austenite). In the ER430+EC410Ni sample, similarly, the predominant phase is the α-ferrite phase, along with the presence of γ (austenite) phase and M6C phases.
3. The coating thickness and microhardness values of the obtained coating layers were determined as 1.5 mm and 3.75 mm for ER430 and ER430+410NiMo, respectively. The hardness values were measured as 533±42 HV0.1 and 473±35 HV0.1, respectively.
4. Coated samples exhibited lower friction coefficient values compared to the uncoated sample at 300 °C, while at room temperature and 600 °C, although coated samples generally showed lower friction coefficient values, in some conditions, they exhibited higher friction coefficient values.
5. Due to their higher hardness values, coated samples exhibited better abrasion resistance in all abrasion tests compared to the uncoated sample.
6. The lowest wear volume losses occurred in the tests conducted at 300°C, while the highest abrasion resistance was observed in the tests conducted at 600°C.
7. Regarding wear mechanisms, abrasive and oxidative wear mechanisms were dominant in the uncoated AISI 4140 steel due to its low hardness value, while adhesive and oxidative wear mechanisms prevailed in the coated samples. The increase in temperature intensified the oxidative wear mechanism in all samples.
8. The 52100 bearing steel ball used in the wear process completed the tests without worn at room temperature and 300 °C, while in the 600°C 500 mm/s wear testing, the 52100 bearing steel ball worn, hence a WC ball was used instead. This indicates that using WC balls instead of 52100 bearing steel balls is necessary to achieve more accurate results at high temperatures.
9. Despite having a lower hardness compared to ER430, ER430+410NiMo (duplex coating) generally exhibited better abrasion resistance in the abrasion conditions of this study. This can be attributed to the higher toughness of ER430+EC410NiMo, containing γ (austenite) phase and M6C phases.
10. As a result of this study, it is concluded that by applying ER430 and ER430+410NiMo coatings to hot rolling vertical rolls made from AISI 4140 steel using the submerced arc welding method, wear resistances exceeding 5 fold were achieved, reducing unplanned downtime and increasing production can be achieved.

5. ACKNOWLEDGEMENTS

This study did not benefit from any support.

6. CONFLICT OF INTEREST

Authors approve that to the best of their knowledge, there is not any conflict of interest or common interest with an institution/organization or a person that may affect the review process of the paper.

7. AUTHOR CONTRIBUTION

Erdoğan Kanca determined and managed the concept and design process of the research. Hikmet Gizem Sarsılmaz collected the data of the experiments related to the study and made the necessary graphic drawings. Ali Günen analyzed the SEM, EDS, XRD and microhardness data for the study and interpreted the results. All authors prepared and critically analyzed the manuscript.

8. REFERENCES

Ardigo-Besnard M.R., Tellier A., Besnard A., & Chateau-Cornu J.P., Effect of the microstructure on the tribological properties of HIPed and PTA-welded Fe-based hardfacing alloy. Surface and Coatings Technology 425, 127691, 2021.

Bembenek M., Prysyazhnyuk P., Shihab T., Machnik R., Ivanov O., & Ropyak L., Microstructure and Wear Characterization of the Fe-Mo-BC—Based Hardfacing Alloys Deposited by Flux-Cored Arc Welding. Materials 15(14), 5074, 2022.

Brühl S.P., Cabo A., Tuckart W.R., & Prieto G., Tribological behaviour of nitrided and nitrocarburized carbon steel used to produce engine parts. Industrial Lubrication and Tribology 68(1), 125-133, 2016.

Bowden D., Krysiak Y., Palatinus L., Tsivoulas D., Plana-Ruiz S., Sarakinou E., … & Preuss M., (A high-strength silicide phase in a stainless steel alloy designed for wear-resistant applications. Nature Communications 9(1), 2018.

Çelik O., Ahlatci H., Kayali E.S., & Cimenoglu, H., High temperature abrasive wear behavior of an as-cast ductile iron. Wear 258(1-4), 189-193, 2005.

Çürük A., Farklı kaplama teknikleri ile kaplanmış duşlu masa rollerinin yüksek sıcaklık aşınma korozyon davranışlarının incelenmesi, Yüksek Lisans Tezi, İskenderun Teknik Üniversitesi/Mühendislik ve Fen Bilimleri Enstitüsü/İleri Metalurji ve Malzeme Teknolojileri Mühendisliği Anabilim Dalı, 2017.

Davis J.R., ASM Handbook Hardfacing, Chapter 6, Weld Cladding, and Dissimilar Metal Joining, https://doi.org/10.31399/asm.hb.v06.a0001442, 2017.

Garbade R.R., & Dhokey N.B., Overview on hardfacing processes, materials and applications. In IOP Conference Series: Materials Science and Engineering, IOP Publishing. 1017, 1, 2021.

Girisken, I., & Çam, G., Characterization of microstructure and high-temperature wear behavior of pack-borided Co-based Haynes 25 superalloy. CIRP Journal of Manufacturing Science and Technology, 45, 82-98, 2023.

Grützmacher P.G., Rosenkranz A., Rammacher S., Gachot C., & Mücklich F., The influence of centrifugal forces on friction and wear in rotational sliding. Tribology International, 116, 256-263, 2017.

Günen A., Ulutan M., Gok M., Kurt B., & Orhan N., Friction and wear behaviour of borided aisi 304 stainless steel with nano particle and micro particle size of boriding agents. Journal of the Balkan Tribological Association, 20(3), 2014.

Günen A., Kanca E., Karakaş M.S., Koç V., Gök M.S., Kanca Y., ... & Demir M., High temperature wear behavior of the surface-modified externally cooled rolls. Surface and Coatings Technology, 348, 130-141, 2018.

Hamada A., Sahu P.C., & Porter, D., Indentation property and corrosion resistance of electroless nickel–phosphorus coatings deposited on austenitic high-mn twip steel. Applied Surface Science, 356, 1-8, 2015.

Jiang W.H., Kovacevic, R., Laser deposited TiC/H13 tool steel composite coatings and their erosion resistance.” Journal of Materials Processing Technology 186, 331–338, 2007.

Jilleh A., Babu N.K., Thota, V., Anis A.L., Harun M.K., & Talari M.K., Microstructural and wear investigation of high chromium white cast iron hardfacing alloys deposited on carbon steel. Journal of Alloys and Compounds, 857, 157472, 2021.

Khan T.I., Khalid F.A., & Orhan N., Surface modification of tool steel using tungsten arc heat source. Surface Engineering 20(3), 215-219, 2004.

Kaptanoğlu M., & Eroğlu, M., Ferroniyobyum ve Ferrobor İçeren Tozaltı Kaynak Tozları ile Elde Edilen Kaplamaların Mikroyapı ve Aşınma Özelliklerinin Araştırılması. Kahramanmaraş Sütçü İmam Üniversitesi Mühendislik Bilimleri Dergisi 20(1), 64-75, 2017.

Kayalı Y., Kanca E., & Gunen A., Effect of boronizing on microstructure, high-temperature wear and corrosion behavior of additive manufactured Inconel 718. Materials Characterization, 191, 112155, 2022.

Kazemipour M., Shokrollahi H., & Sharafi S., The influence of the matrix microstructure on abrasive wear resistance of heat-treated fe–32cr–4.5c wt% hardfacing alloy. Tribology Letters 39(2), 181-192, 2010.

Kiryukhantsev-Korneev P.V., Sheveyko A. N., Shvindina N.V., Levashov E.A., & Shtansky D.V., Comparative study of Ti-C-Ni-Al, Ti-C-Ni-Fe, and Ti-C-Ni-Al/Ti-C-Ni-Fe coatings produced by magnetron sputtering, electro-spark deposition, and a combined two-step process. Ceramics International 44(7), 7637-7646, 2018.

Koçyiğit F., Yıldız F., Gök M.S & Çay V.V., Dry-sliding wear behavior of AISI 4140-barrel steel at elevated temperatures. Materials Testing, 62(2), 189-195, 2020.

Ortner H.M., Ettmayer P., & Kolaska H., The history of the technological progress of hardmetals. International Journal of Refractory Metals and Hard Materials 44, 148-159, 2014.

Padilla E.H., Béjar L., Sánchez-Carrillo M., Medína A., Carreón-Garcidueñas H., Borjas-García S. E., … & Huirache–Acuña R., XPS study of corrosion deposit in stainless steel hardfacing. Microscopy and Microanalysis, 24(S1), 1086-1087, 2018.

Podgornik B., Vižintin J., Ronkainen H., & Holmberg K., Wear resistance of dcl coating deposited on pretreated aisi 4140 steel. Advanced Engineering Materials 2(7), 444-448, 2000.

Rovatti L., Lemke J.N., Lecis N., Stejskal O., & Vedani M., Effect of dilution on microstructure and wear resistance of a fe-based hardfacing alloy with a high amount of carbide-forming elements. Conference Papers in Science, 2015, 1-10, 2015.

Saklakoğlu N., İrizalp S.G., Doğan S., Ildas G., & Saklakoğlu I., Performance of fe-based hardfacings on hot forging die: experimental, numerical and industrial studies. Metallic Materials 56(01), 15-27, 2018.

Singh J., & Kumar Shukla D., Hardfacıng Wıth Saw Method On Mıld Steel-A Crıtıcal Revıew, International Journal of Technical Research & Science, V:3 I: XI, 2018.

Suraj R., Hardfacing and its effect on wear and corrossion performance of various ferrous welded mild steels. Materials Today: Proceedings 42, 842-850, 2021.

Şen U., Çeşitli yenileme işlemlerine uğratılan SAE 4140 tank palet çeliklerinin özellikleri. Doktora tezi, İstanbul Teknik Üniversitesi, Fen Bilimleri Enstitüsü, 1993.

Turunç U.D., Farklı Kimyasal Bileşimlerdeki sert Dolgu Aşınma Plakalarının Özelliklerinin İncelenmesi, Geliştirilmesi ve Optimizasyonu (Doctoral dissertation, İstanbul Teknik Üniversitesi, Fen Bilimleri Enstitüsü, 2015.

URL-1 https://en.wikipedia.org/wiki/List_of_countries_by_steel_production

Yang J., Wang C., Xing X., Yang Y., Ren X., & Yang Q., Stress induced phase transition on the medium-high carbon alloy steel hardfacing coating during the work hardening process: experiments and first-principles calculation. Materials Science and Engineering: A 670, 49-56, 2016.

Zahiri R., Sundaramoorthy R., Lysz P., & Subramanian C., Hardfacing using ferro-alloy powder mixtures by submerged arc welding. Surface and Coatings Technology, 260, 220-229, 2014.

JOURNAL of
MATERIALS and MECHATRONICS:A

e-ISSN 2717-8811
JournalMM, 2024, 5(1), 87-105
https://doi.org/10.55546/jmm.1451429

Araştırma Makalesi / Research Article

Large Deflection Analysis of Functionally Graded Beam by Using Combining Method

Ersin DEMİR[1*], Hasan ÇALLIOĞLU[2], Zekeriya GİRGİN[3]

[1*] Pamukkale University, Faculty of Technology, Department of Mechatronics Engineering, Denizli, Turkey,
ORCID ID: https://orcid.org/0000-0001-8222-5358, edemir@pau.edu.tr
[2] Pamukkale University, Faculty of Technology, Department of Mechatronics Engineering, Denizli, Turkey,
ORCID ID: https://orcid.org/0000-0002-4598-7975, hcallioglu@pau.edu.tr
[3] Pamukkale University, Faculty of Engineering, Department of Mechanical Engineering, Denizli, Turkey
ORCID ID: https://orcid.org/0000-0001-5958-9735, (Retired)

Geliş/ Received: 12.03.2024**;** **Revize/Revised:** 20.04.2024 **Kabul / Accepted:** 08.05.2024

ABSTRACT: In this study, the large deflection behavior of a circular cross-section beam is examined using the Combining Method (CM). The CM is a numerical solution method that uses block diagrams in the Matlab-Simulink program and weighting coefficients in the Differential Quadrature Method (DQM). The beam material considered is Functionally Graded Material (FGM). Boundary conditions of the beam are taken as clamped-free (C-F) and a singular load is assumed to be applied from the free end of the beam. Geometric nonlinear analysis is performed while calculating the large deflection equations of the beam and performing numerical analysis. The effects of increasing the force applied to the beam, changing the beam cross-section in the longitudinal direction, and changing the material index of the FGM on the extreme deflection behavior of the beam were examined. For comparison purposes, the results obtained from CM are compared with the results obtained from both SolidWorks-Simulation and Ansys-Workbench programs. As a result of the analysis, increasing the applied force causes the x and y coordinates of the end point of the beam to decrease. The change in geometry and material index greatly affects the large deflection occurring in the beam.

Keywords: Large Deflection, Functionally Graded Material, Beam, Combining Method, Finite Element Method

1. INTRODUCTION

Beams are widely used in many fields of engineering applications (mechanical, civil, etc.). Therefore, the behavior of beam structures (deflection, vibration, buckling, etc.) has been studied intensively by many researchers. When studying the deflection behavior of beams, simplifications are made based on certain assumptions due to the non-linearity of the governing equation representing

*Sorumlu yazar / Corresponding author: edemir@pau.edu.tr
Bu makaleye atıf yapmak için /To cite this article

Demir, E., Çallıoğlu, H., Girgin, Z. (2024). Large Deflection Analysis of Functionally Graded Beam by Using Combining Method. Journal of Materials and Mechatronics: A (JournalMM), 5(1), 87-105.

the deflection behavior of the beam. In recent years, especially with the development of numerical analysis techniques, the default simplifications have been removed to make more accurate analysis. Therefore, the problem of large deflection of beams has attracted the attention of many researchers. For example, Belendez et al. (2002) examined the large deflection behavior of a cantilever beam under a singular load from its free end. In their study, they expressed the nonlinear governing equation that represents the system. They solved the governing equation theoretically and compared it with the experimental results. Dado and Al-Sadder (2005) studied the large deflection behavior of prismatic and non-prismatic cantilever beams under different loads. The nonlinear governing equation they established has been solved theoretically for the problem considered. They also compared their results with the results obtained from the Msc/Nastran program.

Another issue addressed in this study is FGM. The concept of FGM was first proposed in 1984 in Japan by Japanese scientists during thermal barrier research conducted for a spacecraft (Koizumi, 1993). The use of FGM materials is advantageous because the material properties of the mentioned structure can be modified as desired from one surface to another. Below, some of the articles in the open literature examining the large deflection behavior of beams made of FGM are summarized.

Kang and Li (2010) studied the large deflection of a cantilever beam made of FGM. It is assumed that a moment is applied from the free end of the beam under consideration. They derived the explicit expression of the beam considered in their study. As a result, they determined the optimum gradient distribution for FGM and suggested the appropriate beam design. Davoodinik and Rahimi (2011) studied the large deflection of a FG beam. The beam is assumed to be flexible, with a tapered cross-section. It is also assumed that the considered beam is subjected to inclined end loading and intermediate loading. As a result of using the semi-analytical method, the effects of the taper ratio, inclined end loading, and material distribution on the large deflection behavior were examined. Brojan et al. (2012) studied the large deflections of thin non-prismatic beams under non-uniform distributed load and concentrated load acting from the free end. The material of the beam is assumed to be a nonlinear elastic material. They compared the theoretical results obtained with experimental results and existing results in the literature. Soleimani (2012) derived the large deflection equation of a beam consisted of FGM under arbitrary load. In the study, it is assumed that the elasticity modulus of the beam varies with the exponential and power function in the longitudinal direction of the beam. Shooting Method was used for analysis. As a result of the analysis, the effect of using different elasticity modulus functions and applying different loadings on the large deflection behavior of the beam was examined. Kien (2013) examined the large deflection behavior of a cantilever beam made of axial FGM with a tapered cross-section. In the study, the effects of inhomogeneity of the beam material, shear deformation, and non-uniform section on the large deflection behavior of the beam were investigated. Sitar et al. (2014) studied the solution of the differential equation obtained for the large deflection behavior of a thin inhomogeneous beam. It is assumed that the beam consists of thin layers throughout the thickness. In this way, it was desired to obtain an FG beam whose material properties change continuously throughout the thickness. They solved the derived equations numerically and compared them with the existing results in the literature. Horibe and Mori (2018) solved the equation for the large deflection behavior of a thin tapered beam made of FGM. A transverse load is applied to the free end of the beam. They used the Runga-Kutta method in their solutions. They compared the deflection and bending stress results obtained as a result of their solutions with the existing results. Lin et al. (2019) overcame the large deflection problem of the axial FG beam with the Homotopy Analysis Method. It is assumed that the beam is cantilever and the load

is applied from its free end. Moreover, it is assumed that the elasticity modulus varies along the beam length. They compared their results with the results obtained from the finite element method and previous studies. Saraçoğlu et. al. (2019) calculated the deflections of orthotropic beams using Euler-Bernoulli and Timoshenko beam theories. In their study, orientation angle, material properties, and length/depth ratio were examined in the static analysis of orthotropic beams. Saraçoğlu et. al. (2022) studied equal strength cantilever and simply supported beams made of functionally graded material under uniformly distributed load or point load. Dimensionless deflections of the beams considered were obtained for different material indices. Nguyen et. al. (2022a) studied the large deflection behavior of a two-phase FG sandwich beam with different homogeneity. They used a nonlinear finite element method in their study. In their study, they used four types of homogenization methods to obtain the effective elastic modulus of the beam. In the study, the Newton-Rapson Method and Arc-Length technique were used to find the large deflection and stress distribution of the beam. Nguyen et al. (2022b) developed a model based on Isogeometric analysis for the large deflection of curved FG beams. They also used a 3-dimension beam theory in their study. They considered five benchmark test cases to demonstrate the accuracy of their proposed solution technique. Additionally, the effect of material variations on curved beam behavior under different loads is also expressed. Li et al. (2022) proposed a non-local numerical model for large deformation analysis of variable cross-section FG beam. They used the peridynamic differential operator in the solution of their study. They also used variational analysis, the Lagrange multiplier method, and the Newton-Rapson method to solve the governing equation. They applied their proposed method to the large deflection analysis of a homogeneous cantilever beam and a linearly and parabolically varying cantilever FG beam. They also compared their results with finite element results.

With the development of technology in the last twenty years, computer processor speeds have increased considerably. Thus, the interest in numerical techniques has constantly increased accordingly. Numerical techniques attract the attention of scientists in solving problems that cannot be easily solved with theoretical calculations. CM, one of these numerical techniques, was first proposed by Girgin (2008) for the solution of nonlinear differential equations. Girgin stated in his study that the conditions cannot be applied at any instant in the time domain while making solutions in computer-aided numerical programs. He stated that this problem could be overcome by combining Matlab/Simulink, one of the computer-aided numerical programs, and the DQM, another numerical technique. Thus, the shortcomings of DQM, which cannot be easily used in solving nonlinear problems, and the shortcomings of Matlab/Simulink in applying boundary conditions have been eliminated. After this study, Girgin (2009) applied the same technique to the Integral Quadrature Method (IQM). Thus, derivative and integral operations in nonlinear equations with boundary conditions can be easily performed. Moreover, Girgin et al. (2014) applied CM to four different nonlinear differential equations. These equations have not only initial conditions but also boundary conditions. They compared the results obtained from CM with the results available in the literature. In addition, Girgin et al. (2020) carried out a large deflection analysis of the prismatic embedded beam for different loading conditions. Unlike this study, the material is isotropic and the beam cross-section is taken as constant. Additionally, the iterative DQM method was also proposed in this study.

Furthermore, there are a few studies in which only DQ methods are used when performing large deflection analyses of beams. Kurtaran (2015) examined the large deflection of moderately thickness FG curved beams for static and transient behavior using the generalized DQM. He expressed the spatial derivatives in the equilibrium equation with generalized DQM. He solved the static

equilibrium equation using the Newton method and the dynamic equilibrium equation using the Newmark method. Hu et al. (2017) formulated the nonlinear large deflection contact problem for curved beams. They proposed a new adaptive DQ element method to predict the contact positions in the curved beam. Demir (2023) solved the problem of large displacement behavior of a Functionally Graded beam under uniform thermal load. He examined the effects of temperature, material, geometry, slenderness, force, and boundary conditions on the large displacement of the beam.

In this study, the large deflection behavior of a cantilever beam with a variable cross-section made of FGM is studied. CM method is used to solve the complex nonlinear governing differential equation. In addition, the results obtained with CM were compared with the results obtained from Ansys-Workbench and SolidWorks-Simulation programs for comparison purposes. Since the problem addressed in the literature research has strong non-linearity, the studies generally require the application of complex calculation procedures. However, the complex nonlinear differential equation mentioned with CM can be easily solved. As a result of comparison with the results obtained from finite element-based programs, it is seen that quite compatible values are obtained.

2. GEOMETRIC AND MATERIAL PROPERTIES OF THE BEAM

2.1 Geometry

The geometry of the FG beam is shown in Fig. 1. It can be seen from the figure that the boundary condition of the beam is C-F and the cross-section of the beam is a variable that depends on the variable r(s) along the longitudinal direction. ro is the radius of the beam at the clamped end.

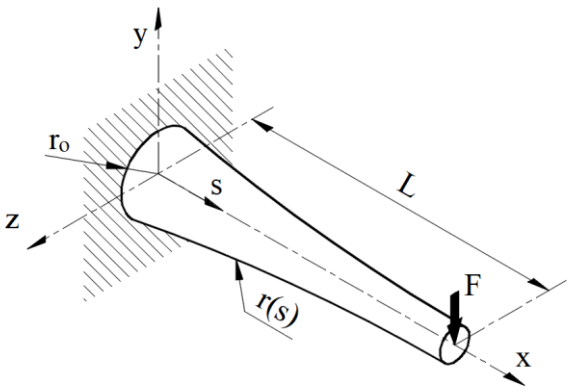

Figure 1. The FG beam with variable cross-section

The force (*F*) is applied at the free end of the beam. *L* is the length of the beam. *x*, *y* and *z* refers to the coordinates in the longitudinal, transverse, and normal direction and *s* is the curvilinear coordinate of the beam along the deflection direction. The radius of the beam varies along the *s* coordinate and is given by the formula in Eq. 1.

$$r(s) = r_o\left(1 + \left(\frac{s}{L}\right)\right)^{n1} \tag{1}$$

where *n1* is a geometric index. In this study, *n1* is taken as -0.3, -0.15, 0, 0.15 and 0.3. r_o and *L* are taken as 10 and 1000 mm, respectively. So, the variation of *r(s)* depending on the geometric index is obtained as shown in the Figure 2. As can be seen from the figure, the cross-section of the beam is constant when *n1*=0.

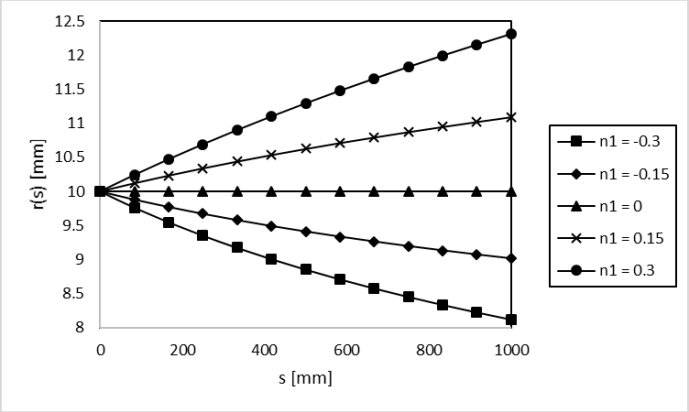

Figure 2. Variation of the radius of the beam with *s* coordinate

Additionally, it can be seen from the figure that the cross-section increases when the *n1* value is positive and decreases when it is negative.

2.2 Material

It is assumed that the material of the beam is functionally graded material. The properties of the beam material are varied from the clamped end to the free end. That is, similar to the change in radius, the material properties of the beam also vary along the s coordinate. This variation is given for the Elasticity Modulus in the Eq. 2.

$$E(s) = E_o\left(1 + \left(\frac{s}{L}\right)\right)^{n2} \tag{2}$$

where *n2* is a material index. *n2* is taken as -0.7, -0.4, 0, 0.4 and 0.7. E_o is the Elasticity Modulus of the beam at the clamped end. In this study, the material at the clamped end is taken as Aluminum and its Elasticity modulus is 70000 N/mm^2. The variation in the elasticity modulus (*E(s)*) depending on the material index is obtained as shown in the Fig. 3.

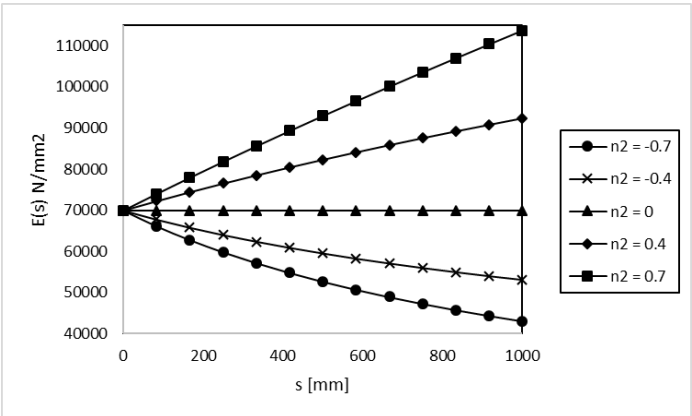

Figure 3. Variation in the Elasticity modulus of the beam with *s* coordinate

As can be seen from the figure, the Elasticity modulus of the beam is constant when *n2*=0 and it increases when the *n2* value is positive and it decreases when *n2* is negative.

3. THEORETICAL FORMULATION OF THE BEAM

The large deflection behavior of a functionally graded beam with variable cross-section is considered in this study. The variable cross-section beam with a singular load applied from its free end is shown on the left in Fig. 4 (Dado and Al-Sadder, 2005).

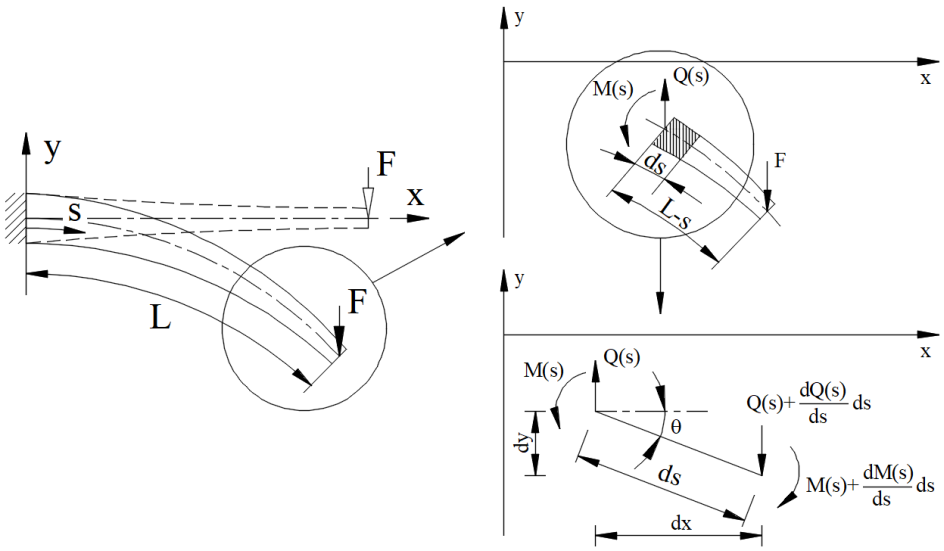

Figure 4. Variation in the Elasticity modulus of the beam with *s* coordinate

The free-body diagram of the free-end section of the considered beam is shown in the upper right of Fig. 4. When the force equilibrium in the vertical direction is written here, the following equation is obtained.

$$Q(s) = F \tag{3}$$

Here Q(s) and F are the internal and external vertical forces, respectively. In the bottom right corner of Fig. 4, a free-body diagram is shown by considering the infinitesimal element of the beam section under consideration. If the moment equilibrium is written in the infinitesimal element, it yields:

$$\frac{dM(s)}{ds} ds + Q(s)\, dx = 0 \tag{4}$$

When both sides of the equation are divided by ds, it gives,

$$\frac{dM(s)}{ds} + Q(s)\, \frac{dx}{ds} = 0 \tag{5}$$

The following equations can be obtained from the figure showing the infinitesimal element.

$$\frac{dy}{ds} = sin\theta \tag{6}$$

$$\frac{dx}{ds} = cos\theta \tag{7}$$

where θ is the slope of the beam.

When Eq. 7 is substituted into Eq. 5, the following equation yields.

$$\frac{dM(s)}{ds} = -Q(s)\,cos\theta \tag{8}$$

When Eq. 3 is substituted into Eq. 8, it gives,

$$\frac{dM(s)}{ds} = -F\,cos\theta \tag{9}$$

In addition, according to the Euler–Bernoulli law, the following equation can be written.

$$M(s) = E(s)I(s)\frac{d\theta}{ds} \tag{10}$$

E(s) in Eq. 10 was given in Eq. 2. *I(s)* is the variable area moment of inertia of the beam and, it is given in Eq. 11.

$$I(s) = \pi\frac{\left(r(s)\right)^4}{4} \tag{11}$$

r(s) in Eq. 11 was given in Eq. 1. The derivative of Eq. 10 with respect to *ds* is given in Eq. 12.

$$\frac{dM(s)}{ds} = \left(\frac{dE(s)}{ds}I(s) + E(s)\frac{dI(s)}{ds}\right)\frac{d\theta}{ds} + E(s)I(s)\frac{d^2\theta}{ds^2} \tag{12}$$

When this resulting equation is substituted in Eq. 9, the following governing equation can be obtained as similar to Reference (Dado and Al-Sadder, 2005).

$$\left(\frac{dE(s)}{ds}I(s) + E(s)\frac{dI(s)}{ds}\right)\frac{d\theta}{ds} + E(s)I(s)\frac{d^2\theta}{ds^2} + F\,cos\theta = 0 \tag{13}$$

When Eqs. 1 and 2 are substituted in Eq. 13, the following general equation is obtained,

$$\frac{d\theta}{ds} = \frac{1}{(n2+4n1)}\left(-\frac{d^2\theta}{ds^2}(L+s) - \frac{4(L+s)\,F\,cos\theta}{E_o\,\pi r_o^4}\left(\frac{L+s}{L}\right)^{-n2}\left(\frac{L+s}{L}\right)^{-4n1}\right) \tag{14}$$

The nonlinear differential equation obtained is normalized for the solution with CM. For this, the expression *s* is made dimensionless as follows,

$$s = S\,L \tag{15}$$

where S is normalized form of s.

Thus, the following normalized equation is obtained. This equation is used to solve the problem.

$$\frac{d\theta}{dS} = \frac{1}{(n2+4n1)}\left(-\frac{d^2\theta}{dS^2}(1+S) - \frac{4L^2(S+1)\,F\,cos\theta}{E_o\,\pi r_o^4}(1+S)^{-n2}(1+S)^{-4n1}\right) \tag{16}$$

The C-F boundary conditions of the beam are given in Eqs. 17-20.

$$y(0) = 0 \tag{17}$$

$$x(0) = 0 \tag{18}$$

$$\theta(0) = 0 \tag{19}$$

$$\left.\frac{d\theta(s)}{ds}\right|_{s=L} = 0 \tag{20}$$

4. THE SOLUTION WITH COMBINING METHOD

The CM used in this study is implemented in the Simulation module of the Matlab program. While CM is applied, the weight coefficients obtained for the derivatives and integrals in DQM are used for the derivative and integration operations needed to solve the nonlinear differential equation. The procedure for obtaining weight coefficients for derivative and integral are explained in Sections 4.1 and 4.2.

4.1 Weighting Coefficients for Derivatives

The first-order derivative of a function *f(x)* is given in DQM as follows (Girgin,2008),

$$\frac{df(x_i)}{dx} = \sum_{j=1}^{N} A_{ij}^{(1)} f(x_i) \qquad (i = 1,2,\dots,N) \tag{21}$$

where $A_{ij}^{(1)}$ is the weighting coefficients of the first-order derivative of the function *f(x)*. The test functions are obtained from the following Lagrange interpolation shape functions.

$$l_i(x) = \frac{\Phi(x)}{(x - x_i)\Phi^{(1)}(x_i)} \qquad (i = 1,2,\dots,N) \tag{22}$$

where

$$\Phi(x) = \prod_{i=1}^{N} (x - x_i) \tag{23}$$

$$\Phi^{(1)}(x_i) = \frac{d\Phi(x_i)}{dx} = \prod_{j=1, j\neq i}^{N} (x_i - x_j) \tag{24}$$

By substituting Eq. 22 into Eq. 21, weighting coefficients for first-order derivatives are obtained as follows.

$$A_{ij}^{(1)} = \frac{dl_j(x_i)}{dx} = \frac{\Phi^{(i)}(x_i)}{(x_i - x_j)\Phi^{(1)}(x_j)} \qquad (i,j = 1,2,\dots,N), \qquad i \neq j \tag{25}$$

$$A_{ii}^{(1)} = \frac{dl_i(x_i)}{dx} = -\sum_{j=1, i\neq j}^{N} A_{ij}^{(1)} \qquad (i = 1,2,\dots,N) \tag{26}$$

These obtained coefficients are the elements of the weighting coefficients matrix of the first-degree derivative $[A^{(1)}]$. The coefficients of higher-order derivatives are calculated with the following formula,

$$[A^{(r)}] = \frac{d^r}{dx^r} = \frac{d}{dx}\frac{d^{r-1}}{dx^{r-1}} = [A^{(1)}][A^{(r-1)}] \tag{27}$$

In this study, widely used equally spaced sampling points are selected in normalized coordinates as given in Eq. 28,

$$x_i = \frac{i-1}{N-1} \qquad (i = 1,2,\dots,N) \tag{28}$$

4.2 Weighting Coefficients for Integrals

Integral coefficients and integral constant coefficients are used to obtain the function itself from its first-order derivative (Girgin, 2009).

$$\int \frac{df(x_i)}{dx}dx = \sum_{j=1}^{N} B_{ij}^{(1)} \frac{df(x_i)}{dx} + \sum_{j=1}^{N} C_{ij}^{(0)} f(x_i) \qquad (i = 1,2,\dots,N) \tag{29}$$

where $B_{ij}^{(1)}$ and $C_{ij}^{(0)}$ are weighting coefficients of the single integral and coefficients of the integral constant, respectively. The following process is applied to find $B_{ij}^{(1)}$ weight coefficients

$$D_{ij} = \frac{x_i - g}{x_j - g} A_{ij}^{(1)} \quad i \neq j \quad (i,j = 1,2,\dots,N) \tag{30}$$

$$D_{ii} = A_{ii}^{(1)} + \frac{1}{x_i - g} \quad i = j \quad (i,j = 1,2,\dots,N) \tag{31}$$

where $A_{ij}^{(1)}$ is the weighting coefficients of the first-order derivative and g is constant and is not equal to x_i. If the inverse of matrix $[D]$ is taken as matrix $[H]$, the elements of matrix $[B]$ are obtained from the elements of matrix $[H]$ as follows:

$$B_{ij}^{(1)} = H_{ij} - H_{1j} \qquad (i,j = 1,2,\dots,N) \tag{32}$$

As for the coefficients of the integral constant $C_{ij}^{(0)}$, they are given in Eq. 33.

$$C_{ij}^{(0)} = \begin{cases} 1 & for \quad j = 1 \\ 0 & for \quad j \neq 1 \end{cases} \qquad (i, j = 1,2, \dots, N) \tag{33}$$

4.3 Solution

The normalized governing differential equation (Eq. 16) is integrated to find the θ rotation function in the solution of the problem under consideration. To make the solution more understandable with CM, complex expressions are embedded into subsystems as shown in Eq. 34.

$$\theta = \int \left(\underbrace{\frac{1}{(n2 + 4n1)}}_{Subsystem\ A} \left(-\frac{d^2\theta}{dS^2} \underbrace{(1+S)}_{Subsystem\ B} - \underbrace{\frac{4L^2(S+1)\,F}{E_o\ \pi r_o^4}}_{Subsystem\ C} cos\theta \underbrace{(1+S)^{-n2}}_{Subsystem\ D} \underbrace{(1+S)^{-4n1}}_{Subsystem\ E} \right) \right) dS \tag{34}$$

Eq. 34 can be written briefly as Eq. 35,

$$\theta = \int \left(A \left(-\frac{d^2\theta}{dS^2}\ B - \ C\ cos\theta\ D\ \ E \right) \right) dS \tag{35}$$

After finding the θ value in Eq. 35, x and y values at each point of the beam are obtained from Eqs. 6 and 7 as Eqs. 36 and 37, respectively.

$$y = \underbrace{\int sin\theta\, dS}_{Subsystem\ F} \tag{36}$$

$$x = \underbrace{\int cos\theta\ dS}_{Subsystem\ G} \tag{37}$$

While solving a differential equation with Matlab/Simulink, the blocks in the library are brought to the work area by drag and drop method and combined to define the equation. Although it is very easy to define the initial conditions in solving the differential equation with Matlab/Simulink, the boundary conditions needed in the differential equation expressing the beam problem cannot be entered. Therefore, this problem was overcome by combining this method with the DQM. Fig. 5 shows the design of Eqs. 34, 36, and 37 using CM in the Matlab/Simulink environment.

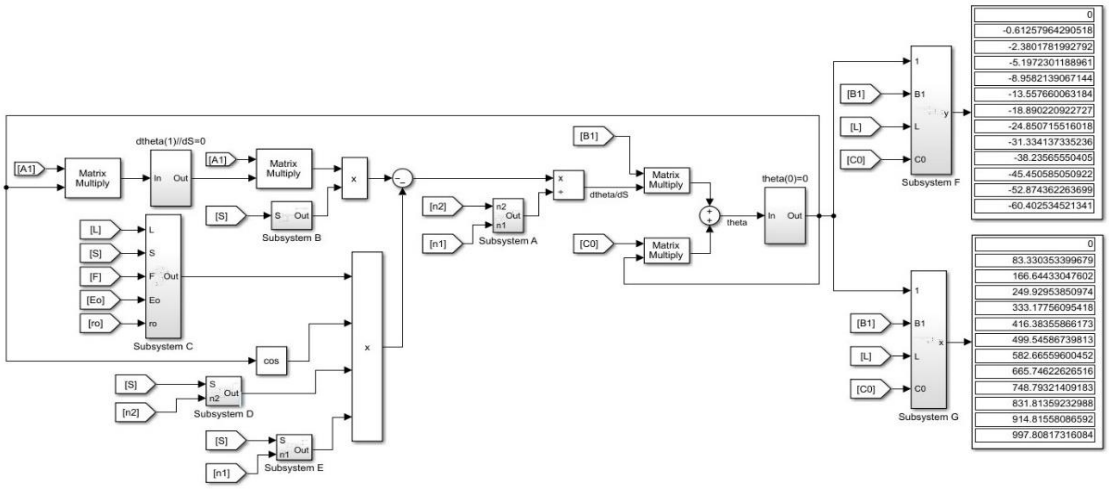

Figure 5. Block diagram of Eqs. 34, 36 and 37

First of all, the four operations in Eq. 34 are performed by combining the necessary blocks (sum, subtract, etc.), and the integral and derivative operations are performed using the weight coefficients in DQM. The operations in Eqs. 36 and 37 are shown on the right side of the main block diagram. The constants and weighting coefficients shown in Fig. 5 are also defined as shown in Fig. 6.

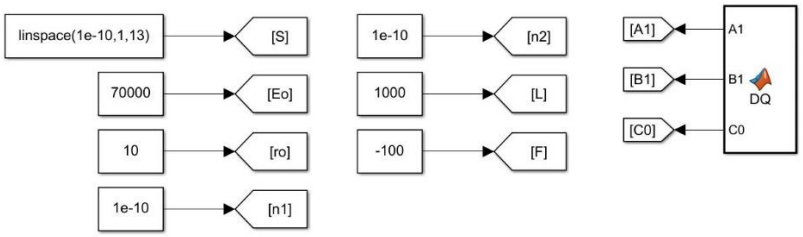

Figure 6. Constants and weighting coefficients in the previous figure

The weighting coefficients expressed in Sections 4.1 and 4.2 are defined in the DQ block shown in Fig. 6. As seen in the figure, the S value is normalized and taken within the range [0,1]. It is assumed that there are 13 sampling points in the beam. In addition, the subsystems shown in Fig. 5 are given in Figs. 7-13, respectively.

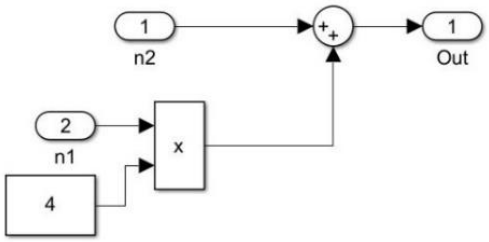

Figure 7. Block diagram of Subsystem A

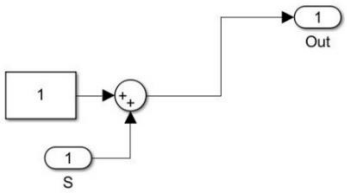

Figure 8. Block diagram of Subsystem B

Subsystems A and B given in Eq. 34 are shown in Figs. 7 and 8. Subsystem A is the denominator of the fractional expression. The other subsystems C, D, E, F, and G are shown in Figs. 9-13, respectively.

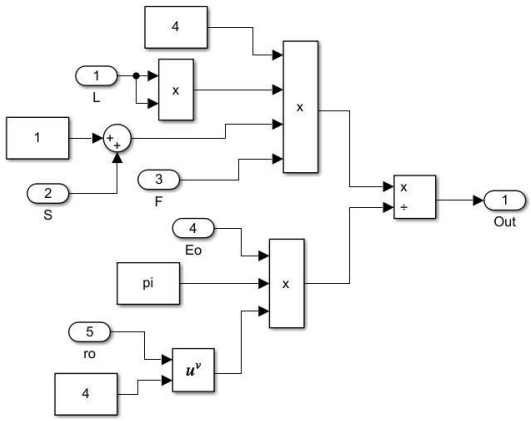

Figure 9. Block diagram of Subsystem C

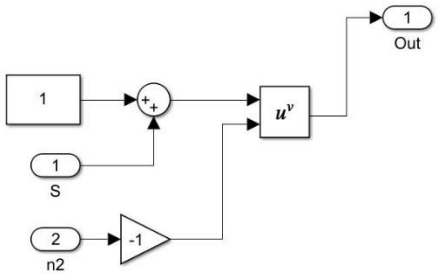

Figure 10. Block diagram of Subsystem D

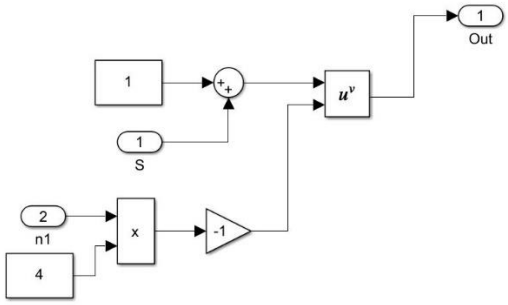

Figure 11. Block diagram of Subsystem E

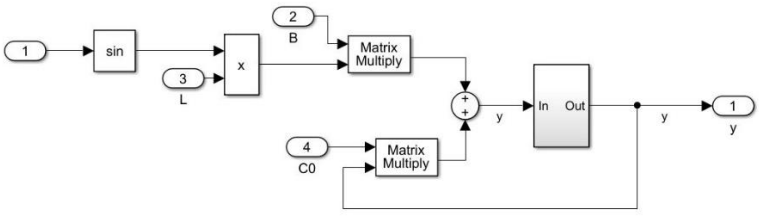

Figure 12. Block diagram of Subsystem F

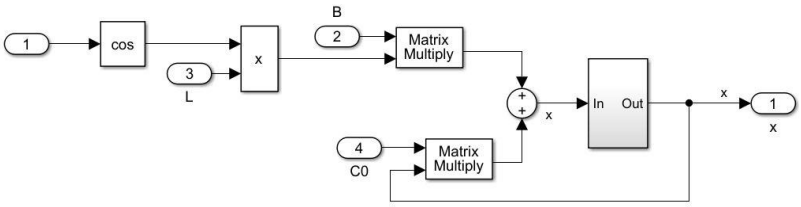

Figure 13. Block diagram of Subsystem G

Additionally, the subsystems where boundary conditions are entered, as seen in the main block diagram, are provided in Fig. 14.

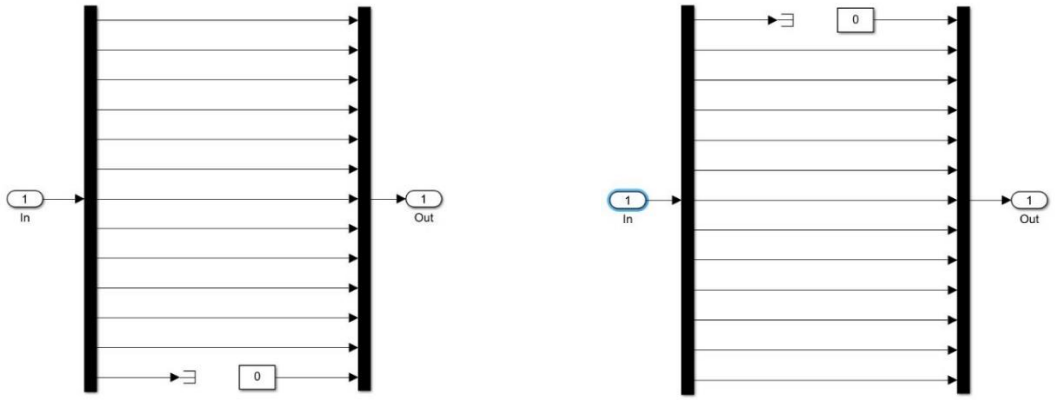

(a) $\frac{d\theta(1)}{ds} = 0$ **(b)** $\theta(0) = 0$

Figure 14. Block diagrams of boundary conditions.

As mentioned above, assuming that there are 13 sampling points in the beam, the incoming signal has been divided into 13 branches and later merged. The boundary condition is entered from the relevant sampling point.

5. FINITE ELEMENT-BASED SOLUTION

In order to verify the results obtained with CM, the problem is also solved with SolidWorks and Ansys-Workbench programs. SolidWorks program can make three-dimensional designs of structures. In addition, the Simulation module in the SolidWorks program allows different analyses of structural elements. Furthermore, the Ansys-Workbench program has also the capability to perform various analyses on structural elements. In this study, static analysis including large displacements is performed in both programs. In both programs, the uniform model is obtained before analysis. In the study, a three-dimensional solid beam model is used in the SolidWorks program and a one-dimensional line beam model is used in the Ansys-Workbench program for ease of definition. These models are shown in Fig. 15.

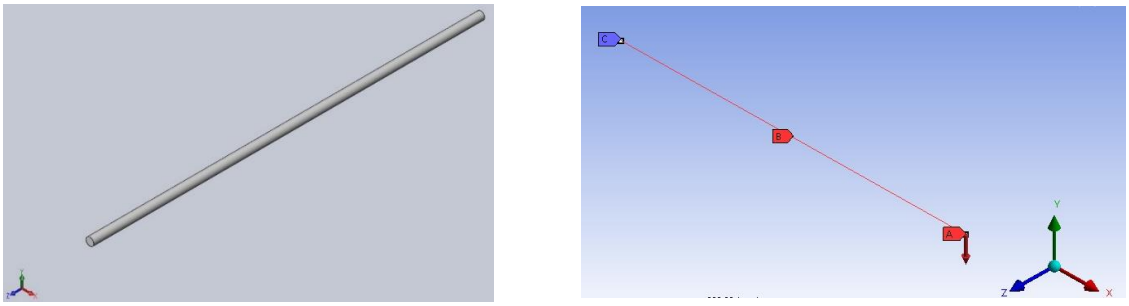

(a) Solid beam model in SolidWorks. **(b)** Line beam model in Ansys-Workbench.

Figure 15. Beam models.

After the uniform models are obtained in both programs, the material definition process is carried out. For this purpose, special material definition is made in both programs. Eq. 2 is taken as a basis when defining the special material. After the material is defined, the meshing process should be

done. In finite element-based programs, the meshing process needs to be carried out. The meshing process performed in both programs is shown in Fig. 16. As a result of the meshing process, the meshed model has 11707 nodes and 6555 element numbers in the SolidWorks program, and 201 nodes and 100 element numbers in the Ansys-Workbench program.

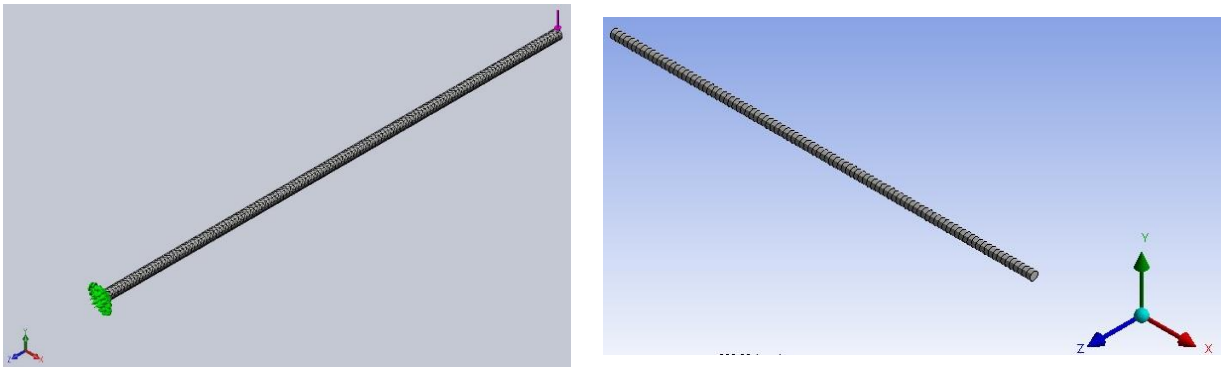

(a) Meshed model in SolidWorks. **(b)** Meshed model in Ansys-Workbench.

Figure 16. Meshed models.

Clamped boundary condition is applied at one end and a singular load is applied at the other end of the meshed models. The static analysis is then started. The models obtained as a result of the analysis are given in Fig. 17.

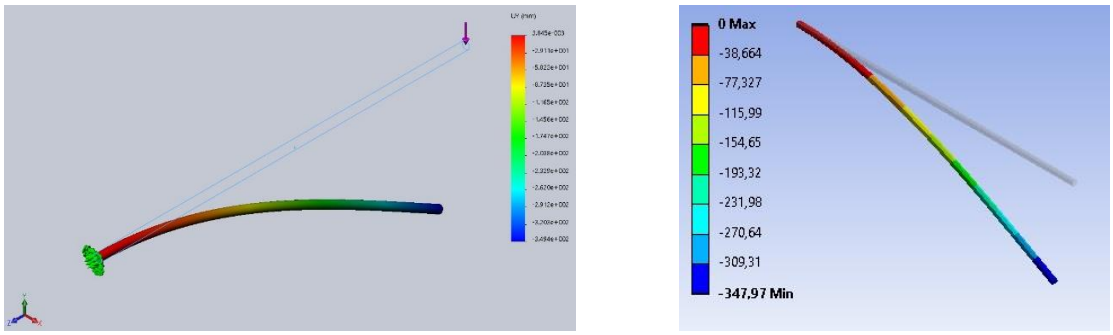

(a) The model after analysis in SolidWorks. **(b)** The model after analysis in Ansys-Workbench.

Figure 17. The models after analysis.

6. RESULT AND DISCUSSION

In this study, a large deflection analysis of a functionally graded beam using the CM is carried out. Moreover, especially, the effects of increasing the force applied to the endpoint of the beam, changing the material index, and changing the beam cross-section on the large deflection of the beam are investigated. Also, the results obtained with CM are compared with the results obtained from SolidWorks and Ansys-Workbench programs for comparison.

6.1 Effect of Force

The force applied to the end of the beam is increased to see the effect of the force magnitude on the large deflection of the beam. The force is taken as 100 N, 200 N, 400 N, 800 N, and 1600 N, respectively. Additionally, when examining the force effect, it is assumed that the indexes *n1* and *n2* are taken to be equal to zero. Hence, from Eqs. 1 and 2, *r(s)* and *E(s)* are equal to r_o and E_o respectively. In this study, the radius r_o is constant and equal to 10 mm. As for E_o elasticity modulus,

the material of the beam is assumed to be homogenous, isotropic Aluminum, and its properties are given in Table 1.

Table 1. The material properties of Aluminum

Material	Elasticity Modulus [MPa]	Density [kg/m^3]	Poisson's Ratio
Aluminum	70000	2700	0.3

Fig. 18 shows the behavior of large deflection of the beam under various loads. As can be seen in Fig. 18(a), the beam contains 13 sampling points. The *x* and *y* coordinates of these points are obtained from the CM for the loads mentioned above. Fig. 18(b) shows the large deflection in the *x* and *y* directions of the free end of the beam for given loads.

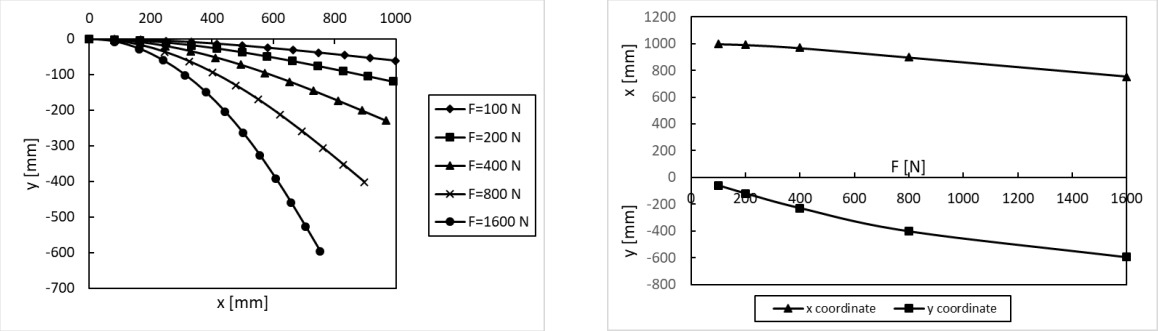

(a) Large deflection profiles. **(b)** Coordinates of the free end.

Figure 18. The large deflection behavior under various loads.

As shown in the figures, the applied forces are chosen twice the previous one each time. The deflection in the *y* coordinate of the free end of the beam is -60.4025 mm when the force is equal to 100 N, and -595.5787 mm when the force is equal to 1600 N. Therefore, when the force increases by 16 times, the deflection value increases by approximately 9.86 times. As for the variation in the *x* coordinate of the free end of the beam, it is 997.8082 mm when the force is equal to 100 N, and 753.1908 mm when the force is equal to 1600 N. The displacement in the *x* coordinate of the free end of the beam decreases by approximately 1.33 times. In other words, as seen in Fig. 18(b), the position in the y coordinate increases towards to negative direction gradually as the applied force increases. On the other hand, the position in the x coordinate decreases slightly until the force reaches 400N and then decreases rapidly.

6.2. Effect of Radius

In order to examine the effect of variation in the cross-sectional area of the beam in the longitudinal direction on large deflection, the radius of the beam is given depending on *s* as seen in Eq. 1. *n1* in this equation is the geometric index, and the variation in beam radius for various values of *n1* is given in Fig. 2. *n1* values are taken as -0.3, -0.15, 0, 0.15, 0.3 in this study. As seen in Fig. 2, when the value of *n1* is equal to zero, the radius of the beam is 10 mm, and the cross-sectional area of the beam is constant. At negative values of the geometric index *n1*, the radius decreases from the clamped end to the free end, and when it is positive, it increases. As for the material index *n2*, it is taken as 0.5. Therefore, the material considered is FGM.

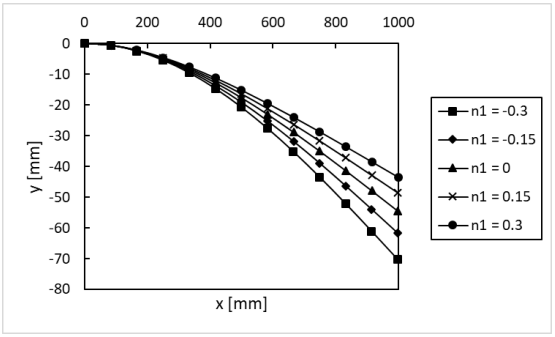

(a) Large deflection profiles.

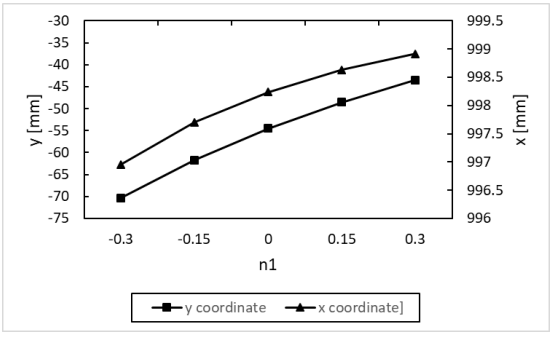

(b) Coordinates of the free end.

Figure 19. Variation in large deflection with geometric index.

The effect of variation in the geometric index on the large deflection is shown in the two figures above. While examining this effect, it is assumed that the magnitude of the force applied from the free end of the beam is 100 N. When Fig. 19(a) is examined, as expected, the large deflection value increases more as the *n1* value decreases. Because, as the *n1* value decreases, the cross-sectional area of the beam decreases gradually in the longitudinal direction. Fig. 19(b) shows the change of the *x* and *y* coordinates of the free end of the beam with the geometric index *n1*. As can be seen from the figure, the change in both the *x* and *y* coordinates of the free end of the beam increased as the *n1* value decreased.

6.3 Effect of Material

As seen in Fig. 3, as the material index (*n2*) changes, the content of the beam material also changes. For positive values of *n2*, the material of the clamped end of the beam becomes *Al*, while the free end is a material with a higher modulus of elasticity than *Al*. When *n2* is equal to zero, the beam material becomes pure *Al*. When *n2* takes a negative value, the clamped end of the beam is again *Al*, but unlike the first case, the free end is a material with a lower modulus of elasticity than *Al*. When examining this effect, *n1* and *F* values are taken as -0.5 and 100 N, respectively. As for *n2* values, they are taken as -0.7, -0.4, 0, 0.4, 0.7.

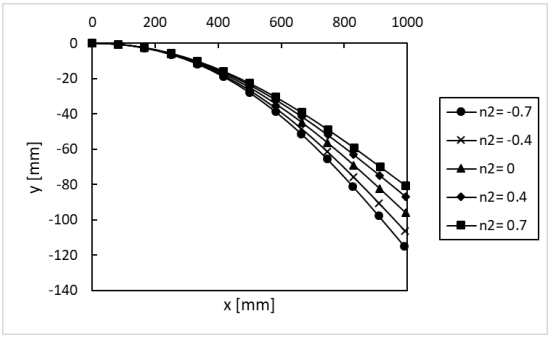

(a) Large deflection profiles.

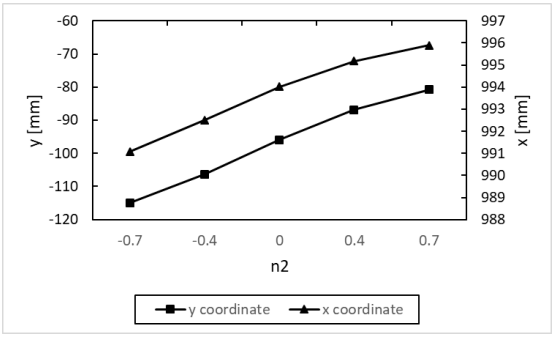

(b) Coordinates of the free end.

Figure 20. Variations in large deflection with material index.

Fig. 20 shows the effect of the material index on the large deflection behavior of the beam. When Fig. 20 (a) is examined, beams with positive *n2* values deflect less as expected, since the modulus of elasticity directly affects the large deflection of the beam. Fig. 20(b) shows the *x* and *y* coordinates of the deflection of the free end of the beam for different *n2* values. As seen in the figure, the change in both coordinates increases as the *n2* value decreases.

6.4 Comparison

In this study, the large deflection behavior of a functionally graded variable cross-section beam is investigated using CM. In order to prove the accuracy of the results obtained with CM, the problem is solved by modeling with SolidWorks-Simulation and Ansys-Workbench programs. Both programs mentioned here are based on the finite element method in their calculations. For comparison purposes, solutions are made in all three methods for different force values by considering a beam of *n1*=0 and *n2*=1. Table 2 shows the comparison of results obtained from CM and Finite Element based programs (FEBP).

Table 2. Comparison of results obtained from CM and Finite Element based programs

Method	Axis	Force [N]				
		50	100	400	800	1600
Combining Method (CM)	x	999.64220	998.57300	978.40620	925.78940	801.32990
	y	-24.77620	-49.46500	-191.32000	-349.32700	-550.59300
SolidWorks Simulation	x	999.29280	997.87800	975.81000	921.50000	794.90000
	y	-24.74000	-49.41000	-191.30000	-349.40000	-552.80000
Ansys Workbench	x	999.64580	998.58720	978.61100	926.40000	802.46000
	y	-24.65300	-49.22100	-190.43000	-347.97000	-549.2700
% CM-Solid Difference	x	0.03496	0.06962	0.26571	0.46440	0.80563
	y	-0.14603	-0.11129	-0.01043	-0.02086	-0.40011
% CM-Ansys Difference	x	0.00036	0.00142	0.02093	0.06593	0.14093
	y	-0.49831	-0.49454	-0.46625	-0.38926	-0.24051

The following formula was used when calculating the differences between the results obtained from CM and Finite Element based programs.

$$Percentage\ Difference = 100\ x\ \frac{|\mathrm{FEBP} - \mathrm{CM}|}{\left(\frac{\mathrm{FEBP} + \mathrm{CM}}{2}\right)} \tag{38}$$

When the percentage differences in the table are examined, it is seen that the results obtained with CM are very close to the results obtained with FEBP. When the results are examined, it is seen that the differences in the x coordinate are lower in the one-dimensional finite element analysis, and the differences in the y coordinate are lower in the three-dimensional finite element analysis.

7. CONCLUSION

The numerical large deflection solution of a FG beam with variable cross-section is overcome by using CM in this study. Additionally, the problem under consideration is also solved using two finite element-based programs, and a comparison is made. As a result of the numerical analysis, the following results are obtained.

- By increasing the force applied from the free end of a beam with C-F boundary conditions, the y coordinate of the position of the free end of the beam gradually decreases, while the x coordinate decreases slightly until a certain value and decreases rapidly after this value.

- As the cross-section of a beam with C-F boundary conditions decreases from the clamped end to the free end, the large deflection value increases proportionally compared to the constant cross-sectional beam.
- When an FG beam is designed in such a way that the elasticity modulus decreases from the clamped end to the free end, the large deflection amount obtained is greater than the homogenous isotropic beam whose elasticity modulus is not reduced.
- In comparison with the results obtained from finite element-based programs, CM is recommended because it can be easily used in solving geometric nonlinear problems.
- It is seen from the results that the differences in the x coordinate are lower in the one-dimensional finite element analysis, but the differences in the y coordinate are lower in the three-dimensional finite element analysis.
- When the extreme values of the differences between the results obtained from the CM and finite element methods are examined, it is obtained as 0.80563 percent for 1600 N in the x coordinate, while it is -0.49831 percent for 50 N in the y coordinate.

8. CONFLICT OF INTEREST

Authors approve that to the best of their knowledge, there is not any conflict of interest or common interest with an institution/organization or a person that may affect the review process of the paper.

9. AUTHOR CONTRIBUTION

Ersin DEMİR; Determining the concept and design process of the research, Data Collection, Data analysis and interpretation of the results, Preparation of the manuscript, Critical analysis of the intellectual content, Final approval and full responsibility. Hasan ÇALLIOĞLU; Determining the concept and design process of the research, Data analysis and interpretation of the results, Critical analysis of the intellectual content. Zekeriya GİRGİN; Management of the concept and design process of the research

10. REFERENCES

Belendez T., Neipp C., Belendez A., Large and small deflections of a cantilever beam. European Journal of Physics 23, 371-379, 2002.

Brojan M., Cebron M., Kosel F., Large deflections of non-prismatic nonlinearly elastic cantilever beams subjected to non-uniform continuous load and a concentrated load at the free end. Acta Mechanica Sinica 28(3), 863-869, 2012.

Dado M., Al-Sadder S., A new technique for large deflection analysis of non-prismatic cantilever beams. Mechanics Research Communications 32, 692-703, 2005.

Davoodinik A.R., Rahimi G.H., Large deflection of flexible tapered functionally graded beam. Acta Mechanica Sinica 27(5), 767-777, 2011.

Demir E, A numerical study on the large displacement in a functionally graded beam under thermal effect. Journal of Materials and Mechatronics: A 4(2), 492-503, 2023.

Girgin Z., Aysal F.E., Bayrakçeken H., Large deflection analysis of prismatic cantilever beam comparatively by using Combing method and iterative DQM. Journal of Polytechnic 23 (1), 111-120, 2020.

Girgin Z., Combining differential quadrature method with simulation technique to solve non-linear differential equations. International Journal for Numerical Methods in Engineering 75, 722-734, 2008.

Girgin Z., Combining modified integral quadrature method with simulation technique to solve nonlinear initial and boundary value problems. International Journal of Nonlinear Sciences & Numerical Simulation 10(4), 475-482, 2009.

Girgin Z., Yilmaz Y., Demir E., A Combining method for solution of nonlinear boundary value problems. Applied Mathematics and Computation 232, 1037-1045, 2014.

Horibe T., Mori K., Large deflections of tapered cantilever beams made of axially functionally graded material. Bulletin of the JSME Mechanical Engineering Journal 5(1), 1-10, 2018.

Hu Y.J., Liu M., Zhu W., Jiang C., An adaptive differential quadrature element method for large deformation contact problems involving curved beams with a finite number of contact points. International Journal of Solids and Structures 115–116, 200-207, 2017.

Kang Y.A., Li X.F., Large deflections of a non-linear cantilever functionally graded beam. Journal of Reinforced Plastics and Composites 29(12), 1761-1774, 2010.

Kien N.D., Large displacement response of tapered cantilever beams made of axially functionally graded material. Composites Part B 55, 298-305, 2013.

Koizumi M., The concept of FGM. Ceramic Transactions, Functionally Gradient Materials 34, 3-10, 1993.

Kurtaran H., Large displacement static and transient analysis of functionally graded deep curved beams with generalized differential quadrature method. Composite Structures 131, 821-831, 2015.

Li Z., Huang D., Yan K., Xu Y., Large deformation analysis of functionally graded beam with variable cross-section by using peridynamic differential operator. Composite Structures 279, 1-13, 2022.

Lin X., Huang Y., Zhao Y., Wang, T., Large deformation analysis of a cantilever beam made of axially functionally graded material by homotopy analysis method. Applied Mathematics and Mechanics (English Edition) 40(10), 1375-1386, 2019.

Nguyen D.K., Bui T.T.H., Tran T.T.H., Alexandrov, S., Large deflections of functionally graded sandwich beams with influence of homogenization schemes. Archive of Applied Mechanics 92, 1757-1775, 2022a.

Nguyen V.X., Nguyen K.T., Thai S., Large deflection analysis of functionally graded beams based on geometrically exact three-dimensional beam theory and isogeometric analysis. International Journal of Non-Linear Mechanics 146, 1-16, 2022b.

Saraçoğlu M.H., Güçlü G., Uslu F., Deflection analysis of functionally graded equal strength beams. European Mechanical Science 6(2), 119 - 128, 2022.

Saraçoğlu M.H., Güçlü G., Uslu F., Static Analysis of Orthotropic Euler-Bernoulli and Timoshenko Beams with Respect to Various Parameters 8(2), 628 - 641, 2019.

Sitar M., Kosel F., Brojan M., Large deflections of nonlinearly elastic functionally graded composite beams. Archives of Civil and Mechanical Engineering 14, 700-709, 2014.

Soleimani A., Large deflection of various functionally graded beam using Shooting Method. Applied Mechanics and Materials 110-116, 4705-4711, 2012.

JOURNAL of
MATERIALS and MECHATRONICS:A

e-ISSN 2717-8811
JournalMM, 2024, 5(1), 106-116
https://doi.org/10.55546/jmm.1460140

Araştırma Makalesi / Research Article

Effect of Cold Compaction Pressure on Porous NiAl Articles Produced by Using Space Holder Urea via VCS

Gülizar SARIYER [1], Hasan Erdem ÇAMURLU [2*]

[1]Akdeniz University, Faculty of Science, Department of Space Sciences and Technologies, Antalya, Turkey,
ORCID ID: https://orcid.org/0000-0001-7754-4549, glzrysn@gmail.com
[2*] Akdeniz University, Faculty of Engineering, Department of Mechanical Engineering, Antalya, Turkey,
ORCID ID: https://orcid.org/0000-0003-3170-4492, erdemcamurlu@gmail.com

Geliş/ Received: 27.03.2024**;** **Revize/Revised:** 09.05.2024 **Kabul / Accepted:** 12.05.2024

ABSTRACT: Porous NiAl samples were obtained by using 20, 40, 60 vol.% space holder urea particles. The urea particle size was in the range of 150-300 μm. Pressures of 50, 100, 200 and 300 MPa were applied by cold press to the mixtures formed by nickel, aluminum, preformed NiAl powders and urea particles. The dimensions, macrostructure, microstructure and compressive strength of the parts produced with different cold compaction pressures were analyzed after volume combustion synthesis (VCS). The aim of the study is to determine the cold compaction pressure which provides the closest dimensional changes after VCS, in samples having different urea amounts. These samples will be used for forming a multi-stack article in a further study. Since a high difference in dimensional change of different layers during VCS will lead to cracking and separation, similar dimensional change is required for different layers in a multi-stack sample design. The samples which were cold pressed with 300 MPa pressure sometimes contained cracks after they were taken out of the die after cold pressing or after VCS. Therefore, they could not be subjected to characterization. The closest dimensional change and higher compressive strength values after VCS were obtained in samples having different urea contents, when they were cold pressed at 200 MPa. The highest mean compressive strength (218.8±29.5 MPa) was attained in the sample which was prepared with 20% urea particles and which was cold compacted with 200 MPa.

Keywords: NiAl, Combustion synthesis, Space holder method, Porous intermetallic

1. INTRODUCTION

Porous materials are produced using spacer method, gas expansion method and chemical reaction techniques (Michailidis and Stergioudi, 2011; Kanetake and Kobashi, 2006). They have been widely used in fields such as medical, biological, energy saving, chemical industry due to their organizable permeability, thermal shock resistance, controlled pore size properties (Qin et al., 2016).

*Sorumlu yazar / Corresponding author: erdemcamurlu@gmail.com
Bu makaleye atıf yapmak için /To cite this article

Sarıyer, G., Çamurlu, H. E. (2024). Effect of Cold Compaction Pressure on Porous NiAl Articles Produced by Using Space Holder Urea via VCS. Journal of Materials and Mechatronics: A (JournalMM), 5(1), 106-116.

NiAl intermetallic has attracted attention as a light weight material that can be used at high temperatures due to its high temperature strength and low specific gravity (Dey, 2003).

It is known that the porosity and pore size of the material decrease with increasing pressure in the production of porous materials through powder metallurgy methods (Gülsoy and German, 2008; Dessai et al., 2013). Gao et al. (2015) produced the FeAl intermetallic using the reactive synthesis method by applying cold compaction pressures between 60 and 360 MPa. The effect of pressure on the pore structure of the obtained porous FeAl intermetallics was investigated. The manufactured parts were sintered at a sintering a temperature of 1200 °C for 60 minutes. Due to the Kirkendall effect (Gao et al., 2015) between Fe and Al elements, a large number of pores were produced along the diffusion direction of the Al element as Al atoms diffuse faster than Fe atoms. In addition, since the yield strength of pure Al is lower than that of Fe, Al particles undergo plastic deformation and take an elongated shape along the Fe particles. It was observed that the maximum pore size decreased by 33.7% when the pressure was increased from 60 MPa to 360 MPa. It has been reported (Gao et al., 2015) that by increasing the pressure, the pores between the particles and the diffusion distance can be reduced, and as a result, the degree of solid and liquid reaction may change. It was concluded (Gao et al., 2015) that the open porosity, maximum pore size and permeability of the porous FeAl intermetallics produced by reactive synthesis can be reduced with increasing pressure. No information was provided on the mechanical properties of the obtained samples.

It is known that the strength of porous intermetallics decreases with increasing porosity (Jiang et al., 2021). In the study of Jie et al. (2011), Ni+Al+urea mixtures were cold pressed at 200 MPa for compaction. The reaction was carried out in SHS mode. Pore size and amount of 0.4-2.0 mm and 58-85%, have been reported, respectively. The sample with 58% porosity exhibited a compressive strength of 27 MPa. Strength values decreased with increasing amount of porosity. Huang et al. (2020) used elemental Mo, Si and B powders and NH_4HCO_3 particles in the size range of 48 μm to 230 μm to form pores. A pressure of 300 MPa was applied to the green compacts. In the study, the size of the small pores was 0.1–10 μm, and the size of the large pores was obtained as 10–300 μm. It was observed that the compressive strength decreased rapidly from 329 MPa to 87.3 MPa at 40 vol.% porosity, as compared to 0 vol.%.

In this study, experiments were carried out to determine the cold compaction pressure for the production of porous NiAl parts. For this purpose, parts were produced by applying cold compaction pressure of 50, 100, 200 and 300 MPa by using nickel, aluminum, preformed NiAl (30 vol.%) powder and urea particles as a space holder. The aim of the study is to determine the cold compaction pressure which provides the closest dimensional changes after VCS, in samples having different urea amounts.

2. MATERIALS AND METHODS

The effect of cold compaction pressure on the dimensional change and strength of the porous NiAl parts produced via VCS was investigated. The aim of the study was to determine the cold compaction pressure which provided the closest dimensional changes after VCS, in samples having different urea amounts. Close dimensional change is necessary to design a multi-stack sample having layers containing 20, 40 and 60 % porosity. Because a large difference in the dimensions change of different layers during VCS of a multi-stack sample would lead to cracking and separation of layers.

2.1 Materials Used

In this study, Nickel (Merck, <10 μm, 99%), aluminum (Alpha Aesar, <10 μm, 99.5%), preformed NiAl (Sarıyer and Çamurlu, 2022) powders and 150-300 micron sized urea (NH_4HCO_3

Merck) particles were used. It was observed that nickel powder consistsed of spherical agglomerates of around 10 micrometers in diameter. Aluminum powder consisted of irregular shaped non-faceted particles of 20 micrometer size. In order to preserve the shape of the produced samples in the volume combustion synthesis (VCS) process, 30 vol.% preformed NiAl powder was used as the thermal diluent in the samples. Preformed NiAl powder was obtained in this study through the reaction of Ni and Al powders. It was observed that preformed NiAl particles generally consisted of 5-10 micron sized particles.

2.2 Sample Preparation

Porous NiAl parts were prepared according to Equation (1). Nickel, aluminum, preformed NiAl and space holder urea particles were weighed on an analytical balance and mixed homogeneously in the mixing bowl. Preformed NiAl powder was used as thermal diluent since Equation (1) is highly exotermic. During VCS, the sample was seen to partially melt as a result of the high combustion temperature attained when thermal diluent is not utilized.

$$(a)\ Ni + (a)\ Al + (b)\ NiAl\ (preformed) = (a+b)\ NiAl \quad (1)$$

The powder mixture was transferred into a 10 mm diameter steel die was prepared in a cold press by applying three different pressures (50, 100, 200 and 300 MPa). Samples were coded according to their cold compaction pressure and their urea space holder particle content. For example, the sample code 50M20U refers to the sample which was cold compacted by using 50 MPa pressure and which contains 20% space holder urea particles. In order to dissolve the urea particles which were added to create pores, the parts were kept in distilled water for one day. They were dried at 65 ^{o}C for one day. Then, they were heated to 700 ^{o}C, at a heating rate of 10 ^{o}C/min in a tube furnace under argon atmosphere and volume combustion synthesis was accomplished.

2.3 Characterization

The parts obtained after volume combustion synthesis were subjected to compression test with a Shimadzu Autograph Universal Tension-Compression Device (50 kN) according to ISO 13314 standard. The compresive strength values of the materials produced with three different cold compaction pressures were measured. The produced porous NiAl parts were ground and polished on 600, 1200 and 3000 grit sandpaper. Then, the macro and micro structures of the samples were examined by stereo and optical microscope, respectively. The porosity values were calculated by using the dimensions and weight of the samples.

3. RESULTS AND DISCUSSION

3.1 Macrostructure

The macro images of the samples which were obtained by stereo microscope are presented in Figure 1. These images show the top circular side of the cylindrical samples, which were produced by using 20, 40 and 60% urea and by applying 50, 100 and 200 MPa cold compaction pressure. It was determined that the pores were generally homogeneously distributed and the volumetric pore ratio increased with increasing urea content. Parts in all systems were seen to retain their shapes. It was understood that the pore shape and dimensions were also preserved. It was found that the 30%

thermal diluent NiAl powder in the initial mixture was beneficial in this context. In a recent study which was conducted by Sarıyer and Çamurlu (2022), it was reported that addition of 30 % preformed NiAl was effective in preventing the melting of formed NiAl during VCS. Additionally, MgO powder was used as an inert thermal diluent in the synthesis of NiAl powder (Sarıyer and Çamurlu, 2024).

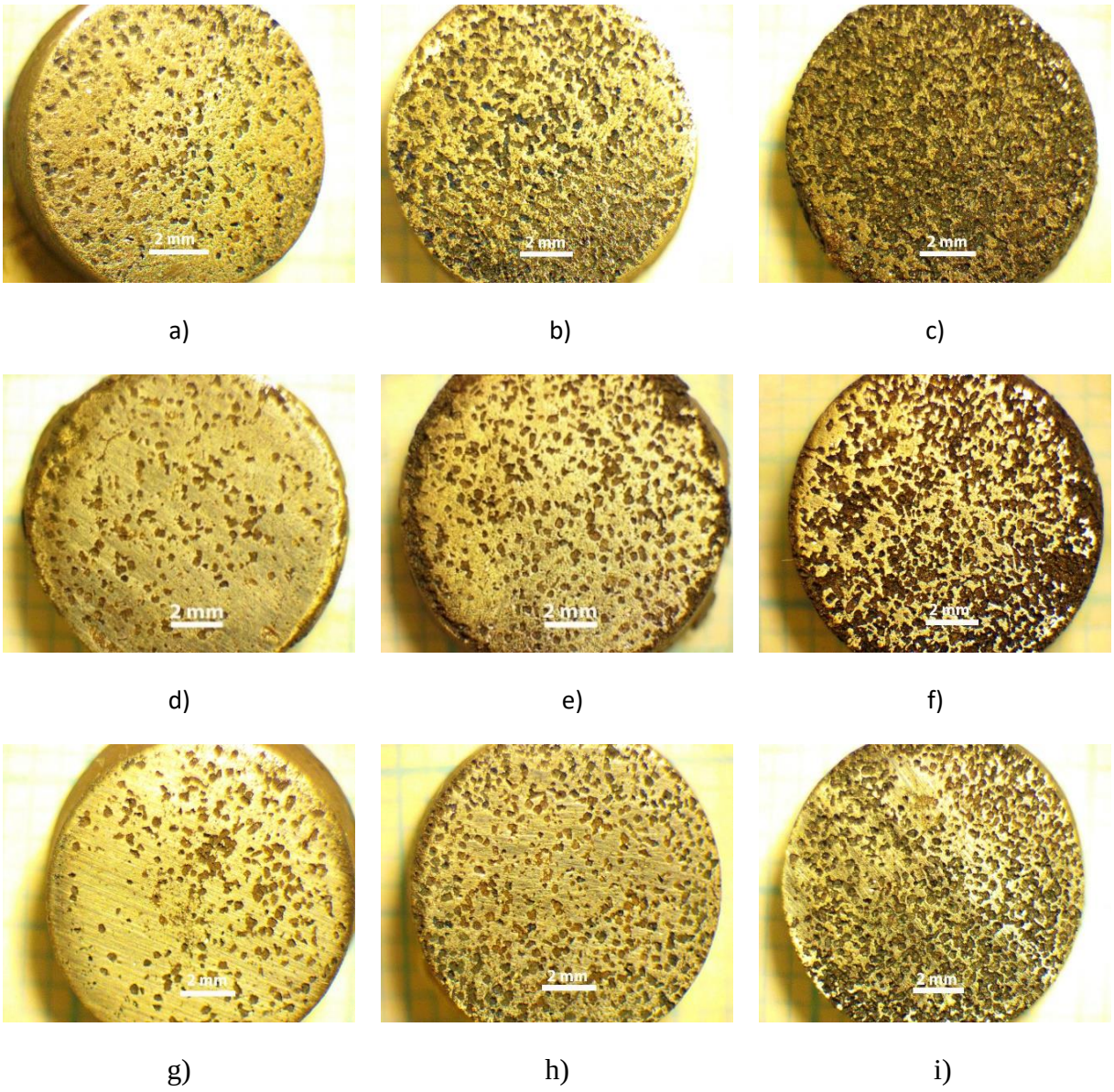

Figure 1. Macrostructure (stereo microscope) images of samples produced with different cold compaction pressure a) 50M20U , b) 50M40U, c) 50M60U, d)100M20U, e)100M40U, f)100M60U g) 200M20U, h) 200M40U, i) 200M60U

3.2 Microstructure

The microstructure images of the parts, which were cold compacted with 50, 100 and 200 MPa pressure and produced by using 40% space holder urea, are presented in Figure 2 (a-c), respectively. The large and small dark regions in these micrographs are pores and the light gray parts are the NiAl cell (or pore) walls around these pores. Two kinds of porosity were observed in the microstructure. The large pores, which have the same dimensions of the urea particles are referred to as primary pores and the small ones which are on the cell walls are secondary pores ((Shu et al. 2019; Jiang 2021). The primary pores are formed by the spaces left by space-forming urea particles. The secondary pores

were reported to form due to the presence of i) porosity in the green sample, ii) density difference between the reactant and product phases and also iii) due to Kirkendal effect (Jiao et al. 2021; Salamon and Mehrer, 2005).

In the microstructure examinations, it was observed that pore walls (or the cell walls) were less connected to each other and there were discontinuities in the post-VCS structure of the parts which were pressed at 50 MPa pressure. It was found that the cell walls of the parts pressed with 100 and 200 MPa were more continuous and less porous. This is believed to be due to the lower green density of the pellets when they are compacted with lower pressures. It can be seen in Table 1 that the amount of porosity before VCS was the highes when 50 MPa compaction pressure was applied. On the other hand, porosity of the green samples was seen to decrease with increasing compaction pressure (Table1). The discontinuous structure of the cell walls which was observed in the microstructure of the 50M samples can be explaned by the lower green density of these pellets. Similar resuls were observed in another system (FeAl) by Gao et al. (2015). It was proposed that the pores between the particles and the diffusion distance decreased by increasing the compaction pressure, thus lower porosity could be attained after VCS.

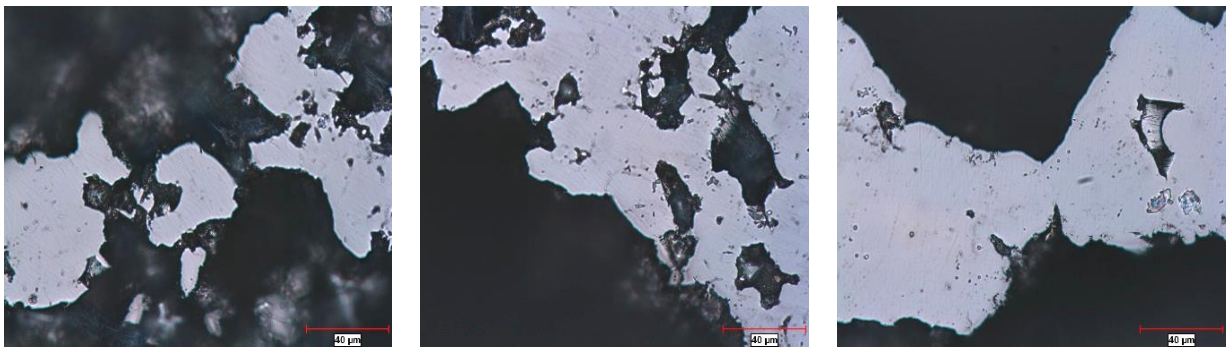

a) b) c)

Figure 2. Microstructure (optical microscope) images of the produced samples a) 50M40U, b) 100M40U c) 200M40U (500x)

3.3 Change in Porsity and Dimensions During VCS

Mean total porosity before and after VCS, and changes in diameter and height of the parts produced at different pressures (50, 100 and 200 MPa) are presented in Table 1 and Figure 3. It can be seen that the amount of porosity increased with increasing urea content in all the series, before and after VCS, as expected. Before VCS, it was observed that the total porosity amount in the green samples was higher than the amount of urea added. The difference is thought to be due to the fact that the Ni+Al parts (cell walls) of the green pellets are not fully dense and they contain pores (termed as the secondary pores) after cold compression. This difference decreases with increasing rate of space holder urea. For example, the porosity of the green sample which contained 20 % urea was 46.2%, whereas that of the sample which contained 60 % urea was 67.3, when they were compressed at 50MPa.

Before VCS, it was observed that the amount of pores in the green parts decreased with the increase in the cold compaction pressure. This effect was less pronounced in the green samples which contained 60% urea particles. These green samples (100M60U and 200M60U) exhibited similar porosity (about 62%) after compacting with 100 and 200 MPa pressure.

After VCS, an increase was observed in the average porosity of all samples. For example, the average porosity of the green pellet produced at 100 MPa cold compaction pressure and with 60 vol.% urea addition (100M60U) was 62.1% before VCS, while it was 66.9% after VCS. The increase in the

secondary pores is believed to be responsible for the overall porosity increase after VCS. Secondary pores are believed to form in the cell walls primariliy due to two reasons: i) density difference between the reactant and product phases and also ii) due to Kirkendal effect. The density of Ni is 8.90 g/cm^3, and that of Al is 2.70 g/cm^3 whereas that of NiAl is 5.90 g/cm^3. Aluminum particles, having a large volume, occupy most of the volume of the reactant mixture. When the VCS reaction is completed, the formed phase with less volume (higher density) causesa shrinkage inside the pellet. This results in the formation of the pores due to density difference (Jiang 2021). The formation of the secondary pores is believed to take place due to Kirkendal effect. According to this phenomena, the difference in the diffusion coefficient of the reactant phases results in an insufficient exchange of atom among these phases. The species with the higher diffusion coefficient accumulates at a higher rate in the other species, whereas the species with the lower diffusion coefficient creates voids and pores inside the other species (Jiao et al. 2021; Salamon and Mehrer, 2005). Gao et al. (2015) reported that majority of the pores FeAl were seen to form at the locations which were originally occupied by Al particles.

Table 1. The percentages of change in porosity and dimensions of porous parts produced at different pressures (50 MPa, 100MPa, 200MPa) using 20%, 40% and 60% space holder urea (150-300 micron) (PBV: Porosity Before VCS, SD: Standard Deviation, CH: Change in Height CD: Change in Diameter, PAV: Porosity After VCS)

Sample Code	PBV (%)	SD (%)	CH (%)	SD (%)	CD (%)	SD (%)	PAV (%)	SD (%)
50M20U	46.2	0.1	-4.79	0.93	-3.33	0.47	47.5	0
50M40U	55.4	0.3	-3.60	0.03	-1.63	0.03	58.4	0.3
50M60U	67.3	0.1	-1.91	0.67	-2.44	1.75	69.8	1.3
SD			1.45		0.85			
100M20U	41.1	0.4	-4.40	0.08	-1.94	0.29	44.5	0.4
100M40U	51.9	0.1	-3.59	0.06	-1.46	0.73	55.1	0.2
100M60U	62.1	0.3	-1.22	0.21	-0.57	0.52	66.9	1.5
SD			1.65		0.69			
200M20U	34.3	0.2	-1.00	0.83	-0.25	1.56	44.2	2.1
200M40U	47.4	0.2	-1.38	2.34	-0.70	2.04	56.2	2.9
200M60U	62.0	0	-0.69	1.40	-1.08	0.69	66.0	0.3
SD			0.35		0.42			

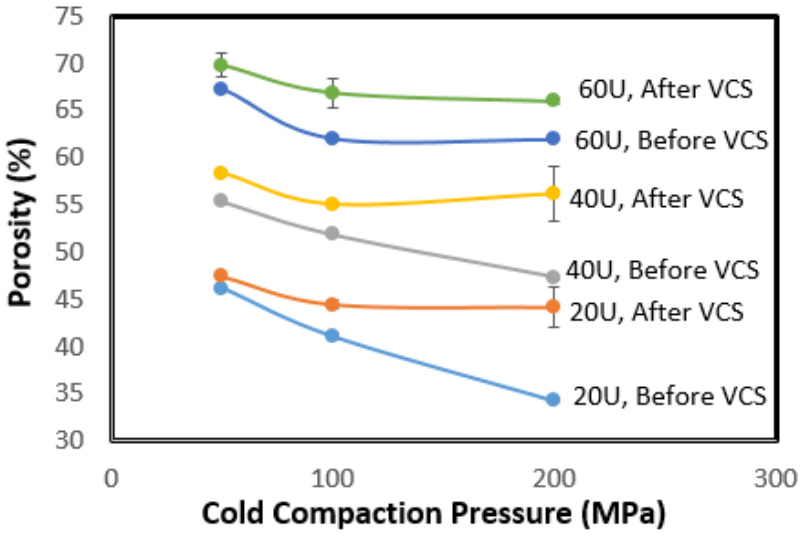

Figure 3. % changes in the porosity before and after VCS of samples produced at 50, 100 and 200 MPa cold compaction pressure using 20, 40 and 60 vol.% space holder urea

The changes in height and diameter of parts during VCS are presented in Figure 4 (a) and (b) as a function of cold compaction pressure. When the size changes of the parts produced by applying different cold compaction pressure are examined, it is understood that the change in height is below 4.8% and the change in diameter is below 3.3% in all systems. These largest dimensional change values occurred in the parts pressed with 50 MPa. In both graphs, it is seen that with increasing cold compaction pressure, large negative values approach to zero, indicating that the dimensional change decreases when the cold compaction pressure increases. During VCS, as a result of the increase in temperature, partial sintering of the product pellet occurs. Sintering involves diffusion, mass transport and decrease in the porosity. In powder metallurgy, during sintering the external dimensions of the sample decreases as a result of the decrease in the internal porosity (German, 2005). Therefore, when the porosity of the green sample is high, the shrinkage or the change in the dimensions of the sample is higher. The green samples which were produced by lower compaction pressure were seen to have higher amount of porosity before VCS (Table 1). Therefore, higher amount of shrinkage in the samples which were produced by lower compaction pressure is in accord with this explanation. Amount of shrinkage decreases when high compaction pressure is applied.

The change in height and diameter values of the parts containing different ratios of space holder urea which were compacted with 200 MPa are closer to each other than the parts which were compacted with 50 and 100 MPa. This situation is also understood from the standard deviation values of change in dimensions given for each compaction pressure value in Table 1. When the change in height and diameter are examined, the smallest absolute values (0.35 and 0.42, respectively) for the parts containing different ratios of urea were found in the samples compacted with 200 MPa.

A large difference in the dimensionsional change of different layers during VCS of a multi-stack sample would lead to cracking and separation of layers. Similar dimensional change is necessary to design a multi-stack sample having layers containing 20, 40 and 60 % porosity. It was seen from the dimensional changes that promising results were obtained for design of multi-stack samples.

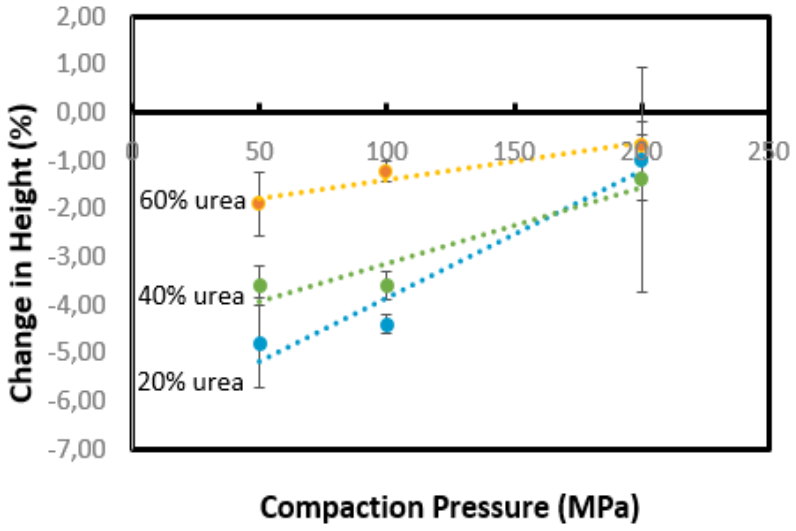

(a)

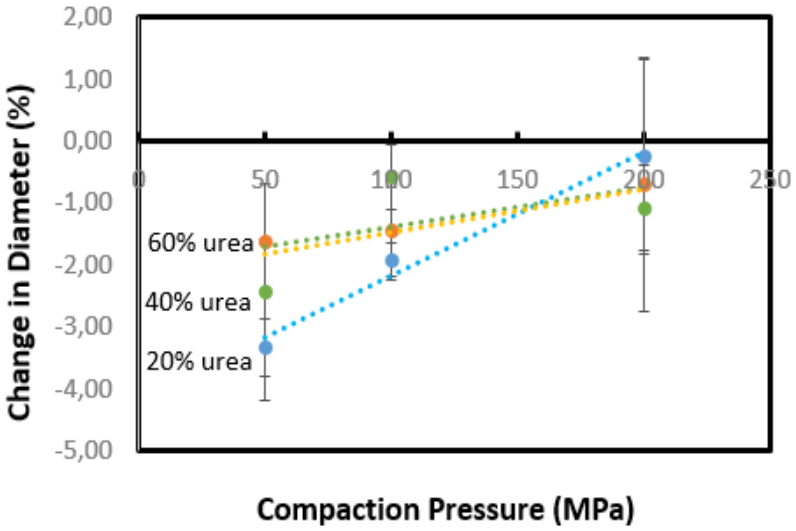

(b)

Figure 4. % changes in a) height and b) diameter during VCS of samples produced at 50, 100 and 200 MPa cold compaction pressure using 20, 40 and 60 vol.% space holder urea

3.4 Mechanical Properties

In Table 2 and Figure 5, strength values of samples cold compacted at different pressures (50, 100, 200 MPa) using 20, 40 and 60% space holder urea (150-300 microns) after VCS are presented. The samples which were cold pressed with 300 MPa pressure sometimes contained cracks after they were taken out of the die after cold pressing or after VCS. Therefore, they could not be subjected to characterization. This was attributed to the high springback effect that formed when high compaction pressure was applied (German, 2005).

The strength was observed to decrease with the increase in the amount of urea in each applied pressure group. The decrease in the strength was attributed to the increase in the amount of porosity. The density of a material is a chief trait to foresee its mechanical properties and permeability. As pointed out by Smith and Brown (1985) that density decreases (and porosity increases), mechanical properties decline and also permeability increases. It was stated that the mechanical traits of porous substances, like ductility, strength and fatigue life basically rely on the porosity and manufacturing method (Lenel, 1980; Eisenmann and Morgan, 2015).

It was observed in Table 1 that the amount of porosity was higher in the samples after VCS, when they were compacted with lower compaction pressure. Strength of materials was reported to decrease with increasing porosity due to the decrease in the load bearing cross section of the material when porosity is present. In addition, pores can act as stress concentrating regions under tensile forces, which also results in a decrease in the strength of the material (German, 2005). When the samples containing the same amount of space holder urea were cold compacted at different pressures, it was observed that the strength increased with increasing compacting pressure (Figure 5). This is due to the fact that higher compaction pressure results in lower amount of porosity after VCS, as can be seen in Table 1. It can be seen in Figure 5 that the strength values of the parts produced with 200 MPa cold compaction pressure are the highest. This result is in accord with the explanation that higher compaction pressure results in lower amount of porosity, which leads to higher strength.

Table 2. Strength values of samples cold pressed at different pressures (50, 100 and 200 MPa) and VCS applied using 30 vol.% preformed NiAl powder and 20, 40, 60% space holder urea

Cold Press Pressure (MPa)	Sample Code	Strength	Standard deviation
50	50M0U	216.76	94.43
	50M20U	109.90	16.89
	50M40U	56.90	3.14
	50M60U	18.67	0.27
100	100M0U	311.49	22.44
	100M20U	181.77	1.60
	100M40U	84.64	0.73
	100M60U	33.36	5.03
200	200M0U	290.54	75.98
	200M20U	218.86	29.47
	200M40U	91.27	2.04
	200M60U	34.06	1.43

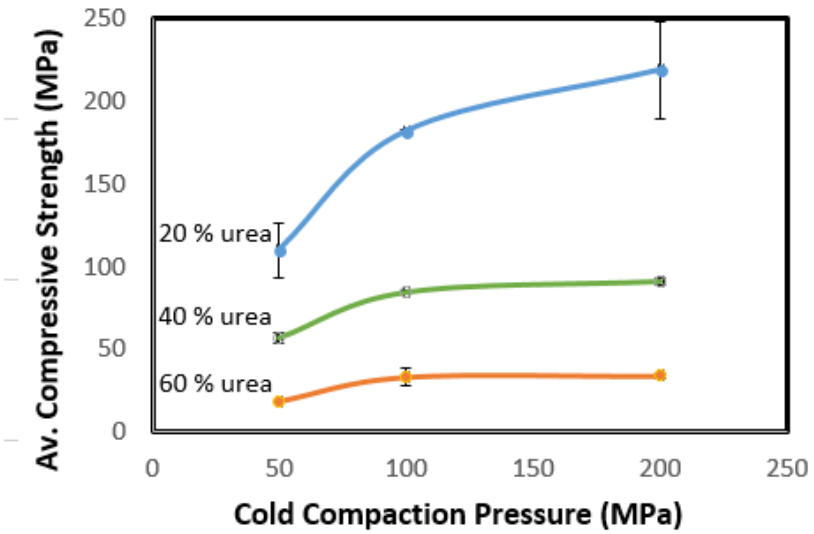

Figure 5. Strength values of the samples (after VCS) which contained 20, 40 and 60% space holder urea, as a function of compacting pressure

4. CONCLUSION

The results obtained in this study are summarised below:

- Porous NiAl samples were obtained by using 20, 40, 60 vol.% space holder urea particles and pressures of 50, 100, 200 and 300 MPa were applied by cold press to the mixtures formed by nickel, aluminum, preformed NiAl powders and urea particles. The samples which were cold pressed with 300 MPa could not be characterized since they contained cracks. This was attributed to the high springback effect that formed when high compaction pressure was applied.
- The dimensions, macrostructure, microstructure and compressive strength of the parts produced with different cold compaction pressures were analyzed after volume combustion synthesis (VCS). The compressive strength values of the porous NiAl samples after VCS were the highest when the samples were cold pressed with 200 MPa as compared to lower cold compaction pressures. This was attributed to the lower porosity content of these samples, as compared to the ones obtained with lower compaction pressures.
- The aim of the study is to determine the cold compaction pressure which provides the closest dimensional changes after VCS, in samples having different urea amounts. Minimum and the closest dimensional change values after VCS were obtained with in samples having different urea contents, when they were cold pressed at 200 MPa. This was attributed to the lower shrinkage of these samples during VCS, as a result of their lower porosity amount. Lower porosity was achieved with high compaction pressure. Therefore, it was concluded that 200 MPa pressure was optimum for cold pressing a multi-stack sample having layers of different urea content.

5. ACKNOWLEDGEMENTS

Authors thank to Akdeniz University Scientific Research Projects Coordination Unit for supporting this study with Project No: FDK-2021-5653.

6. CONFLICT OF INTEREST

Author(s) approve that to the best of their knowledge, there is not any conflict of interest or common interest with an institution/organization or a person that may affect the review process of the paper.

7. AUTHOR CONTRIBUTION

Gülizar Sarıyer contributed in experimental preparation and characterization of the samples. Hasan Erdem Çamurlu contributed in design of the experiments, and analysis and interpretation of the results.

8. REFERENCES

Dessai R.R., Desa J.A.E., Sen D., Mazumder S., Effects of pressure and temperature on pore structure of ceramic synthesized from rice husk: A small angle neutron scattering investigation. Journal of Alloys and Compounds 564, 125-129, 2013.

Dey G.K., Physical metallurgy of nickel aluminides. Sadhana *28*, 247-262, 2003.

Eisenmann M. and Morgan R., Porous powder metallurgy technology, in ASM Handbook Volume 7: Powde Metallurgy, ASM International, 2015.

Gao H.Y., He Y.H., Shen P.Z., Jiang Y., Liu C.T., Effect of pressure on pore structure of porous FeAl intermetallics. Advanced Powder Technology 26(3),882-886, 2015.

Gülsoy H.Ö., German R.M., Production of micro-porous austenitic stainless steel by powder injection molding. Scripta Materialia 58(4), 295-298, 2008.

Huang Y., Zhang L., Wei S., Double-pore structure porous Mo–Si–B intermetallics fabricated by elemental powder metallurgy method using NH_4HCO_3 as pore-forming agent. Materials Research Express 7(9), 096518, 2020.

Jiang Y., He Y., Gao H., Recent progress in porous intermetallics: Synthesis mechanism, pore structure, and material properties. Journal of Materials Science & Technology, 74, 89-104, 2021.

Jiao X., Liu Y., Cai X., Wang J., Feng P., Progress of porous Al-containing intermetallics fabricated by combustion synthesis reactions: a review, Journal of Materials Science, 56, 11605 11630,2021

Jie W., Cui H.Z., Cao L.L., Gu Z.Z. Open-celled porous NiAl intermetallics prepared by replication of carbamide space-holders. Transactions of Nonferrous Metals Society of China 21(8), 1750-1754, 2011.

Kanetake N., Kobashi M., Innovative processing of porous and cellular materials by chemical reaction. Scripta Materialia 54(4), 521-525, 2006.

Lenel F.V., Powder metallurgy: principles and applications, Metal Powder Industry, 1980.

Lepage G., Albernaz F.O., Perrier G., Merlin G. 2012. Characterization of amicrobial fuel cell with reticulated carbon foam electrodes. Bioresource technology, 124: 199-207.

Michailidis N., Stergioudi F., Establishment of process parameters for producing Al-foam by dissolution and powder sintering method. Materials & Design 32(3), 1559-1564, 2011.

Qin J., Chen Q., Yang C., Huang Y., Research process on property and application of metal porous materials. Journal of Alloys and Compounds 654, 39-44, 2016.

German R.M., Powder Metallurgy and Particulate Materials Processing: The Processes, Materials, Products, Properties and Applications, Metal Powder Industries Federation, 2005.

Salamon M., Mehrer H., Interdiffusion, Kirkendall effect, and Al self-diffusion in iron-aluminium alloys, International Journal of Materials Research. 96 (1), 4–16, 2005

Sarıyer G., Çamurlu H.E., Effect of Diluent Amount on Properties of Porous NiAl. Gazi University Journal of Science Part A: Engineering and Innovation 9(4), 429-438, 2022.

Sarıyer G., Çamurlu H.E., Production and Characterization of Ni0.50 Al0.50 and Ni0.55 Al0.45 Powders by Volume Combustion Synthesis. Cumhuriyet Science Journal 45(1), 94-99, 2024.

Shu, Y., Suzuki, A., Takata, N.,Kobashi, M., Fabrication of porous NiAl intermetallic compounds with a hierarchical open-cell structure by combustion synthesis reaction and space holder method. Journal of Materials Processing Technology, 264, 182-189, 2019.

Smith, D. W. and Brown, E., Characterization of Controlled Density P/M Structures for Filtration Applications. Progress in Powder Metallurgy, 41, 653-667,1985.

Wu J., Yang Z.T., Cui H.Z., Wei N., Song X.J., Fabrication, Pore Structures and Mechanical Properties of $(TiB_2–Al_2O_3)$/NiAl Porous Composites. Acta Metallurgica Sinica (English Letters) 30(12), 1145-1154, 2017.

JOURNAL of
MATERIALS and MECHATRONICS:A

e-ISSN 2717-8811
JournalMM, 2024, 5(1), 117-129
https://doi.org/10.55546/jmm.1459415

Araştırma Makalesi / Research Article

Low Velocity Impact Behavior of Curved Composite Panels Reinforced with Different Types of Stiffeners Used in Air Vehicle

Tolunay DAĞ[1], Mehmet Ali GÜVENÇ[2*], Mesut UYANER[3]

[1] Iskenderun Technical University, Faculty of Aeronautics and Astronautics, Department of Aerospace Engineering, Hatay, Turkey, ORCID ID: https://orcid.org/0000-0003-1514-5336, tolunay.dag@iste.edu.tr
[2*] Iskenderun Technical University, Faculty of Aeronautics and Astronautics, Department of Aerospace Engineering, Hatay, Turkey, ORCID ID: https://orcid.org/0000-0002-4652-3048, mali.guvenc@iste.edu.tr
[3] Necmettin Erbakan University, Faculty of Aeronautics and Astronautics, Department of Aircraft Engineering, Konya, Turkey, ORCID ID: https://orcid.org/0000-0003-2743-2340, muyaner@erbakan.edu.tr

Geliş/ Received: 27.03.2024**;** **Revize/Revised:** 07.05.2024 **Kabul / Accepted:** 13.05.2024

ABSTRACT: This study aims to investigate the low-velocity impact behavior of curved composite plates commonly employed in aviation fuselage and wing surfaces using numerical methods. Layered plates fabricated from E-Glass Epoxy were reinforced with various types of stiffeners and subjected to impacts whit a 12 mm diameter impactor at a velocity of 2.5 m/s. The time-dependent variation of force and displacement on the stiffened curved plates resulting from the impact was analyzed. Furthermore, the temporal variation in the amount of energy absorbed by the plate was observed. The results indicate that plates reinforced with I, T, and blade-type stiffeners absorbed 35.78%, 38.11%, and 37.78% of the impact energy, respectively. Among these, plates with T-type reinforcements exhibited the least post-impact deformation. Particularly noteworthy is the permanent deformation of 3.7 mm experienced by the plate reinforced with blade-type stiffeners.

Keywords: Curved plate, Impact behaviour, Low velocity impact, Stiffeners type

1. INTRODUCTION

Many impact types are studied on composite structures. Armors with low weight and high impact resistance are produced in impact events with speeds up to 1000 m/s, which are examined in the ballistic field (Aytav and Işık, 2023). In the field of aviation, in addition to ballistic impact tests,

*Sorumlu yazar / Corresponding author: mali.guvenc@iste.edu.tr
Bu makaleye atıf yapmak için /To cite this article

Dağ, T., Güvenç, M. A., Uyaner M. (2024). Low Velocity Impact Behavior of Curved Composite Panels Reinforced with Different Types of Stiffeners Used in Air Vehicle. Journal of Materials and Mechatronics: A (JournalMM), 5(1), 117-129.

the behavior of low-speed impact in composite materials is at the forefront. For a collision to be classified as a low velocity impact, the speed of the striker must be 10 m/s or less (Khalili and Ardali, 2013; Hossein et al., 2022)

Fibre reinforced composite plates and stiffened plates are rapidly gaining ground in the aerospace industry. Layered composite plate structures are materials with high strength and impact damping properties (Quaresimin et al., 2013; Santiago et al., 2018; Özbek et al., 2022;). Layered composite plates can be hardened with different types of stiffeners to achieve high strength properties. Such structures are generally used in wing and fuselage structures in aerospace structures (Gök et al., 2023). The mechanical behaviour of the sample as a consequence low velocity impact to be applied on stiffened layered composite plates will differ according to the type of stiffeners (Khan et al., 2021). It has been observed that the stiffeners absorb some of the energy generated on the plate as a result of low impact. The energy absorbed by the reinforcing element reduces the amount of deformation on the surface of the plate to lower levels (Wang et al., 2015).

Optimization and forecasting studies are ongoing, especially to reduce the amount of damage. There are studies on the effects of mechanical properties or geometric properties of the structure on damage behavior. In these studies, prediction and optimization can be performed with statistical or artificial intelligence based software (Güvenç et al., 2023).

Metals are used in many fields such as aviation, aerospace, automotive and industry. Alumium is the most preferred production material due to its light weight and easy formability. Despite this, composite plates are rapidly replacing metals in aircraft due to their light weight and high strength properties. Especially in helicopter blades, UAV wings and tails, composite materials can be reinforced to provide higher strength values (Barkanov et al., 2014; Dag et al., 2023; Pan et al., 2019). Stiffened panels are used extensively in aircraft fuselages and wings and tail elements. The most important advantage in the design of these panels is to provide rigidity to the structure (Correas et al., 2021; Güvenç et al., 2023; Sun et al., 2018).

The plate is the element that holds the stiffeners together. Stiffened panels are connected to beam webs to strengthen structures against out-of-plane deformations (Quinn et al., 2009). The orientation of the reinforcing columns called stiffeners varies depending on the desired property according to the area of use of the stiffened panel.

Composite structures, which are especially important components of aircraft, are composites that have a curvature as a result of processing. In addition to normal flat plate composites, the damage behavior of these curved plates is important in an industry such as aerospace, where high loads act on the structures (Adali and Cagdas, 2011; Erdoğan et al., 2019; Saghafi et al., 2014).

Many factors can cause damage to composite materials. The most common of these is impact damage. This is also frequently seen in composite materials used in aviation. These damages, especially when landing and taking off on the runways, can cause major damage to the vehicle or cause damage that will cause these critical damages to occur (Gebhardt et al., 2023).

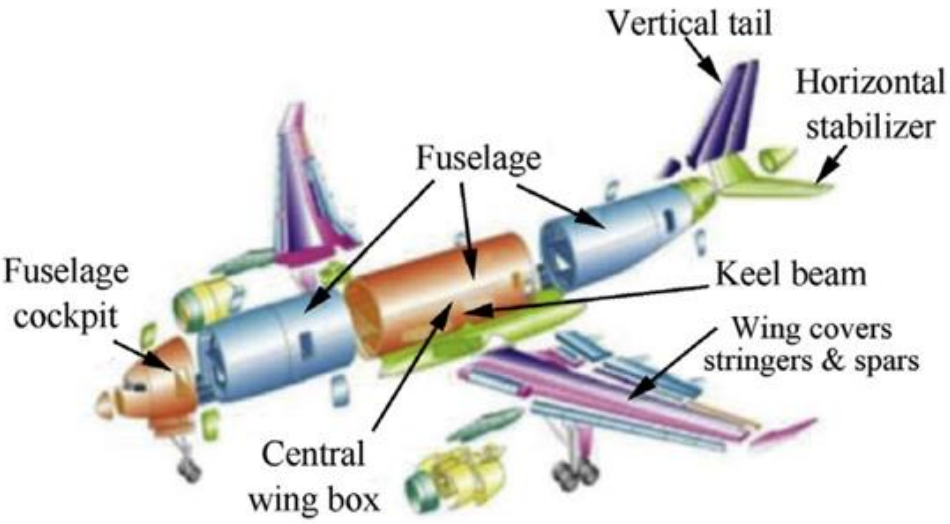

Figure 1. Where composite structures are used extensively on the Airbus 350 (Karataş and Gökkaya, 2018)

W. Sun and al. (Sun et al., 2018) conducted experiments to examine the damage response of the sample in impact tests applied to composite panels and the changes in the damage behavior of the reinforced composite panel with the addition of reinforcement. The three T-strengtheners added were significantly effective against buckling of the panel and the formation of damaged surfaces. The damage threshold of the panel was determined as 34 J, and it was observed that if an impact above this energy was applied, the panel would be damaged. It has been evaluated that there is no need to apply reinforcement elements to the panel for impact energies below this energy level. It was observed that if the impact energy was higher than 34 J, the reinforcement element was disconnected from the panel and delamination occurred between the plates. However, since there was no damage to the panel and only the booster in the middle lost its function, it was seen that the panel could continue to be used with two boosters instead of three boosters.

K. S. Kumar et al. (Kumar et al., 2019) performed low-velocity impact simulations on Glass/Epoxy and Carbon/Epoxy plates consisting of many layers formed with different laying angles. As a result of the test simulated with the finite element method, the impact behavior of the materials was examined. It has been observed that the data of layered plates produced with Glass/Epoxy and Carbon/Epoxy are very close to each other. Gangwar et al. (Gangwar et al., 2024) investigated the change in the mechanical behavior of a curved layered composite plate as a result of loads acting on it depending on the properties of the plate such as thickness and aspect ratio. As a result of numerical analysis by finite element method, the frequency values of the specimen as a result of loading for two different modes were analyzed. When these studies are examined, it is thought that the analysis of the change of mechanical behavior of the curved plate as a result of impact loading depending on the type of sitiffener using the finite element method is incomplete.

In this study, low-velocity impact simulation on a composite plate reinforced with different types of stiffeners, which has a curved form such as wing or fuselage geometries, was carried out by finite element method. The 300x200x4 mm sized curved plate is reinforced with 5 blades, T and I type stiffeners (Jain and Upadhyay, 2010; Tan et al., 2020).

The impactor was modeled as a sphere with a radius of 6 mm and a mass of 15 kg. As a result of the analyses, the effect of stiffener type on impact behaviour was examined. The effect of the stiffener type on the amount of energy accumulated on the curved panel, the maximum contact force value and the amount of deformation was observed.

2. MATERIALS AND METHODS

LS-Dyna software was preferred to perform the finite element method in the study. Curved plate and stiffeners modeling were performed using the LS-PrePost interface. The structure with a radius of 6 mm and a mass of 15 kg, which will be used as the impactor, was created with the Sphere Solid command from the LS-PrePost interface. Table 1 shows the dimensions of the striking mass, plate and reinforcing structures. The curved plate is modeled with dimensions of 300x200 mm. The radius of curvature is 469.25 mm and the plate consists of 16 layers. Each ply is 0.25 mm thick and modeled with a laying angle of $[0/45/-45/90]_4$ The stiffeners have a lay-up angle of $[0/90]_4$ and each layer is 0.25 mm thick like the ply. The plate is 4 mm thick and formed with three different types of stiffeners.

Table 1. Geometrical properties of the curved plate, stiffeners and impactor mass

	Curved Plate [mm]	Stiffeners [mm]
Width	200	200
Length	300	16
Heigth	-	16
Thickness	4	2.0
	Impactor	
Radius	6	

Figure 2 shows the modeling of the stiffener types used in the study and their integration with the curve panel.

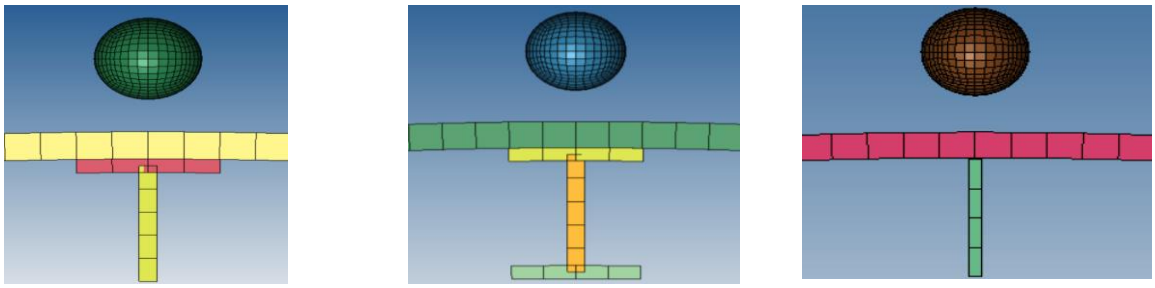

(a) (b) (c)

Figure 2. LS-Dyna modeling of a)T-type, b) I-type and c) Blade-type reinforcers

In order to make the modeled sample suitable for numerical analysis and recognisable for the finite element method, a mesh is applied. The curved panel was modeled with different mesh sizes and analyses were performed at a speed of 2.5 m/s. In these analyses, the mesh element sizes applied on the panel were determined as 10, 5, 4.5, 4 and 3 mm and low velocity impact analyses were performed on the curved panel by applying these element sizes. The force-time curves obtained in these analyses were evaluated and the most suitable mesh size was selected to be applied to the panel and reinforcements. The maximum contact force value, which is the peak of the force-time curve, was evaluated for each mesh size and the deviation amount was determined as 0.5%. Figure 3 shows the force-time curves obtained as a result of the approach for mesh convergence. As a result of these analyses, it was decided that 4 mm mesh size was the most appropriate mesh size in terms of geometry and accuracy of the results.

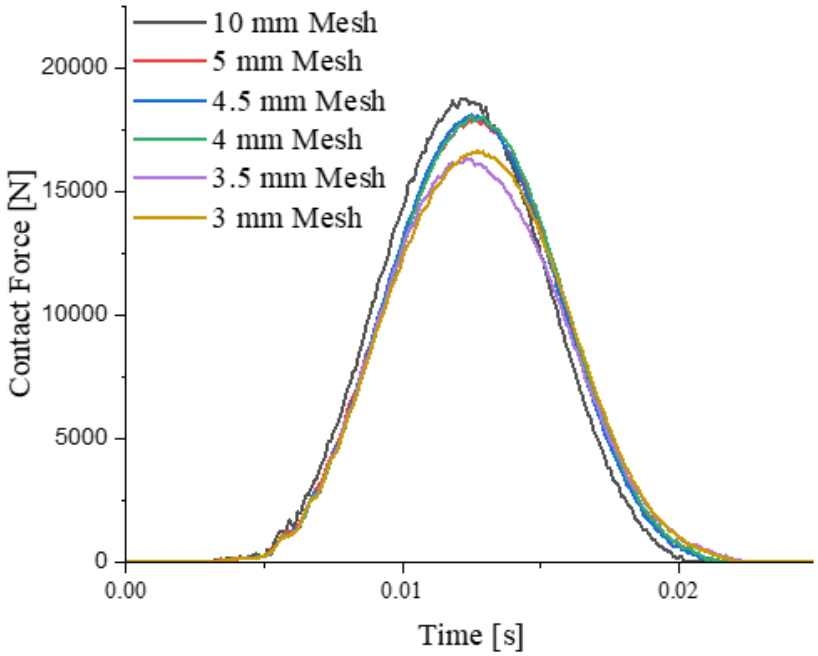

Figure 3. Contact force-time output according to different mesh size

Figure 4 shows a sample T-type stiffened curved panel and impactor mass formed with a mesh size of 4 mm. The curved composite panel is modeled with a total of 13 000 mesh elements.

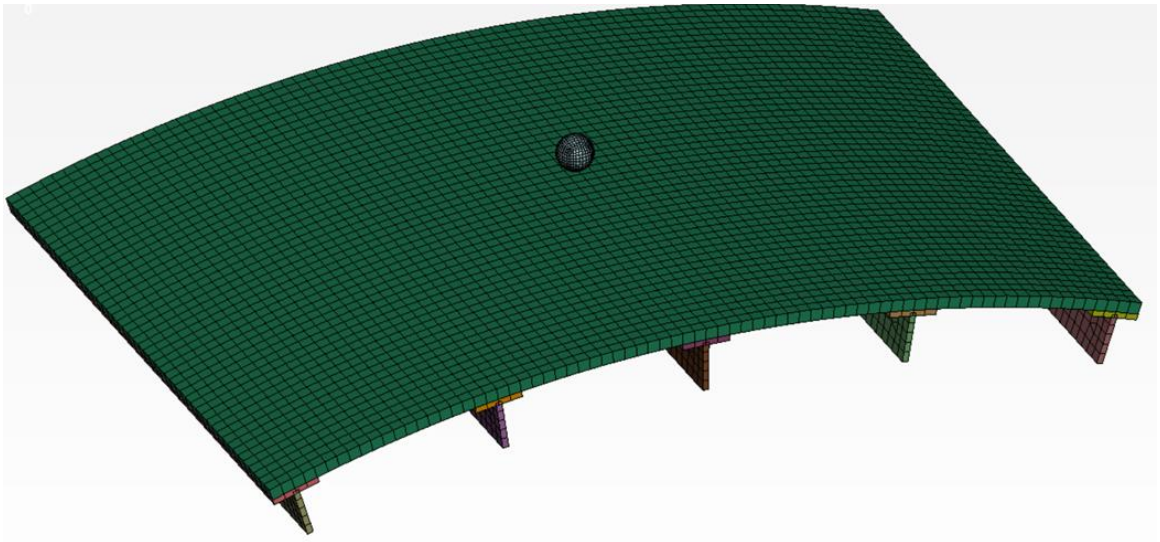

Figure 4. Mesh image of curved panel with T-type stiffener and impactor generated in LS-PrePost interface

The mechanical properties of the impactor are defined by the *Mat Rigid* material card in the LS-Dyna software (Dağ et al., 2022). The striking part of a low velocity impact device with a measured mass of 15 kg was modeled. The geometrical shape of the striking tip of the test device is partially modeled. Since only the impactor tip was modeled, the entire mass was modeled on this sphere. This was achieved by increasing the density of the sphere. Table 2 shows the mechanical properties of the 15-kilogram spherical striker.

Table 2. Impactor mass mechanical properties

	Symbol	Value
Density	ρ	1.685e+07 kg/m^3
Elasticity Modulus	E	207 GPa
Poisson Ratio	ν	0.30

Mat Enhanced Composite Damage card was used to define the material for the curved plate and stiffeners. This composite card provides different damage criteria options. This material card, which covers Chang-Chang and Tsai-Wu damage criteria, can provide various simulation results outputs (Akbulut and Sonmez, 2011; Nyambeni and Mabuza, 2018). The material card with *Mat-055: Enhanced Composite Damage* damage criterion is the material card where Tsai-Wu damage criteria are applied in the matrices of composite structures and Chang-Chang damage criteria are applied in fiber reinforcements. *Mat-055: Enhanced Composite Damage* card inputs are modeled with E-Glass Epoxy mechanical properties as given in Table 3.

Table 3. E-Glass Epoxy Mechanical Properties

	Symbol	Value
Density	ρ	1840 kg/m^3
Elasticity Modulus [Longitudinal]	E_1	42 GPa
Elasticity Modulus [Transverse]	E_2	9.5 GPa
Poisson Ratio	ν	0.34
Shear Modulus	G_{12}	3.5 GPa
Compressive Strength [Longitudinal]	X_C	300 MPa
Tensile Strength [Longitudinal]	X_T	690 MPa
Compressive Strength [Transverse]	Y_C	147 MPa
Tensile Strength [Transverse]	Y_T	66 MPa
Shear Strength	S_C	56 MPa
Maximum Strain for Matrix	DFAILM [Y_C/E_2]	0.001547
Maximum Shear Strain	DFAILS [S_C/G_{12}]	0.016000
Maximum Compressive Strain	DFAILC [$-X_C/E_1$]	-0.007143
Maximum Tensile Strain	DFAILT [X_T/E_1]	0.0164286

After the material assignments of the impactor, plate and stiffeners were completed, the contact cards were defined. The contact card between the impactor and the plate is the *Contact Automatic Nodes to Surface* contact card. The contact card between the plate and the stiffeners was associated with the *Contact Automatic Surface to Surface* contact card (Uyaner et al., 2023).

3. RESULTS AND DISCUSSION

In this section, the results of numerical analyses of the low velocity impact response of the inclined panel supported with 3 different geometries as flat, I and T type as stiffener type are given. Force-time, energy-time and force-displacement graphs were obtained as a result of numerical simulations (Tan et al., 2018; Y. Zhang et al., 2022).

Low velocity impact simulation with a speed of 2.5 m/s on a 200x300x4 mm curved plate with stiffeners was carried out with LS-Dyna software. As a result of the finite element analysis, the variations of contact force, energy and displacement values of the plate after impact against time were obtained. Maximum contact force, energy dissipation rates and permanent deformation amounts are also obtained as a result of the analyses.

Figure 5 shows the time dependent variation of the contact force obtained as a result of the low velocity impact applied on the curved plates supported with different reinforcements.

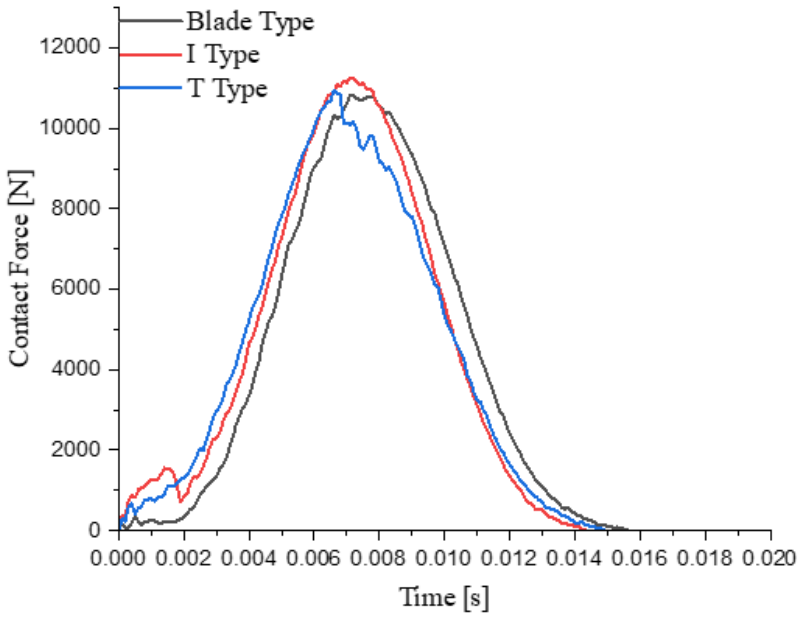

Figure 5. Variation of the contact force on the plate after impact according to the type of stiffener

The maximum contact force value of the plate supported with I-type stiffeners after 2.5 m/s impact is higher than the other two types of stiffeners. Figure 6 shows the curve of the amount of displacement resulting from the contact force.

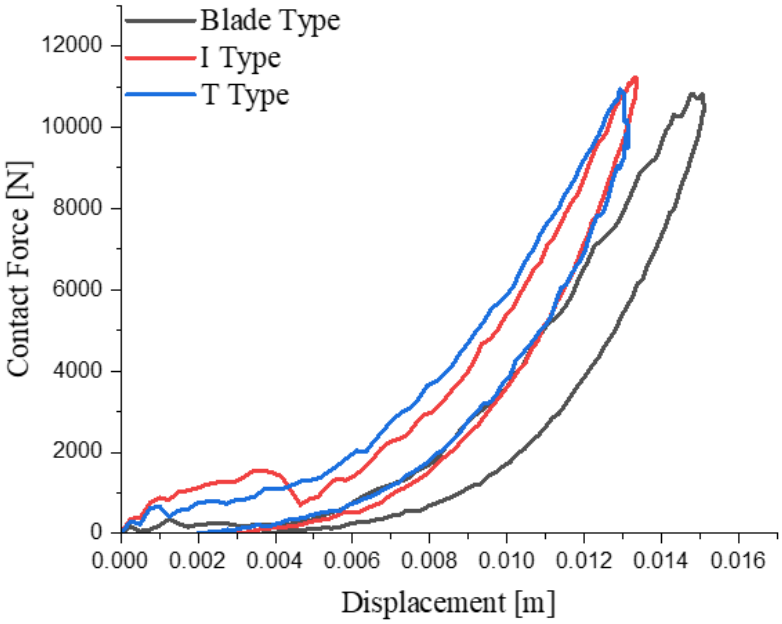

Figure 6. Variation of contact force-displacement of the plate after impact according to the type of stiffener

The curved plate with Blade-type stiffener, which has the maximum displacement value on the plate as a result of the contact force, absorbed 37.78% of the kinetic energy of the striker. Figure 7 shows the time-dependent change in the amount of energy accumulated on the plates after impact (D. Zhang et al., 2013).

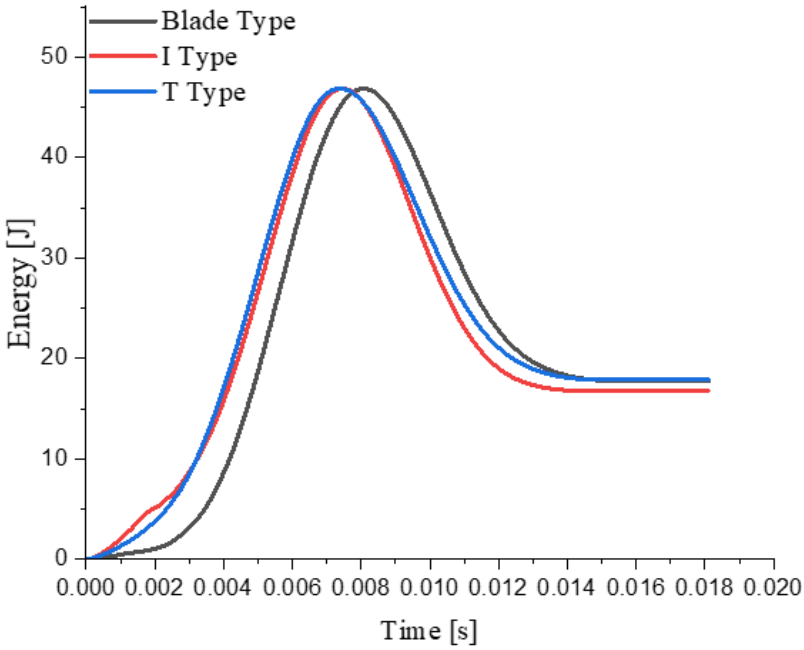

Figure 7. Time-dependent variation of the energy deposited on the plate after impact according to the stiffener type

As seen in Figure 7, the plates with I and T-type stiffeners can reach the maximum energy amount earlier than the plate with Blade-type stiffeners. This is due to the rigidity provided to the plate by the stiffener types.

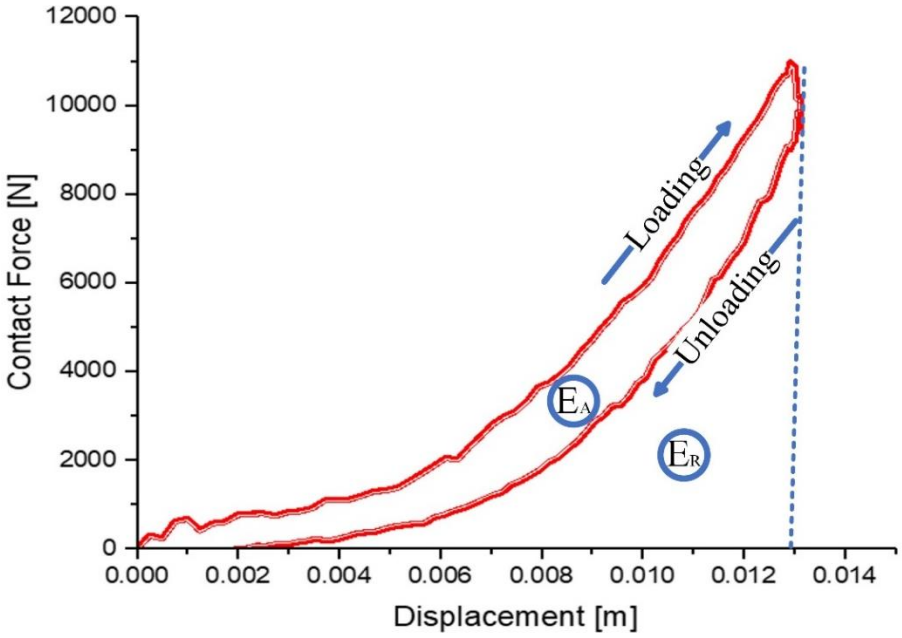

Figure 8. Post-impact displacement-contact force curve of T-type stiffener plate

Figure 8 shows the post-impact displacement-contact force curve of the plate with T-type stiffener. With the sudden loading of the plate after impact and the subsequent rebound effect, the material absorbs some of the kinetic energy of the striker. The area inside the displacement curve in Figure 8 shows the energy absorbed by the plate and the area below the curve shows the energy returned (Tan et al., 2018).

Impact behavior of a curved plate reinforced with T-type stiffeners impacts by a spherical impactor at 2.5 m/s. The impact resulted in delamination of the plate and reinforcement and damage to the vertical flange of the stiffener.

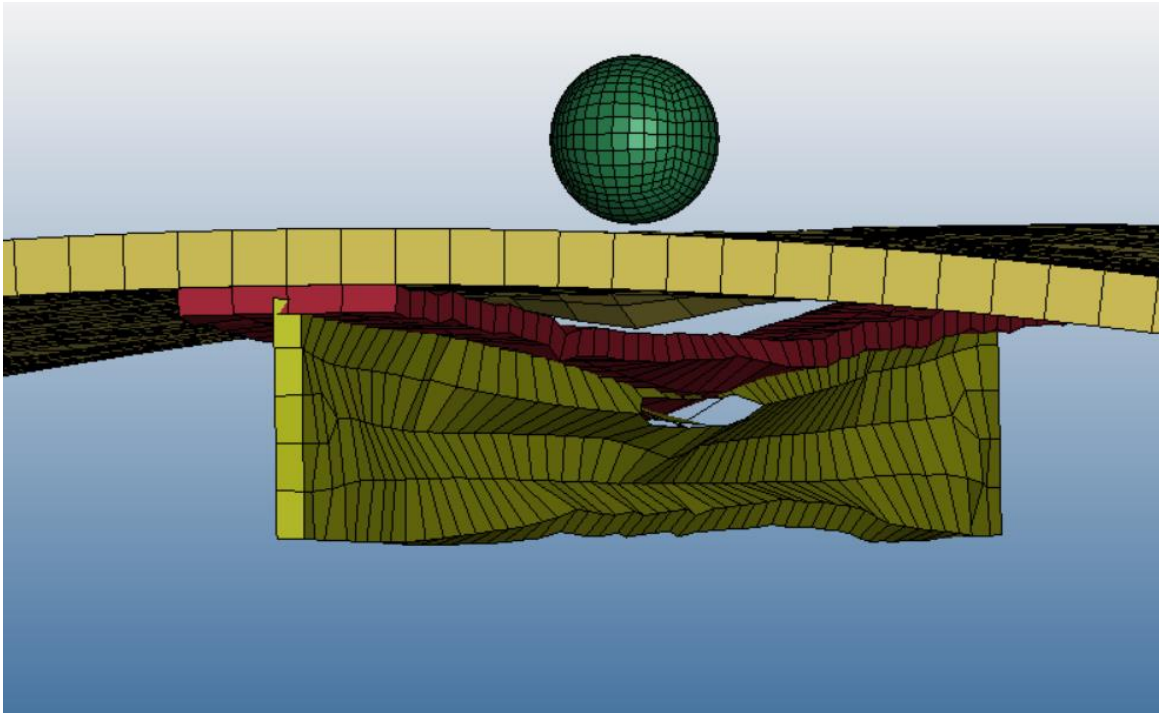

Figure 9. View of curved panel with T-type stiffener after impact

Figure 10 shows the permanent damage of the curved plate without stiffener and the curved plate with T-type stiffener after impact. The permanent deformation of the plate without stiffener is 19.8 mm, while the permanent damage of the plate reinforced with T-type stiffener is 2 mm. Thanks to the horizontal flange of the T-type stiffener, the curved plate takes less damage and prevents critical damage to the plate. The horizontal flange absorbs the loading acting on the plate and minimizes the amount of plate damage.

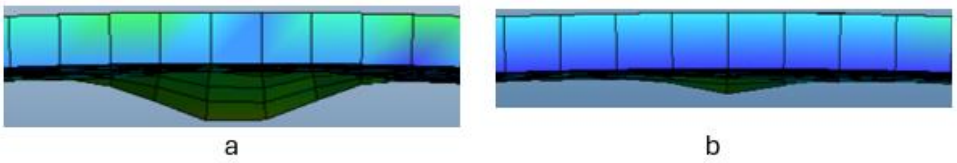

Figure 10. a) Curved plate without stiffeners, b) Curved plate with T-type stiffeners

The form of the center stiffener after the impact is as shown in Figure 11. It prevents damage to the plate by absorbing some of the impact energy.

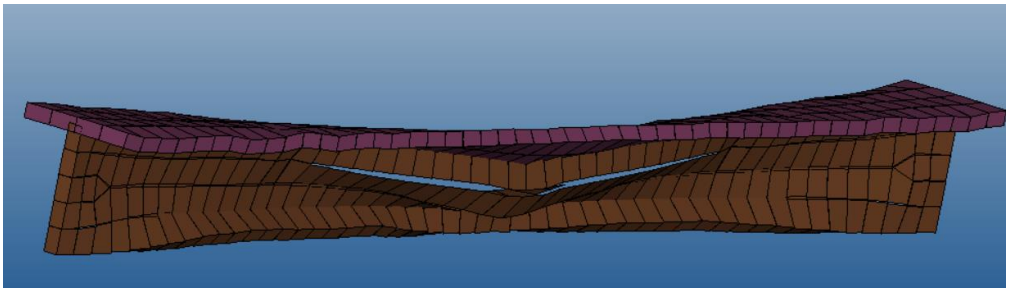

Figure 11. The appearance of the T-type stiffener after the impact

Even if the stiffener, which is seen to have received critical damage, has become unusable, the plate continues to function by maintaining its structural integrity. However, in case of any loading after the impact, the structure with low strength can be severely damaged (Li et al., 2014).

In Table 4, the changes of the maximum contact force, energy absorption amount and deformation amount of the curved plate after impact are given numerically according to the stiffener types.

Table 4. Impact behaviour of plates with different stiffeners

	I Type	T Type	Blade Type
Maximum Contact Force [N]	11241.81	10944.08	10822.96
Energy Damping Rate [%]	35.78	38.11	37.78
Maximum Deformation Amount [m]	0.0134	0.0131	0.0151
Permanent Deformation Amount [m]	0.0026	0.0019	0.0037

4. CONCLUSION

As a result of the 2.5 m/s low velocity impact applied on the curved plate reinforced with different stiffeners, it was observed that the plate with T-type stiffener was less damaged than the others. The maximum contact force of 10.94 kN was determined on the plate with 1.9 mm permanent

deformation. It absorbed 38.11% of the kinetic energy of the impactor mass and rebounded the impactor.

- Considering the maximum deformation and permanent deformation amounts, the most damaged structure is the curved plate reinforced with Blade type stiffener. As a result of the impact, the structure was deformed by 3.7 mm and damage occurred.
- As a result of the numerical analysis performed with the finite element method, the T-type stiffener element reduces the amount of damage by a significant amount of 90%. In the future, the effect of changing the geometric properties of stiffener types on impact behavior may be the subject of investigation.
- As a result of the impact applied on the plate with I-type stiffener, it absorbed more than one third of the energy and was subjected to a maximum contact force of 11.24 kN.

5. ACKNOWLEDGEMENTS

This work was conducted scope of Master of Science Thesis of Tolunay Dağ.

6. CONFLICT OF INTEREST

Authors approve that to the best of their knowledge, there is not any conflict of interest or common interest with an institution/organization or a person that may affect the review process of the paper.

7. AUTHOR CONTRIBUTION

Tolunay Dag: Conceptualization, Methodology, Software, Visualization, Investigation. Mehmet Ali Guvenc: Investigation, Resources, Data curation, Writing-original draft, Supervision. Mesut Uyaner: Data analysis and interpretation of results, Supervision.

8. REFERENCES

Adali, S., Cagdas, I. U., Failure analysis of curved composite panels based on first-ply and buckling failures. Procedia Engineering, 10, 1591–1596, 2011.

Akbulut, M., Sonmez, F. O., Design optimization of laminated composites using a new variant of simulated annealing. Computers and Structures, 89(17–18), 1712–1724, 2011.

Altin Karataş, M., Gökkaya, H., A review on machinability of carbon fiber reinforced polymer (CFRP) and glass fiber reinforced polymer (GFRP) composite materials. In Defence Technology 14(4), 318–326, 2018.

Aytav, E., Işık, A. M., Experimental Investigation of Ballistic Performance of Free Particle Armor Systems. Journal of Materials and Mechatronics: A, 4(2), 518–543, 2023.

Barkanov, E., Ozoliņš, O., Eglitis, E., Almeida, F., Bowering, M. C., Watson, G., Optimal design of composite lateral wing upper covers. Part I: Linear buckling analysis. Aerospace Science and Technology, 38, 1–8, 2014.

Correas, A. C., Crespo, A. C., Ghasemnejad, H., Roshan, G., Analytical Solutions to Predict Impact Behaviour of Stringer Stiffened Composite Aircraft Panels. Applied Composite Materials, 28(4), 1237–1254, 2021.

Dag, T., Yildirim, N., Senturk, G., Durmazoglu, M., Yildirim, S., Uyaner, M., Virtual Investigation on the Response of Glare to Low Velocity Impact. Proceedings of 10th International Conference on Recent Advances in Air and Space Technologies, RAST 2023, 2023.

Dağ, T., Yıldırım, N., Kepir, Y., Uyaner, M., E/Cam Epoksi Laminelerin Üzerine Uygulanan Düşük Hızlı Darbe Davranışının Sayısal Simülasyonu. ASREL, 2022

Erdoğan, A., Gök, M. S., Koç, V., Günen, A., Friction and wear behavior of epoxy composite filled with industrial wastes. Journal of Cleaner Production, 237, 2019.

Gebhardt, J., Schlamp, M., Ehrlich, I., Hiermaier, S., Low-velocity impact behavior of elliptic curved composite structures. International Journal of Impact Engineering, 180, 2023.

Gök, M., Küçük, Y., Pehlivanlı, M., Erdoğan, A., Investigation of Dry Sliding Wear Behavior of CFRP Composite Used in New Generation Aircraft Wings. Journal of Aviation, 7(2), 190–195, 2023.

Guvenc, M. A., Bilgic, H. H., Mistikoglu, S., Identification of chatter vibrations and active vibration control by using the sliding mode controller on dry turning of titanium alloy (Ti6Al4V). Facta Universitatis, Series: Mechanical Engineering, 21(2), 307, 2023.

Guvenc, M. A., Eren, B., Basar, G., Mistikoglu, S., A new hybrid meta-heuristic optimization method for predicting UTS for FSW of Al/Cu dissimilar materials. Proceedings of the Institution of Mechanical Engineers, Part C: Journal of Mechanical Engineering Science, 237(20), 4726–4738, 2023.

Hossein Alizadeh, M., Kamali Dolatabadi, M., Shaikhzadeh Najar, S., Eslami-Farsani, R., Energy absorption of the Kevlar®/PP hybrid composite: fabric to composite optimization. Journal of the Textile Institute, 113(6), 1018–1026, 2022.

Jain, H. K., Upadhyay, A., Buckling behavior of blade-, angle-, T-, and hat-stiffened FRP panels subjected to in-plane shear. Journal of Reinforced Plastics and Composites, 29(24), 3614–3623, 2010.

Khalili, S. M. R., Ardali, A., Low-velocity impact response of doubly curved symmetric cross-ply laminated panel with embedded SMA wires. Composite Structures, 105, 216–226, 2013.

Khan, S. H., Khan, A. A., Husain, A., Effect of fibre orientation on damage resistance of composite laminates. International Journal of Crashworthiness, 26(3), 270–282, 2021

Li, D. H., Liu, Y., Zhang, X., Low-velocity impact responses of the stiffened composite laminated plates based on the progressive failure model and the layerwise/solid-elements method. Composite Structures, 110(1), 249–275, 2014.

Nyambeni, N., Mabuza, B. R., Considerations of Failure Analysis in a Multi-Layered Composite Structure under Thermomechanical Loading. Proceedings, 2, 447, 2018.

Özbek, Ö., Çakır, M. V., Doğan, N. F., Halloysit Nanotüp Katkısının Al-GFRP Tek Bindirmeli Yapıştırma Bağlantısında Kayma Dayanımına Etkisi. Journal of Materials and Mechatronics: A, 3(1), 117–128, 2022.

Pan, J., Li, N., Song, Z. J., Xu, M. C., Influence of boundary condition and stiffener type on collapse behaviours of stiffened panels under longitudinal compression. Advances in Mechanical Engineering, 11(10), 2019.

Quaresimin, M., Ricotta, M., Martello, L., Mian, S., Energy absorption in composite laminates under impact loading. Composites Part B: Engineering, 44(1), 133–140, 2013.

Quinn, D., Murphy, A., McEwan, W., Lemaitre, F., Stiffened panel stability behaviour and performance gains with plate prismatic sub-stiffening. Thin-Walled Structures, 47(12), 1457–1468, 2009.

Saghafi, H., Minak, G., Zucchelli, A., Effect of preload on the impact response of curved composite panels. Composites Part B: Engineering, 60, 74–81, 2014.

Santiago, R. C., Cantwell, W. J., Jones, N., Alves, M., The modelling of impact loading on thermoplastic fibre-metal laminates. Composite Structures, 189, 228–238, 2018.

Sun, W., Guan, Z., Ouyang, T., Tan, R., Zhong, X., Effect of stiffener damage caused by low velocity impact on compressive buckling and failure modes of T-stiffened composite panels. Composite Structures, 184, 198–210 2018

Tan, R., Guan, Z., Sun, W., Liu, Z., Xu, J., Experiment investigation on impact damage and influences on compression behaviors of single T-stiffened composite panels. Composite Structures, 203, 486–497, 2018.

Tan, R., Xu, J., Guan, Z., Sun, W., Ouyang, T., Wang, S., Experimental study on effect of impact locations on damage formation and compression behavior of stiffened composite panels with L-shaped stiffener. Thin-Walled Structures, 150, 2020.

Uyaner, M., Kara, M., Kepir, Y., Gunoz, A., Virtual Testing of Laminated Composites Subjected to Low-Velocity Impact. Iranian Journal of Science and Technology- Transactions of Mechanical Engineering, 47 (2), 595–610, 2023.

Wang, X. M., Cao, W., Deng, C. H., Wang, P. Y., Yue, Z. F., Experimental and numerical analysis for the post-buckling behavior of stiffened composite panels with impact damage. Composite Structures, 133, 840–846, 2015.

Zhang, D., Sun, Y., Chen, L., Pan, N., A comparative study on low-velocity impact response of fabric composite laminates. Materials & Design, 50, 750–756, 2013.

Zhang, Y., Zhou, Y., Sun, Y., Bird-strike damage analysis of composite panels with different stiffeners. Aircraft Engineering and Aerospace Technology, 94 (6), 933–947, 2022.

JOURNAL of
MATERIALS and MECHATRONICS:A

e-ISSN 2717-8811
JournalMM, 2024, 5(1), 130-142
https://doi.org/10.55546/jmm.1459329

Araştırma Makalesi / Research Article

Predicting the Corrosion Rate of Al and Mg Alloys Coated by Plasma the Spraying Method with Machine Learning

Hüseyin ÖZKAVAK[1*], Recai Fatih TUNAY[2]

[1*] Isparta University of Applied Sciences, Isparta OSB Vocational School, Department of Mechanical and Metal Technology, Isparta, Turkey,
ORCID ID: https://orcid.org/0000-0003-2857-4500, huseyinozkavak@isparta.edu.tr
[2] Süleyman Demirel Üniversitesi, Faculty of Engineering, Department of Mechanical Engineering, Isparta, Turkey,
ORCID ID: https://orcid.org/0000-0002-9877-9379, recaitunay@sdu.edu.tr

Geliş/ Received: 26.03.2024**;** **Revize/Revised:** 12.05.2024 **Kabul / Accepted:** 17.05.2024

ABSTRACT: Developing technology has increased the need for materials that are more economical in terms of cost and more reliable in terms of strength, chemical and physical properties in all industrial areas. This has necessitated the development of new materials or the improvement of existing material properties. Surface coating methods are used to improve existing material properties. In this study, Al and Mg alloys, which are considered as an alternative to steel material in terms of being lightweight materials, were coated with Al_2O_3 and TiO_2 at different rates by plasma spraying method, and the corrosion behaviors of the coatings in different environments were predicted using machine learning methods. AA7075 and AZ91 non-metal materials were chosen as the substrate for the study. Different ratios of Al_2O_3 and TiO_2 ceramic materials were coated on the substrates. To determine the corrosion resistance of the coated samples, corrosion experiments were carried out in 3.5% NaCl and 0.3M H_2SO_4 environments. Using the experimental results, corrosion rate values were estimated using machine learning algorithms such as XGBoost, Random Forest (RF) and artificial neural networks (ANN) methods, depending on the substrate material, corrosive environment and coating rates. At the end of the study, corrosion rate values were estimated with low error rates and the best estimate was obtained with the XGBoost method (0.9968 R^2 value).

Keywords: Coating, AZ91,AA7075,Seramic Materials, Machine Learning

1. INTRODUCTION

Al is a metal with a density of 2.7 g/cm^3, good corrosion resistance and easy production. The strength/density ratio is approximately 3 times higher than structural steels. Due to its non-toxic structure, it is a material group suitable for use in sectors such as the beverage industry and medical

*Sorumlu yazar / Corresponding author: huseyinozkavak@isparta.edu.tr
Bu makaleye atıf yapmak için /To cite this article

Özkavak, H., Tunay, R. F. (2024). Predicting the Corrosion Rate of Al and Mg Alloys Coated by Plasma the Spraying Method with Machine Learning. Journal of Materials and Mechatronics: A (JournalMM), 5(1), 130-142.

pharmaceuticals. Al is a preferable engineering material due to its high electrical conductivity, thermal conductivity, magnetic and high reflection properties, as well as its low cost. Due to all these features, it is widely preferred in many areas, especially defense, space, automotive industry (Ashby,2004; Picas et al.,2005; Gibbons et al.,2006). Metal materials are used in the manufacturing of many machine elements such as construction, oil, heat exchangers and valves, and there are problems with resistance to corrosion and abrasion (Bolelli,2009; He et al.2007).

Mg began to take its place as the lightest material group among green metallic materials in the 21st century. It is a group of non-metallic materials used in the aviation and automotive industries due to their properties such as low density (1.73 g/cm^3), high specific strength and hardness, excellent castability and good magnetic shielding performance (Kojima et al., 2001; Mordike et al., 2001; Rotshtein et al.,2004). Although it has many superior properties, its low corrosion resistance has limited the use of Mg and its alloys (Shi et al., 2005, Song Gand StJohn,2004).

Alloying and surface coating methods are used to increase the corrosion and wear resistance of Al and Mg materials, which are candidates to replace metal materials because they have many superior properties. In order to improve the wear and corrosion resistance of light metal alloys, thermal spray surface coating methods such as atmospheric plasma spray (APS), high velocity oxygen fuel (HVOF) and wire arc are used (Ernst P and Fletcher K., 2011). In thermal spray coating methods, metals and ceramic materials as well as hard metals are widely used as coating materials. Atmospheric plasma spraying method is one of the methods used to make ceramic coatings due to its high melting temperatures (Toma et al.,2010). Al_2O_3 is a brittle ceramic material, and with the addition of TiO_2, the hardness value decreases and the toughness value increases (Šuopys et al., preprint; Basha et al.,2020). In addition, TiO_2, which has a low melting point, increases the coating performance by lowering the melting point when added to Al_2O_3. For this reason, instead of using only Al_2O_3 for surface coating, coatings obtained by adding TiO_2 into Al_2O_3 are used and studies have focused on this type of coatings. Ya-Li et al. (2007) in their study, applied Al_2O_3 ceramic coating process on Mg alloy using plasma coating and laser melting plasma spraying methods. They investigated the wear and corrosion resistance of the coatings. At the end of the study, the authors determined that there was a 3-fold increase in wear resistance compared to uncoated materials and a 1-fold increase compared to coatings using the plasma coating method. In addition, the authors determined that there was a 5-fold increase in corrosion resistance in uncoated samples and a 3-fold increase compared to the plasma coating method (Ya-li et al., 2007). In their study, Morks and Akimato (2008) examined the effect of nozzle diameter on the quality of Al_2O_3/TiO_2 coated materials by plasma spraying method. At the end of the study, a denser coating was obtained with a 7.5 mm nozzle diameter compared to 8 mm, Micro Vickers hardness values decreased as the nozzle diameter increased, and greater wear resistance was obtained with a lower nozzle diameter (Morks et al., 2008).In their study, Islak and Buytoz (2011) coated Al_2O_3/TiO_2 materials on AISI 304 steel. Authors who examined the coatings concluded that as the amount of Al_2O_3/TiO_2 increased, the porous structure decreased and the hardness increased four to five times compared to the substrate (Islak and Buytoz (2011). Jia et al. (2015) coated Al_2O_3/TiO_2 coating materials with different ratios of TiO_2 added on AA6061 aluminum material using the plasma spraying method and examined the corrosion resistance of the coatings. At the end of the study, the authors concluded that as the TiO_2 ratio increases, corrosion resistance increases and thermal insulation properties decrease (Jia et al. 2015). Basha et al. (2020) discussed the Al_2O_3-TiO_2 coating process using the atmospheric plasma method in their study. At the end of the study, they determined that the coatings obtained from agglomerated powders of nano-sized alumina-titania showed better wear resistance than the coatings of conventional powders (Basha

et al. 2020). In their study, Bakhsheshi-Rod et al. (2020) applied nanostructured titania (TiO2, n-TO) and nanostructured alumina alumina-titania (Al_2O_3-13% TiO2; n-ATo) coatings on the AA6061 substrate. At the end of the study, they determined that n-TO coatings had superior hardness and higher wear resistance than uncoated and n-ATO coatings. In addition, electrochemical examinations of the coatings were made and it was determined that n-ATO coatings have 50% lower corrosion resistance due to their looser structure than n-TO coatings (Bakhsheshi-Rod et al. 2020). In their study, Harju et al. (2007) examined the effects of surface properties, surface stress and phase inhomogeneity of TiO_2, Al_2O_3based coatings (Harju et al. 2007). Toma et al. (2009) examined the corrosion behavior of materials coated with different ratios of Al2 Al_2O_3/TiO_2. At the end of the study, the authors determined that there was an increase in corrosion resistance with the addition of TiO_2 (Toma et al. (2009). Michalak et al. (2020) in their study, they discussed the determination of tribological properties of samples coated with 3, 13 and 40% TiO_2. In the study, they concluded that when the TiO_2 ratio increased, the pure Al_2O_3 phases decreased and the TiO_2 phases increased. They also determined that the best tribological performance was obtained in coatings with 13% TiO_2 added, where a decrease in hardness occurred as TiO_2 increased (Michalak et al. 2020).

When the literature studies were examined, it was determined that many studies were carried out to determine the behavior of different corrosive environments and different coatings. The most important problem experienced in experimental studies is the losses in terms of time and cost due to the large number of experiments. In order to eliminate this problem, analytical methods are used to determine the optimum parameters (Giard and Karlsson, 2021; Altinkok, and Koker,2004). In recent years, the data-driven machine learning approach has been used in optimizing the performance of materials and designing new materials (Xinming et al.,2023; Lei et al., 2022; Cheng et al.,2021; Dey et al.,2016). In their studies, the authors used machine learning (ML) and ANN methods to predict the mechanical properties of materials. Dey et al. discussed the prediction of mechanical properties of ageable wrought alloys using the ANN method (Dey et al.,2016). Again, Giard and Karlsson used the ANN method in their study to predict the mechanical properties of duplex stainless steel (Giard and Karlsson, 2021). El Rehim et al. aimed to determine the change in hardness of AZ91 magnesium alloy using the ANN method (El Rehim et al.,2020). In addition, different statistical methods have been used to develop prediction models using real corrosion data for corrosion rate prediction and to develop prediction models using real corrosion data. Some of the methods used in the studies are linear regression (LR) (Al-Fakih et al.,2016); It can be expressed as multivariate regression (Vel´azquez et al. 2009). However, when the basic assumptions in statistical methods are not fully met, there is difficulty in making accurate predictions. For this reason, methods such as machine learning have been used. For example, Liu et al. (2012) proposed a support vector machine (SVM) regression model with a radial basis function (RBF) kernel for oil boat line corrosion prediction in their study. They used the particle swarm optimization (PSO) algorithm in SVM regression (Liu et al.,2012). Chern-Tong and Aziz (2016) used the CMARGA model to create an optimal decision tree model using a genetic algorithm (Chern-Tong and Aziz 2016). In his study, developed machine learning approaches (component analysis (PCA) and reinforcement machine (GBM)) to predict corrosion defect depth growth in pipelines. Among these approaches, it was determined that the PCA-GBM model achieved 3.52-5.32 times more accuracy than the others (Ossoi, 2019). Ren et al. estimated the internal control rate of underground natural gas pipelines using backpropagation artificial neural networks.In the study, it was determined that the performance of the prediction made using the model was high (Ren et al.,2012).

When the studies are examined, the use of machine learning in the development of new materials for material selection, performance evaluation and lifetime prediction is increasing (Kılıç et al.,2020; Yan et al.,2020; Liu et al.,2022). Machine learning is a particularly suitable method for modeling the relationship between nonlinear material behavior and complex influencing factors (Tian et al.,2017; Shi et al., 2018). For this, Random Forest (RF) (Pei et al., 2020) ; Popular machine learning methods such as adaptive boosting (AD) (Schmidt et al.,2017) , light gradient boosting machine (LGB) (Behara et al; 2021). Gradient boosting (XGBoost) (Fan et al.,2018) and artificial neural network (ANN) (Kumari and Tiyyagura; 2018) are used.ANN model is a comprehensive database; It is suitable for conditions where the data set is incomplete and complex (Hongyu et al.,2023). If the data set is small, the RF model gives the best prediction result (Shi et al., 2018). The RF model is used in many areas such as image recognition (Yang et al.,20179) and corrosion [(Hou et al.,2018) because it is easily applicable, has a simple structure, is suitable for non-linear data, and is suitable for a small number of data.

In this study, ANN; RF and XGBoost regression methods were used to predict the corrosion behavior of AA7075 and AZ91 alloys coated with different ratios of Al_2O_3 and TiO2 in different corrosive environments. In addition, determining the most appropriate method by using more than one method is another aim of the study.

2. MATERIALS AND METHODS

2.1 Experimental Procedure

AA7075 Al alloy and AZ91 Mg alloy were selected as the substrate materials in the study. The chemical compositions of the selected materials are given in Table 1.

Table 1. Chemical properties of the substrate materials used in the study

AZ91	Alloy element	Al	Zn	Mn	Fe	Si	Cu
	%	8.8	0.61	0.18	0.02	0.02	0.005
AA7075	Alloy element	Zn	Mg	Cu	Fe	Si	Mn
	%	6.2	2	1.7	0.5	0.4	0.1

Al_2O_3 and TiO_2 ceramic materials were chosen as coating materials for the study. Al_2O_3-TiO_2 powders with an average size of 40-80 μm were used and these powders were mixed homogeneously. Before the coating process, surface preparation processes were applied to the substrates and the substrates were prepared for coating. For this purpose, the substrate materials are first sandblasted and then ultrasonically cleaned. Then, by applying Ni-Cr primer material to the substrates, the bonding ability of the coating is increased. Atmospheric plasma spraying method was used in the study. The plasma spray coating process parameters used in the study are given in Table 2. Coated samples are given in Figure 1.

Table 2. Process parameters used in the study

Coating Material	Spraying distance (cm)	Ampere (A)	Voltage (V)	Powder feed rate (g/saat)	Argon /Hidrogen (l/dak)
%40 TiO_2	6	530	55-58	1,38	40-42,5/59-63,72
%13 TiO_2	7	550	58-60	1,84	40,59-42,5/56,64
%3 TiO_2	8	570	60-62	1,61	40,59-43,42/61,36-64,66
%100 Al_2O_3	9	580	69	1,73	40-42,5/59-63,72

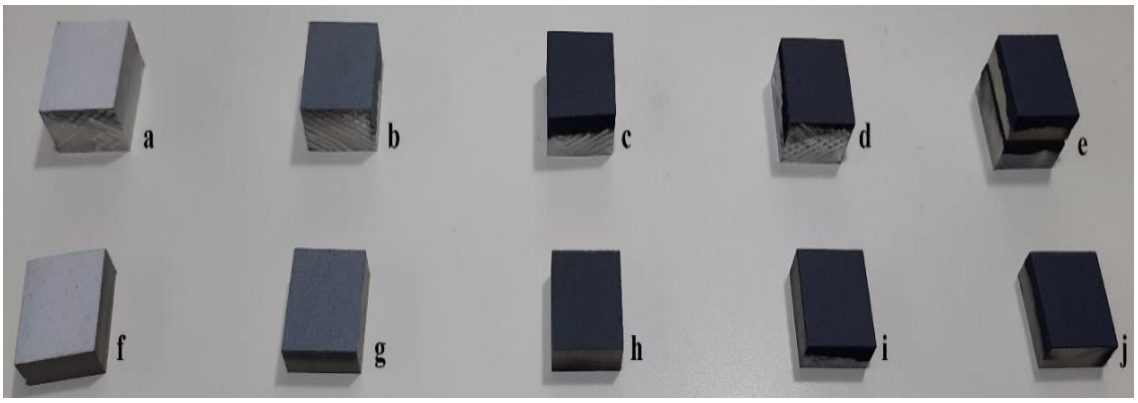

Figure 1. Coated samples by using Atmospheric plasma spraying method (a) AA7075 Saf Al_2O_3 (b) AA7075 %97 Al_2O_3 + %3 TiO_2 (c) AA7075 %87 Al_2O_3 + %13 TiO_2 (d) AA7075 %60 Al_2O_3 + %40 TiO_2 (e) AA7075 Saf TiO_2 (f) AZ91 Saf Al_2O_3 (g) AZ91 %97 Al_2O_3 + %3 TiO_2 (h) AZ91%87 Al_2O_3 + %13 TiO_2 (i) AZ91 %60 Al_2O_3 + %40 TiO_2 (j) AZ91 Saf TiO_2

Corrosion tests were carried out to determine the corrosion resistance of the coatings. Gamry Reference 600 potentiostat/galvonostat device was used for the experiments. Since the study aimed to determine the effects of different corrosive environments, 3.5% NaCl and 0.3 M H_2SO_4 corrosive liquids were used. Before corrosion experiments, the samples were cleaned ultrasonically for 15 minutes with acetone, 15 minutes with ethanol and double distilled water for 15 minutes, and dried in an oven at 50^oC for 1 hour. Experiments were repeated 3 times. Before the corrosion tests, the samples were kept in a corrosive environment for 1 hour to ensure that the system reached equilibrium. The general view of the electrodes and corrosion cell used for corrosion experiments is given in Figure 2. In the study, SEM examinations were also performed before and after corrosion.

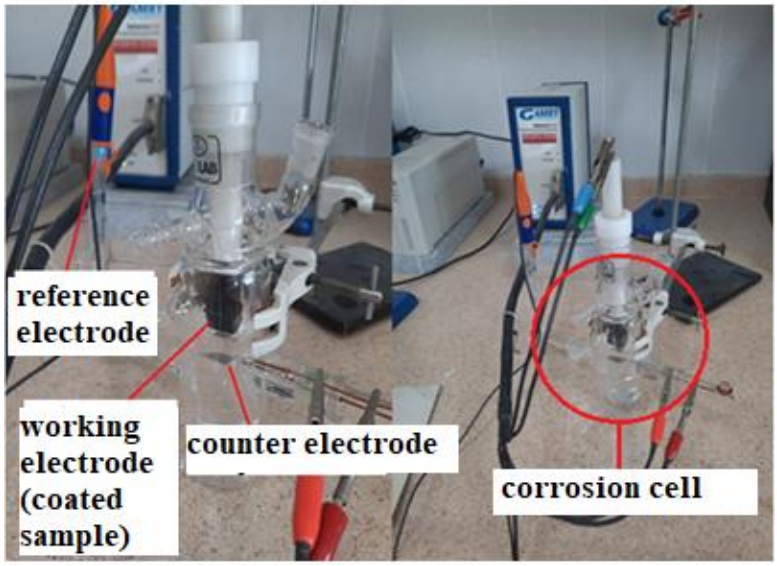

Figure 2. The general view of the electrodes and corrosion cell used for corrosion experiments

2.2 Machine Learning Methods

In this study, corrosion rate values of different non-metal materials were tried to be determined by using different coating rates and different corrosive media. For this purpose, the study tried to estimate corrosion rate values using XGBoost regression, Artificial Neural Network (ANN) and random Forest regression methods. Artificial neural networks (ANN) are expressed as an artificial intelligence method in which the concept of learning is modeled in computer systems (Han et al.2023). Artificial neural networks are widely used in many fields such as financial affairs and

computer image processing. In addition, artificial neural networks are frequently used in regression and classification processes (Aslan, 2022). In addition to ANN, regression methods are also used to solve prediction problems. XGBoost algorithm is one of the decision tree-based ensemble learning-based machine learning algorithms that uses the gradient boosting framework (Morde, 2023; Kurt et al., 2020) . In this algorithm, it is used in structured or tabular data sets in classification and regression problem (Brownlee,2020). This method has advantages such as calculation speed and regularization, such as focusing on the performance of the model (Verma et al.,2018). Random Forest algorithm is among the commonly used methods among community classification algorithms. This algorithm is a type of classifier in tree structure and consists of multiple trees. When predicting the class of new data, predictions are made from each of the multiple trees created in the training phase. The predictions made are called votes, and the class with the most votes is determined as the predicted value of the new data (Bilgin et al.,2018; Breiman, and Cutler; 2020).

In forecasting techniques, it is important to evaluate the performance of the technique. The standard deviation of the forecast errors was determined as the root mean square error (RMSE) by Chai and Draxler (Chai and Draxler, 2014). A low RMSE value is a desirable situation. How close the regression line is to the actual data is indicated by R2 (Cameron and Windmeijer,1997). The important thing here is that the R2 value must be between 0-1 and close to 1.

3. RESULTS AND DISCUSSION

3.1 Experimental Results

In the study, AA7075 aluminum alloy and AZ91 magnesium alloy were coated with different ratios of Al_2O_3 and TiO_2 ceramic materials using the atmospheric plasma method. The corrosion resistance of the coatings made after the coating process was determined. SEM examinations of the coated samples were carried out before and after the corrosion tests. The absence of errors during coating can be expressed as an indication that the coating regime between the substrate and coating material is regular. SEM images of the samples before corrosion tests are given in Figure 3. When the Figure 3 is examined, it is determined that the amount of pores occurring in TiO_2-doped coatings on both AA7075 substrate and AZ91 substrate is higher than Al_2O_3 coatings. This is due to the presence of pores formed during the nucleation of TiO_2.

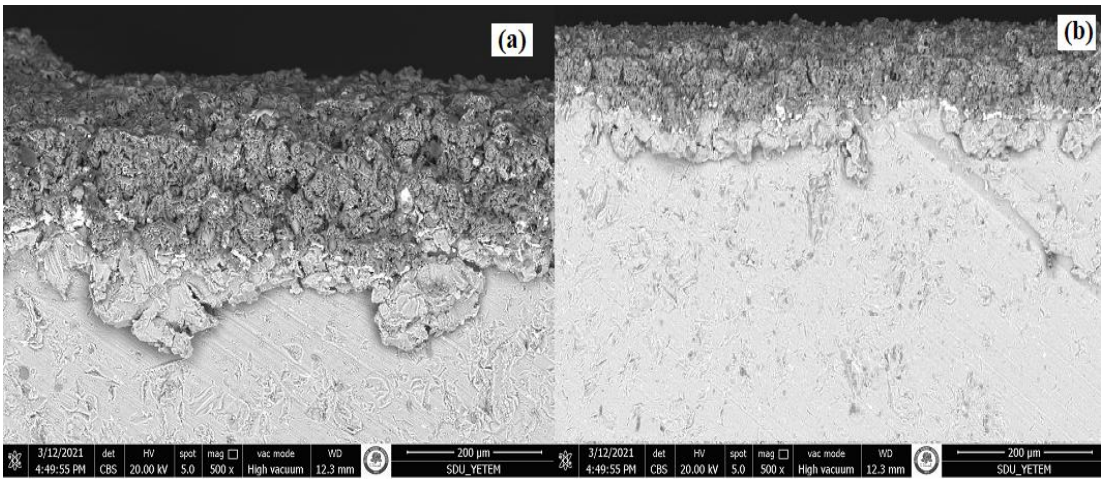

Figure 3. SEM images of the samples before corrosion tests (a) %40 TiO_2 and %60 Al_2O_3 coated AA7075 substrate (b) %40 TiO_2 and %60 Al_2O_3 coated AZ91 substrate

In the study, SEM examinations were also carried out after the corrosion test.SEM examinations of AA7075 substrate after the corrosion tests in 3.5%NaCl and 0,3M H_2SO_4 enviroments in Figure 4; SEM examinations of AZ91 substrate after the corrosion tests in 3.5%NaCl and 0,3M H_2SO_4 enviroments are given in Figure 5. Al added into Mg eliminates the destructive effect of aggressive Cl- ions with its oxide film on the surface. For this reason, with the coating of Al_2O_3 on AZ91 material, the corrosion resistance (1,044 mpy) of AZ91 material increased and the situation is supported in SEM images. The addition of TiO_2 into Al_2O_3 caused the formation of cracks and pits in the samples, and these formations are observed in SEM images. When SEM images of corrosion experiments performed in 0.3M H_2SO_4 environment were examined, a decrease in corrosion resistance occurred with the increase in TiO_2 ratio, similar to 3.5%NaCl environment. After the corrosion tests of the coatings made on AA7075 substrate in 3.5% NaCl solution, the highest corrosion resistance value was obtained in 100% Al_2O_3 (3,486 mpy) coated samples due to the absence of defects such as porosity, and this is supported by SEM examinations. In 0.3M H_2SO_4 solution, the highest corrosion resistance was obtained in 100%TiO_2 coated samples (). This is due to the fact that TiO_2, which has a low melting temperature, melts and disperses into Al_2O_3, increasing the effectiveness of the coating (Jia et al.,2015). This situation is supported by SEM images.

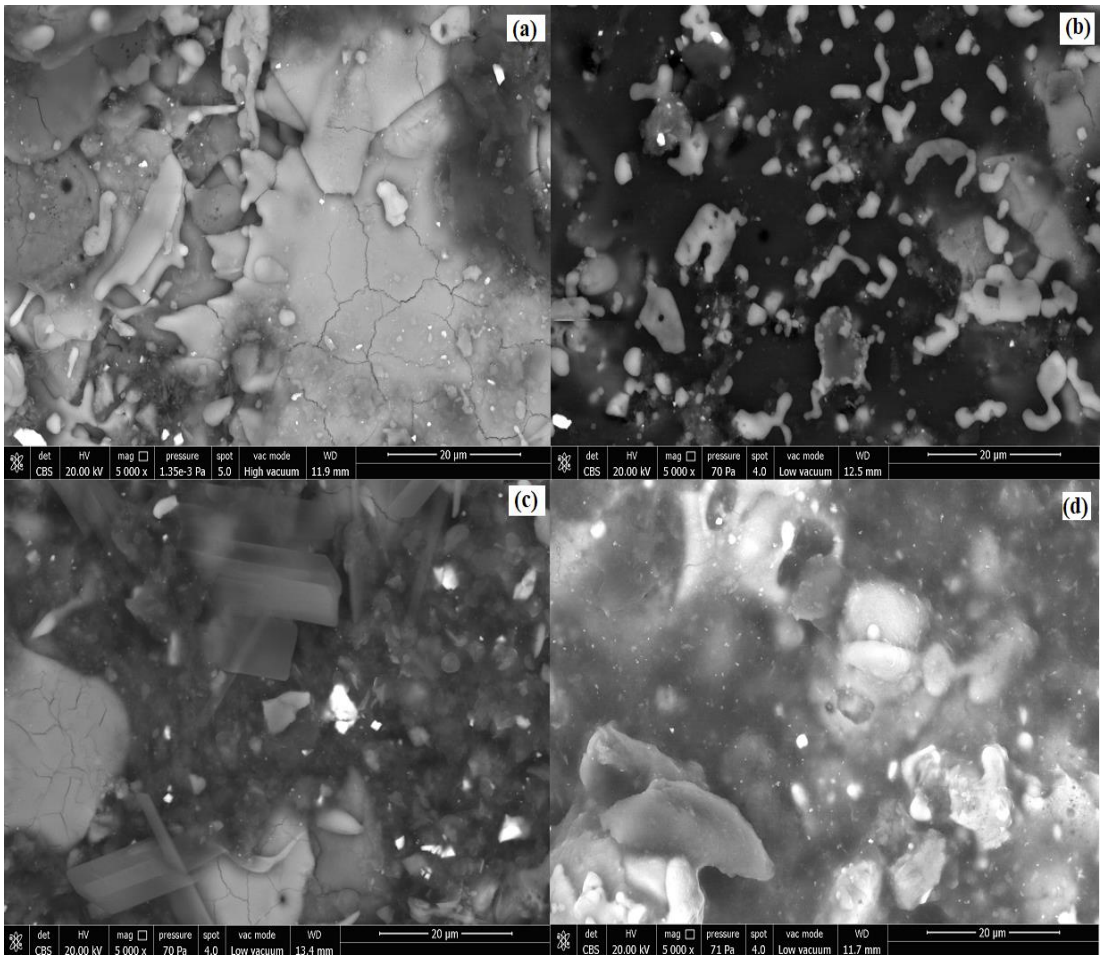

Figure 4. SEM examinations of AA7075 substrate after the corrosion tests in (a) %40 TiO2 coated samples in %3,5 NaCl enviroment (b) %100 Al_2O_3 coated samples in %3,5 NaCl enviroment (c) %40 TiO2 coated samples in 0,3M H_2SO_4 enviroment (d) %100 Al_2O_3 coated samples in 0,3M H_2SO_4 enviroment

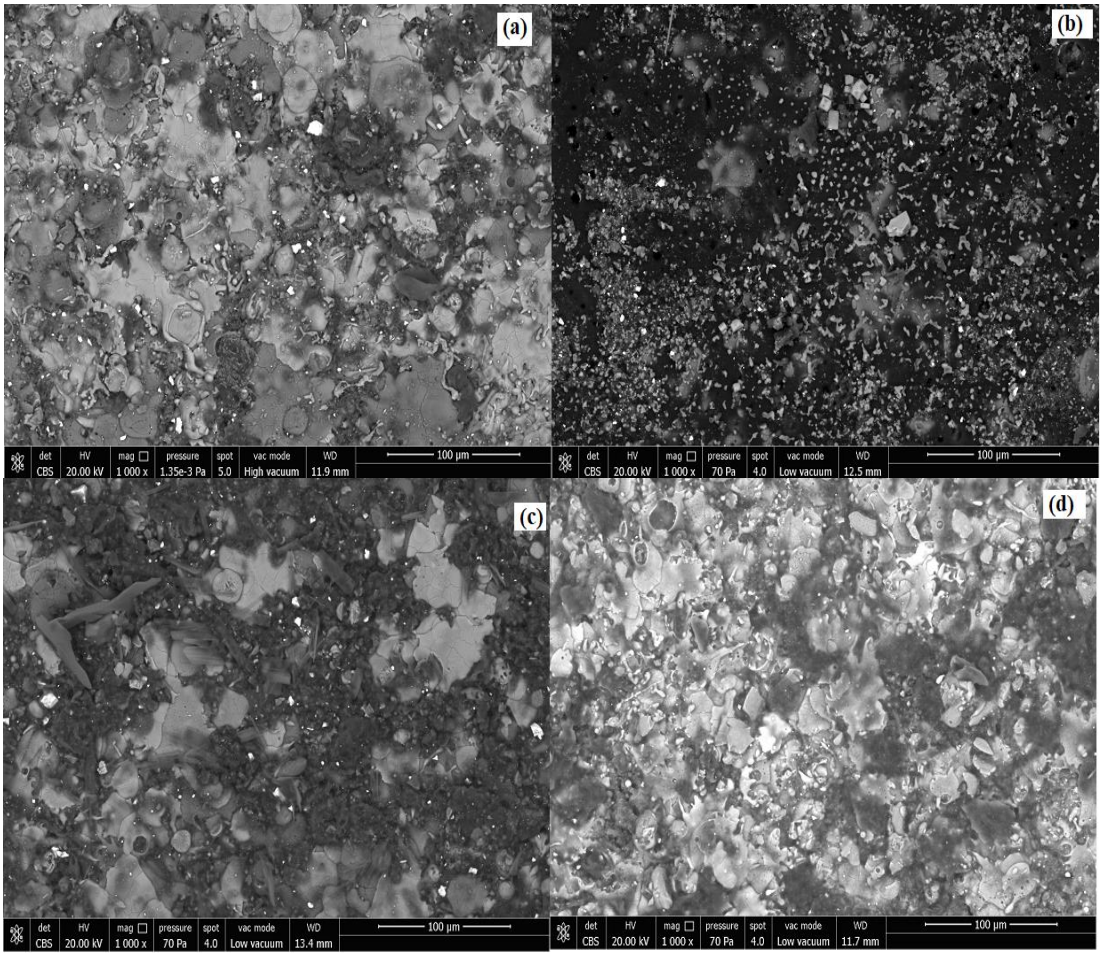

Figure 5. SEM examinations of AZ91 substrate after the corrosion tests in (a) %40 TiO2 coated samples in %3,5 NaCl enviroment (b) %100 Al_2O_3 coated samples in %3,5 NaCl enviroment (c) %40 TiO2 coated samples in 0,3M H_2SO_4 enviroment (d) %100 Al_2O_3 coated samples in 0,3M H_2SO_4 enviroment

3.2 Dataset and Implementation Details

In this study, boosting (XGboost), tree-baggaging (randomforest) and neural network (ANN) structures were used. 80% of the 24 data was used for training and 20% for testing.It consists of corrosion rate values depending on the different corrosive environment and coating material for the study. Accordingly, the values of the substrate (I1), corrosive environment (I2) and coating material (I3) were taken as input, and the corrosion rate value (Q1) was taken as output. Python was used for this study.

3.3 Test and Evaluation

The important point in machine learning methods is to determine the features in the data set very well. In the study, firstly, training and test datasets were created. The developed model can then be used to predict the properties of the studied coating ratios. In this way, determination of optimum coating rates can be achieved quickly. In this study, 5 real test data and corrosion rate values predicted by machine learning models were compared (Table 3). When the results were examined, the best results were obtained as XG Boost Regression, Random Forest Regression and ANN, respectively.

Table 3. Test and predicted corrosion rate values

Experimental Results				XG Boost Regression	Random Forest	ANN
Substrate	Coating material	Corrosive enviroment	Real Output	Predict	Predict	Predict
AZ91	Uncoated	NaCl	826,9522	834,400	734,0888	833,8445
AA7075	%40 TiO_2	NaCl	89,2100	100,6060	123,0795	68,0182
AZ91	%3 TiO_2	NaCl	75,5805	75,7700	43,7842	1,7842
AZ91	%40 TiO_2	H_2SO_4	130,2622	97,6800	169,9654	3,4454
AZ91	%100 Al_2O_3	NaCl	45,9537	59,500	34,2997	1,1855

In addition, R^2, RMJE and MAE values were calculated for all 3 methods and are given in Table 4.

Table 4. Algorithm performances according to estimation results

Algoritma	R^2	RMJE	MAE
XG Boost Regression	0,9968	0,0203	0,0156
Random Forest Regression	0,9614	0,0709	0,0605
ANN	0,9584	0,0736	0,0023

When Table 4 is examined, the best results were obtained in the XG Boost Regression algorithm with 0.9968 R^2 value, 0.0203 RMJE and 0.0156 MAE values. This algorithm is followed by Random Forest and ANN.

When the results were examined, machine learning algorithms to obtain the corrosion rate value depending on different corrosive environment, substrate and coating material ratios gave results close to the real test data. Accordingly, time and cost savings can be achieved by using machine learning methods.

4. CONCLUSION

In the study, AA7075 aluminum alloy and AZ91 magnesium alloy were coated with different ratios of Al_2O_3 and TiO_2 ceramic materials using the atmospheric plasma method. It was observed that the amount of pores occurring in TiO2-doped coatings on both AA7075 substrate and AZ91 substrate is higher than Al_2O_3 coatings after coating process. coating of Al_2O_3 on AZ91 material, the corrosion resistance of AZ91 material increased both in %3,5NaCl and 0,3M H_2SO_4 enviroment. the coatings made on AA7075 substrate in 3.5% NaCl solution, the highest corrosion resistance value was obtained in 100% Al_2O_3 coated samples. In 0.3M H_2SO_4 solution, the highest corrosion resistance was obtained in 100%TiO_2 coated samples.

In this study, it is aimed to predict corrosion rate values using machine learning algorithms depending on different substrate material, corrosive environment and coating material ratios. At the end of the study, it was determined that corrosion rate values could be estimated with low error rates within the acceptable range. Thus, it has been concluded that estimating each time without experimenting can provide significant savings in terms of time and cost.

5. ACKNOWLEDGEMENTS

This study was supported by Süleyman Demirel University Scientific Research Projects Coordination Unit with Project number of FDK-2019-7386. The authors thank Prof. Dr. Yusuf Kayalı for their contributions to this work. This study was produced from Hüseyin Özkavak's PhD thesis.

6. CONFLICT OF INTEREST

The authors reported no conflict of interest.

7. AUTHOR CONTRIBUTION

Hüseyin ÖZKAVAK and Recai Fatih TUNAY determining the concept and design process of the research and research management, data collection and analysis, data analysis and interpretation of results'.

8. REFERENCES

Al-Fakih, A.M., Algamal, Z.Y., Lee, M.H., Abdallah, H.H., Maarof, H., Aziz, M, Quantitative structure–activity relationship model for prediction study of corrosion inhibition efficiency using two-stage sparse multiple linear regression. Journal of Chemometrics 30, 361–368,2016.

Altinkok, N., Koker, R., Neural network approach to prediction of bending strength and hardening behaviour of particulate rein forced (Al–Si–Mg)-aluminium matrix composites. Materials & Design 25(7), 595–602,2004.

Aslan, A. (ICSAR'22) Akciğer Kanserinin Derin Öğrenme Yaklaşımları Kullanılarak Tespit Edilmesi. 1076-1082, 2022.

Ashby, M.F., Bréchet, Y.J.M., Cebon, D., Salvo, L., Selection strategies for materials and processes. Material&Design 25,51-67,2004.

Basha, M. T., Srikantha, A., Venkateshwarlua, B., A Critical Review on Nano structured Coatings for Alumina-Titania (Al2O3-TiO2) Deposited by Air Plasma Spraying Process (APS). Materials Today: Proceedings 22, 1554–1562, 2020.

Bakhsheshi-Rad, H.R., Daroonparvar, M., Yajid, M.A.M., Kumar, P., Razzaghi, M., Ismail, A.F., Sharif, S., Berto, F., Characterization and Corrosion Behavior Evaluation of Nanostructured TiO2 and Al2O3-13 wt.% TiO2 Coatings on Aluminum Alloy Prepared via High-Velocity Oxy-Fuel Spray. Journal of Materials Engineering and Performance, 30, 1356–1370, 2021.

Behara, S., Poonawala, T., Thomas, T., Crystal structure classification in ABO3 perovskites via machine learning. Comp. Mater. Sci., 188, 2021.

Bilgin, M. Makine Öğrenmesi. Papatya Yayincilik, Istanbul,2018.

Bolelli, G., Lusvarghi, L., Barletta, M., HVOF-Sprayed WC-CoCr coatings on Al alloy: Effect of the coating thickness on the tribological properties. 17th International Conference on Wear of Materials 267, 944-953,2009.

Cameron, A.C.and Windmeijer, F. A., An R-squared measure of goodness of fit for some common nonlinear regression models. Journal of Econometrics 77, no. 2,329-342, 1997.

Chai, T. and Draxler, R. R., Root mean square error (RMSE) or mean absolute error (MAE) ?–Arguments against avoiding RMSE in the literature. Geoscientific Model Development 7 (3), 1247-1250,2014.

Cheng, W., Changxin, W., Yan, Z., Stoichko, A., Dezhen, X., Turab, L., Yanjing, S., Modeling solid solution strengthening in high entropy alloys using machine learning. Acta Materialia, 212, 116917,2021.

Chern-Tong, H. and. Aziz, I. B. A., A corrosion prediction model for oil and gas pipeline using CMARPGA. 2016 3rd International Conference on Computer and Information Sciences (ICCOINS), Kuala Lumpur, Malaysia, 403-407,2016.

Dey, S., Sultana, N., Kaiser, M.S., Dey, P., Datta, S., Computational intelligence based design of age-hardenable aluminium alloys for different temperature regimes. Materials Design 92, 522–534, 2016.

El-Rehim, A.; Alaa, F.; Zahran, H.Y.; Habashy, D.M.; Al-Masoud, H.M., Simulation and prediction of the Vickers hardness of AZ91 magnesium alloy using artificial neural network model. Crystals 10(4), 290,2020.

Ernst, P., Fletcher, K., SUMEBore – thermally sprayed protective coatings for cylinder liner surfaces,1–12,2011.

Fan, J., Wang, X., Wu, L., Zhou, H., Zhang, F., Yu, X., Lu, X., Xiang, Y., Comparison of support vector machine and extreme gradient boosting for predicting daily global solar radiation using temperature and precipitation in humid subtropical climates: A case study in China. Energy Convers. Manag. 164,102–111,2018.

Giard, B., Karlsson, S., Machine learning for the prediction of duplex stainless steel mechanical properties: hardness evolu tion under low temperature aging. Examensarbete Inom Teknik, Grundnıvå, 15 Hp Stockholm, Sverige,2021.

Gibbons, G.J., Hansell, R.G., Down-selection and optimization of thermal-sprayed coatings for aluminum mould tool protection and upgrade. J. Thermal Spray Technology 15, 340-347,2006.

He, S.M., Zeng X., Peng, L.M., Gao, X., Nie, J.F., Ding, W.J., Microstructure and strengthening mechanism of high strength Mg-10Gd-2Y-0.5 Zr alloy. Journal of. Alloy Compounds 427(1), 316-323, 2007.

Han, K., Öztürk, G., Aslan, A., Yapay Sinir Ağları Kullanarak Yüzey Pürüzlülüğü Tespiti. 1st International Conference on Pioneer and Innovative Studies, Konya, Turkey June 5-7, 2023.

Harju, M., Halme, J., Jarn, M., Rosenholm, J.B., Mantyla, T., Influence of Aqueous Aging on Surface Properties of Plasma Sprayed Oxide Coatings. Journal of Colloid Interface Science, 313(1), 194-201, 2007.

Hou, Y., Aldrich, C., Lepkova, K., Kinsella, B., Identifying corrosion of carbon steel buried in iron ore and coal cargoes based on recurrence quantification analysis of electrochemical noise. Electrochim. Acta, 283, 212–220,2018.

Hongyu, M., Pengfei, Q.,Yu, C., Rui, L., Peiling, K.,Fuhui, W., Li, L., Prediction of multilayer Cr/GLC coatings degradation in deep-sea environments based on integrated mechanistic and machine learning models.Corrosion Science, 224, 111513,2023.

Islak, S., Buytoz, S. Plazma Püskürtme Yöntemiyle AISI 304 Paslanmaz Çelik Yüzeyinde Elde Edilen ZrO2/Al2O3-%13 TiO2 Kompozit Kaplamasının Mikroyapı Özellikleri. 6th International Advanced Technologies Symposium, 16-18 May, Elazığ, 6-12, 2011.

Jia, S., Zou, Y., Xu, J., Wang, J., Yu, L., Effect of TiO2 Content on Properties of Al2O3 Thermal Barrier Coatings by Plasma Spraying. Transactions of Nonferrous Metals Society of China, 25, 175-183, 2015.

Jian, F., Xiao, C., Huilong, G., Sidney, L., Helen, L., Development of machine learning algorithms for predicting internal corrosion of crude oil and natural gas pipelines. Computers & Chemical Engineering 177, 108358,2023.

Kilic, A., Odabası, Ç., Yildirim, R., Eroglu, D., Assessment of critical materials and cell design factors for high performance lithium-sulfur batteries using machine learning. Chemical Engineering Journal,390,2020.

Kojima, Y., Project of platform science and technology for advanced magnesium alloys. Materials Transactions 42,1154–1159,2001.

Kumari, S., Tiyyagura, H.R., Douglas, T.E.L., Mohammed, E.A.A., Adriaens, A., Fuchs-Godec, R., Mohan, M.K., Skirtach, A.G., ANN prediction of corrosion behaviour of uncoated and biopolymers coated cp-Titanium substrates. Materials Design 157, 35–51, 2018.

Kurt, A., Buldu, B., Cedimoğlu, İ.H., XGBOOST ve Rastgele Orman Algorıtmalarının Ağ Tabanlı Saldırı Tespıtıne Yönelık Performanslarının Karşılaştırılması. International Marmara Sciences Congress (Spring) Proceedings Book3,2020.

Lei, J., Changsheng, W., Huadong, F., Jie, S., Zhihao, Z., Jianxin. X., Discovery of aluminum alloys with ultra-strength and high-toughness via a property-oriented design strategy. Journal of Materials Science & Technology 98,33-43,2022.

Liu, J., Wang, H., Yuan, Z., Forecast model for inner corrosion rate of oil pipeline based on PSO-SVM. International Journal of Simulation Process Modelling 7, 74–80, 2012.

Liu, R., Wang, M., Wang, H., Chi, J., Meng, F., Liu, L., Wang, F., Recognition of NiCrAlY coating based on convolutional neural network, Material. Degradation 6, 2022.

Michalak, M., Toma, F.-L., Latka, L., Sokolowski, P., Barbosa, M.; Ambroziak, A, A Study on the Microstructural Characterization and Phase Compositions of Thermally Sprayed Al2O3-TiO2 Coatings Obtained from Powders and Water-Based Suspensions. Materials 13, 2638,2020.

Mordike, B.L., Ebert, T., Magnesium properties-application-potential. Materials Science Engineering A, 30237–30245,2001.

Morks, M., Akimoto, K., The Role of Nozzle Diameter on the Microstructure and Abrasion Wear Resistance of Plasma Sprayed Al2O3/TiO2 Composite Coatings. Journal of Manufacturing Processers 10, 1-5, 2008.

Ossai, C.I., A data-driven machine learning approach for corrosion risk assessment-a comparative study. Big Data Cognitive Computer 3, 1–22,2019.

Pei, Z., Zhang, D., Zhi, Y., Yang, T., Jin, L.Fu, D., Cheng, X.,Terryn, H.A., Mol, J.M. C., Li, X., Towards understanding and prediction of atmospheric corrosion of an Fe/Cu corrosion sensor via machine learning. Corros. Sci.,170,2020.

Picas, J.A., Forn, T.A., Rilla, R., Martín, E., HVOF thermal sprayed coatings on aluminium alloys and aluminium matrix composites. Surface and Coating Technology 200, 1178–1181,2005.

Ren, C.-Y., Qiao, W., Tian, X., Natural gas pipeline corrosion rate prediction model based on BP neural network, In Proceedings of the Fuzzy Engineering and Operations Research. Babolsar, Iran, 25–26 October 2012; Springer: Berlin/Heidelberg, Germany, 449–455,2012.

Rotshtein, V.P., Yu, F.I., Proskurovsky, D.I., et al., Microstructure of the near-surface layers of austenitic stainless steels irradiated with a low-energy, high-current electron beam. Surface Coating Technology 180, 382–386,2004.

Shi, Z., Song, G., Atrens, A., Influence of the b phase on the corrosion performance of anodised coatings on magnesium–aluminium alloys. Corrosion Science 47,2760–2777,2005.

Shi, Y., Fu, D., Zhou, X., Yang, T., Zhi, Y., Pei, Z., Zhang, D., Shao, L., Data mining to online galvanic current of zinc/copper Internet atmospheric corrosion monitor. Corros. Sci. ,133, 2018.

Schmidt, J., Shi, J., Borlido, P., Chen, L., Botti, S., Marques, M.A.L., Predicting the thermodynamic stability of solids combining density functional theory and machine learning. Chem. Mater. 29, 5090–5103, 2017.

Song, G., StJohn, D., Corrosion behaviour of magnesium in ethylene glycol, Corrosion Science 46,381–1399,2004.

Šuopys, A., Marcinauskas, L., Kėželis, R., Aikas, M., Uscila, R., Thermal And Chemical Resistance of Plasma Sprayed Al2O3, Al2O3-TiO2 Coatings. Research Square preprint.

Toma, F., Et, A., Corrosion Resistance of Aps and Hvof Sprayed Coatings in The Al2O3-TiO2 System. Journal of Thermal Spray Technology 19,137-147,2009.

Toma, F., Et, A., Corrosion Resistance of Aps and Hvof Sprayed Coatings in The Al2O3-TiO2 System. Journal of Thermal Spray Technology 19, 137-147,2010.

Tian, W., Meng, F., Liu, L., Li, Y., Wang, F., Lifetime prediction for organic coating under alternating hydrostatic pressure by artificial neural network, Sci. Rep. 7, 40827, 2017.

URL: Morde, V., XGBoost Algorithm: Long May She Reign!, Medium , https://towardsdatascience.com/https-medium-com-vishalmorde-xgboost-algorithm-long-she-may-rein edd9f99be63d adresinden alındı.

URL: Brownlee, J., A Gentle Introduction to XGBoost for Applied Machine Learning, 10 Haziran 2020 tarihinde https://machinelearningmastery.com/gentle-introduction-xgboost-applied-machine-learning/

URL: Breiman, L., Cutler, A., Random Forests, 10 Haziran 2020 tarihinde Berkeley Üniversitesi: https://www.stat.berkeley.edu/~breiman/RandomForests/cc_home.htm.

Verma, P., Anwar, S., Khan, S., & Mane, S. B, Network intrusion detection using clustering and gradient boosting, In 2018 9th International Conference on Computing. Communication and Networking Technologies (ICCCNT) ,1-7,2018.

Vel´azquez, J.C., Caleyo, F., Valor, A., Hallen, J.M., Predictive model for pitting corrosion in buried oil and gas pipelines. Corrosion 65, 332–342, 2009.

Xinming, F., Zhilei, W., Lei, J., Fan, Z., Zhihao, Z., Simultaneous enhancement in mechanical and corrosion properties of Al-Mg-Si alloys using machine learning. Journal of Materials Science & Technology 167, 1–13,2023.

Yan, Y., Mattisson, T., Moldenhauer, P., Anthony, E.J., Clough, P.T., Applying machine learning algorithms in estimating the perforamance of heterogeneous, multi-component materials as oxygen carriers for chemical-looping processes. Chemical Engineering Journal, 387,2020.

Yang, B., Cao, J.-M., Jiang, D.-P., Lv, J.-D. Facial expression recognition based on dual-feature fusion and improved random forest classifier. Multimed. Tools Appl. 77, 20477–20499, 2017.

Ya-li G., Cun-shan, W., Man, Y., Hong-bin, L., The Resistance to Wear and Corrosion of Laser-Cladding Al2O3 Ceramic Coating on Mg Alloy.Applied Surface Science 253, 5306-5311,2007.

JOURNAL of
MATERIALS and MECHATRONICS:A

e-ISSN 2717-8811
JournalMM, 2024, 5(1), 143-153
https://doi.org/10.55546/jmm.1481871

Araştırma Makalesi / Research Article

Seçici Katalitik İndirgeme (SCR) Sisteminde Statik Karıştırıcı Kullanımının NO_x Emisyonlarına Etkisinin Deneysel İncelenmesi

Şükrü Ayhan BAYDIR[1]*, Emrah ERÇEK[2]

[1*] Afyon Kocatepe Üniversitesi, Teknoloji Fakültesi, Otomotiv Mühendisliği Bölümü, Afyonkarahisar, Türkiye,
ORCID ID: https://orcid.org/0000-0001-7136-7860, abaydir@aku.edu.tr
[2] Afyon Kocatepe Üniversitesi, Sultandağı Meslek Yüksekokulu, Ulaştırma Hizmetleri Bölümü, Afyonkarahisar, Türkiye,
ORCID ID: https://orcid.org/0000-0001-6441-4200, eercek@aku.edu.tr

Geliş/ Received: 10.05.2024; **Revize/Revised:** 26.05.2024 **Kabul / Accepted:** 28.05.2024

ÖZET: NO_x emisyonlarının canlılar ve çevre üzerindeki olumsuz etkilerinden dolayı dizel motorlardan kaynaklanan NO_x emisyonlarını azaltmak için çeşitli emisyon kontrol sistemleri kullanılmaktadır. Euro-6 standartlarının karşılanabilmesi için dizel motorlarında NO_x emisyonlarının Euro 5 standartlarına göre yaklaşık %60 oranında azaltılması gerekmektedir. Bu kuralları karşılamak için NO_x azaltma teknolojileri geliştirilmiştir ve Seçici Katalitik İndirgeme (SCR), bu düzenlemeleri karşılamak için en etkili yöntemlerden birisidir. Bu çalışmada tek silindirli bir dizel motora SCR sistemi kurularak statik karıştırıcının NO_x emisyonlarına etkisi incelenmiştir. Ortalama egzoz gazı sıcaklığı 345-350 °C aralığında ve püskürtülen Dizel Egzoz Sıvısı (DEF) sıcaklığı oda şartlarında iken altı farklı (80, 160, 240, 320, 400 ve 480 mg/s) DEF debisinde deneyler gerçekleştirilmiştir. Bu debi değerlerinde sistemde statik karıştırıcı olduğu ve olmadığı durumlarda NO_x dönüşüm değerleri arasındaki yüzdesel farklar 6 farklı DEF debisine göre sırasıyla %0,07, %3,01, %16,63, %15,97, %0,39 ve %0,1 olarak hesaplanmıştır. Sisteme statik karıştırıcı eklendiğinde özellikle 240 mg/s DEF debisinde NO_x dönüşüm oranında %17'lik belirgin bir iyileşme tespit edilmiştir. Sonuç olarak yapılan deneyler ile SCR sistemlerinde optimum şartların belirlenmesi ile en iyi NO_x dönüşümünün sağlandığı, minimum DEF tüketiminin elde edilebildiği ve sistemde tortu oluşması gibi olumsuz durumları azaltarak sistem verimliliğini artıran veriler elde edilmiştir.

Anahtar Kelimeler: SCR, NO_x, Statik karıştırıcı, Dizel egzoz sıvısı (DEF), Egzoz emisyon, Dizel motor.

*Sorumlu yazar / Corresponding author: abaydir@aku.edu.tr
Bu makaleye atıf yapmak için /To cite this article

Baydır, Ş. A., Erçek, E. (2024). Seçici Katalitik İndirgeme (SCR) Sisteminde Statik Karıştırıcı Kullanımının NOx Emisyonlarına Etkisinin Deneysel İncelenmesi. Journal of Materials and Mechatronics: A (JournalMM), 5(1), 143-153.

Experimental Investigation of the Effect of Static Mixer Usage on NOx Emissions in Selective Catalytic Reduction (SCR) System

ABSTRACT: Various emission control systems are used to reduce NOx emissions from diesel engines due to their adverse effects on living organisms and the environment. To meet Euro-6 standards, diesel engines need to reduce NOx emissions by approximately 60% compared to Euro 5 standards. NOx reduction technologies have been developed to meet these regulations, and Selective Catalytic Reduction (SCR) is one of the most effective methods. In this study, the effect of a static mixer on NOx emissions was investigated by installing an SCR system on a single-cylinder diesel engine. Experiments were conducted at six different Diesel Exhaust Fluid (DEF) flow rates (80, 160, 240, 320, 400, and 480 mg/s) while the average exhaust gas temperature was in the range of 345-350°C and the injected DEF temperature was at ambient conditions. Percentage differences in NOx conversion values between cases with and without a static mixer in the system for six different DEF flow rates were calculated as 0.07%, 3.01%, 16.63%, 15.97%, 0.39%, and 0.1%, respectively. A significant improvement of 17% in NOx conversion rate was observed, especially at a DEF flow rate of 240 mg/s when a static mixer was added to the system. Consequently, experiments have determined the optimum conditions in SCR systems, achieving the best NOx conversion, minimizing DEF consumption, and reducing adverse conditions such as sediment formation in the system, thereby enhancing system efficiency.

Keywords: SCR, NO_x, Static mixer, Diesel exhaust fluid (DEF), Exhaust emission, Diesel engine.

1. GİRİŞ

Azot oksit (NO_x) emisyonları ulaşım, sanayi ve ısınma kaynaklı olup çevre ve insan sağlığı üzerinde olumsuz etkisi olan hava kirleticilerdir. Taşıtlarda kullanılan içten yanmalı motorlar da yüksek yanma sıcaklıkları sonucu oluşan NO_x emisyonları özellikle dizel motorlarda büyük bir çevre sorunu haline gelmiştir. NO_x emisyonlarını azaltmak için Egzoz Gazları Resikülasyonu (EGR) gibi çeşitli yöntemler kullanılmıştır. Yanma esnasında alınan bu yöntemler hala kullanılmakta olup emisyon standartlarını karşılayamadığı için yanma sonrası birtakım önlemler alınmıştır. NO_x emisyonlarının düşürülmesi amacıyla yanma sonrası uygulanan en etkin yöntem Seçici Katalitik İndirgeme (SCR) sistemidir. Seçici katalitik indirgeme, günümüz dizel motorlarında NO_x emisyonlarını azaltmak için kullanılan yanma sonrası egzoz emisyon kontrol sistemlerinden en etkili ve yaygın teknolojilerdendir (Braun ve ark., 2019).

SCR işleminde otomotiv uygulamalarında kullanılan Dizel Egzoz Sıvısı (DEF) olarak adlandırılan sulu üre çözeltisi enjektör ile SCR katalizörünün önüne egzoz gazı üzerine püskürtülür. Yüksek sıcaklığın etkisiyle ilk olarak termoliz reaksiyonu ile üre ayrışarak amonyağa (NH_3) ve izosiyanik aside (HNCO) dönüşür. Daha sonra izosiyanik asit hidrolize uğrayarak amonyak (NH_3) ve karbondioksit (CO_2) ürünleri meydana getirir. Termoliz ve hidroliz reaksiyonları sonrası elde edilen amonyak (NH_3) bileşikleri katalizör içerisinde azot oksit (NO_x) emisyonları ile reaksiyona girerler. NO_x emisyonları zararsız olan azot (N_2), su (H_2O) ve daha az zararlı olan N_2O'ya indirgenirler. Şekil 1'de SCR sisteminde gerçekleşen kimyasal olaylar şematik olarak gösterilmektedir (Erçek ve Baydır, 2023a).

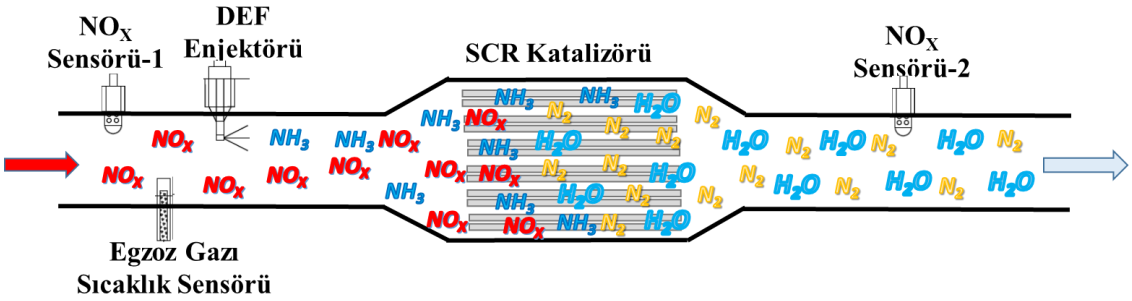

Şekil 1. SCR sistemi gerçekleşen kimyasal olaylar (Erçek ve Baydır, 2023a)

SCR performansı değerlendirilmesinde iki önemli tasarım değişkeni dikkate alınır. Bunlar NO_x'u düşürmek ve katalizörde "NH_3 slip" olarak adlandırılan amonyak birikimini engellemektir. Ürenin eksik ayrışması tortu türü yan ürünleri meydana getirebilir (Braun ve ark., 2019). Bu tortular, SCR katalizörünün uzun vadeli katalitik performansına zarar verebilir. Aynı zamanda NH_3 birikimi, büyük miktarlarda amonyağın atmosfere yayılımına sebep olur. Yönetmelik gereği NH_3 kayması (slip) maksimum 10 ppm'i geçmemelidir. Amonyak zehirli olduğu kadar tehlikelidir. Ayrıca son derece uçucudur ve amonyum sülfat ve amonyum nitrat tuzları gibi zararlı maddeler oluştururlar (Stelzer, 2014).

Azot oksitleri (NO_x) düşürmek, amonyağın egzoz gazı ile ne kadar etkili karıştığına bağlıdır. SCR tasarımında yüksek miktarlarda NO_x düşüşü veya dönüşümü hedeflenir. Katalizör girişinde amonyağın egzoz gazı ile homojen karışımı katalizör ömrünü uzattığı gibi NO_x dönüşümü için gerekli olan katalizör boyutlarını azaltır (Stelzer, 2014).

SCR sistemlerinde egzoz gazının hava akış yönünü değiştirerek farklı yönlerde türbülanslı akışı sağlamak için egzoz borusuna bir statik karıştırıcı yerleştirilmiştir. Bu yöntem, ürenin radyal yönde hızla hareket etmesini ve karışmasını sağlamaktadır. Böylece egzozun enine kesitinde homojen bir dağılım elde edilmektedir. Karıştırıcı egzoz gazı ile amonyak gazını tam olarak karıştırabilmesine rağmen belli bir basınç kaybına da neden olacaktır (Zhu ve ark., 2022).

SCR sistemlerindeki karıştırıcıların performansları egzoz borusu çapına, enjektör tipine ve montaj açısına, kütlesel akış hızına ve yönüne, sıcaklığına ve karıştırma uzunluğuna bağlıdır (Kurzydym ve ark., 2022).

Kurzydym ve arkadaşları SCR karıştırıcısı önünde enjektör borusunun iki çeşidini (S tipi ve düz boru tasarımı) kullanarak deneysel çalışma yapmışlardır. S-tipi boru tasarımında ürenin egzoz gazlarının akışı yönünde eş merkezli olarak enjekte edilmesi sağlanmıştır. Sonuç olarak S tipi borunun, düz boru tasarımına kıyasla ürenin daha iyi ayrıştığını, üre birikimi tortularının azaldığını ve ayrıca optimum NO_x azalma verimliliğini elde etmişlerdir (Kurzydym ve ark., 2022).

Cho ve ark., 2014 tarafından gerçekleştirilen sayısal ve deneysel analiz, üre-SCR sisteminde amonyak dağılımının homojenliği ve NO_x dönüşüm verimliliğini araştırmak için çoklu karıştırıcıların ve ayrıştırıcıların uygulanmasının amonyak dağılımını önemli ölçüde iyileştirdiğini ve oluşan türbülanslı girdabın sulu üre çözeltisinin daha iyi ayrışmasını desteklediğini göstermiştir (Zhu ve ark., 2022).

SCR tasarımlarında karıştırma oranının iyileştirilmesi için yapılabilecek işlemler şunlardır (Sorrels ve ark., 2019);

- Egzoz gazı ve amonyağın yeterince karışımını sağlamak için amonyak enjeksiyonu ve katalizör arasında yeterli kanal uzunluğu,
- Enjekte edilen sıvının akış yönüne statik karıştırıcı montajı,
- Enjekte edilen sıvının basıncını artırma,

- Enjektörlerin ve/veya enjeksiyon bölgelerinin sayısını artırma ve reaktif dağılımını, püskürtme açısını ve yönünü iyileştirmek için enjeksiyon meme tasarımını değiştirmektir.

Bu çalışmada SCR verimini ve çalışmasını etkileyen statik karıştırıcının NO_x emisyonlarına etkisi deneysel olarak incelenmiştir.

2. MATERYAL VE YÖNTEM

Bu çalışmada tek silindirli dizel motora SCR sistemi düzeneği kurulmuştur (Erçek ve Baydır, 2023a). Deney düzeneği Şekil 2'de görülmektedir. Deney düzeneğinde sensörlerden gelen analog sinyaller National Instruments USB-4716 veri toplama kartı ile dijital sinyallere dönüştürülerek veriler bilgisayarda LabVIEW program ara yüzünde işlenmekte ve excel formatında saklanmaktadır.

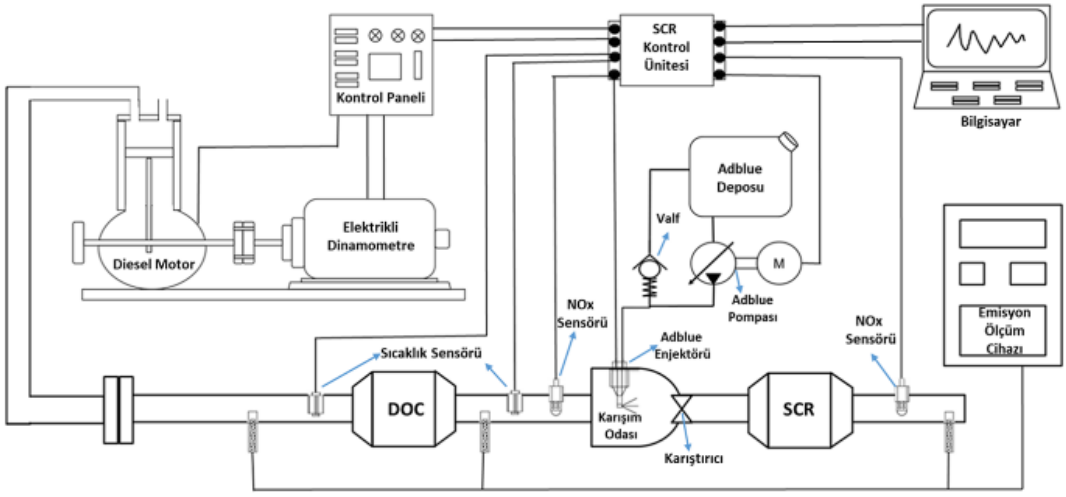

Şekil 2. Deney düzeneğinin şematik görünümü

Deney düzeneğinde Antor 3LD 510 marka ve modelli doğal emişli, hava soğutmalı, direkt enjeksiyonlu, tek silindirli dizel motor kullanılmıştır. Deneylerde kullanılan dizel motorunun teknik özellikleri Çizelge 1'de verilmiştir.

Çizelge 1. Deney motorunun teknik özellikleri (Anonymous, 2023a)

Özellik	Değer
Model	Antor 3LD 510
Silindir Sayısı	1
Silindir Hacmi	510 cm³
Sıkıştırma Oranı	17,5:1
Motor Devri	3000 rpm
Motor Gücü	12 hp (8,84 kW)
Maksimum Tork	3,35 kg-m @1800 rpm
Özgül Yakıt Sarfiyatı	190 g/HP-h
Soğutma Tipi	Hava soğutmalı

Egzoz gazı sıcaklık ölçümlerinde NiCr-Ni, K tipi termokupl kullanılmıştır. Deney düzeneğinde yoğunluğu 400 cpsi olan vanadyum bazlı V_2O_5-WO_3/TiO_2 SCR katalizörü kullanılmıştır. Dizel oksidasyon katalizörü (DOC), seramik malzemeden yapılmış evrensel tip standart katalizördür. DEF olarak ISO 22241 standardına uygun üretilmiş doğayla uyumlu su bazlı üre çözeltisi kullanılmıştır. SCR katalizör öncesi ve sonrası iki adet Continental marka UniNO_x

sensörü kullanılmaktadır. Ancak bu sensörler anlık olarak SCR sistemi katalizör verimlerini takip etmekte olup NO_x emisyonları egzoz gaz analizöründen ölçülmektedir. Egzoz çıkışındaki NO_x ölçümleri Bosch BEA060 egzoz gaz analizörü ile yapılmıştır. Egzoz emisyon ölçüm cihazı teknik özellikleri Çizelge 2'de görülmektedir.

Çizelge 2. Egzoz emisyon ölçüm cihazı teknik özellikleri (Anonymous, 2023b)

Bileşenler	Ölçüm aralığı	Çözünürlük
NO (ppm)	0 - 5000	1
CO (% hacimsel)	0 - 10	0,001
CO_2 (% hacimsel)	0 - 18	0,01
HC (ppm)	0 - 9999	1
O_2 (% hacimsel)	0 - 22	0,01
Lambda	0,5 – 9,999	0,001

SCR sisteminde DEF'in egzoz gazı içerisine püskürtülmesinde kullanılan Bosch marka 2. nesil (deNOX 2.2) DEF enjektörü Şekil 3'te gösterilmiştir.

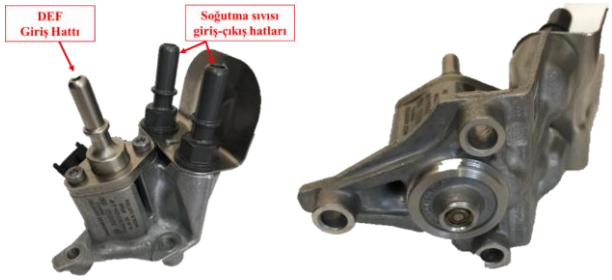

Şekil 3. Dizel Egzoz Sıvısı (DEF) enjektörü

Elektronik olarak anlık kumanda edilebilen, çok hızlı açılıp kapanabilme özelliği olan kademeli olarak püskürtme yapılabilen selenoid (elektrovalf) tip enjektördür. Pompa tarafından basınçlandırılan DEF enjektörde basınçlı halde bulunur ve sinyal gönderildiği an püskürtme gerçekleştirilir. 12 volt gerilimle çalışan 9 bar'a kadar basınçla üç delikten püskürtme yapabilmektedir. Çizelge 3'de enjektöre ait teknik özellikler verilmiştir.

Çizelge 3. DEF enjektörü teknik özellikleri (Anonymous, 2023c; Anonymous, 2023d)

Özellik	Değer
Hizmet Ömrü	35.000 saate kadar
Maksimum Ortam Sıcaklığı	180 °C
Çalışma Basıncı	9 bar
DEF Giriş Sıcaklığı	90 °C

SCR sistemlerinde NO_x dönüşüm oranlarına büyük etkisi olan egzoz gazı ile dizel egzoz sıvısı karışımının daha iyi olması için enjektör önüne konumlandırılan portatif (gerektiğinde çıkartılabilen) statik karıştırıcı ve montajı Şekil 4. e görülmektedir. Statik karıştırıcı bağlandığı noktada sabit durmaktadır. Herhangi bir dönme hareketi yapmamaktadır. Statik karıştırıcı çapı 49 mm, uzunluğu 40 mm olup içerisinde girdap oluşturabilmesi için kıvrımlar bulunmaktadır. Enjektör püskürtme noktasından statik karıştırıcı girişine kadar olan uzaklık 60 mm'dir. Statik karıştırıcı çıkışından SCR katalizör girişine kadar olan uzaklık 143 mm'dir.

Şekil 4. SCR statik karıştırıcı ve montajı

Egzoz gazı sıcaklığının motor sonrası emisyon kontrol sistemleri (DOC, DPF ve SCR) üzerinde önemi oldukça büyüktür. DOC ve SCR katalizörlerindeki kimyasal reaksiyonların etkin bir şekilde gerçekleşebilmesi için belirli bir sıcaklığa ihtiyaç duyulmaktadır. Bu sıcaklık değeri katalizörün niteliğine ve katalist maddesine göre değişim gösterebilmektedir. Sıcaklık değerindeki aşırı artışlar (600 ^{o}C ve üzeri) katalizörler için tehlike arz etmektedir. Yüksek sıcaklıklar katalizörün yapısının bozulmasına ve katalizörün zarar görmesine yol açmaktadır (Reşitoğlu, 2020).

SCR sistemlerinde NO_x'in dönüşüm verimliliği yüksek oranda egzoz gazı sıcaklığına bağlıdır. Sistemde kullanılan statik karıştırıcının NO_x dönüşüm oranına etkisini test edebilmesi için ilk aşamada sistemde statik karıştırıcı varken deneylerin sabit bir egzoz gaz sıcaklığında yapılması gerekmektedir. Bu nedenle optimum egzoz gaz sıcaklığı belirlenmelidir.

- Deney öncesinde dizel motoru yarım gaz kolu açıklığında 10 dakika boşta çalıştırılarak çalışma sıcaklığına getirilmiştir.
- Daha sonra gaz kolu tam açık konuma getirilerek yüksüz durumda iken motor devri 3200 rpm olarak ölçülmüştür.
- Gaz kolu tam açık konumda ve motor yüksüz iken maksimum egzoz gaz sıcaklığının 180-190 °C seviyelerine ulaştığı tespit edilmiştir.
- Egzoz gaz sıcaklığını artırmak için motor elektrikli dinamometre ile yüke bindirilmiş ve egzoz gazı sıcaklık sensörünün ölçmüş olduğu sıcaklık istenilen değere geldiğinde gaz kolu sabitlenmiştir.
- Birinci aşamada 5 farklı (210, 258, 308, 350, 385 °C) egzoz gazı sıcaklığında ve iki farklı (240-320 mg/s) DEF püskürtme debisinde NO_x değerleri kayda alınmıştır ve NO_x dönüşüm oranları hesaplanmıştır.
- Püskürtülen DEF sıcaklığı oda şartlarındadır.
- Optimum egzoz gazı sıcaklığı 300-360 °C aralığında iken maksimum NO_x dönüşüm oranı elde edilmiştir.

İkinci aşamada statik karıştırıcının NO_x dönüşüm oranına etkisini belirleyebilmek için sistemde statik karıştırıcı varken altı farklı (80, 160, 240, 320, 400 ve 480 mg/s) DEF püskürtme debisinde ilk aşamada belirlenmiş olan optimum egzoz gaz sıcaklığı değerlerine göre daha dar 345-350 °C'lik sıcaklık aralığı kullanılmıştır.

Üçüncü aşamada sistemde statik karıştırıcı yokken ikinci aşamadaki şartlar altında deneyler tekrarlanmıştır.

İkinci ve üçüncü aşama deneyleri en az üçer defa tekrarlanarak yapılmış ve yüzdesel NO_x dönüşüm oranlarının ortalamaları alınarak değerlendirmeler gerçekleştirilmiştir.

Gaz kolu tam açık konumda, motor yüke bindirildiğinde yaklaşık 2800 rpm devirde çalışırken ikinci ve üçüncü aşamalardaki egzoz gaz sıcaklığı elde edilebilmektedir.

Deneyler tekrarlanırken istenilen egzoz sıcaklığına ulaştıktan sonra DEF püskürtmesi gerçekleştiği için motor yükünün önemi bulunmamaktadır. Motor yüküne göre deney yapılması halinde egzoz gaz sıcaklıkları değişiklik göstereceği için sıcaklıktan bağımsız sadece statik karıştırıcının etkisi doğru belirlenemeyecektir.

3. BULGULAR VE TARTIŞMA

3.1. SCR Sisteminde Farklı Egzoz Gazı Sıcaklıklarının NO_x Dönüşümüne Etkisi

SCR sistemlerinde yapılan çalışmalar NO_x'in dönüşüm verimliliğinin yüksek oranda egzoz gazı sıcaklığına bağlı olduğunu göstermektedir. NO_x dönüşüm oranı egzoz gazı sıcaklığının artmasıyla önce artar, sonra düşer. Reaksiyon genellikle 200 °C'de başlar ve 350 °C'de maksimum dönüşüm oranına ulaşır. 200 °C'nin altındaki egzoz gazı sıcaklıklarında üre ayrışma reaksiyonu SCR sisteminin iç çeperlerinde kaldırması oldukça zor olan tortular oluşturabilir. Bu sorunu önlemek için üre enjeksiyonu genellikle egzoz gazı sıcaklığı 200 °C'nin üzerine çıktığında başlamaktadır (Wang ve ark., 2019).

Sıcaklık aralıkları kullanılan SCR katalizör tipine göre değişmektedir. Deney düzeneğinde vanadyum bazlı SCR katalizörü kullanılmıştır. Vanadyum bazlı V_2O_5 gibi katalizörler 260 °C ile 450 °C arasında en verimli çalışan malzemelerdir (Braun, 2019).

Materyal ve yöntem bölümünde birinci aşamada belirtilen farklı egzoz gaz sıcaklıklarına ve farklı DEF püskürtme debilerine göre DEF püskürtüldükten sonraki ölçüm verilerinden hesaplanan NO_x emisyonlarındaki yüzdesel dönüşüm oranları Çizelge 4 ve Şekil 5'de gösterilmiştir.

Çizelge 4. Farklı egzoz gazı sıcaklıklarına ve DEF debilerine bağlı NO_x dönüşüm değerleri

Sıcaklık (°C)	209,5	258	307,5	350,4	385
NO_x Dönüşümü (%) 240 (mg/s) DEF Debisinde	3,57	13,83	22,4	24,17	25,32
NO_x Dönüşümü (%) 320 (mg/s) DEF Debisinde	3,95	17,48	19,4	22,83	26,83

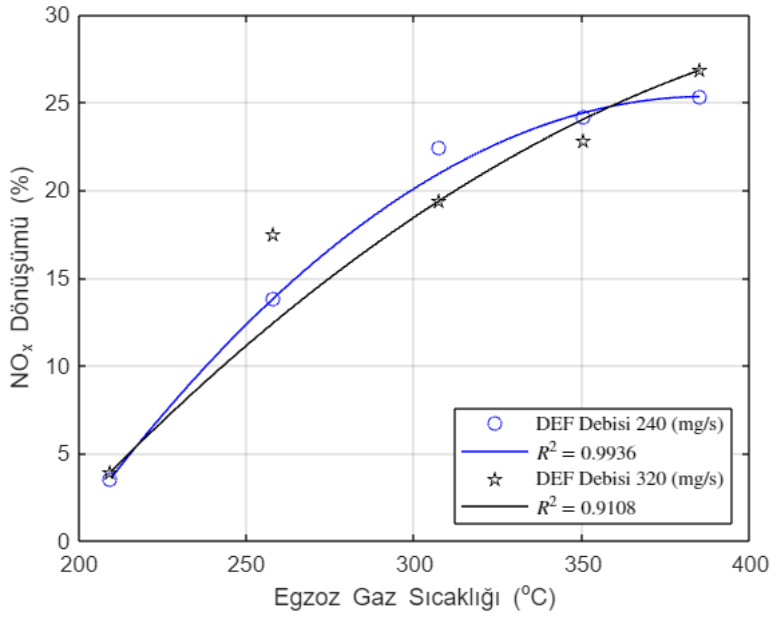

Şekil 5. Farklı egzoz gazı sıcaklıklarına bağlı NO_x dönüşüm oranı

3.2. SCR Statik Karıştırıcısının NO_x Emisyonlarına Etkisi

SCR sistemlerinde katalizör önüne sıcak egzoz gazına püskürtülen DEF, termoliz ve hidroliz reaksiyonlarının gerçekleşmesi ile NH_3 gazı üretimi sağlar. SCR katalizör girişinde NH_3 gazı ile NO_x emisyonları reaksiyona girerek azot ve oksijene ayrışır. Üre-SCR reaktörleri yüksek NO_x dönüşüm performansı, düşük NH_3 kayması ve düşük üre tüketimini sağlayacak şekilde kontrol edilir. NO_x dönüşüm verimini en üst düzeye çıkarmak ve NH_3 kaymasını en aza indirmek için püskürtülen DEF ile egzoz gazı akışının türbülanslı karıştırılması ve SCR katalizörü önünde homojen bir akış elde edilmesi önemlidir. Özellikle, ürenin NH_3'e ayrışma hızını iyileştirmek, amonyak (NH_3) ve izosiyanik asidin (HNCO) homojen dağılımını sağlamak için sisteme karıştırıcılar eklenmektedir.

Yapılan deneysel çalışmalarda motor tipi ve büyüklüğüne bağlı olarak karıştırıcıların %20 oranında NO_x dönüşümüne olumlu etki ettiği görülmüştür. SCR deney sistemi tasarımında bu durumu göz önüne tutarak sisteme portatif takılıp çıkarılabilir statik karıştırıcı eklenmiştir. Statik karıştırıcı sisteme dahil edildiğinde veya çıkarıldığında SCR sisteminin verimi tespit edilmiştir.

Sistemde öncelikle statik karıştırıcı var iken ikinci aşama ve statik karıştırıcı çıkartılıp üçüncü aşama deneyleri yapılmış, NO_x dönüşüm oranları hesaplanmıştır. Şekil 6'da SCR sisteminde statik karıştırıcı durumuna ve 6 farklı DEF püskürtme debisine göre elde edilen verilerden hesaplanan NOx dönüşümü yüzdelerinin değişimi gösterilmektedir.

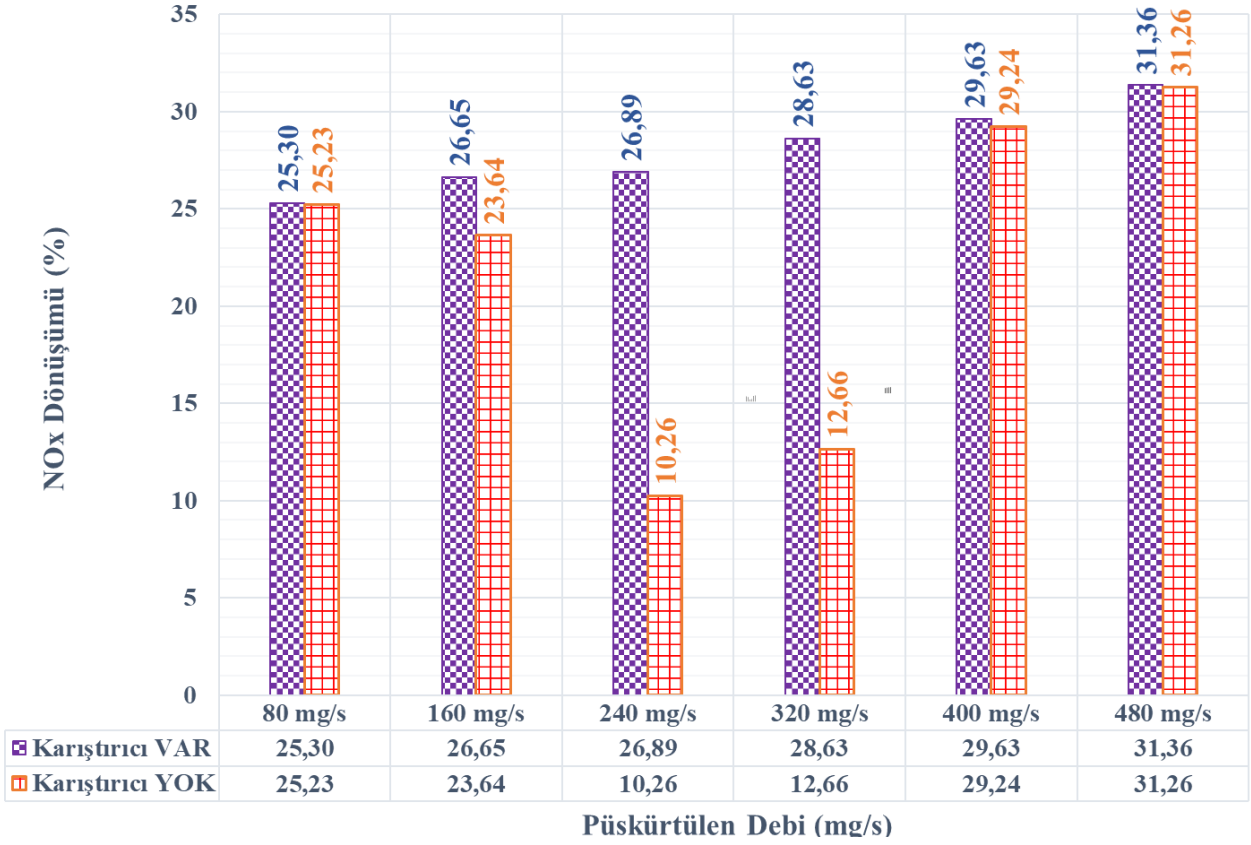

Şekil 6. SCR statik karıştırıcısının farklı DEF püskürtme debilerinde NO_x emisyon dönüşümüne etkisi

Şekil 80 mg/s'lik DEF debisinde statik karıştırıcı olduğunda %25,30, olmadığında %25,23'lük bir NO_x dönüşüm oranı elde edilmektedir. Arada büyük bir fark olmadığı neredeyse aynı performansın olduğu söylenebilir. Bunun nedeni püskürtülen DEF miktarı çok düşük olduğundan egzoz gaz basıncı ve hızı ile yeterince türbülansın meydana geldiği ve karışımın katalizöre girmeden yeterince homojen hale geldiği söylenebilir.

DEF debisi arttırılıp 160 mg/s'ye çıkarıldığında statik karıştırıcı olduğunda %26,65'lik NO_x dönüşüm oranı gerçekleşirken statik karıştırıcı olmadığında bu oran %23,64'e düşmektedir.

Statik karıştırıcının etkisini görebilmek için DEF debisi 240 mg/s'ye çıkarıldığında statik karıştırıcının varlığında %26,89'luk bir değişim gerçekleşirken statik karıştırıcı kaldırıldığında bu oran %10,26'lara kadar düşmektedir.

Yapılan bu deneyler göz önüne alındığında DEF debisi artırılarak 320 mg/s'de statik karıştırıcı var ve yok iken sırasıyla %28,63 ve %12,66'lık bir değişim gerçekleştiği görülmüştür.

Özellikle 240 ve 320 mg/s'lik DEF debilerinde statik karıştırıcının SCR performansı üzerinde büyük rol oynadığı görülmektedir. Statik karıştırıcı olduğunda NO_x dönüşüm oranında yaklaşık %16'lık bir artış olduğu gözlemlenmiştir.

DEF debisi artırılarak 400 ve 480 mg/s'de deneyler yapıldığında statik karıştırıcının NO_x dönüşüm oranına etkisinin düştüğü gözlemlenmiştir. SCR sistemlerinde olması gerekenden fazla DEF püskürtülmesi durumunda NH_3 kayması meydana gelmektedir. NH_3, NO_x emisyonları ile reaksiyona girmeden dışarı atılmaktadır. Bu istenmeyen bir durumdur. Yapılan deneylerde 400 ve 480 mg/s debilerde DEF püskürtüldüğünde ortamda fazladan NH_3 oluşmuştur. Katalizör girişinde karışım yoğun bir şekilde amonyak içerdiği için kendi içinde homojenlik sağlamıştır. SCR sistemine püskürtülecek DEF miktarı için optimum şartlar sağlandığında statik karıştırıcının büyük ölçüde önem taşıdığı yapılan deneylerde görülmektedir.

4. SONUÇ

SCR sistemlerinde püskürtülen DEF ile egzoz gazı akışının homojen karışımının sağlanması katalizör önünde düzgün dağılımlı bir akış elde edilmesi önemlidir. Yapılan deneysel çalışmalarda motor tipi ve büyüklüğüne bağlı olarak karıştırıcıların %20-30 oranlarında NO_x dönüşümüne etki ettiğini gösterilmiştir. Kurulan SCR deney sisteminde bu durumu dikkate alınarak sisteme portatif, takılıp çıkarılabilir statik karıştırıcı eklenmiştir.

Deneyler birinci aşamada belirlenen ortalama egzoz gazı sıcaklığı 345-350 °C aralığında iken altı farklı DEF debisinde gerçekleştirilmiştir. Bu DEF debi değerlerinde sistemde statik karıştırıcının olduğu ikinci aşama ve olmadığı üçüncü aşama deneylerinde NO_x dönüşüm değerleri arasındaki yüzdesel farklar 6 farklı DEF debisine göre sırasıyla %0,07, %3,01, %16,63, %15,97, %0,39 ve %0,1 olarak hesaplanmıştır.

Özellikle 240 ve 320 mg/s'lik DEF debilerinde statik karıştırıcının SCR sisteminde NOx dönüşüm performansı üzerinde büyük etkisinin olduğu görülmektedir. 240 mg/s'lik DEF debisinde statik karıştırıcı olduğunda NO_x dönüşümünde yaklaşık %17'lık bir iyileşme olduğu tespit edilmiştir. Literatürde yapılan çalışmalar ile benzerlik göstermektedir.

Abdulhamid ve ark. SCR katalizör girişine bıçaklı karıştırıcı ve kanatlı karıştırıcı olmak üzere iki farklı tipte statik karıştırıcı yerleştirerek hesaplamalı akışkanlar dinamiği (HAD) analizi gerçekleştirmişlerdir. Her iki statik karıştırıcının birlikte sistemde kullanıldığında %92,8'lik en iyi üre dönüşüm veriminin elde edildiği, tek başına kullanımlarda kanatlı karıştıcının ise bıçaklı karıştırıcıya göre %10,86 daha yüksek üre dönüşüm verimliliği sağladığını ortaya koymuşlardır. Statik karıştırıcı tasarımları değiştirilerek verimin daha da artırılacağı anlaşılmaktadır (Abdulhamid ve ark., 2017).

Düşük ve yüksek DEF debilerinde SCR sisteminde statik karıştırıcının varlığı veya yokluğunda NOx dönüşüm oranında büyük bir fark olmadığı, püskürtülen DEF'in egzoz gazı ile yeterince homojen karıştığı söylenebilir. Yüksek debilerde ise gereğinden fazla DEF püskürtüldüğü için ortamda yeterince NH_3 oluşmuş ve karışım yoğun bir şekilde kendi içinde homojenlik sağlamıştır. 3

kata varan DEF debisi artışına rağmen NOx dönüşüm oranları aynı oranda artmamış, bununla birlikte amonyak salınımı ve tortu oluşma riski artmıştır.

SCR sistemine püskürtülecek DEF miktarı için optimum şartlar sağlandığında statik karıştırıcının büyük ölçüde önem taşıdığı yapılan deneylerde görülmektedir.

5. TEŞEKKÜR

Bu çalışma Afyon Kocatepe Üniversitesi Bilimsel Araştırma Projeleri Koordinasyon Birimi tarafından 20.FEN.BİL.27 nolu proje kapsamında desteklenmiştir. Yazarlar desteklerinden dolayı BAP birimine, proje kapsamında görev alan elektronik altyapının hazırlanmasında destek veren Manisa Celâl Bayar Üniversitesi Elektrik Mühendisliği Bölümünden Sayın Doç. Dr. İsmail YABANOVA'ya, motor test düzeneğinin hazırlanmasında destek veren Afyon Kocatepe Üniversitesi Otomotiv Mühendisliği Bölümünden Sayın Doç. Dr. Yaşar Önder ÖZGÖREN'e, Katalizör malzemesinin tedarikinde ve bilgisinde desteğini esirgemeyen Mersin Üniversitesi Otomotiv Teknolojisi Bölümünden Sayın Doç. Dr. İbrahim Aslan REŞİTOĞLU'na teşekkür eder.

6. ÇIKAR ÇATIŞMASI

Yazarlar, bilinen herhangi bir çıkar çatışması veya herhangi bir kurum/kuruluş ya da kişi ile ortak çıkar bulunmadığını onaylamaktadırlar.

7. YAZAR KATKISI

Şükrü Ayhan BAYDIR: Kavramsallaştırma, Süpervizyon, Proje Yönetimi, Yazılım, Veri Toplama ve İşleme, Kaynaklar, İlk Analiz, Doğrulama, Veri Görselleştirme, Araştırma, Yazım - Gözden Geçirme ve Düzenleme ve Emrah ERÇEK: Kavramsallaştırma, Yazım - İlk Taslak, Kaynaklar, Veri Toplama ve İşleme, İlk Analiz, Doğrulama, Araştırma, Yazım - Gözden Geçirme ve Düzenleme ile çalışmaya katkı sağlamışlardır.

8. KAYNAKLAR

Abdulhamid, J., Bhanuprakash, T. V. K., Rao, P. V. J. M., Numerical Analysis of the Effect of Static Mixer on SCR System Performance of Marine Diesel Engine. International Journal of Engineering and Techniques 3(5), 183–188, 2017.

Anonymous, 2023a. ANTOR 3LD510 Use and Maintenance Manual, https://anadolumotor.com/_docs/uploads/pdf/ANTOR_3LD510_Kullanim_Bakim_El_Kitapcigi_TR_ENG_FR.pdf(Erişim Tarihi: 13.02.2023).

Anonymous, 2023b. BEA 060-Bosch Emissions Analysis-Technical Data, http://mediathek.bosch-automotive.com/files/bosch_wa/989/182.pdf(Erişim Tarihi: 13.02.2023).

Anonymous, 2023c. Diesel Systems Denoxtronic 2.2 – Urea Dosing System for SCR systems - Technical Features, https://www.yumpu.com/en/document/read/7945158/diesel-systems-denoxtronic-22-bosch-automotive-technology(Erişim Tarihi: 13.02.2023).

Anonymous, 2023d. The dosing module is designed to inject AdBlue® into the exhaust system-Technical specifications, https://www.bosch-mobility-solutions.com/en/solutions/exhaust-gas-treatment/dosing-module-cv/(Erişim Tarihi: 13.02.2023).

Braun, P., Rabl, H., Matysik, F., Investigations on the Liquid-Phase Decomposition of AdBlue Urea for the Selective Catalytic Reduction Process. Chemie Ingenieur Technik, 91(7), 961–968, 2019.

Erçek, E., Baydır, Ş. A., A Study on the Effect of Injection Injection Amount on NO_x Emissions in the Selective Catalytic Reduction (SCR) System in a Single Cylinder Diesel Engine. International Journal of Automotive Science And Technology, 7(1), 37–43, 2023a

Erçek, E., Baydır, Ş. A., Tek Silindirli bir Dizel Motoru için Seçici Katalitik İndirgeme (SCR) Sistemi Tasarımı ve İmalatı, The 3rd International Symposium on Automotive Science and Technology (ISASTECH 2023), Ankara, 7-8 Eylül, pp: 546–560, 2023.

Kurzydym, D., Żmudka, Z., Perrone, D., Klimanek, A., Experimental and numerical investigation of nitrogen oxides reduction in diesel engine selective catalytic reduction system. Fuel, 313, 2022.

Reşitoğlu, İ. A., Effect of Catalyst Used in Exhaust Line on Emission Characteristics of a Single-Cylinder Diesel Engine. Journal of Current Research on Engineering, Science and Technology, 6 (2), 95-102, 2020.

Stelzer, D. M., Design and Evaluation of an Improved Mixer for a Selective Catalytic Reduction System, University of Toronto Graduate Department of Mechanical Engineering & Industrial Engineering, Master Thesis, 2014.

Wang X., Song G., Wu .Y, Yu L., Zhai Z. A., NOx emission model incorporating temperature for heavy-duty diesel vehicles with urea-SCR systems based on field operating modes. Atmosphere (Basel) 10(6), 2019.

Zhu, Y., Zhou, W., Xia, C., Hou, Q., Application and Development of Selective Catalytic Reduction Technology for Marine Low-Speed Diesel Engine: Trade-Off among High Sulfur Fuel, High Thermal Efficiency, and Low Pollution Emission. Atmosphere, 13(5), 731, 2022.

JOURNAL of
MATERIALS and MECHATRONICS:A

e-ISSN 2717-8811
JournalMM, 2024, 5(1), 154-167
https://doi.org/10.55546/jmm.1468390

Araştırma Makalesi / Research Article

Investigation of Wear Behaviour of TiO_2 and Al_2O_3 Reinforced YSZ Coating

Ali AVCI[1]*, Muhammet KARABAŞ[2]

[1*] Hakkari University, Faculty of Engineering, Hakkari, Türkiye,
ORCID ID: https://orcid.org/0000-0003-3901-6248, aliavci@hakkari.edu.tr
[2] Kırklareli University, Faculty of Aeronautics and Astronautics of Science, Kırklareli, Türkiye,
ORCID ID: https://orcid.org/0000-0002-0666-6132, mkarabas@klu.edu.tr

Geliş/ Received: 15.04.2024**;** **Revize/Revised:** 30.05.2024 **Kabul / Accepted:** 03.06.2024

ABSTRACT: In this study, three different ceramic powders used as thermal barriers were coated on AISI304 stainless steel by the atmospheric plasma spray method. A pin-on-disc apparatus was utilised to investigate the wear characteristics of the coatings. The effect of wear behavior of the addition of Al_2O_3 and titanium dioxide (TiO_2) into the YSZ coating was investigated. Before the wear test, sanding and polishing processes were carried out to ensure that the average surface roughness of the coatings was less than 0.8 µm. The wear test according to ASTM G99-04, was conducted on a pin-on-disc device at a speed of 143 rpm. The test was performed in a dry condition, with a minimum of 8000 cycles. The wear test utilised a 4N load and 6 mm-diameter Al_2O_3 balls. The surface properties and wear characteristics of the coatings were analysed using a scanning electron microscope (SEM) and energy-dispersive X-ray spectroscopy (EDS) after conducting coating and wear tests. The wear rate of the samples was assessed using optical profilometry. A micro Vickers test equipment was employed to assess the microhardness of the materials. The findings demonstrated that the inclusion of Al_2O_3 in YSZ led to an enhancement in wear resistance, but the incorporation of TiO_2 resulted in a notable reduction in wear resistance.

Keywords: Wear, Ceramic coatings, YSZ coating, Hardness.

1. INTRODUCTION

Ceramic materials provide many advantages when coated on metal or plastic due to their properties such as high hardness, high thermal-corrosion resistance, and low specific gravity. The coatings produced have the potential to be used in many different areas due to their superior properties such as high hardness, low density, high melting point, low thermal conductivity, and oxidation resistance, for example; microelectronics, automotive, and wear parts (Thakare et al., 2021),(Özçelik et al., 2024). These coatings are utilised for safeguarding gas turbines and engine components that

*Sorumlu yazar / Corresponding author: aliavci@hakkari.edu.tr
Bu makaleye atıf yapmak için /To cite this article

Avcı, A., Karabaş, M. (2024). Investigation of Wear Behaviour of TiO2 and Al2O3 Reinforced YSZ Coating. Journal of Materials and Mechatronics: A (JournalMM), 5(1), 154-167.

are subjected to high temperatures, particularly zirconium, because of their exceptional thermal insulating properties, high density, strong resistance to abrasion, and low thermal conductivity. In particular, gas turbines subjected to elevated temperatures utilise gearbox components, turbine blades, rocket nozzles, exhaust systems, bearings, and rings. Similarly, internal combustion engines employ piston cylinder heads, valves, internal combustion chambers, and exhaust systems (Noroozpour and Akbari, 2023),(Iqbal et al., 2024). Ceramic coating enhances engine efficiency, prolongs engine lifespan, and diminishes fuel consumption and petrol emissions (Avci et al., 2018). Thermal barrier coatings (TBC) typically include two distinct layers: a metallic bond layer and a ceramic layer. The metal bond layer treated the thermal expansion disparities between the metal material and the ceramic. A ceramic layer is a thermally insulated layer that is subjected to heat and often coated using the APS process. The significant porosity of APS coatings enables the movement of oxygen from the upper layer to the lower layer, resulting in the formation of a thermal-growing oxide between the bond layer and the ceramic layer. As temperatures grow, the generation of TGO also increases, which might result in damage. To enhance the durability of coatings and enhance their strength, it is necessary to regulate the level of porosity, optimise coating parameters, employ laser modification techniques, and utilise a suitable micro structure. Yitria stabilezed zirconium (YSZ), which is stabilised with 8% wt. of yttrium, is commonly utilised as a ceramic layer material in TBC systems due to its exceptional resilience to thermal shock and oxidation, corrosion, high thermal insulating capacity, and low thermal conductivity (Avci et al., 2023). Nevertheless, the coating experiences an expansion in volume due to the phase change of YSZ coatings taking place at temperatures over 1200 °C (Jun et al., 2023). These powders enhance the resistance of calcium-magnesium-aluminosilicate (CMAS) to corrosion caused by temperature and decrease structural damage resulting from phase change at higher temperatures. Hot corrosion occurs due to chemical reactions between foreign chemicals, such as vanadium pentoxide and sodium sulfate, present in gas turbine fuel, and the stabiliser phase of ZrO_2 (Javadi Sigaroodi et al., 2024). During operation, gas turbines may come into contact with airborne particles that contain compounds of calcium, magnesium, aluminium, and silicon. When these particles make contact with high-temperature components like the wings and blades of the engine turbine, they adhere to the surfaces and lead to corrosion (Han et al., 2022), (Guo et al., 2024). Researchers are always researching ways to enhance materials and coatings in order to minimize the impact of CMAS corrosion and prolong the lifespan of turbine engines. In order to mitigate the influence of corrosion, TiO_2 and Al_2O_3 powders are incorporated into YSZ to enhance its volume, and cover any faults, cracks, and porosities that may arise during manufacture. Wang et al. (Wang et al., 2022) reported that the YSZ was mixed with 80% Al_2O_3 and 20% TiO_2 powder by weight in a mechanical mixer at a molar mass ratio of 1:3. Subsequently, an isothermal oxidation test was conducted on both the traditional TBCs and the Al_2O_3-TiO_2 composite coating. A morphological and hardness examination was performed to assess the properties of the samples. The addition of Al_2O_3 in the coatings resulted in a higher level of resistance in comparison to traditional TBCs. The interaction between TiO_2 and liquid CMAS is responsible for this development, as it aids in the concentration process of CMAS. Yuan et al. (Yuan et al., 2021) manufactured ceramic powders and formed plates using various compositions of Al_2O_3 and TiO_2, together referred to as ATYSZ. The findings demonstrated that the addition of 10% mol Al_2O_3 and 5% mol TiO_2 (10A5TYSZ) to YSZ resulted in a material that effectively endured CMAS corrosion and had suitable thermal conductivity.

The plasma spray technique yields coatings that exhibit favorable tribological properties and exceptional resistance to wear. The wear and friction characteristics of plasma spray ceramic coatings are primarily influenced by the coating's composition and microstructural properties, including

porosity, morphology, microcracks, and distribution. Based on current literature, the tribological performance of YSZ coatings is influenced by several factors such as different contaminants, dust formations, and operational conditions, including applied loads and wear rates. Various techniques can be employed to prevent metal surfaces from experiencing leakage, including mechanical, chemical, electrochemical, or laser modification methods (Critchlow and Brewis, 1996). Lima and Marple (Lima and Marple, 2005) incorporated TiO_2 into Al_2O_3 using the high-velocity oxygen and fuel (HVOF) technique. The HVOF must be applied through spraying and have to demonstrate exceptional resistance to wear and hardness. Bai et al. (Bai et al., 2023) investigated the abrasion resistance of YSZ coatings over a temperature range of 25 to 800 °C. In addition, the wear and tear of the equipment was exacerbated by the increasing temperatures. Nevertheless, the tribolayer, which is facilitated by the creation of alumina tracks on the surface, provides protection against wear at temperatures exceeding 200 °C. Ormancı et al. (Ormanci et al., 2014) examined the fracture strength and stiffness properties by incorporating both YSZ and TiO_2 into Al_2O_3. The researchers discovered that Al_2O_3-YSZ compounds exhibit greater hardness compared to monolithic Al_2O_3. Furthermore, they observed that the hardness of these compounds diminishes as the YSZ content increases. In order to investigate the effects of wear on TBCs in the workplace, three distinct thermal barriers were coated using atmospheric plasma techniques. These barriers included YSZ, YA, and YAT. A wear test was conducted utilising the pin-on-disk method to investigate the wear characteristics of the coatings under dry conditions. The deformation features and microstructure were investigated using electron microscopy and EDS analysis.

2. MATERIALS AND METHODS

2.1 Materials

The investigation involved the use of AISI 304 austenitic stainless steel (SS) substrate materials, which were precisely cut into circular shapes with a diameter of 1 inch using a laser technique. To improve the mechanical adhesion of the bonding layer, the surfaces of SS coupons were abraded using alumina a fine abrasive material called 200 grit alumina was applied. The alumina particles were abraded from a distance of 30 cm at an angle of approximately 90°, and the spraying process lasted for at least 1 minute. Figure 1a) depicts a three-dimensional representation of the surface smoothness of SS following the process of sanding. The 3D pictures were quantified using the Veeco WYKO NT1100 optical profilometer, resulting in a notable enhancement in smoothness following the sanding process. The substrate material exhibited a Ra value of 358.68 nm in terms of surface roughness, while the grit-blasted substrate material showed a Ra value of 2.69 µm.

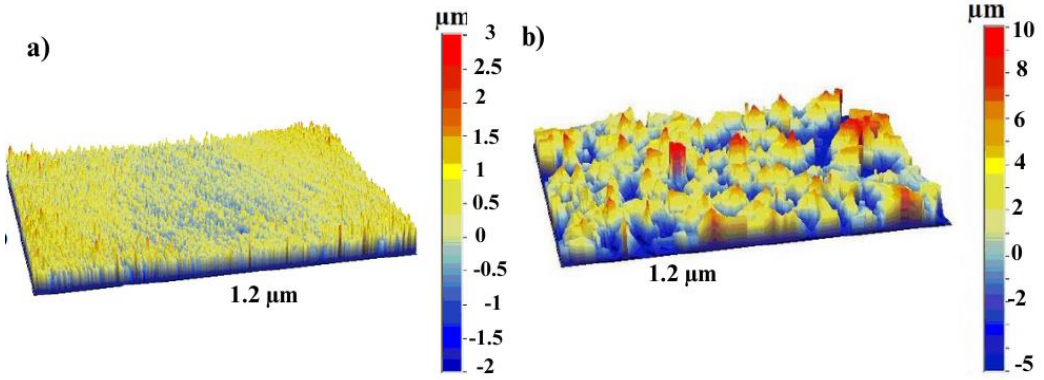

Figure 1. Surface roughness of a)AISI304 before grit blasting, b) AISI304 after grit blasting (Bal et al., 2018)

In the production of TBCs, Sulzer Metco AMDRY 997 (Ni 23Co 20Cr 8.5Al 4Ta 0.6Y) is used for the production of bond layer coatings, and YSZ 204B-NS, commercially offered by Sulzer Metco, is used for the production of ceramic top layer coatings, Al_2O_3 with a purity rate of 98.0%. Metco 105 NS White and TiO_2 powders were used. Figure 2 shows SEM images of the powders. The mixing ratios of the composite composites produced are given in Table 1.

Table 1. Chemical composition of the deposited coating

Sample Name	Feedstock powders		
	YSZ	Al_2O_3	TiO_2
YSZ	100	-	-
YA	83	17	
YAT	80	17	3

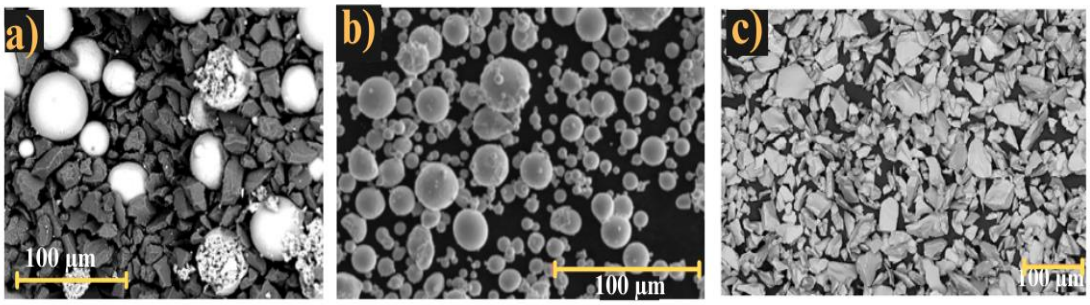

Figure 2. Microstructure of deposited powders; a) Al_2O_3 /YSZ and b) AMDRY 997 bod coat c) TiO_2

A three-axis CNC table supported a Metco DJ2700 HVOF gun that run at a 200 mm/min. The nozzle utilised in the coating procedure was positioned along the central axis of the 3-axis CNC machine, and the mobile nozzle facilitated the uniform coating of the samples on the revolving table. The coupling layer is coated using the HVOF process, and the parameters specified in Table 2 are maintained at a constant value. Within this method, precise control over the gun's movement and the speed of the samples allows for the attainment of coatings with the necessary thicknesses. The energy was derived from the combustion of the air-propane gas mixture with oxygen. In order to achieve the requisite bond layer thickness of 85 ± 15 µm using the HVOF approach, the metal subsurface was coated with 12 passes.

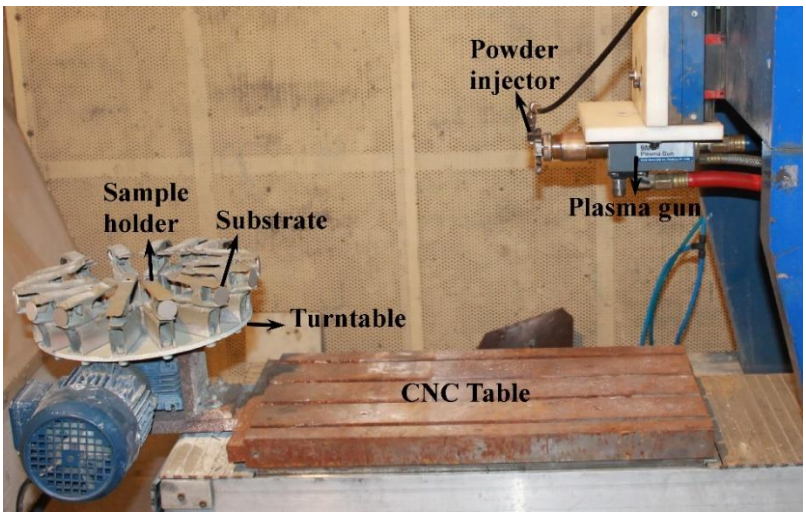

Figure 3. Schematic view of the APS system

Table 2. HVOF deposition parameters

Material	Pressure (Bar)			Flow rate (SCFH)			Process parameters		
Amdry 997 (Ni23Co20Cr8.5Al4Ta 0.6Y)	Oxygen	Propane	Air	Oxygen	Propane	Air	Spray distance (mm)	Feeding speed (g/s)	Spray angle (°)
	10.3	6.2	7.2	24	40	50	250	50	90

Ceramic top layer coatings are produced by atmospheric plasma spraying (APS). The primary and secondary gases and production parameters used in the APS method are shown in Table 3. Before coating, YSZ, alumina, and TiO_2 composite powders were mixed in alcohol for 4 hours in a mixer (turbula). The dried ceramic powders were successfully coated by plasma spraying method using Sulzer Metco 9 MBM plasma spray gun.

Table 3. APS deposition parameters

Parameters							
Current (A)	Primary Gas, Ar(scfh)	Secondary Gas, H_2(scfh)	Carrier Gas Ar(scfh)	Spray Distance (mm)	Gun Speed (mm/s)	Rotation Speed (Hz) rpm	Voltage (V)
500	90	15	13.5	75	200	40	60

2.2 Microstructural Characterization

The surface and cuts of the produced coatings were examined with an electron microscope. For this purpose, the coatings were primarily subjected to metallographic grinding and polishing. For the examination of the cuts, the coatings were cut with a diamond cutter and then mowed and metallographic polishing. The microstructure tests of the samples were carried out with the optional EDS Phenom XL SEM device in different sizes. The worn tracks were examined with an optical microscope and SEM as well. In SEM studies, different detectors were used to understand the characteristics of the type of wear. EDS analyses were carried out using the mapping method for wear tracks.

2.3 Wear and Microhardness

The state of the surface is the primary determinant of the tribological performance of the coatings. The samples' surface smoothness after coating ranges from 1.5 to 2.4 μm. The melting and polishing procedures were performed to achieve an average surface roughness (Ra) of less than 0.8 μm for the coatings. The surface roughness was quantified by taking measurements at a minimum of five distinct locations on the surface, using a radius of 5 μm. Next, the sample surfaces are thoroughly cleansed using acetone to remove any oils or undesired debris and then dried using hot air. The weight of the coatings has been measured both before and after wear using a precise track in order to determine the amount of wear loss. The displacement test for each sample was conducted using a pin-on-disk device (Tribo Tester, France) operating at a speed of 143 revolutions per minute (rpm) and a minimum of 8000 cycles in a dry environment, following the guidelines of ASTM G99-04. The wear test utilised 6 mm diameter Al_2O_3 balls under a fixed load of 4N. The thickness of the traces produced during the wear test was measured using an optic microscope in order to estimate the amount of deformation.

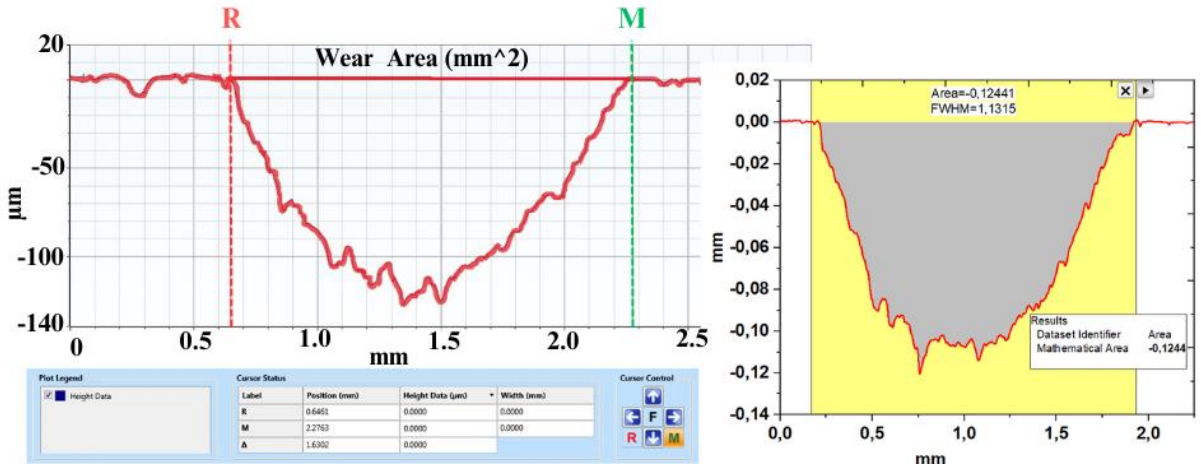

Figure 4. Wear volume measurement

Figure 4 shows the 2D profile of the wear trace taken from the mechanical profilometer. For area calculation, the area of the curve was redrawn with the help of Origin Lab Pro software, and the amount of wear was found with the help of the formulas below.

$$\textbf{Equation:1}\ Volumetric\ wear\ rate\ \frac{mm^3}{Nm} = \frac{Volume\ loss\ (mm^3)}{Sliding\ Distance\ (m)\ x\ Applied\ load\ (N)}$$

The volumetric wear rate was calculated from Equation 1 (Franco et al., 2024). The friction coefficient was provided directly by the wear tester device. The wear volume was calculated with the help of a profilometer as seen in Figure 4. In this study, the sliding distance was used as 250 m and the applied load was 4 N for each sample. Since there is no obvious wear on the alumina abrasive ball; the wear of the alumina ball is ignored in calculations.

The coatings produced in the atmospheric plasma spraying technology get increasingly tougher as the spraying speed increases. The presence of oxides in the coating often enhances its hardness while reducing its adhesive strength. The hardness of the coating layers fluctuates based on factors such as porosity, the heterogeneous structure of the layer, and the applied stress values. The hardness measurements were obtained from the surface of the coatings using the HVS1000 micro-vickers, manufactured by Bulut Machine in Türkiye. The charging duration for a mass of 300 grams is established as 15 seconds. The outcome was obtained by calculating the arithmetic mean of 10 hardness values that were randomly tested at 12 distinct points on the surface of the sample. The highest and smallest measurement values were disregarded in this calculation. The measurement was conducted with a minimum distance of 3 mm from the edges to prevent errors that could lead to the building of tension on the edges and an uneven distribution of the applied load when the floating end comes into contact with the sample. The surface roughness has been evaluated at a Ra below 0.8 µm due to its impact on the mechanical characteristics of the material.

3. RESULTS AND DISCUSSION

3.1 Microstructural characterization

Figure 5 shows micro-SEM images of coatings deposited by the APS process. Figure 5a shows a cross-sectional SEM image of YSZ coating. Upon examination of the cross-sectional SEM image, it was found that there was a ceramic top layer measuring roughly 135 µm and a bond layer measuring 75 µm. The YSZ exhibits a laminar structure and contains some voids. Figure 5b presents a cross-sectional of the YA coating. Deposition of lamellar alumina and YSZ plates has been achieved

effectively. The dark regions depicted in the image correspond to alumina, whilst the white regions correspond to YSZ. Figure 5c displays the cross-section and specific features of the YAT coating. The grayscales in the microstructure of the plates are attributed to TiO_2. Additionally, the slices exhibited both porosity and inter-splat crackles. These structures are all created by the inherent properties of the APS coating in TBCs. Porosities are formed from the consecutive deposition of unmelted or partially melted particles during the coating process. Intersplat crackles are created through a process of cooling and collision, where hot particles pass through a plasma flame and gather as splats upon impact with a surface. In thermal barrier applications, the presence of porosity and interplate fissures hinders the transport of phonons. This diminishes the layer's heat conductivity. Porosity in TBC applications can reach a maximum of 20%. Coatings with a porosity exceeding this amount exhibit reduced adhesion and cohesiveness. During the investigation of porosity using image analysis, it was found that the YSZ coating has a porosity level of around 15%, while the YAT coating has a porosity level of 4.5% and the YAT coating has a porosity level of 3.8%. The presence of Al_2O_3 and TiO_2 in YSZ greatly decreased the porosity rate of the coated layer (Özçelik et al., 2024). The combination of Al_2O_3 (2000 ºC) and TiO_2 (1850 ºC) powders, which have a lower erosion point, led to the development of a denser layer of splats during plasma spraying compared to YSZ (2700 ºC). The thickness of the binding layer is 85±15 µm. The addition of alumina and TiO_2 to YSZ resulted in a reduction in porosity of around 65% and 70% respectively.

In Figure 5d, the surface SEM of the YSZ coating shows spaces with semi-melted or non-melted particles. The areas shown as black in Figure 5e belong to alumina, whereas the areas seen as YSZ are white. Similar microstructural defects were observed in Figure 5f above.

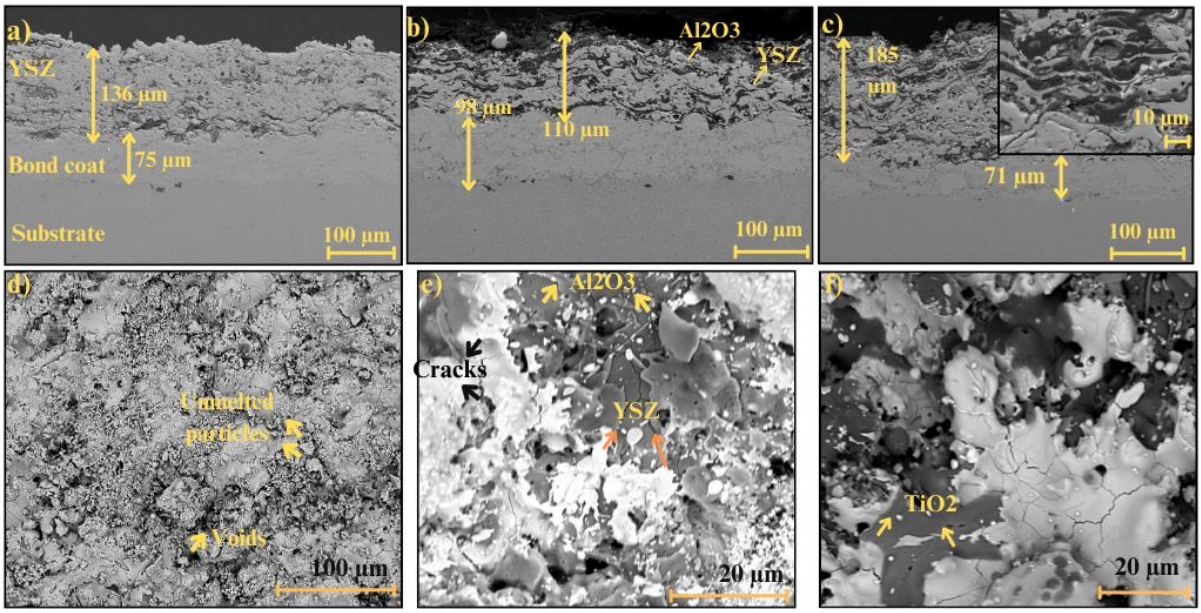

Figure 5. SEM images of coatings; a) Cross-sectional SEM image YSZ, b) Cross-sectional SEM image YA, c) Cross-sectional SEM image YAT, d) Surface SEM image YSZ, e) Surface SEM image YA, e) Surface SEM image YAT

3.2 Hardness and wear behavior of coatings

The impact of incorporating Al_2O_3 and TiO_2 particles into YSZ on the mechanical characteristics of the composite coating was assessed by a hardness test and a wear test. Figure 6a displays a graph that shows the hardness test results of the coatings. The SS substrate was determined to have the lowest hardness value. The YSZ coating exhibited a hardness of 1030±30 HV, which was

enhanced by roughly 25% to 1294±34 HV upon the incorporation of 10% alumina particles. Nevertheless, it was discovered that the inclusion of the TiO_2 addition had a substantial impact on the hardness of the material, causing structural damage. The impact of adding TiO_2 to YSZ on its hardness is typically influenced by the composition, microstructure, and treatment factors. Wang et al. (Wang et al., 2024) reported that the microhardness and porosity of Al_2O_3-13 wt%TiO_2 coating are 856.6HV0.5 and 12.77 %, respectively. When the porosity of the coating decreased to around 8.21%, the hardness value increased and became 1061.4HV(0.5). This is a similar example of how decreasing porosity increases hardness. However, in general, the addition of TiO_2 into YSZ matrix can increase the mechanical properties. This increase can often manifest itself in properties such as fracture, fracture toughness, and wear resistance. The variation in material characteristics is likely due to the essential role played by the quantity of TiO_2 incorporated into the YSZ. Elevated quantities of TiO_2 typically lead to an augmentation in hardness. Moreover, the mechanical properties of the material are determined by the distribution and crystalline structure of TiO_2 within the YSZ. Probably, the reduced TiO_2 concentration resulted in a decrease in the hardness measurement. The enhancement of microcirculation is a result of dispersion. When a good dispersion is achieved, the hardness and mechanical characteristics of TiO_2 particles, which hinder plastic deformation, will increase (He et al., 2022). When the cross-sectional SEM images are examined in Fig. 5c, the distribution of TiO_2 is largely understood. However, due to the nature of the APS technique, agglomeration during flow and voids in the microstructure reduced the hardness value. The higher alumina particle size and being more compatible with YSZ increased the hardness. The hardness value of SS material was found to be 216 ±19 HV. This value is compatible with the austenitic stainless steel mentioned in the literature (Zhao et al., 2005). TiO_2 is utilised for its ability to enhance the resistance of TBCs against calcium-magnesium-aluminosilicate (CaO-MgO- Al_2O_3 -SiO_2) and hot corrosion. Wang et al. (Wang et al., 2022) conducted a study where they combined YSZ with 80% Al_2O_3 and 20% TiO_2 powder by weight to create a composite coating. The YSZ hardness value of the composite coating was initially measured at 920 HV. However, the inclusion of TiO_2 resulted in a reduction of this value to 577 HV. Nevertheless, the presence of the thermal barrier enhanced the coating's resistance to CMAS and thermal shock by facilitating the transformation from t-ZrO_2 to m-ZrO_2. Shen et al. (Shen et al., 2019) investigated the impact of TiO_2 and samarium-added serum oxide (SDC) supplementation on the characteristics of YSZ electrolytes. The hardness results are highly similar. Luo et al. (Luo et al., 2019) investigated the microstructure and the impact of TiO_2 concentration on the mechanical and wear characteristics of YSZ ceramics produced using pressure-free sintering. It was discovered that the YSZ ceramics seen a drop in micro-hardness and wear resistance as the TiO_2 level rose. The researchers discovered that the TiO_2 ratio that induced the highest level of sleepiness was 5%. Yuan et al. (Yuan et al., 2021) utilised the APS approach to coating YSZ with Al_2O_3 and TiO_2 particles at various concentrations. They next examined the impact of CMAS corrosion on the mechanical characteristics. The addition of Al_2O_3 and TiO_2 composite coatings has resulted in an increase in the CMAS resistance and hardness levels. According to the literature, adding TiO_2 in amounts less than 5% does not consistently lead to the required enhancement in mechanical characteristics. On the other hand, TBCs enhance the expected resistance to thermal shock and CMAS. The method of manufacture and the porosity rate of the coating have a substantial impact on this condition. In our previous study, the hardness of the nano YSZ coating created using the electrophoretic deposition technique was measured to be 729 ± 78.6 HV. However, when we introduced TiO_2 in the nanoscale, the hardness decreased to 714.2 ± 92.3 HV.

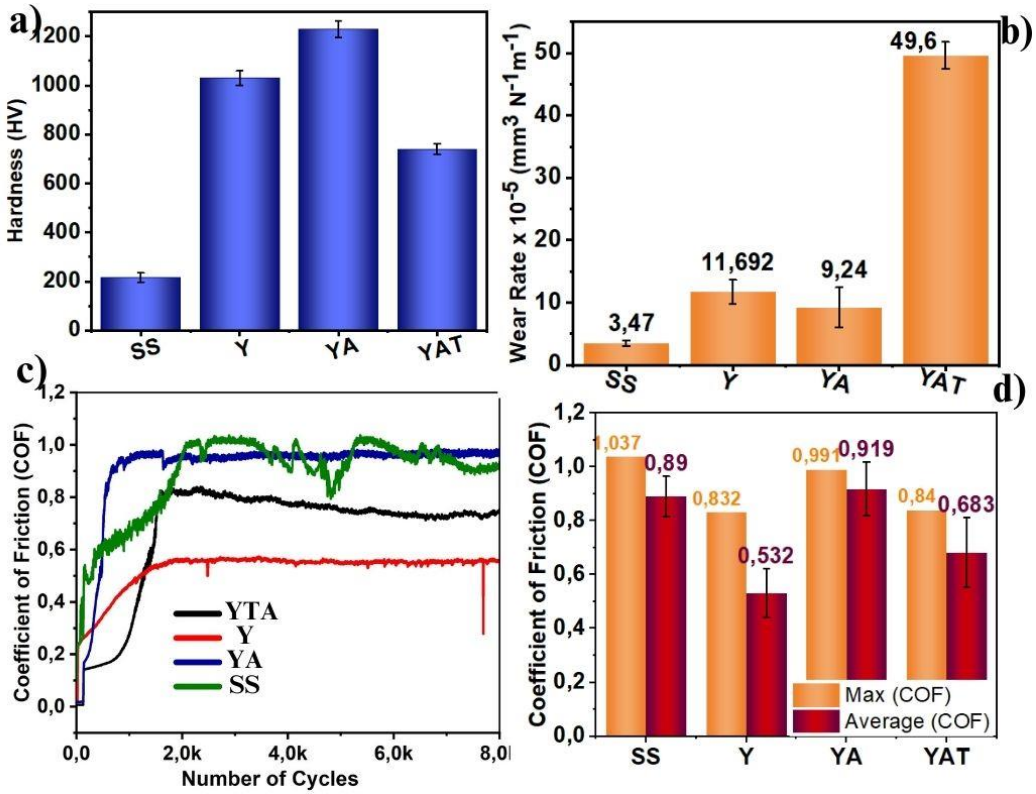

Figure 6. a) Hardness values, b) Wear rate, c), d) Coefficient of friction of coatings and SS

Figure 6b shows the rates at which the coatings and substrate experience wear and tear when subjected to a load of 4N. The distortion rates were derived from Archard's equation. A profilometer was employed to ascertain the magnitude of the displacement's volume. Based on these findings, the YAT sample exhibited the most significant wear, measuring around 50 x 10^{-5}mm^3 N^{-1}m^{-1}. The YSZ coating exhibits a wear resistance of 11.6 x 10^{-5}mm^3 N^{-1}m^{-1}, whereas alumina has a lower wear rate. The reduction in the porosity rate had a notable impact when a denser microstructure was achieved. Franco et al. discovered that as the porosity of the YSZ coating decreased, the resistance to wear rose (Franco et al., 2024). The inclusion of alumina resulted in a notable 26% enhancement in the wear resistance of YSZ, but the addition of TiO_2 had a considerable detrimental effect on its wear resistance. The friction ratio and hardness values of the coatings exhibited a direct correlation with the degree of wear. Coatings that exhibit a lower average friction rate also demonstrate a correspondingly lower wear rate. Furthermore, the presence of the newly formed Al0.1Zr0.9O1.95 (Chen et al., 2018) phase has significantly enhanced the durability of the coating. Enhanced toughness can also enhance the coating's resistance to wear. The friction coefficients are provided in Figures 6c and 6d, based on the number of cycles of the sub-material and the coatings. The friction coefficients acquired from the wear test equipment during the abrasion test are provided in Figure 6c. It was observed that the friction coefficient of the SS substrate material fluctuated under 4 N load and 60 mm s^{-1} speed conditions. The coefficient of friction (COF) exhibited a fluctuating pattern and gradually rose until the 2000th cycle. However, after the 2000th cycle, it reached a stable value of the 3500th cycle. The mean COF value was 0.89 ± 0.075. The coefficient of friction (COF) of the Al_2O_3/TiO_2 coating reduced as the YSZ percentage increased. In Mehar's study (Mehar and Sapate, 2024) similar results were obtained, with the YSZ coating exhibiting the lowest friction coefficient. The probable reason for this variation is the exhaustion of metallic components, as seen by the visible signs of erosion in Figure 7. Additionally, it is recognised that the SS substrate, which has an

austenitic structure, undergoes a partial martensitic transformation when subjected to a load. This transformation leads to an increase in its hardness (Özçelik et al., 2024). In this instance, it results in an increase in the COF value (Zandrahimi et al., 2007). Upon examination of the YSZ COF chart, it was found that the average coefficient of friction was 0.53±0.09. Additionally, the curve showed a steady progression towards the end, which occurred after about 2000th cycles. The average coefficient of friction between the YSZ and Al_2O_3 values rose from 0.53±0.09 to 0.91±0.01. The coefficient of friction increased due to the presence of hard alumina particles surrounding the ZrO_2 particles, similar to the findings of microhardness tests. The YAT sample exhibited an average friction coefficient of 0.68 ± 0.13. The addition of an extra 3% TiO_2 by weight resulted in a fall in hardness and a reduction in wear resistance. Like other coatings, the graphic in the YAT sample started to become less raised around the end of the 2000 cycle. However, in contrast to others, the rate of friction decreased.

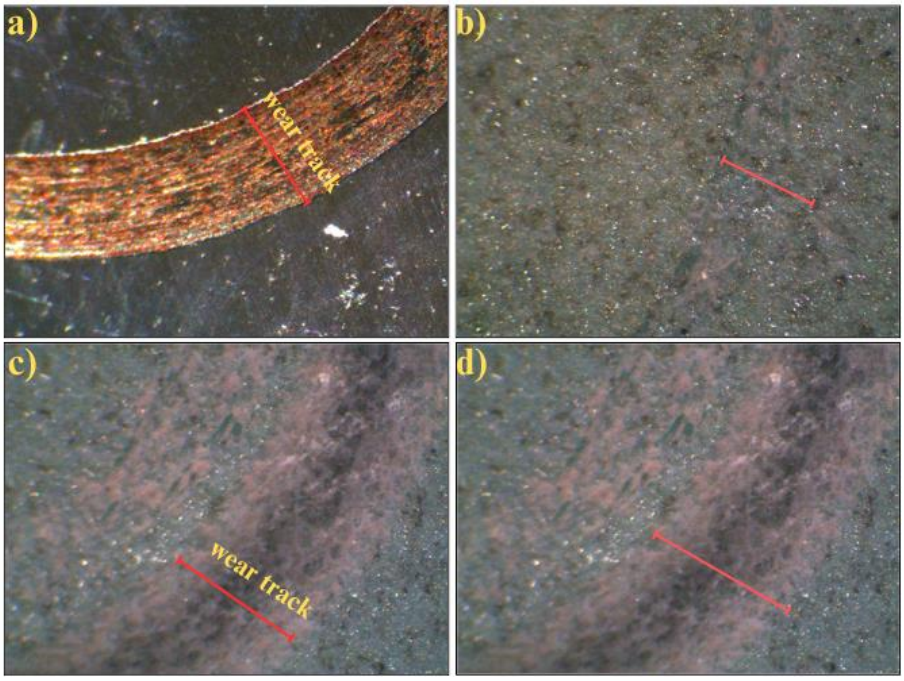

Figure 7. AISI, YSZ, YA, YTA Microscopic image of the marks formed after the wear test; a) SS, b) YSZ coating, c) YA, and d) YTA

Figure 7 shows optical microscopic images of the traces that were created following the wear test. The ceramic coatings exhibit wear marks and profiles that are distributed across the surface, whereas the metal substrate leaves behind a single mark. The size of the SS sample was 0.75±0.0075 mm, whereas the ceramic coatings had measurements of YSZ 0.86±0.46 mm, YA 1.072±0.13 mm, and YTA 1.71±0.05 mm, respectively. Figure 8 depicts the microscopic structure of the coatings that have undergone wear. The SEM images display accurate wear surfaces, instances of pull-out defects, and wear debris. Additionally, it has been noted that ceramic coatings exhibit indications of wear that result from several wear mechanisms. The SEM picture of SS is depicted in Figure 8 a,e. The AISI 304 surface underwent scratching, leading to the production of straight grooves and plastic deformation. Despite the low surface hardness, ceramics exhibit superior wear resistance compared to SS because of two primary factors. The first transformation is the conversion of the austenitic phase into martensite under load, as previously mentioned in the hardness section. Furthermore, the SEM photos clearly demonstrate that the folding of the metal leads to an enhanced surface flatness following a certain circuit. Upon examining the coated surface, it was seen that the presence of rigid,

abrasive particles or a higher level of hardness on the top surface compared to the lower layer could result in abrasive phenomena. The presence of solid corrosive particles is a result of the transformation of austenite and the creation of martensite residues during the wear test (Zandrahimi et al., 2007). For both coatings, ductile wear, deformation wear and brittle deformation, and finally ductile deformation wear mechanisms were observed for ceramic coatings. These wear types have been reported for YSZ and YA (Franco et al., 2021, 2019). Figure 9a displays the outcomes of the mapping EDS examination conducted on the surface of the SS sample. The EDS analysis revealed the existence of oxygen.

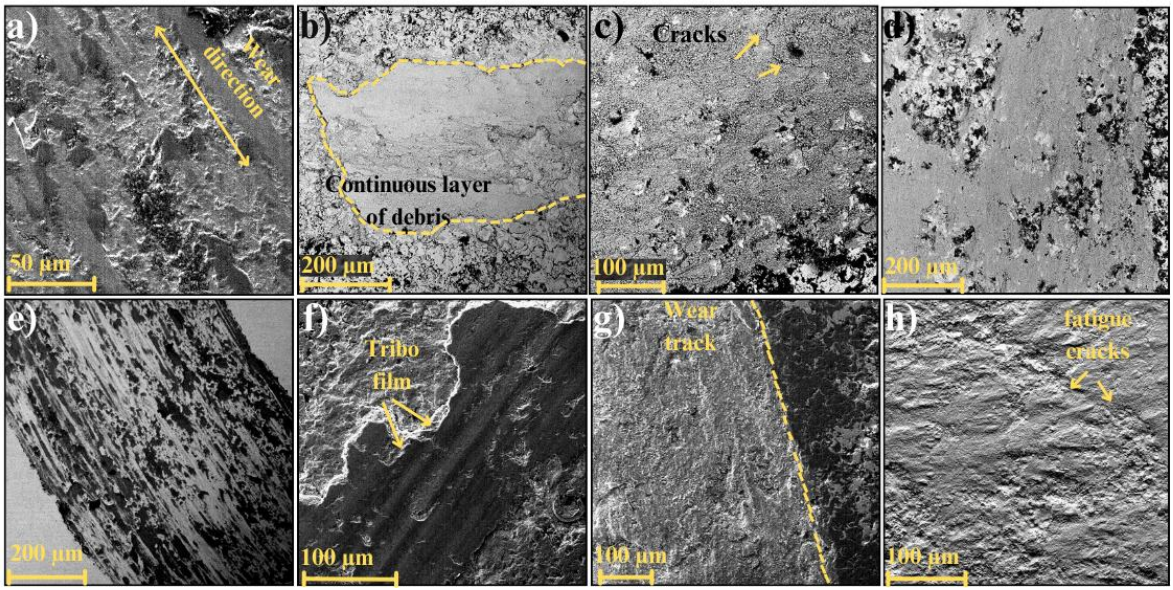

Figure 8. SEM images of wear tracks; a),e) SS, b),f) YSZ coating, c),g) YA coating, and d),h) YAT coating

Figure 8b, f displays evidence of erosion on the YSZ coating. Tribofilm formation may occur in the trace of dislocation. This phenomenon arises when the worn coating powder is retained on the surface due to the applied load. The SEM pictures revealed the presence of worn grooves. At the conclusion of each circuit of the bullet, various types of creases are created. Figure 9b shows the EDS examination of the YSZ worn surface, which revealed the presence of acceptable levels of take and oxygen elements. Adhesive wear was identified as the specific type of wear in this case. Adhesive wear is a type of wear that occurs when materials make contact and rub against each other. Due to this friction, thea atoms on the surfaces of the materials interpenetrate, resulting in surface damage to the material. The SEM image data for the YA sample is represented in Figure 8 c, g. The SEM images acquired indicated the presence of microcracks. The cracks originated from fatigue caused by repeated use. The presence of micrometer-sized imperfections, such as fractures in the mechanism and splinters in the coatings, could potentially be the cause of the cracking. The EDS analysis results of the YA sample reveal the presence of Al and O elements, as depicted in Figure 9c. Both the deceiver and the flock possess the presence of Al and O. However, SEM images showed that the coating was in the correct direction. This can be explained by abrasion in case of abrasion, that is, the wear of surfaces without contact with hard diseases or other hard surfaces that can damage their surface. SEM images of the YTA sample are given in Figure 8 d,h. In the EDS results of the YAT sample in Figure 9d, it was understood that the black areas where corrosion was allowed were alumina.

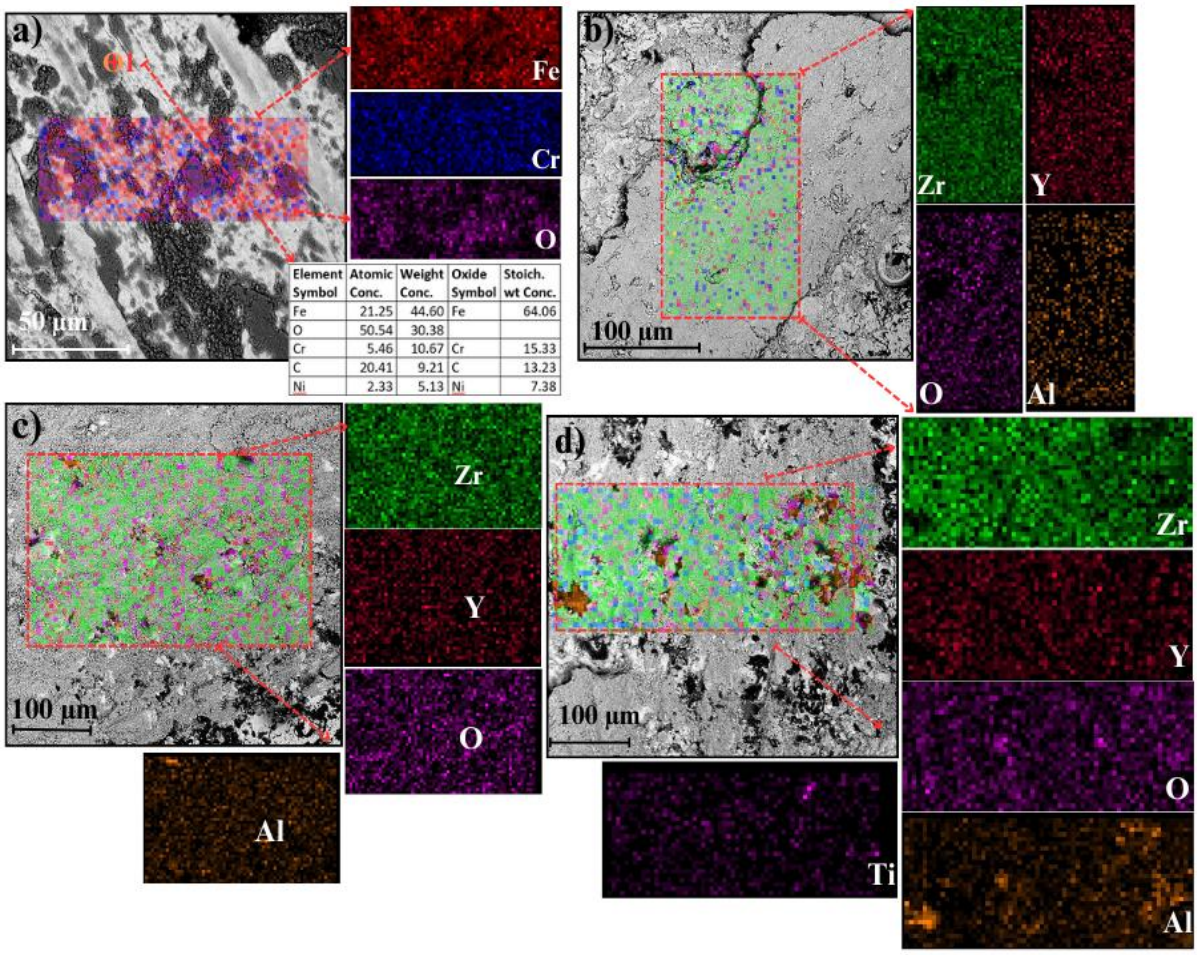

Figure 9. EDS mapping results a) SS, b) YSZ coating, c) YA coating, and d) YAT of samples after wear tests

4. CONCLUSION

The investigation involved applying atmospheric plasma spray to an SS substrate in order to coat it with composite TBCs. These coatings included YSZ, YA, and YAT. A pin-on-disc tribological test was conducted to investigate the wear characteristics of the coatings. The acquired results are summarized below:

-The inclusion of Al_2O_3 in YSZ resulted in a 25% increase in microhardness. Nevertheless, the additional TiO_2 resulted in a reduction in hardness.

-As the discharge rate increases, the wear rate of the samples decreases. The YAT sample has the highest wear rate.

-The YSZ sample exhibited abrasive adhesive wear upon the introduction of Al_2O_3.

-By incorporating alumina and TiO_2 into YSZ, the porosity was reduced by roughly 65% and 70% respectively.

5. ACKNOWLEDGEMENTS

The authors thank Dr. Emre BAL and Dr. Ayşegül ADOĞAN EKER for their wear test contributions.

6. CONFLICT OF INTEREST

Author(s) approve that to the best of their knowledge, there is not any conflict of interest or common interest with an institution/organization or a person that may affect the review process of the paper.

7. AUTHOR CONTRIBUTION

Ali AVCI: Testing and Analyzing-Writing-original draft, Resources, Methodology, Supervision, Investigation. Muhammet KARABAŞ: Coating-Writing-original draft, Funding acquisition, Data curation.

8. REFERENCES

Avci A., Eker A. A., and Eker B., Exergetic, Energetic and Environmental Dimensions, Elsevier Publications, Academic Edition, Netherlands, pp. 793-814, 2018.

Avci A., Karabaş M., Akdoğan Eker A., Akman E., & Aslan C., Improvement of CMAS resistance of laser glazed and nano-modified YSZ thermal barrier coatings, Ceramics International, 50 (7), 9985-9999, 2024.

Bai L., Zhang H., Wan S., Yi G., Sun H., Tailoring wear and tribo-induced interaction of YSZ coating sliding against Si3N4 and Al2O3 counterparts, Wear, 518–519 (1), 204628, 2023.

Bal E., Karabaş M., Yılmaz Taptık İ., The effect of CMAS interaction on thermal cycle lifetime of YSZ based thermal barrier coatings, Materials Research Express, 5(6), 065201, 2018.

Chen, K., Song, P., Hua, C., Zhou, Y., Huang, T., Li, C., Lu, J., Effect of YSZ-dopant on microstructure and hardness property of the Al2O3–40%TiO2 plasma sprayed coating, Materials Research Express, 5, 086504, 2018.

Critchlow G. W., Brewis D. M., Review of surface pretreatments for aluminium alloys. International Journal of Adhesion and Adhesives, 16(4), 255–275, 1996.

Franco D., Ageorges H., López E., Vargas F., Tribological performance at high temperatures of alumina coatings applied by plasma spraying process onto a refractory material, Surface and Coatings Technology, 371, 276–286, 2019.

Franco D., Ageorges H., López E., Vargas F., Wear behavior at high temperatures of ZrO2 - Al2O3 plasma sprayed coatings and an electro-melted AZS refractory, Surface and Coatings Technology, 425, 127715, 2021.

Franco D., Vargas F., López E., Ageorges H., Wear behavior at high temperature of ZrO2–Y2O3 (YSZ) plasma-sprayed coatings, Journal of Materials Science, 59(1), 20–37, 2024.

Guo L., Zhang B., Gao Y., Yan K., Interaction laws of RE2O3 and CMAS and rare earth selection criterions for RE-containing thermal barrier coatings against CMAS attack, Corrosion Science, 226, 111689, 2024.

Han J., Zou Y., Wu D., Chen J., Zhang Y., Improving CMAS-corrosion resistance of YSZ-based thermal barrier coatings with Al2O3 addition, Surface and Coatings Technology, 446, 128799, 2022.

He Y., Zhang S., He Y., Song R., Zhang Z., Liu B., Li H., Shang guan, J., Effects of yttrium-stabilized zirconia (different yttrium content) doping on the structure, corrosion resistance and wear resistance of Ni-P electroless coating, Colloids and Surfaces A: Physicochemical and Engineering Aspects, 654, 130059, 2022.

Iqbal A., Moskal G., Cavaleiro A., Amjad A., khan M. J., The current advancement of zirconate based dual phase system in thermal barrier coatings (TBCs): New modes of the failures: Understanding and investigations, Alexandria Engineering Journal, 91, 161–196, 2024.

Javadi Sigaroodi, M., Rahimi J., Poursaeidi, E., Montakhabi F., Impact of bond coat types on calcium-magnesium-alumina-silicate and hot corrosion behavior in thermal barrier coatings, Corrosion Science, 227, 111742, 2024.

Jun B., Jonsson N., Jordan E. H., Cooper R. C, CMAS deposition rate and sequence effects on cyclic life in gradient testing, SN Applied Sciences, 5(5), 138, 2023.

Lima R. S., Marple B. R., Superior performance of high-velocity oxyfuel-sprayed nanostructured TiO2 in comparison to air plasma-sprayed conventional Al2O3-13TiO2, In Journal of Thermal Spray Technology, 14 (3397), 397–404, 2005.

Luo P., Zhang J., You, Z., Ran X., Liu, Y., Li, S., & Li, S., Effect of TiO2 content on the microstructure and mechanical and wear properties of yttria-stabilized zirconia ceramics prepared by pressureless sintering, Materials Research Express, 6(12), 125211, 2019.

Mehar, S., Sapate, S.G., Contact severity maps for plasma sprayed YSZ modified Al2O3-3% TiO2 coatings Ceramic International, 50(8),13003–13013, 2024.

Noroozpour M., Akbari A., YSZ–Al2O3 thermal barrier nanocomposites coatings: Electrophoretic deposition and characterization, International Journal of Applied Ceramic Technology, 21(1) 888-899, 2024.

Ormanci O., Akin I., Sahin F., Yucel O., Simon V., Cavalu S., Goller G., Spark plasma sintered Al2O3–YSZ–TiO2 composites: Processing, characterization and in vivo evaluation, Materials Science and Engineering: C, 40, 16–23., 2014.

Özçelik A., Akdoğan Eker A., Karabaş M., Avcı A., Küçükyıldırım B. O.3, Enhanced CMAS and hot corrosion degradation of YSZ thermal barrier coating with nano powders, Surface and Coatings Technology, 481, 130624, 2024.

Shen C. T., Lee K. R., Hsieh Y. P., Lee S. W., Chang J. K., Jang S. C., Tseng C. J., Effects of TiO2 and SDC addition on the properties of YSZ electrolyte, International Journal of Hydrogen Energy, 44(56), 29426–29431, 2019.

Thakare J. G., Pandey C., Mahapatra M. M., Mulik R. S., Thakare, J. G., Pandey, C., Mahapatra, M. M., & Mulik, R. S., Thermal Barrier Coatings—A State of the Art Review, MMI, 27(7), 1947–1968,2021.

Wang, C., Liu, M., Wang, H., Jin, G., Ma, G., Zhang, J., Chen, S., Tribological properties and solid particle erosion wear behavior of Al2O3-13 wt%TiO2/Al2O3-PF composite coatings prepared on resin matrix by supersonic plasma spraying, Ceramiz International, 50(4), 2024.

Wang Z., Zhang J., Han S., Liu J., Corrosion resistance of modified YSZ coatings subjected to CMAS attacks, Surface Engineering, 38(4), 393–401, 2022.

Yuan K., Yang L., Wang Q., Zhang F., Zhu W., Zhou Y., Al2O3–TiO2 Codoped Yttria-Stabilized Zirconia Thermal Barrier Coatings Resistant to Damage by Molten Calcium-Magnesium-Alumino-Silicate (CMAS) Glass, Advanced Engineering Materials, 23(6), 1-12, 2021.

Zandrahimi M., bateni M. R., Poladi A., Szpunar J. A., The formation of martensite during wear of AISI 304 stainless steel, Wear, 263 (1–6), 674–678, 2007.

Zhao X., Jing T. F., Gao Y. W., Qiao G. Y., Zhou, J. F., Wang W., Annealing behavior of nano-layered steel produced by heavy cold-rolling of lath martensite, Materials Science and Engineering: A, 397(1–2), 117–121, 2005.

JOURNAL of
MATERIALS and MECHATRONICS:A

e-ISSN 2717-8811
JournalMM, 2024, 5(1), 168-182
https://doi.org/10.55546/jmm.1488880

Araştırma Makalesi / Research Article

Evaluation of the Turning Parameters of AISI 5115 Steel in Dry and MQL Cutting Environments with the Use of A Coated Carbide Cutting Insert: An Experimental Study

Havva DEMİRPOLAT[1*]

[1*] Selçuk University, Faculty of Technology, Department of Mechanical Engineering, Konya, Turkey,
ORCID ID: https://orcid.org/0000-0002-2981-9867, hdemirpolat@selcuk.edu.tr

Geliş/ Received: 23.05.2024; **Revize/Revised:** 10.06.2024 **Kabul / Accepted:** 14.06.2024

ABSTRACT: This study investigates the effects of cutting parameters on turning AISI 5115 steel in both dry and MQL environments using a coated carbide insert. The cutting parameters are determined using a full factorial design. A comprehensive full factorial experimental design was executed in order to investigate the effect of cutting parameters, including cutting speed, feed rate, and depth of cut, on surface roughness, cutting force and cutting temperature. Following the completion of the turning trials, surface roughness measurements were meticulously recorded. Also cutting force and cutting temperature were measured. The results of the study indicated that the most significant influence on surface roughness is exerted by the feed rate. Moreover, the impact of the depth of cut became more significant as the cutting speed decreased. While the surface roughness increased by 23% in the dry environment due to the increased feed rate at low cutting speed, the increase in the MQL environment was 32%. The cutting temperature is influenced by a number of factors, including the cutting parameters and the material properties. The maximum temperature for turning in the MQL environment was 381°C compared with an average cutting temperature of 430°C in dry machining conditions. The application of high-speed cutting in a dry cutting environment was found to result in a 10% increase in cutting temperature. The influence of cutting speed on the outcome was less pronounced in the MQL environment. At high cutting speeds and low parameter values in the MQL environment, the cutting force decreased by 75% in contrast to the low cutting speeds and high cutting parameters in the dry environment. The optimal cutting conditions for minimising cutting force were identified in the MQL environment, characterised by high cutting speeds and low feed rates.

Keywords: 5115 steel, Turning, Dry cutting, MQL, ANOVA

1. INTRODUCTION

In the field of manufacturing, the machinability of metals represents a fundamental aspect, influencing the overall efficiency and quality of machining processes (Kuntoglu, 2022).

*Sorumlu yazar / Corresponding author: hdemirpolat@selcuk.edu.tr
Bu makaleye atıf yapmak için /To cite this article

Demirpolat, H. (2024). Evaluation of the Turning Parameters of AISI 5115 Steel in Dry and MQL Cutting Environments with the Use of a Coated Carbide Cutting Insert: An Experimental Study. Journal of Materials and Mechatronics: A (JournalMM), 5(1), 168-182.

Machinability as a concept refers to how easily a material can be machined using different cutting tools and techniques like milling, turning, drilling, or grinding (Binali, Coşkun, & Neşeli, 2022; Korkmaz & Günay, 2018). Case-hardened steels, are a special group of low-carbon steels for applications requiring a hard, wear-resistant surface with a tough, ductile core. A surface treatment process known as carburisation or cementation achieves this unique combination of properties. The case-hardened steel AISI 5115, also called 16MnCr5, is a low alloy steel. Due to its specific properties and suitability for certain processes, it is widely used in various mechanical components and applications. AISI 5115 is considered a medium strength/toughness steel. Its structure, with a hard outer surface and a softer inner core, enables it to absorb impact. AISI 5115 is used economically in a wide variety of mechanical components such as pulleys, gears, shafts, machine parts, piston rods, washers, chain links, sprockets, extrusions, roller bearings and where shock absorption is required(Selçuk, Ipek, & Karamış, 2003). Conventional surface treatments such as carburisation and nitriding or induction hardening are widely used in 5115 steels for these applications(Selçuk, Ipek, Karamiş, & Kuzucu, 2000). Cementation is a surface hardening process that introduces carbon into the steel surface to form a hard outer layer. Nitriding improves hardness and wear resistance by introducing nitrogen into the surface(Lampman, 1991). This surface provides wear resistance and durability, while the softer core absorbs shocks and impacts, reducing the risk of fracture or failure. AISI 5115 has good mechanical properties including moderate strength and toughness. This makes it suitable for moderate-to-heavy loaded and dynamic stressed components. This grade of steel is generally used for elements where a core tensile strength of 800-1100 Nmm^{-2} is required and a good load bearing capacity is required(Monkova et al., 2019). As well as its importance in industrial applications, the machinability properties of AISI 5115 steel are remarkable due to the material's chemical properties, hardness distribution and surface properties. To increase the machinability of hardened metals, modern cooling techniques that are less harmful to the environment and human health have been the subject of much recent research(Binali, Demirpolat, Kuntoğlu, & Sağlam, 2023; Binali, Demirpolat, Kuntoğlu, & Salur, 2023; Mahapatra, Das, Jena, & Das, 2023). While flood lubrication undoubtedly improves surface quality and tool life, it has a negative impact on human health and the environment due to the use of harmful chemicals (Aslan, Salur, & Kuntoğlu, 2022). Production costs are also significantly increased by the flood lubrication system(Ghosh & Rao, 2015). Cryogenic cooling is becoming increasingly important as an environmentally friendly and sustainable alternative to the use of liquid-based mineral/synthetic cutting fluids in metal cutting(Mia, Gupta, Singh, Królczyk, & Pimenov, 2018). Nano-fluid-based processing methods, which are less harmful to the environment, are also being considered to improve processing performance by creating a film layer on the surface by improving the heat transfer properties of the fluid (Ben Said, Kolsi, Ghachem, Almeshaal, & Maatki, 2023). The use of CNC nano powders was found to improve the machinability of high-strength structural steel with effective lubrication and cooling by Usca (Usca, 2023). Although dry machining is a traditional method of machining without the use of hazardous cutting fluids, it is also a preferred method in modern production systems (Asiltürk, Kuntoğlu, Binali, Akkuş, & Salur, 2023). However, because of very high temperatures during machining on tool wear and surface quality, minimum quantity lubrication (MQL) is accepted as an alternative to the dry environment in sustainable machining (Makhesana & Patel, 2022; Ross et al., 2022; Sen, Mia, Krolczyk, Mandal, & Mondal, 2021).. The efficiency of MQL in machining operations has been investigated in many studies in recent years. They include several studies using different optimization techniques. Response surface methodology and Taguchi's signal-to-noise (S/N) ratio are two prominent methods often used for parameter optimisation. Recently, the Taguchi method has emerged

as the most widely referenced approach (Salur, Kuntoğlu, Aslan, & Pimenov, 2021). Mia et al. (Mia, 2018) investigated several sustainability issues in machining by looking at cutting energy, surface finish and using MQL. This study focuses on the mathematic modelling of specific cutting energies (Esp) and average roughness (Ra) during end milling of hardened AISI 4140 steel by MQL. Amini et al. (Amini, Khakbaz, & Barani, 2015) studied tool wear when turning AISI 4142 alloy steel in the MQL cutting environment and found that tool life was significantly extended compared to dry machining. Sampaio et al. (Sampaio, Machado, Laurindo, Torres, & Amorim, 2018) evaluated the MQL lubrication in turning SAE 1045. They found that cutting in an MQL environment not only required lower cutting forces at lower wear rates, but also reduced white film formation.

The cutting conditions and the condition of the tool are directly related to the cutting force during machining. The interaction between the geometry of the cutting tool and the depth of cut has a direct effect on the dominant cutting force (Mikolajczyk, Paczkowski, Kuntoglu, Patange, & Binali, 2022; Yallese, Chaoui, Zeghib, Boulanouar, & Rigal, 2009). Mondal et al. (Mondal, Das, Mandal, & Sarkar, 2016) evaluated different cutting tool tip options to determine the effect of cutting speed and feed on turning of hardened 16MnCrS5. When compared to dry machining, TiC coated flat and wide channel carbide inserts have shown superior performance in wet conditions at high cutting speeds. Grzesik et al. (Grzesik, Denkena, Żak, Grove, & Bergmann, 2016)investigated the power consumption in turning of AISI 5115 steel with CBN tools at different cutting parameters. At low undeformed chip thickness values, power consumption was also low at low cutting parameters, while at higher cutting parameter values it was in the characteristic high undeformed chip thickness carbon steel machining range. Agarwal et al.(Agarwal et al., 2022) studied the variation of the surface roughness as a function of the cutting parameters in the CNC turning of 16MnCr5 steel materials. Analysis of variance with orthogonal array, signal-to-noise ratio and ANOVA were used in experimental studies using the Taguchi method. Feed rate was the most important parameter in changing surface roughness. However, higher MRR values were obtained with depth of cut.

The objective of this study is to investigate the turning machinability of AISI 5115 steel using experimental methods. The experiments were designed using a full factorial approach. In particular, the effects of cutting parameters such as: cutting speed, feed, depth of cut on surface finish, cutting temperature and cutting forces during turning are evaluated. Understanding AISI 5115's machinability will provide valuable information to help optimise machining processes and increase productivity in manufacturing environments.

2. MATERIALS AND METHODS

2.1 Experimental Design

A sample of hardened AISI 5115 steel with dimensions of 50 mm in diameter and 400 mm in length, the chemical composition of which is given in Table 1, was used in the turning experiment. The experimental setup consisted of a universal lathe (De Lorenzo S547-8899), AISI 5115 workpiece, TiN coated carbide cutting tool (CCMT-09T308-304), perthometer (Mahr), InGaAs (Telc) radiation sensors seen in Figure 1. TiN coated carbide inserts inscribed circle diameter is 9.525mm and corner radius 0.8mm. Turning tests were performed according to ISO 3685, with tool changes after each dry and MQL cutting environment trial period. The STN 15 MQL system was used at 6 bar pressure with a 45° nozzle angle. Vegetable based lubricating oil was sprayed on the cutting zone from 20 mm. A full factorial design of experiments was used for two levels of 3 factors each as well as for two conditions of the cutting environment as given in Table 2. In total, 16 cutting experiments were performed. Recommendations from industry representatives and tool manufacturers, as well as the

results of our previous experimental studies, were used in the determination of the cutting parameters. The cutting parameters were limited to two levels to simplify the experimental design and focus on the most important factors affecting the cutting process. A more manageable number of experiments, essential for maintaining precision and control over the variables, was achieved by limiting the levels. This allows a clearer understanding of how each parameter affects the results obtained. Limiting the parameters to two levels also helps to reduce the complexity and resources required for the study. Previous research and preliminary experiments suggested that these two levels would provide sufficient variation to observe meaningful differences in outcomes, and this limitation was also guided by this research. Surface roughness values were determined by taking the arithmetic mean of 3 different roughness measurements taken from different parts of the cylindrical samples. The ISO 4288:1996 standard was applied in this experimental study to determine the rules and procedures for the evaluation of surface roughness. Ra, or arithmetic mean roughness, is a key parameter in the quantification of surface roughness. It represents the average absolute value of surface profile deviations from the mean line over a specified length. In essence, it measures the average variation in the height of the peaks and valleys of the surface relative to the mean line. Ra is the most used surface roughness parameter because it provides a simple and reliable indication of overall surface texture and smoothness.

Table 1. Chemical composition of workpiece

wt%	%C	%Si	%Mn	%Cr	%P	%Fe
AISI 5115 (sample)	0.16	0.40	1.20	1.10	0,02	Bal.

Orthogonal array, signal/noise (S/N) ratio and analysis of variance (ANOVA) were used to determine the effects and contributions of cutting speed, feed rate and depth of cut on the response variable turning of AISI 5115 operations. To determine the percentage contribution of the factors, statistical analysis was performed on the results of the full factorial experiment.

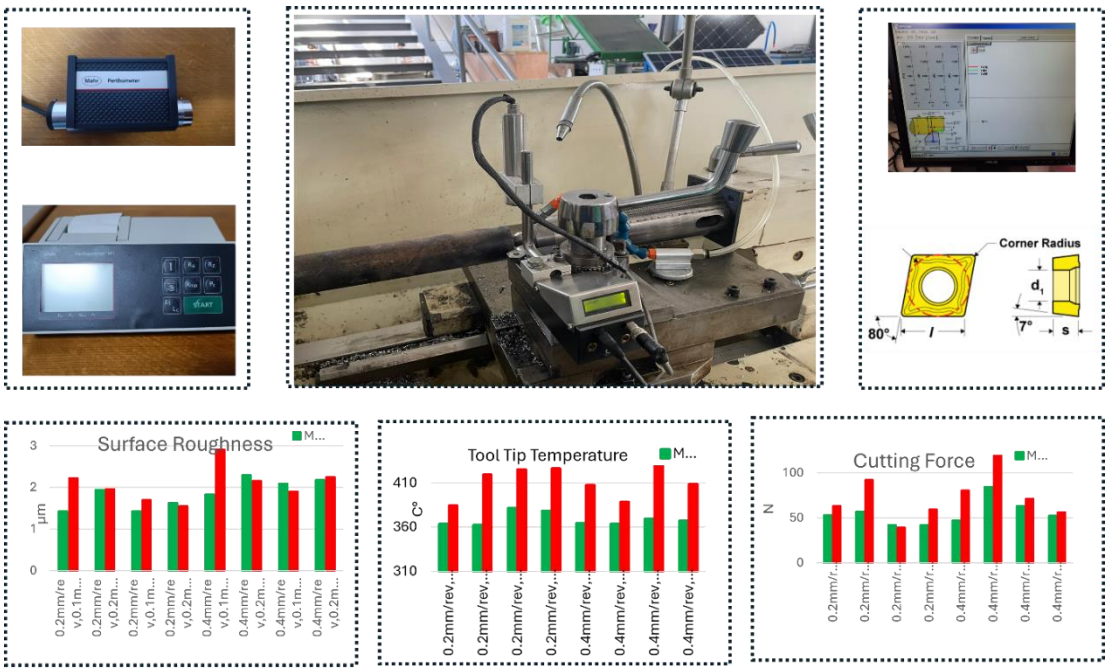

Figure 1. The experimental setup

Table 2. Parameters and levels of machining

Factor	Level I	Level II
V	60	90
f	0.2	0.4
a	0.1	0.2
Environment	DRY	MQL

3. RESULTS AND DISCUSSION

This study evaluates the effects of machining parameters and cutting environment on surface roughness, cutting force and tool tip temperature of AISI 5115 steel.

3.1 Surface Roughness

This study utilises a one-way ANOVA to investigate the influence of distinct cutting parameters (namely feed rate, cutting depth, and cutting speed) on the response variable, which can reasonably be presumed to relate to a signal-to-noise ratio. It can be hypothesised that smaller values of this ratio are preferable. The experimental context is that of MQL given in Figure 2. It can be observed that the feed rate and depth of cut exert a considerable influence on the performance of the process (signal-to-noise ratio) in the MQL cutting environment. It is therefore recommended that lower values for both parameters be employed. Regarding cutting speed, it can be stated that this does not exert a significant effect on surface quality within the specified range of values.

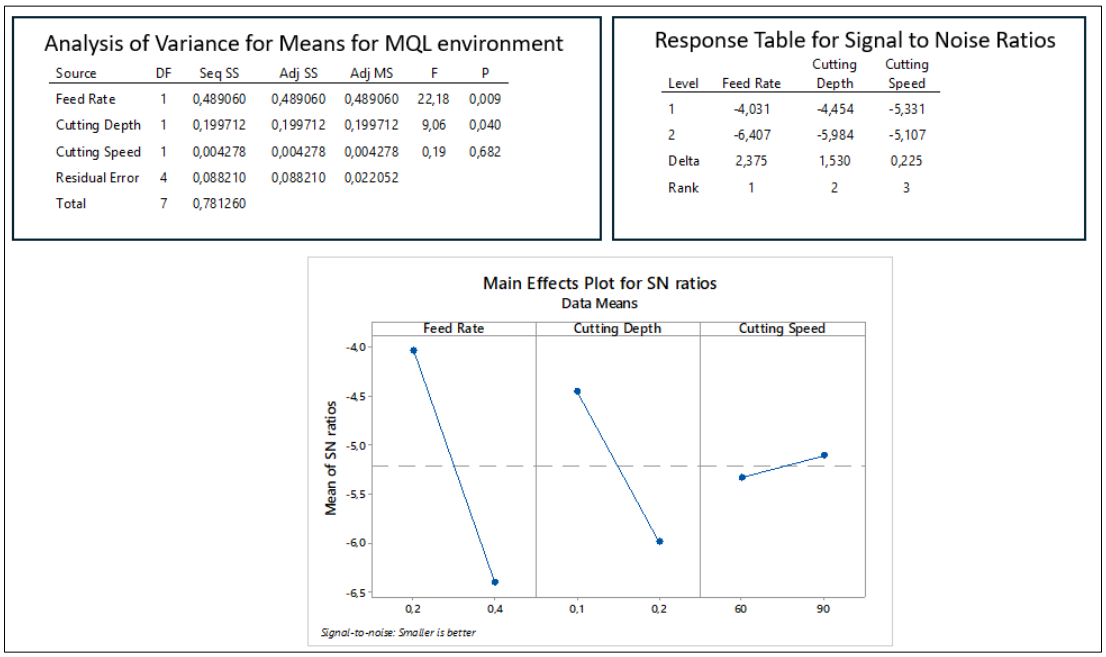

Figure 2. Analysis of ANOVA (Surface Roughness under MQL cutting environment)

Under dry conditions, a trend toward significance can be identified in the results for the feed rate, though the observed values do not reach conventional levels of statistical significance, as determined by a p-value of less than 0.05 as seen in Figure 3. This indicates that the feed rate may exert some influence on the response (signal-to-noise ratio) in the dry cutting environment, although

the effect is not definitive based on this analysis. Cutting speed also exhibits a tendency towards significance, although it fails to attain the conventional levels of statistical significance ($P < 0.05$). This implies that cutting speed might exert an influence on the response (signal-to-noise ratio) in the context of dry cutting, although further investigation or the inclusion of a larger range of cutting parameters may be necessary to confirm this effect. It was observed that the cutting depth had no significant effect on the response (signal-to-noise ratio) in the dry cutting environment. It is more probable that the observed variation in the response is due to random factors rather than the cutting depth parameter.

To ensure the quality of machined components, it is essential to achieve better surface quality. Surface roughness not only defines the topography of a workpiece, but also reflects changes in microstructure that have an impact on mechanical properties. The achievement of the required surface finish is the result of careful attention to several machining factors. Valuable information for optimising machining conditions can be obtained by analysing roughness profiles(Benardos & Vosniakos, 2003; Yurtkuran, Korkmaz, & Günay, 2016).

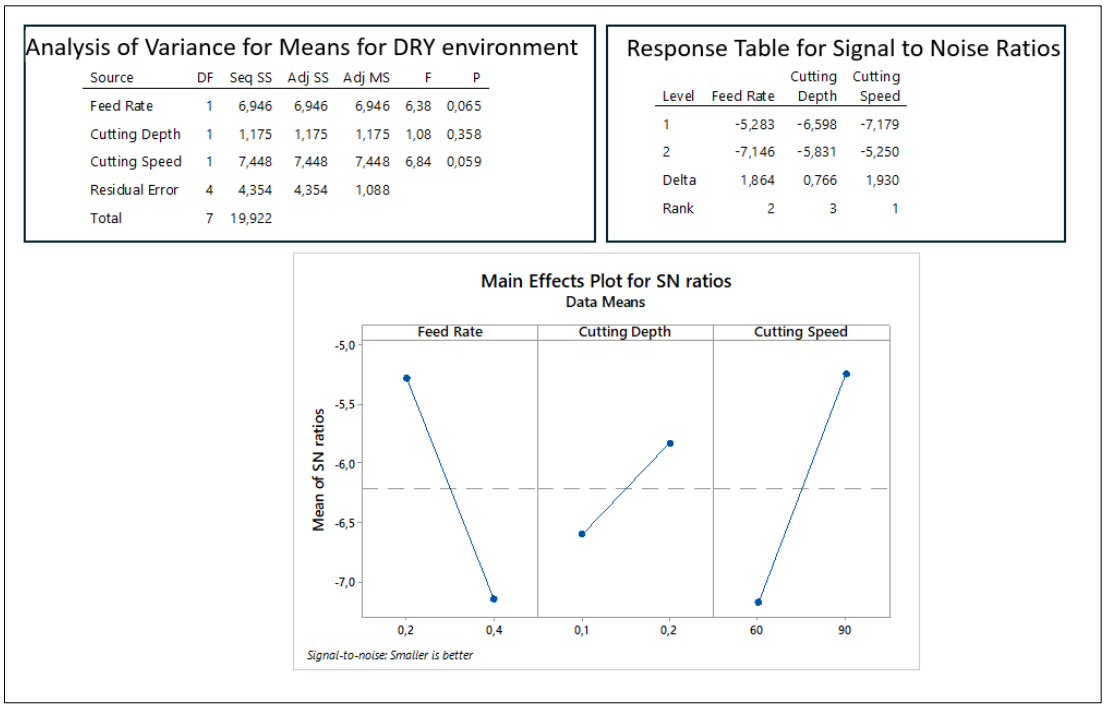

Figure 3. Analysis of ANOVA (Surface Roughness under DRY cutting environment)

A full factorial experimental design was implemented to investigate the effects of cutting parameters such as cutting speed, feed rate and depth of cut on surface roughness. Surface roughness measurements were recorded after turning trials. In this study, Ra was a key factor in modelling cutting conditions to optimise surface characteristics and the results were evaluated graphically to measure effectiveness. From the investigation it was found that the feed rate had the greatest effect on surface roughness. The effect of depth of cut became more pronounced and the surface quality of this combination decreased at low values of cutting speed. The poorest surface quality was observed in dry machining with a low cutting speed, high feed rate, and a low cutting depth value combination, as evidenced by the results. The lowest surface roughness values were observed when machining under MQL conditions, with the combination of high cutting speed and low feed rate exhibiting the

greatest reduction in surface roughness. It can be observed that MQL cutting environment conditions offer a considerable benefit in terms of surface roughness when compared to dry conditions. MQL improves surface lubrication between the cutting tool and the workpiece, whereas the dry cutting environment is characterised by pronounced crests and troughs (E. Şap et al., 2024). It can be observed that MQL cutting environment conditions offer a considerable benefit in terms of surface roughness when compared to dry conditions.

The results of this study indicate that the feed rate and cutting speed may have an impact on the performance of the cutting process in a dry environment. When both high cutting speeds and low feed rates are used together, they have a synergistic effect to minimise surface roughness (Usca, Şap, Uzun, & Değirmenci, 2024). This suggests that further investigation or refinement of the experimental conditions may be necessary to gain a deeper understanding of the effects of these parameters.

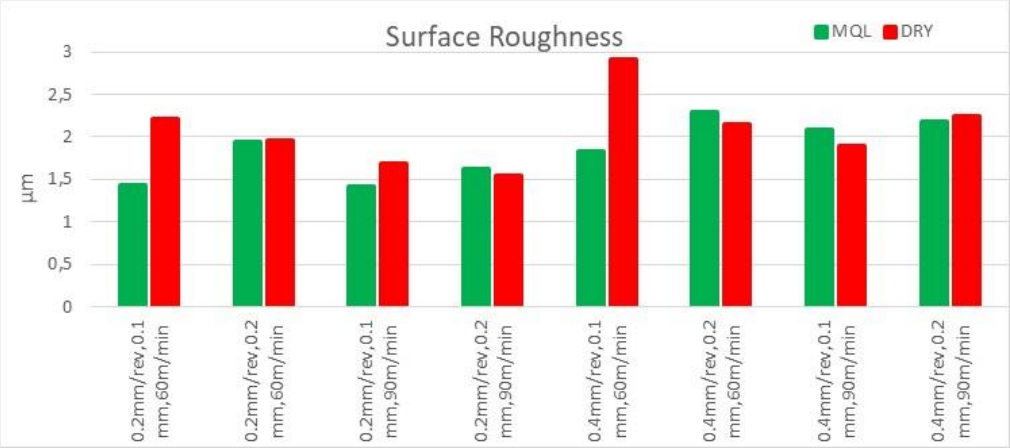

Figure 4. Surface Roughness variation with dry and lubri-cooling environment

3.2 Cutting Temperature

During machining, a significant amount of mechanical energy is converted into heat due to friction in the cutting zone, leading to inevitable temperature increases (Gupta et al., 2023; Mutlu, Binali, Demirsöz, & Yaşar, 2022). The specific heat capacity of the AISI 5115 steel, which is 452 J/kgK, and its thermal conductivity, which is 44 W/mK(Harichand & Sharma, 2012), play a decisive role in determining the temperature changes during the turning operation, especially when machining 16MnCr5(Agarwal et al., 2022). It's worth noting that cutting temperatures can rise to around 410°C as seen in Figure 7. This is close to the tempering threshold of AISI 5115. Cutting speed, as a primary parameter, strongly influences the temperature rise (S. Şap et al., 2024). In addition, in MQL environments, feed rate is closely correlated with temperature changes, affecting heat dissipation and machining efficiency. These factors highlight the complex relationship between cutting conditions, material properties and resulting temperatures in AISI 5115 machining. The process of dry machining, a traditional approach that is environmentally friendly in principle, nevertheless frequently encounters difficulties when it comes to controlling temperature during the cutting process, particularly in zones where chips are retained on the workpiece. While most of the thermal energy produced during machining is dissipated through the chips, the retention of certain chips on the surface of the workpiece remains a critical factor contributing to elevated temperatures. Furthermore,

the specific heat capacity value and conduction effects, in conjunction with the retention of chips, contribute to an elevation of surface temperatures during the dry machining of AISI 5115 Steel.

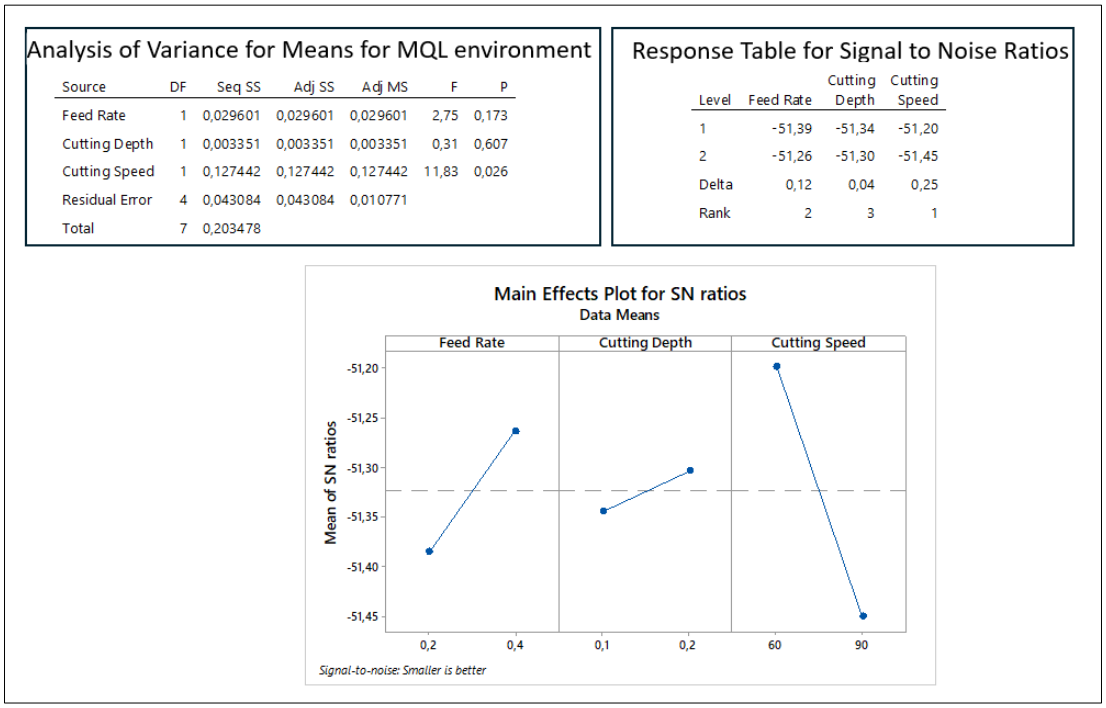

Analysis of Variance for Means for MQL environment

Source	DF	Seq SS	Adj SS	Adj MS	F	P
Feed Rate	1	0,029601	0,029601	0,029601	2,75	0,173
Cutting Depth	1	0,003351	0,003351	0,003351	0,31	0,607
Cutting Speed	1	0,127442	0,127442	0,127442	11,83	0,026
Residual Error	4	0,043084	0,043084	0,010771		
Total	7	0,203478				

Response Table for Signal to Noise Ratios

Level	Feed Rate	Cutting Depth	Cutting Speed
1	-51,39	-51,34	-51,20
2	-51,26	-51,30	-51,45
Delta	0,12	0,04	0,25
Rank	2	3	1

Figure 5. Analysis of ANOVA (Cutting temperature under MQL cutting environment)

The cutting speed significantly influences the cutting temperature (signal-to-noise ratio) in the MQL cutting environment. Higher cutting speeds are associated with lower cutting temperatures, suggesting an improved performance given in Figure 5.

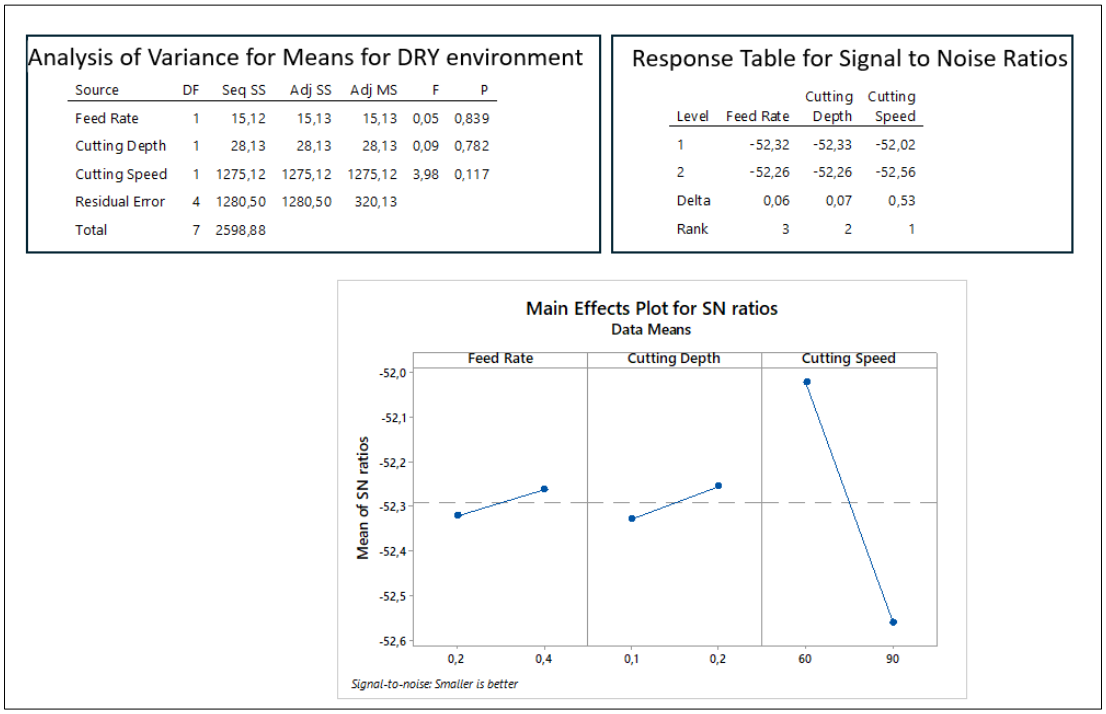

Analysis of Variance for Means for DRY environment

Source	DF	Seq SS	Adj SS	Adj MS	F	P
Feed Rate	1	15,12	15,13	15,13	0,05	0,839
Cutting Depth	1	28,13	28,13	28,13	0,09	0,782
Cutting Speed	1	1275,12	1275,12	1275,12	3,98	0,117
Residual Error	4	1280,50	1280,50	320,13		
Total	7	2598,88				

Response Table for Signal to Noise Ratios

Level	Feed Rate	Cutting Depth	Cutting Speed
1	-52,32	-52,33	-52,02
2	-52,26	-52,26	-52,56
Delta	0,06	0,07	0,53
Rank	3	2	1

Figure 6. Analysis of ANOVA (Cutting temperature under DRY cutting environment)

It can be concluded that the feed rate has no significant effect on cutting temperature (signal-to-noise ratio) within the MQL cutting environment. Furthermore, changes in feed rate do not have a strong association with variations in cutting temperature. Additionally, cutting depth does not significantly influence cutting temperature within the MQL cutting environment. Therefore, it can be stated that variations in cutting depth do not have a meaningful contribution to changes in cutting temperature.

Cutting speed shows a trend towards significance but does not reach conventional levels of statistical significance ($P < 0.05$). This suggests that cutting speed may have a moderate influence on cutting temperature in the dry cutting environment, but further investigation or larger range of turning parameters may be needed to confirm this effect given in Figure 6. The results of the study indicated that the feed rate did not have a statistically significant effect on cutting temperature (signal-to-noise ratio) when the cutting was performed in a dry environment. It can be concluded that changes in feed rate are not associated with variations in cutting temperature. Similarly, cutting depth does not significantly influence cutting temperature in the dry cutting environment. It is not the case that variations in the cutting depth are meaningful contributors to changes in cutting temperature.

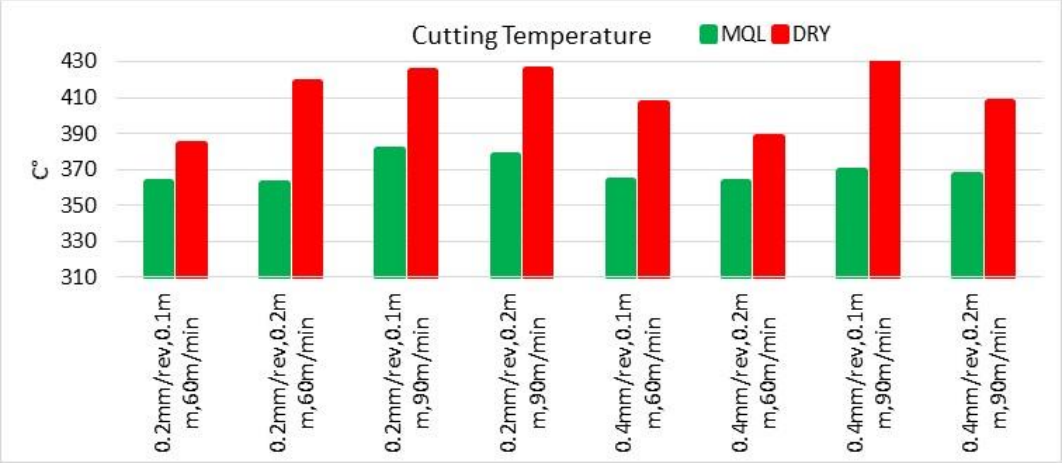

Figure 7. Cutting temperature variation with dry and lubri-cooling environment

3.3 Cutting Force

The AISI 5115 case hardening steel has moderate mechanical properties and strength, which results in a relatively low cutting force and power requirement during the machining process. The cutting force plays a critical role in determining the energy efficiency and the effectiveness of the machining process. The impact of extended cutting operations on sustainable manufacturing goals was investigated. It was found that machining accounts for a significant proportion of the energy consumed in manufacturing processes. Increased cutting force directly correlates with increased energy consumed (Pimenov et al., 2024).

In particular, the maximum cutting force occurs under conditions of low cutting speed and increased feed rate and depth of cut in dry machining environments (Binali, Patange, Kuntoğlu, Mikolajczyk, & Salur, 2022). This is illustrated in Figure 10. Among these factors, feed rate emerges as the primary driver for escalating cutting force. This observation implies that higher feed rates and deeper cutting depths create greater resistance during cutting, requiring increased force to remove material. To optimise machining parameters and minimise energy consumption when machining AISI

5115 steels, it is essential to understand these dynamics. It can be observed that at lower cutting parameters, both low cutting force and reduced power consumption are evident. However, under both conditions, cutting force increases significantly with higher feed rates. It is noteworthy that in dry machining environments, an increase in the depth of cut at lower cutting speeds led to a 32% rise in cutting force. Specifically, under dry machining conditions with low cutting speeds and increased cutting depths, the maximum cutting force reached a peak of 119 N.

Conversely, the lowest cutting force of 32 N was achieved in MQL environments with a combination of high cutting speeds, low feed rates, and shallow cutting depths. An increase of over 100% in cutting force was observed due to higher feed rates. These findings emphasise the pivotal role of optimising cutting parameters in reducing power consumption and achieving sustainable production goals.

The optimal cutting conditions for minimising cutting force in AISI 5115 steel were identified in the MQL environment with high cutting speeds and low feed rates. These findings emphasise the significance of selecting optimal cutting parameters to enhance efficiency and sustainability in machining processes.

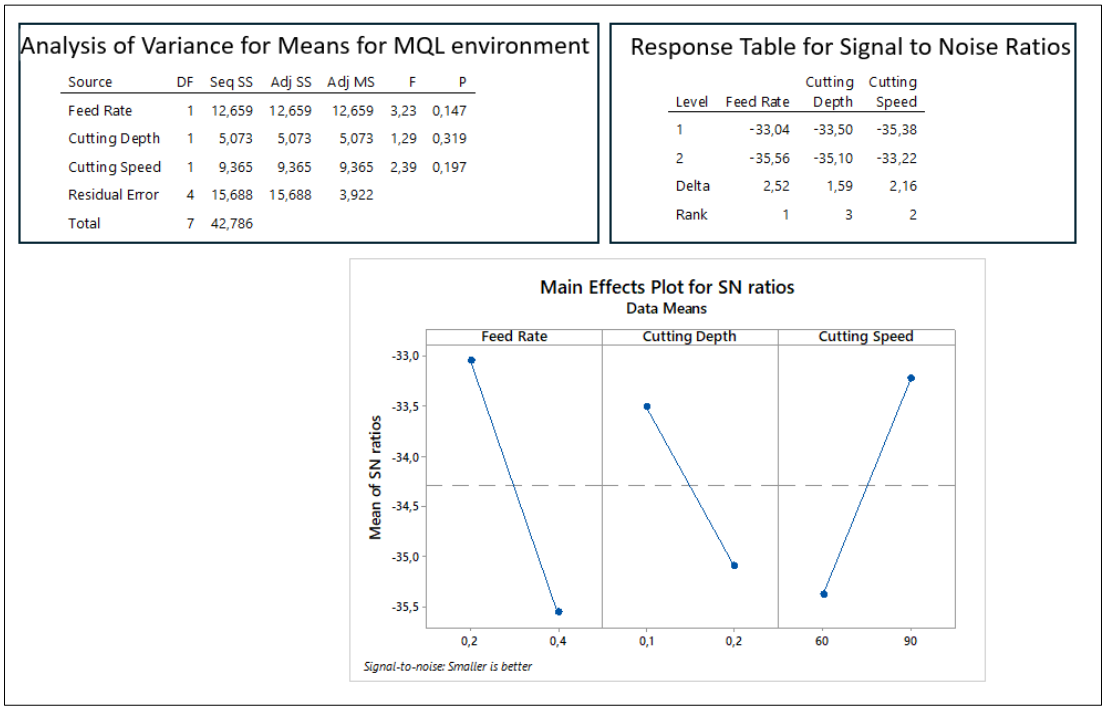

Figure 8. Analysis of ANOVA (Cutting force under MQL cutting environment)

The results of this study indicate that other factors or interactions may be more influential in determining cutting force in MQL cutting operations. It is not possible to observe the individual contributions of changes in cutting parameters to changes in cutting force in Figure 8. Nevertheless, it can be posited that the interactions between the parameters and tool wear mechanisms exert a significant influence on the cutting force. However, it was demonstrated that cutting speed exerts a statistically significant influence on cutting force in the dry cutting environment. A positive correlation exists between the cutting speed and the cutting force seen in Figure 9. It can be

demonstrated that variations in cutting depth and feed rate do not contribute to meaningful changes in cutting force.

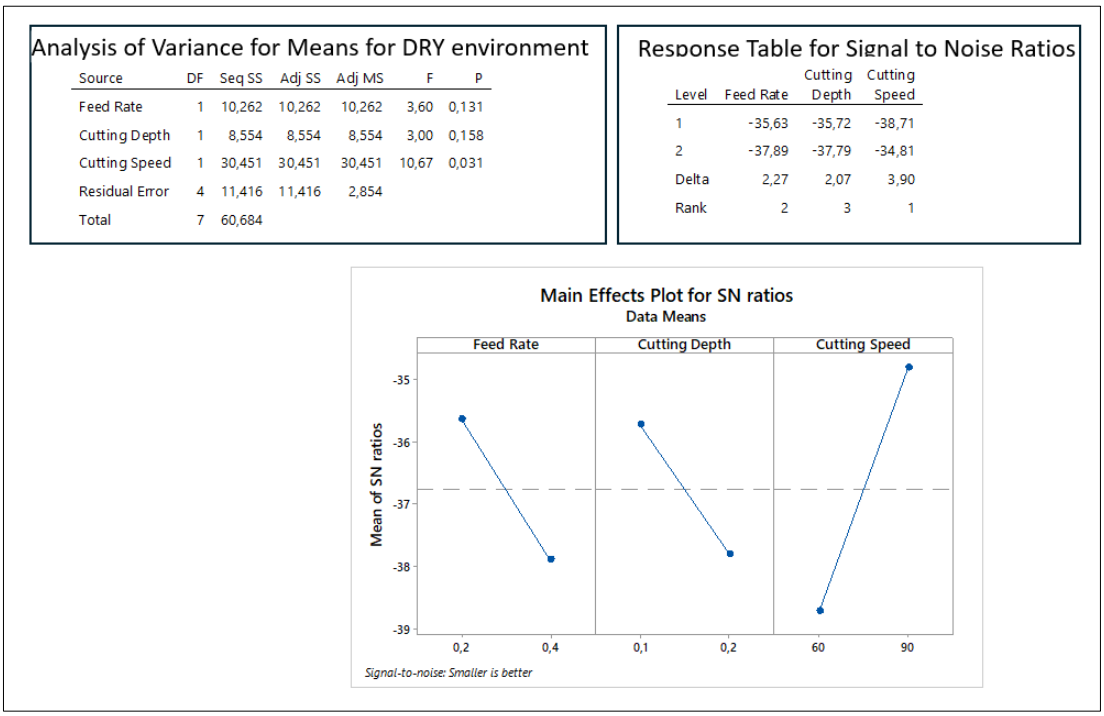

Analysis of Variance for Means for DRY environment

Source	DF	Seq SS	Adj SS	Adj MS	F	P
Feed Rate	1	10,262	10,262	10,262	3,60	0,131
Cutting Depth	1	8,554	8,554	8,554	3,00	0,158
Cutting Speed	1	30,451	30,451	30,451	10,67	0,031
Residual Error	4	11,416	11,416	2,854		
Total	7	60,684				

Response Table for Signal to Noise Ratios

Level	Feed Rate	Cutting Depth	Cutting Speed
1	-35,63	-35,72	-38,71
2	-37,89	-37,79	-34,81
Delta	2,27	2,07	3,90
Rank	2	3	1

Figure 9. Analysis of ANOVA (Cutting force under DRY cutting environment)

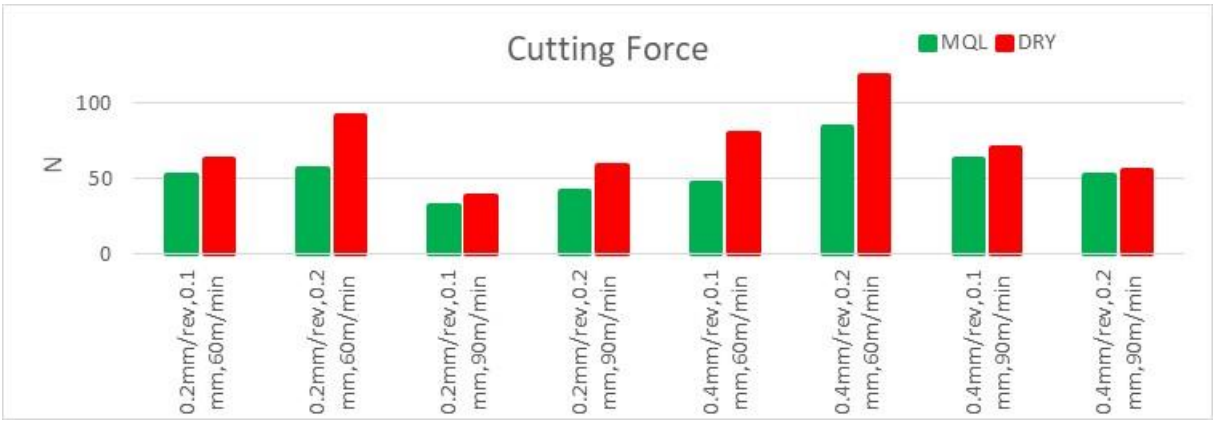

Figure 10. Cutting force variation with dry and lubri-cooling environment

4. CONCLUSION

Achievement of superior surface finishes on machinable components is essential to ensure optimum mechanical performance. This study has highlighted the intricate relationship between machining parameters, material properties and the resulting surface characteristics when machining AISI 5115 steels. A full factorial design was employed to investigate the effects of cutting speed, feed and depth of cut on surface roughness (Ra). The findings demonstrate the critical role of these parameters in optimising surface characteristics. The results demonstrated that feed rate had a profound impact on surface roughness, exhibiting the greatest influence among all the variables examined. Furthermore, the impact of depth of cut became more pronounced, particularly at lower cutting speeds.

In dry machining conditions, the surface roughness increased by 23% due to the higher feed rate at low cutting speeds, while in the MQL environment the increase was 32%. The increase in surface roughness resulting from machining in a dry environment under the same conditions was approximately 40%. Cutting temperature is influenced by several factors, including cutting parameters and material properties. In the MQL environment, the maximum cutting temperature reached 381°C, compared to an average of 430°C in dry machining conditions. Cutting speed is a primary factor influencing temperature rise, especially in MQL environments. Dry machining presents challenges for temperature control due to chip retention and material properties. Additionally, in the MQL environment, cutting forces decreased by 75% at high cutting speeds with low parameter values, in comparison to the high cutting forces observed at low cutting speeds and high parameter values in the dry environment. Dry machining poses a challenge for temperature control due to the retention of chips and the properties of the material.

During the turning operation of AISI 5115 steel, a substantial amount of mechanical energy is converted into heat due to friction in the cutting zone. The specific heat capacity (452 J/kg K) and thermal conductivity (44 W/m K) of AISI 5115 steel serve as key determinants of the resulting temperature changes. Cutting temperatures can reach levels close to the tempering threshold of AISI 5115, particularly under high cutting speeds. In Minimum Quantity Lubrication (MQL) environments, the feed rate exerts a pivotal influence on temperature fluctuations, influencing heat dissipation and machining efficacy. Furthermore, the moderate mechanical characteristics and resilience of the AISI 5115 steel result in relatively low cutting forces and power requirements throughout machining. However, extended cutting operations lead to augmented energy consumption, with cutting force escalating under conditions of low cutting speeds and elevated feed rates and depths of cut.

In order to optimize the parameters used during machining of AISI 5115 steels and to reduce energy consumption, it is crucial to consider the interactions between cutting conditions, material properties and the resulting surface quality. This research offers valuable insights into the optimization of machining processes, with the aim of improving surface finish and enhancing manufacturing efficiency.

Future research should investigate the specific interactions between cutting conditions and material properties, develop advanced predictive models for temperature and force outcomes, and explore sustainable machining practices. It will also be important to investigate the long-term effects of optimised parameters on tool wear and product durability.

5. CONFLICT OF INTEREST

Author(s) approves that to the best of their knowledge, there is not any conflict of interest or common interest with an institution/organization or a person that may affect the review process of the paper.

6. AUTHOR CONTRIBUTION

Havva DEMİRPOLAT has the full responsibility of the paper about determining the concept of the research, data collection, data analysis and interpretation of the results, preparation of the manuscript and critical analysis of the intellectual content with the final approval.

7. REFERENCES

Agarwal, S., Suman, R., Bahl, S., Haleem, A., Javaid, M., Sharma, M. K., . . . Singhal, P., Optimisation of cutting parameters during turning of 16MnCr5 steel using Taguchi technique. International Journal on Interactive Design and Manufacturing (IJIDeM), 1-12, 2022.

Amini, S., Khakbaz, H., & Barani, A., Improvement of near-dry machining and its effect on tool wear in turning of AISI 4142. Materials and Manufacturing Processes, 30(2), 241-247, 2015.

Asiltürk, İ., Kuntoğlu, M., Binali, R., Akkuş, H., & Salur, E., A comprehensive analysis of surface roughness, vibration, and acoustic emissions based on machine learning during hard turning of AISI 4140 steel. Metals, 13(2), 437, 2023.

Aslan, A., Salur, E., & Kuntoğlu, M., Evaluation of the role of dry and MQL regimes on machining and sustainability index of Strenx 900 steel. Lubricants, 10(11), 301, 2022.

Ben Said, L., Kolsi, L., Ghachem, K., Almeshaal, M., & Maatki, C., Application of nanofluids as cutting fluids in machining operations: A brief review. Applied Nanoscience, 13(6), 4247-4278, 2023.

Benardos, P., & Vosniakos, G.C., Predicting surface roughness in machining: a review. International journal of machine tools and manufacture, 43(8), 833-844, 2003.

Binali, R., Coşkun, M., & Neşeli, S., An investigation of power consumption in milling AISI P20 plastic mold steel by finite elements method. Avrupa Bilim ve Teknoloji Dergisi (34), 513-518, 2022.

Binali, R., Demirpolat, H., Kuntoğlu, M., & Sağlam, H., Machinability investigations based on tool wear, surface roughness, cutting temperature, chip morphology and material removal rate during dry and MQL-assisted milling of Nimax mold steel. Lubricants, 11(3), 101, 2023.

Binali, R., Demirpolat, H., Kuntoğlu, M., & Salur, E., Different Aspects of Machinability in Turning of AISI 304 Stainless Steel: A Sustainable Approach with MQL Technology. Metals, 13(6), 1088, 2023.

Binali, R., Patange, A. D., Kuntoğlu, M., Mikolajczyk, T., & Salur, E., Energy saving by parametric optimization and advanced lubri-cooling techniques in the machining of composites and superalloys: A systematic review. Energies, 15(21), 8313, 2022.

Ghosh, S., & Rao, P. V., Application of sustainable techniques in metal cutting for enhanced machinability: a review. Journal of Cleaner Production, 100, 17-34, 2015.

Grzesik, W., Denkena, B., Żak, K., Grove, T., & Bergmann, B., Energy consumption characterization in precision hard machining using CBN cutting tools. The International Journal of Advanced Manufacturing Technology, 85, 2839-2845, 2016.

Gupta, M. K., Niesłony, P., Sarikaya, M., Korkmaz, M. E., Kuntoğlu, M., & Królczyk, G., Studies on geometrical features of tool wear and other important machining characteristics in sustainable turning of aluminium alloys. International Journal of Precision Engineering and Manufacturing-Green Technology, 10(4), 943-957, 2023.

Harichand, S. C., & Sharma, S., Optimization of heat treatment process for 16MnCr5. International Journal of Engineering Science and Technology (IJEST), 4(3), 998-1004, 2012.

Korkmaz, M. E., & Günay, M., Experimental and statistical analysis on machinability of Nimonic80A superalloy with PVD coated carbide. Sigma Journal of Engineering and Natural Sciences, 36(4), 1141-1152, 2018.

Kuntoglu, M., Machining induced tribological investigations in sustainable milling of Hardox 500 steel: A new approach of measurement science. Measurement, 201, 111715, 2022.

Lampman, S., Introduction to surface hardening of steels. ASM International, ASM Handbook., 4, 259-267, 1991.

Mahapatra, S., Das, A., Jena, P. C., & Das, S. R., Turning of hardened AISI H13 steel with recently developed S3P-AlTiSiN coated carbide tool using MWCNT mixed nanofluid under minimum quantity lubrication. Proceedings of the Institution of Mechanical Engineers, Part C: Journal of Mechanical Engineering Science, 237(4), 843-864, 2023.

Makhesana, M. A., & Patel, K. M., Performance assessment of vegetable oil-based nanofluid in Minimum Quantity Lubrication (MQL) during machining of Inconel 718. Advances in Materials and Processing Technologies, 8(3), 3182-3198, 2022.

Mia, M., Mathematical modeling and optimization of MQL assisted end milling characteristics based on RSM and Taguchi method. Measurement, 121, 249-260, 2018.

Mia, M., Gupta, M. K., Singh, G., Królczyk, G., & Pimenov, D. Y., An approach to cleaner production for machining hardened steel using different cooling-lubrication conditions. Journal of Cleaner Production, 187, 1069-1081, 2018.

Mikolajczyk, T., Paczkowski, T., Kuntoglu, M., Patange, A. D., & Binali, R., Research on using an unconventional tool for increasing tool life by selective exchange of worn cutting edge. Applied Sciences, 13(1), 460, 2022.

Mondal, K., Das, S., Mandal, B., & Sarkar, D., An investigation on turning hardened steel using different tool inserts. Materials and Manufacturing Processes, 31(13), 1770-1781, 2016.

Monkova, K., Monka, P. P., Sekerakova, A., Hruzik, L., Burecek, A., & Urban, M., Comparative study of chip formation in orthogonal and oblique slow-rate machining of EN 16MnCr5 steel. Metals, 9(6), 698, 2019.

Mutlu, B., Binali, R., Demirsöz, R., & Yaşar, N., Machinability of CoCrMo Alloy used in Biomedical applications: Investigation of Cutting Tool Type. Gazi Mühendislik Bilimleri Dergisi, 8(2), 215-227, 2022.

Pimenov, D. Y., da Silva, L. R. R., Machado, A. R., França, P. H. P., Pintaude, G., Unune, D. R., . . . Krolczyk, G. M., A Comprehensive Review of Machinability of Difficult-to-Machine Alloys with Advanced Lubricating and Cooling Techniques. Tribology International, 109677, 2024.

Ross, N. S., Ganesh, M., Srinivasan, D., Gupta, M. K., Korkmaz, M. E., & Krolczyk, J., Role of sustainable cooling/lubrication conditions in improving the tribological and machining characteristics of Monel-400 alloy. Tribology International, 176, 107880, 2022.

Salur, E., Kuntoğlu, M., Aslan, A., & Pimenov, D. Y., The effects of MQL and dry environments on tool wear, cutting temperature, and power consumption during end milling of AISI 1040 steel. Metals, 11(11), 1674, 2021.

Sampaio, M. A., Machado, Á. R., Laurindo, C. A. H., Torres, R. D., & Amorim, F. L., Influence of minimum quantity of lubrication (MQL) when turning hardened SAE 1045 steel: a comparison with dry machining. The International Journal of Advanced Manufacturing Technology, 98, 959-968, 2018.

Selçuk, B., Ipek, R., & Karamış, M., A study on friction and wear behaviour of carburized, carbonitrided and borided AISI 1020 and 5115 steels. Journal of Materials Processing Technology, 141(2), 189-196, 2003.

Selçuk, B., Ipek, R., Karamiş, M., & Kuzucu, V., An investigation on surface properties of treated low carbon and alloyed steels (boriding and carburizing). Journal of Materials Processing Technology, 103(2), 310-317, 2000.

Sen, B., Mia, M., Krolczyk, G. M., Mandal, U. K., & Mondal, S. P., Eco-friendly cutting fluids in minimum quantity lubrication assisted machining: a review on the perception of sustainable manufacturing. International Journal of Precision Engineering and Manufacturing-Green Technology, 8, 249-280, 2021.

Şap, E., Usca, Ü. A., Şap, S., Polat, H., Giasin, K., & Kalyoncu, M., Understanding the effects of machinability properties of Incoloy 800 superalloy under different processing conditions using artificial intelligence methods. Materials Today Communications, 108521, 2024.

Şap, S., Usca, Ü. A., Tarih, Y. S., Yar, A., Kuntoğlu, M., & Gupta, M. K., Novel use of cellulose based biodegradable nano crystals in the machining of PPS composites: An approach towards green machining. International Journal of Precision Engineering and Manufacturing-Green Technology, 11(1), 1-19, 2024.

Usca, Ü. A., The Effect of Cellulose Nanocrystal-Based Nanofluid on Milling Performance: An Investigation of Dillimax 690T. Polymers, 15(23), 4521, 2023.

Usca, Ü. A., Şap, S., Uzun, M., & Değirmenci, Ü., Assessment of the machinability and energy consumption characteristics of Cu–6Gr hybrid composites under sustainable operating. Journal of the Brazilian Society of Mechanical Sciences and Engineering, 46(4), 221, 2024.

Yallese, M. A., Chaoui, K., Zeghib, N., Boulanouar, L., & Rigal, J.-F., Hard machining of hardened bearing steel using cubic boron nitride tool. Journal of Materials Processing Technology, 209(2), 1092-1104, 2009.

Yurtkuran, H., Korkmaz, M. E., & Günay, M., Modelling and optimization of the surface roughness in high speed hard turning with coated and uncoated CBN insert. Gazi University Journal of Science, 29(4), 987-995, 2016.

JOURNAL of
MATERIALS and MECHATRONICS:A

e-ISSN 2717-8811
JournalMM, 2024, 5(1), 183-194
https://doi.org/10.55546/jmm.1485312

Araştırma Makalesi / Research Article

Investigation of Nickel and Chromium Ion Release from Simulated Fixed Orthodontic Appliances in Artificial Saliva Containing Fluoride

Serap TİTİZ YURDAKAL[1]*, Safiye Elif KORCAN[2], Atıf KOCA[3], Elif Esin HAMEŞ[4]

[1*] Dokuz Eylül University, Faculty of Dentistry, Department of Orthodontics, İzmir, Turkey,
ORCID ID: https://orcid.org/0000-0002-4999-8727, serap.titizyurdakal@deu.edu.tr
[2] Uşak University, Uşak Health Training School, Uşak, Turkey,
ORCID ID: https://orcid.org/0000-0001-7875-5516, elif.korcan@usak.edu.tr
[3] Marmara University, Department of Chemical Engineering, İstanbul, Turkey,
ORCID ID: https://orcid.org/0000-0003-0141-5817, akoca@marmara.edu.tr
[4] Ege University, Faculty of Engineering, Department of Bioengineering, İzmir, Turkey,
ORCID ID: https://orcid.org/0000-0001-7302-4781, esin.hames@ege.edu.tr

Geliş/ Received: 16.05.2024; **Revize/Revised:** 15.06.2024 **Kabul / Accepted:** 16.06.2024

ABSTRACT: Fluoride is found in many oral hygiene products due to its anti-cariogenic effect. However, fluoride has a corrosive effect that begins at the time of application and continues with the fluoride remaining in the residual saliva. This study aimed to investigate the effect of different fluoride concentrations on the release of nickel and chromium ions from simulated fixed orthodontic appliances made of copper-nickel-titanium (Cu-NiTi), nickel-titanium (NiTi) and stainless steel (SS) archwires. Simulated orthodontic appliances in the experimental groups were immersed in Klimek artificial saliva containing 125, 500, or 900 ppm fluoride (NaF) for one hour and 0.1 ppm fluoride for eleven hours. The process was repeated in subsequent periods. Control groups were exposed to only Klimek artificial saliva. The amounts of nickel and chromium ions released into Klimek artificial saliva were measured using inductively coupled plasma mass spectroscopy (ICP-MS). The morphological characteristics of the archwires were examined using atomic force microscopy (AFM) and scanning electron microscopy (SEM). The average roughness value of SS archwires before and after immersion was lower than that of Cu-NiTi or NiTi archwires (p<0.05). Simulated orthodontic appliances with SS archwires released more chromium ions than simulated orthodontic appliances with Cu-NiTi and NiTi archwires in experimental groups with 125 ppm fluoride (p<0.05). Simulated fixed orthodontic appliances with SS archwires released fewer nickel ions than simulated fixed orthodontic appliances with Cu-NiTi archwires in both control and experimental groups (p<0.05). Additionally, simulated fixed orthodontic appliances with SS archwires released fewer nickel ions than those with NiTi archwires in control and experimental groups with 500 ppm fluoride (p<0.05).

Keywords: Fluoride effect, Corrosion, Cu-NiTi, NiTi, Stainless Steel, Archwire.

*Sorumlu yazar / Corresponding author: serap.titizyurdakal@deu.edu.tr
Bu makaleye atıf yapmak için /To cite this article

Titiz Yurdakal, S., Korcan, S. E., Koca, A., Hameş, E. E. (2024). Investigation of Nickel and Chromium Ion Release from Simulated Fixed Orthodontic Appliances in Artificial Saliva Containing Fluoride. Journal of Materials and Mechatronics: A (JournalMM), 5(1), 183-194.

1. INTRODUCTION

Stainless steel (SS) brackets, nickel-titanium (NiTi), copper-nickel-titanium (Cu-NiTi), and SS archwires are commonly used in fixed orthodontic treatments. Corrosion, defined as the deterioration of metals or metal alloys due to oxidation or other chemical processes (Brantley and Eliades, 2001), is an unavoidable occurrence in the oral environment, leading to the release of ions into the oral cavity (Eliades and Athanasiou, 2002). Nickel and chromium are the predominant ions released from alloys used in orthodontic treatments. The genotoxic, mutagenic, and cytotoxic effects of nickel and chromium ions can contribute to conditions such as contact allergies, asthma, hypersensitivity, and congenital disabilities (Genelhu et al., 2005; Mikulewicz and Chojnacka, 2010).

Fixed orthodontic treatment can lead to worsening of oral hygiene as brushing becomes more complicated and retention areas for plaque accumulation increase. For this reason, anti-cariogenic agents such as fluoride are frequently used in individuals receiving orthodontic treatment. However, fluoride has a corrosive effect. The passive protective oxide layer on metal or alloy surfaces ensures corrosion resistance and self-repair. The oxide layer in titanium-containing alloys is stronger than SS alloys (Schiff et al., 2002); however, fluoride ions can degrade both chromium oxide and titanium oxide layers (Huang, 2002; Nakagawa et al., 2002; Schiff et al., 2002; Huang, 2003; Huang and Lee, 2005; Heravi at al., 2015).

Fluoride-induced corrosion occurs during exposure and is then continued by residual fluoride in saliva. When fluoride products are used regularly, saliva is constantly contained in varying concentrations of fluoride. Baeshen et al. (2010) investigated salivary fluoride levels following the use of oral care products containing sodium fluoride for patients undergoing orthodontic treatment. They found that fluoride concentration in saliva ranged from 100 to 2200 ppm within one hour. When fluoride products are used regularly, saliva maintains therapeutic fluoride levels of around 0.1 ppm (ten Cate and Duijsters, 1983; Campus et al., 2003). Considering the corrosion-promoting effect of fluoride and the potential biological damage of increased corrosion, it is crucial to examine the corrosion behaviour of orthodontic appliances in the presence of fluoride. Consequently, this study aims to address this research gap by examining the corrosion behaviour of simulated orthodontic appliances with Cu-NiTi, NiTi, and SS archwires in the presence of fluoride while considering the fluoride concentration changes over time.

2. MATERIALS AND METHODS

2.1 Materials

Fixed orthodontic appliances consisted of 4 structurally identical lower incisor brackets, 3-cm-long (0.021 x 0.025-inch) Cu-NiTi, NiTi, or SS archwires tied with elastic ligatures (American Orthodontics Inc., Wisconsin, America). Artificial saliva solution was prepared according to the formula given by Klimek et al. (1982). Sodium fluoride (NaF) (Merck Darmstadt, Germany) was used as a fluoride source. The fluoride concentrations of 0.1 ppm, representing residual saliva (ten Cate and Duijsters, 1983; Campus et al., 2003) and 125, 500 and 900 ppm fluoride, representing application and one hour afterwards (Baeshen et al., 2010), were used. Klimek artificial saliva and simulated fixed orthodontic appliances were sterilised before the experiment.

2.2 Methods

This study was designed with nine experimental groups, each replicated three times, and one control group also replicated three times, and consisted of three periods of 12 (1+11) hours (36 hours

in total). In the experimental groups, simulated fixed orthodontic appliances with Cu-NiTi, NiTi, or SS archwires were immersed in 3 mL of Klimek artificial saliva (pH 6.9) containing 125, 500, or 900 ppm sodium fluoride for one hour. Subsequently, the appliances were transferred to 3 mL of Klimek artificial saliva with 0.1 ppm fluoride for an additional 11 hours. The process was repeated in the second and third periods. The same protocol was applied to the control groups, which were only exposed to Klimek artificial saliva. To control the contamination, 100 µL of the liquid was inoculated into Brain Heart Infusion Agar following the transfer of simulated fixed orthodontic appliances to the new environment. The collected liquids were then transferred into containers based on their respective groups.

In this study, the amounts of nickel and chromium ions released into Klimek artificial saliva were determined by inductively coupled plasma mass spectroscopy (ICP-MS). Atomic force microscopy (AFM) and scanning electron microscopy (SEM) were used to analyse the morphological features of archwires before and after immersion. The schematic of the study is illustrated in Figure 1.

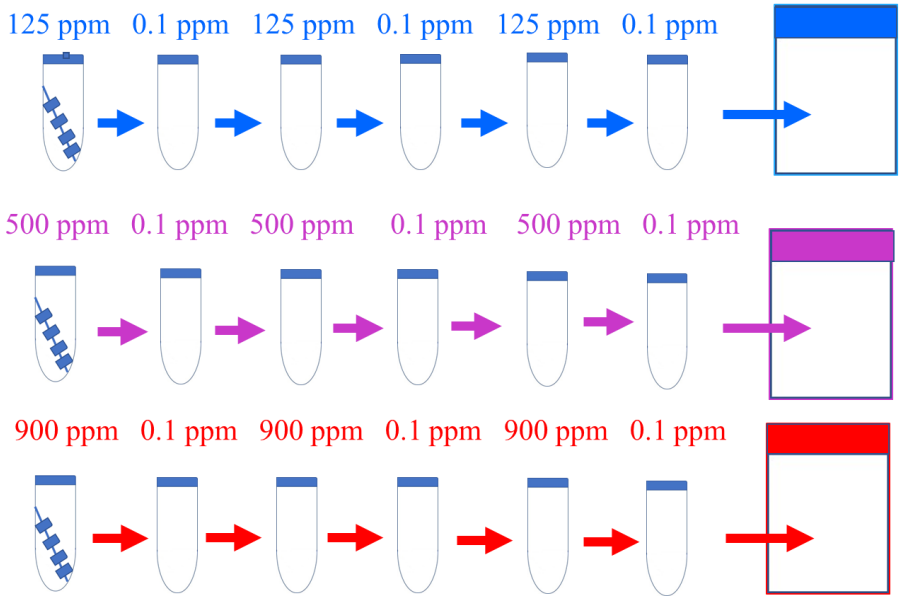

Figure 1: The schematic illustration of the study

2.3 Statistical Analysis

As the first step of the analysis, compliance with normal distribution was tested using the Shapiro-Wilk test. ANOVA test was used for comparisons between three groups regarding a normally distributed independent variable. Post Hoc Bonferroni analysis was conducted to reveal the group or groups that made the difference. An Independent Sample T-test was applied to compare two normally distributed groups. Independent Sample T-test was used when the assumptions were met, and the Whitney U test was used when they were not met.

3. RESULTS AND DISCUSSION

No growth was observed on the Brain Heart Agar, indicating the absence of contamination in the samples.

3.1 Composition of Archwires

The composition of archwires is shown in Table 1.

Table 1: Composition of archwires

	Nickel	Titanium	Chromium	Copper	Iron
	% (w/w)	% (w/w)	% (w/w)	% (w/w)	% (w/w)
Cu-NiTi	48.45	45.26	0.32	5.64	0.33
NiTi	54.28	44.59	0.10	0.62	0.41
SS	7.9	0.34	20.26	0.38	69.40

3.2 Ion Release (ICP/MS Analysis)

In this study, simulated fixed orthodontic appliances comprised structurally identical SS brackets with different orthodontic archwires. The variations in the types of orthodontic archwires are likely attributed to differences in the release of nickel and chromium ions. The comparison of nickel and chromium ion concentrations released in the control groups is presented in Table 2 and Figure 2. No significant difference was detected in the average amount of chromium ion release among the control groups. However, nickel ion was released the most in simulated orthodontic appliances with Cu-NiTi archwires, while the least amount was released in appliances with SS archwires (p=.000*, p=.000*, and p=.000*).

Table 2: Comparison of the concentrations of nickel and chromium ions released in control groups

Ion	Group	Mean (ppb)	SD	Test Statistics	p	Bonferroni results	p
	Cu-NiTi	19.05	1.937	3.789**	.150		
Cr	NiTi	22.08	4.483				
	SS	17.38	1.119				
	Cu-NiTi	25.38	2.535	75.385	.000*	CuNiTi/NiTi	.000*
Ni	NiTi	18.87	1.660			NiTi/SS	.000*
	SS	12.74	0.587			CuNiTi/SS	.000*

p*<0.05. ANOVA, Kruskal Wallis. Abbreviations: Cr: Chromium, Ni: Nickel, SD: Standard Deviation, Cu-NiTi: Simulated orthodontic appliances with Cu-NiTi archwires, NiTi: Simulated orthodontic appliances with NiTi archwires, SS: Simulated orthodontic appliances with SS archwires.

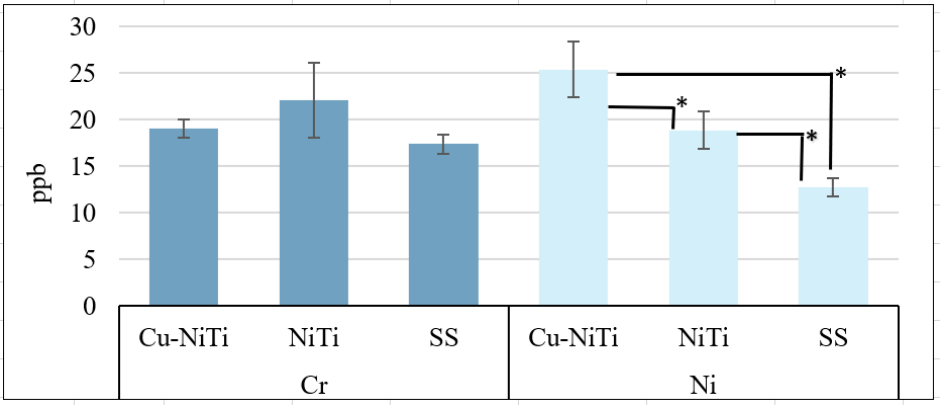

Figure 2: Comparison of the concentrations of nickel and chromium ions released in control groups. Abbreviations: **p*<0.05, Cr: Chromium, Ni: Nickel, Cu-NiTi: Simulated orthodontic appliances with Cu-NiTi archwires, NiTi: Simulated orthodontic appliances with NiTi archwires, SS: Simulated orthodontic appliances with SS archwires.

Although titanium-containing archwires are considered more biocompatible than SS archwires, the results from various studies in the literature are contradictory (Barret et al., 1993; Hwang et al., 2000; Kuhta et al., 2009; Karnam and Reddy., 2012; Močnik et al., 2017; Chantarawaratit and Yanisarapan, 2021; Titiz et al., 2022). In line with the present study, our previous research also indicated a higher rate of nickel release in simulated orthodontic appliances with NiTi archwires than those with SS archwires (Titiz et al., 2022). Similarly, Močnik et al. (2017) reported that SS archwires released 32.6 μg/cm^2/week nickel, while NiTi archwires released 69.4 μg/cm^2/week nickel during

simulated wear in the oral cavity. Consistent with our findings, Chantarawaratit and Yanisarapan (2021) reported that simulated orthodontic appliances with NiTi archwires released more nickel than those with SS archwires in neutral artificial saliva. However, in the related study, simulated orthodontic appliances with SS archwires released more chromium ions than those with NiTi archwires (Chantarawaratit and Yanisarapan, 2021). Similar to the current study, Karnam and Reddy (2012) and Barret et al. (1993) found no difference in chromium ion release in simulated orthodontic appliances with Cu-NiTi, NiTi, and SS archwires (Karnam and Reddy, 2012) or between SS and NiTi archwires (Barret et al., 1993). However, no difference in nickel release was also found between simulated orthodontic appliances in the related studies (Karnam and Reddy, 2012; Barret et al., 1993). Kuhta et al. (2009) and Hwang et al. (2000) reported that SS archwires released more nickel and chromium ions than NiTi archwires. Notably, in the study by Hwang et al. (2000), only SS archwires were heat treated in an electric furnace at 500 ºC for one minute and were then quenched in water. Heat treatment decreases the corrosion resistance of alloys, potentially leading to increased ion release from SS archwires.

In the experimental groups containing 125 ppm fluoride, simulated orthodontic appliances with SS archwires released more chromium ions than those with Cu-NiTi and NiTi archwires (p=.002 and p=.001) (Table 3, Figure 3). Moreover, in groups containing 125, 500 and 900 ppm fluoride, simulated orthodontic appliances with Cu-NiTi archwires released more nickel ions than simulated orthodontic appliances with SS archwires (p=.002, p=.002, p=.003). Additionally, in the groups containing 500 ppm fluoride, simulated orthodontic appliances with NiTi archwires released more nickel ions than those with SS archwires (p=.002) (Table 3, Figure 3).

Table 3: Comparison of the amounts of nickel and chromium ions released in the experimental groups

Fluoride	Ion	Group	Mean (ppb)	SD	Test Statistics	p	Bonferroni results	p
125 pnm	Cr	Cu-NiTi	18.95	0.148	15.041	.000*	CuNiTi/SS	.002*
		NiTi	18.52	0.58			NiTi/SS	.001*
		SS	23.60	2.88				
	Ni	Cu-NiTi	19.18	0.54	8.096	.004*	CuNiTi/SS	.003*
		NiTi	17.43	1.92				
		SS	16.05	1.21				
500 ppm	Cr	Cu-NiTi	19.77	1.32	1.004	.390		
		NiTi	20.60	0.90				
		SS	20.98	2.07				
	Ni	Cu-NiTi	23.21	0.69	23.937	.000*	CuNiTi/SS	.002*
		NiTi	20.36	3.57			NiTi/SS	.002*
		SS	14.77	0.75				
900 ppm	Cr	Cu-NiTi	16.48	1.32	1.354	.292		
		NiTi	16.23	0.36				
		SS	17.09	0.16				
	Ni	Cu-NiTi	47.08	28.32	11.882**	.003*	Cu-NiTi/SS	.002*
		NiTi	18.76	3.09				
		SS	14.95	0.17				

*p<0.05. ANOVA, Kruskal Wallis** Abbreviations: Cr: Chromium, Ni: Nickel, 125 ppm: Experimental groups containing 125 ppm fluoride, 500 ppm: Experimental groups containing 500 ppm fluoride, 900 ppm: Experimental groups containing 900 ppm fluoride, Cu-NiTi: orthodontic appliances with Cu-NiTi archwires, NiTi: Simulated orthodontic appliances with NiTi archwires, SS: Simulated orthodontic appliances with SS archwires

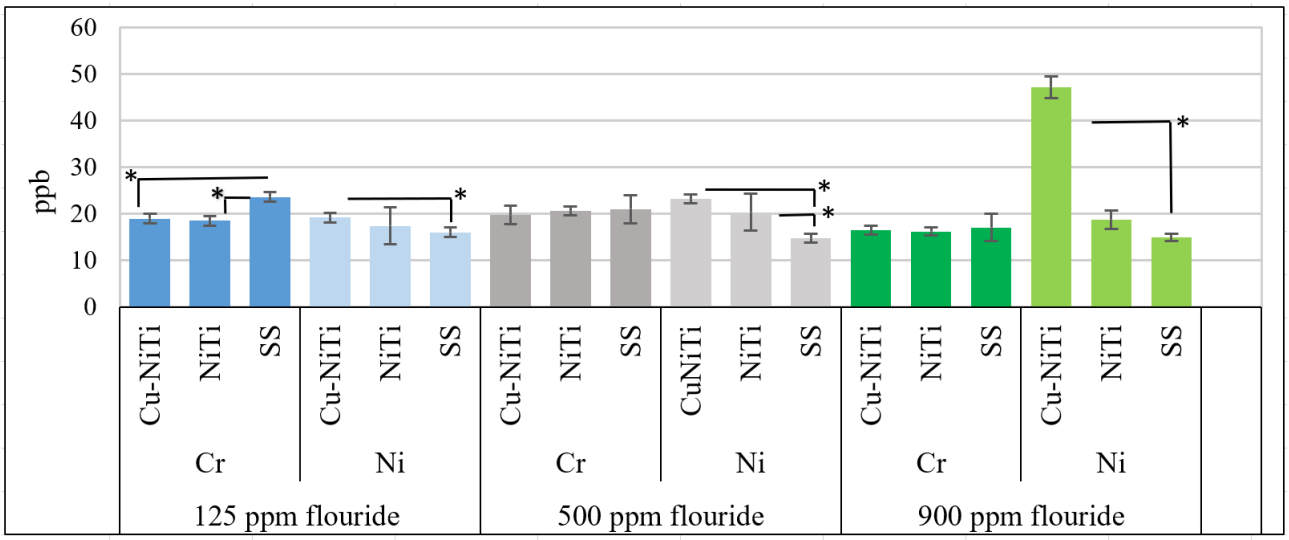

Figure 3: Nickel and chromium release in Experimental Groups at different fluoride concentrations. *p<0.05 Abbreviations: Cr: Chromium, Ni: Nickel, 125 ppm: Experimental groups containing 125 ppm fluoride, 500 ppm: Experimental groups containing 500 ppm fluoride, 900 ppm: Experimental groups containing 900 ppm fluoride, Cu-NiTi: Simulated orthodontic appliances with Cu-NiTi archwires, NiTi: Simulated orthodontic appliances with NiTi archwires, SS: Simulated orthodontic appliances with SS archwires

To the best of our knowledge, relatively few studies have specifically investigated the corrosion behaviours of Cu-NiTi, NiTi, and SS archwires in the presence of sodium fluoride using immersion tests. Chantarawaratit and Yanisarapan (2021) and Yanisarapan et al. (2018) reported that simulated orthodontic appliances with NiTi archwires released more nickel ions than those with SS archwires in artificial saliva containing 1000 ppm sodium fluoride. Similarly, Condò et al. (2022) found that SS archwires released less nickel but more chromium ions after 168 hours of immersion in neutral artificial saliva containing 400 ppm sodium fluoride. Močnik et al. (2017) investigated the effects of fluoride (600 ppm, 1000 ppm, 3200 ppm) on corrosion using electrochemical tests in artificial saliva. They reported that the SS alloy exhibited better properties at high fluoride concentrations than the NiTi alloy. Pulikkottil et al. (2016) found that the corrosion resistance of NiTi archwires was higher than that of the SS archwires in an environment containing 2250 ppm sodium fluoride (pH 6.5). Similarly, Heravi et al. (2014) determined that the corrosion resistance of NiTi archwires was higher than SS archwires in the presence of 500 ppm and 2000 ppm sodium fluoride (pH 5.3).

The resistance of metals or alloys to corrosion can be determined through immersion tests, which measure the number of ions passing into the liquid, or electrochemical tests. However, corrosion resistances determined by electrochemical tests may not fully reflect the conditions in the oral environment. Therefore, immersion tests are more reliable for examining the corrosion behaviour of metals in the oral environment (Luft et al., 2009). While SS wires have demonstrated lower corrosion resistance in electrochemical tests (Pulikkottil et al., 2016; Heravi et al., 2014), numerous studies suggest that SS wires exhibit greater biocompatibility when considering nickel release in artificial saliva containing fluoride (Močnik et al., 2017; Yanisarapan et al., 2018; Chantarawaratit and Yanisarapan, 2021; Condò et al., 2022).

3.3 Surface Roughness

A statistically significant difference was detected in the average roughness (Ra) of Cu-NiTi, NiTi, and SS as-received archwires (Table 4 and Figure 4). The Ra value of NiTi and Cu-NiTi as-received archwires was higher than that of the as-received SS archwires. The Cu-NiTi archwire's Ra value was higher than the SS archwires in the control groups. The Ra values of Cu-NiTi and NiTi

archwires were higher than SS archwires in all experimental groups (125, 500 and 900 ppm). AFM surface morphologies of archwires, both as-received and after immersion, are presented in Figure 5.

Table 4: Comparison of the average roughness values of archwires

Group	Archwire	Mean (nm)	SD	Test Statistic	p	Bonferroni result	p
As-received	Cu-NiTi	32.06	6.34	27.389	<0.001*	Cu-NiTi/NiTi	1.000
	NiTi	35.94	8.30	2.937	0.027*	Cu-NiTi/SS	0.05*
	SS	6.28	2.39	1.893	0.076	NiTi/SS	0.05*
Control group	Cu-NiTi	55.75	15.85			Cu-NiTi/NiTi	0.433
	NiTi	33.18	5.65			Cu-NiTi/SS	0.048*
	SS	19.72	18.98			NiTi/SS	1.000
125 ppm fluoride	Cu-NiTi	61.66	16.33			Cu-NiTi/NiTi	1.000
	NiTi	75.72	25.30			Cu-NiTi/SS	0.002*
	SS	9.02	6.10			NiTi/SS	<0.001*
500 ppm fluoride	Cu-NiTi	67.69	15.59			Cu-NiTi/NiTi	1.000
	NiTi	89.55	74.28			Cu-NiTi/SS	0.002*
	SS	6.12	1.37			NiTi/SS	0.031*
900 ppm fluoride	Cu-NiTi	58.36	22.41			Cu-NiTi/NiTi	1.000
	NiTi	45.00	15.71			Cu-NiTi/SS	0.002*
	SS	4.58	0.98			NiTi/SS	0.031*

*p<0.05. Two-Way ANOVA. Abbreviations: SD: Standard Deviation, 125 ppm: Experimental groups containing 125 ppm fluoride, 500 ppm: Experimental groups containing 500 ppm fluoride, 900 ppm: Experimental groups containing 900 ppm fluoride.

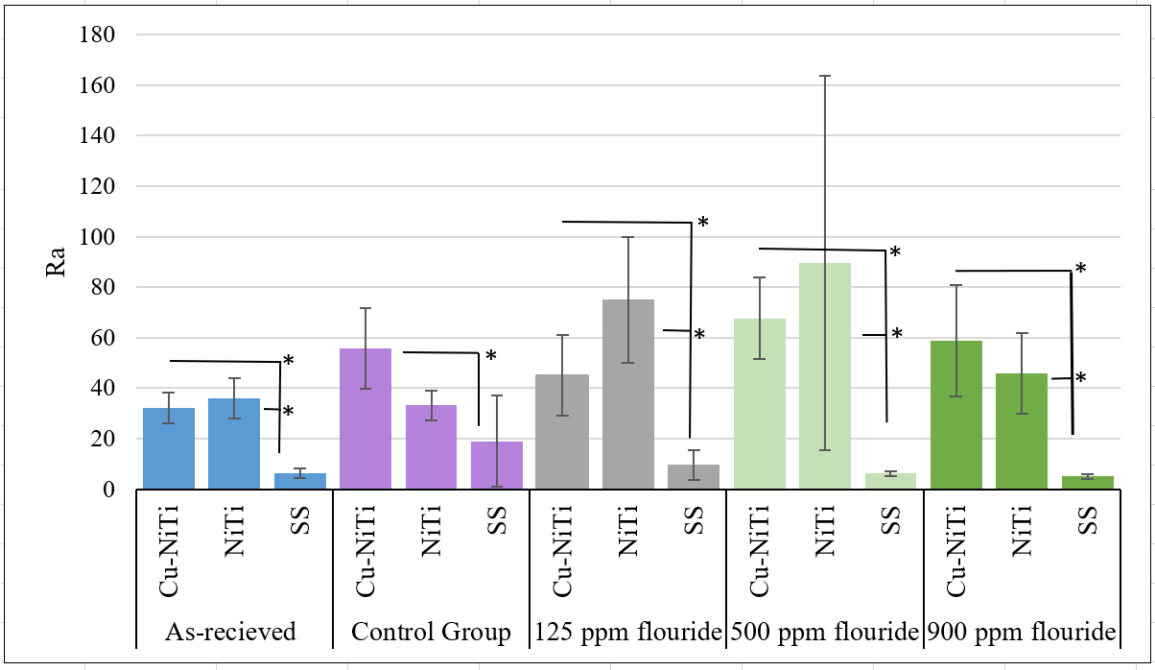

Figure 4: Comparison of the Ra (in nm) values of as-received and post-immersed archwires. *p<0.05. Two-Way ANOVA. Abbreviations: 125 ppm: Experimental groups containing 125 ppm fluoride, 500 ppm: Experimental groups containing 500 ppm fluoride, 900 ppm: Experimental groups containing 900 ppm fluoride.

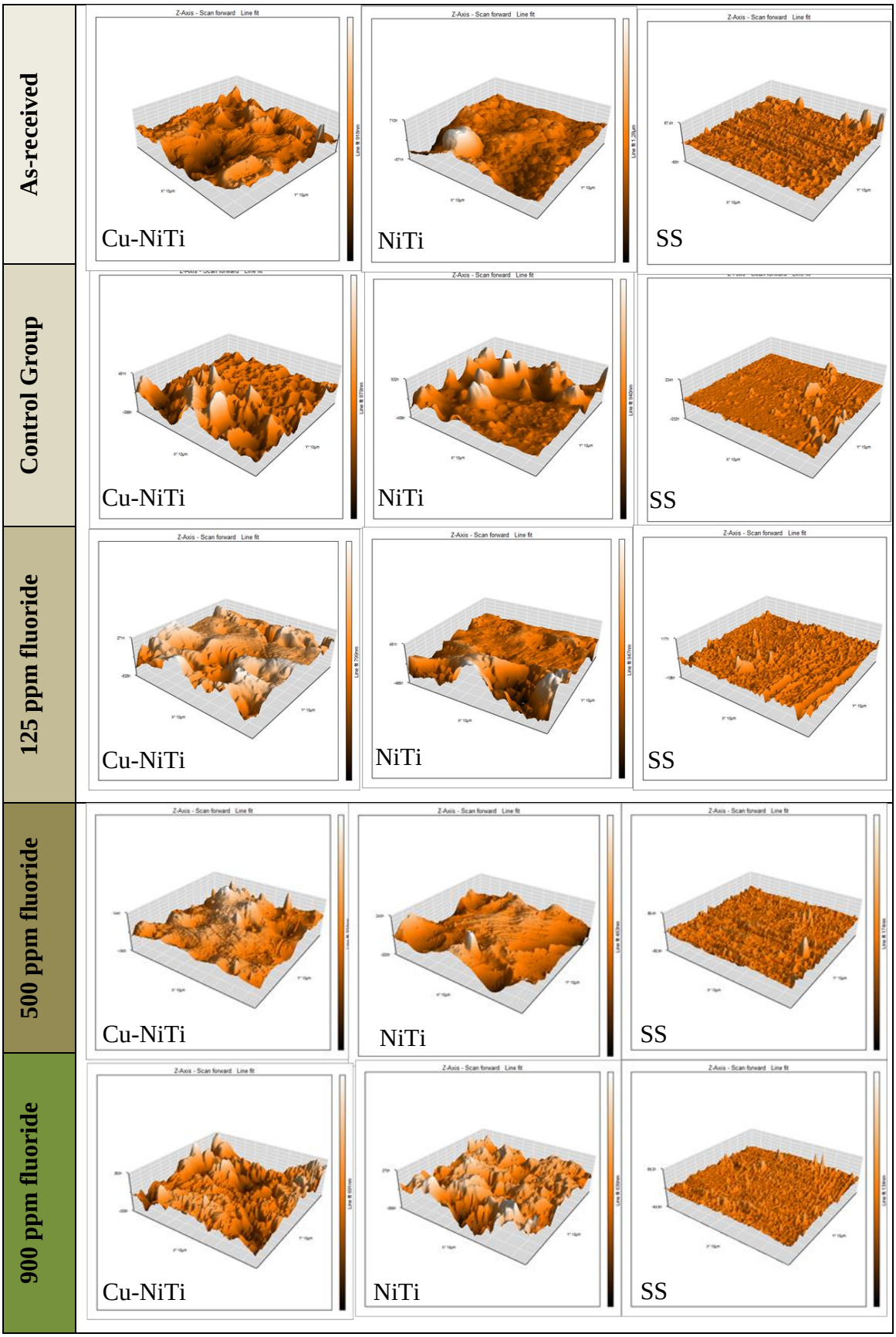

Figure 5: Atomic force microscopy (AFM) surface morphologies of as-received and post-immersed archwires Abbreviations:125 ppm: Experimental groups containing 125 ppm fluoride, 500 ppm: Experimental groups containing 500 ppm fluoride, 900 ppm: Experimental groups containing 900 ppm fluoride Each row belongs to the same group.

3.4 SEM Results

Figure 6 displays SEM images, revealing that the SS archwires appeared smoother than the NiTi and Cu-NiTi archwires, both as-received and post-immersed states. These SEM observations align with the Ra values from AFM.

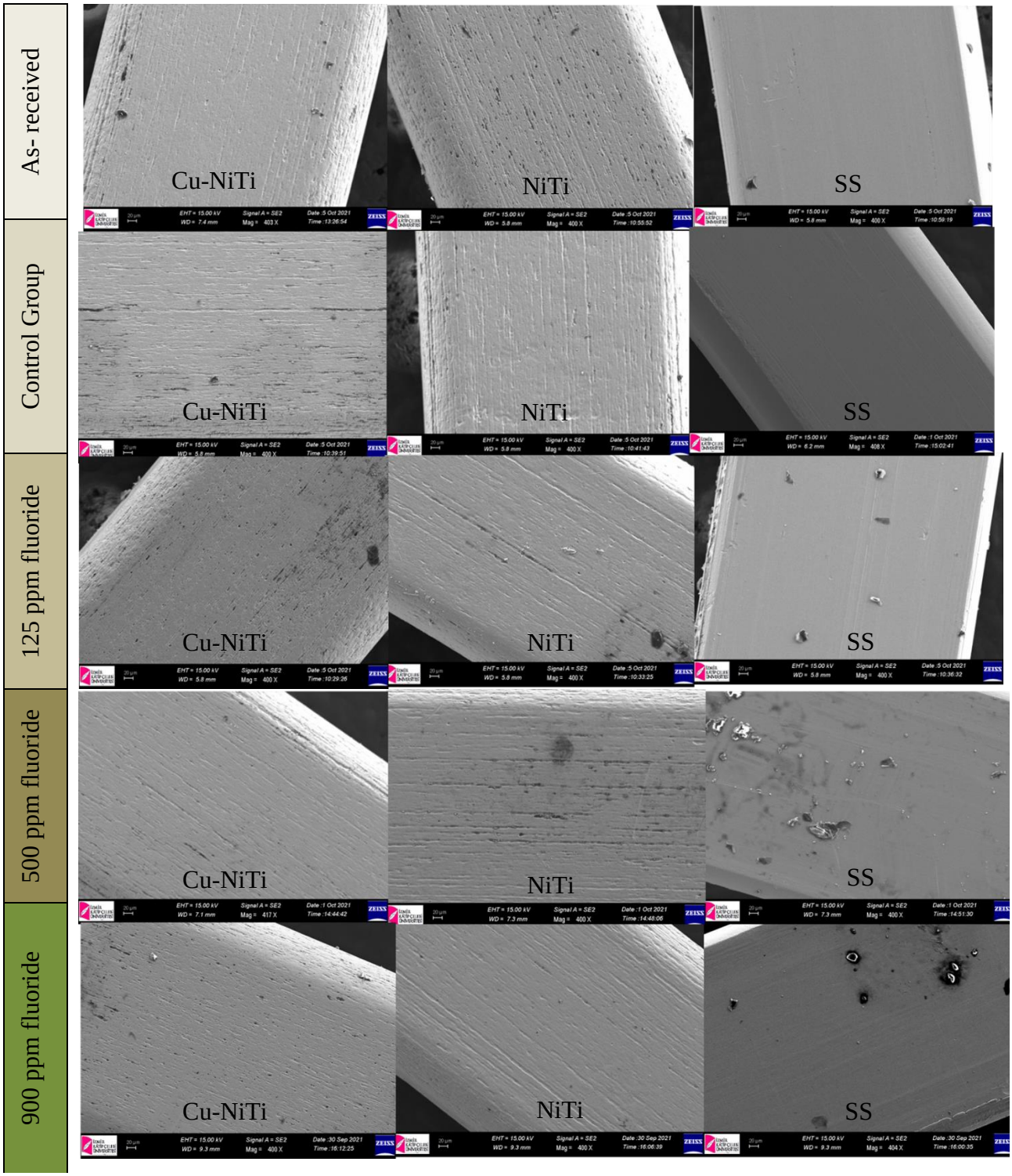

Figure 6: SEM photographs of as-received and post-immersed archwires. Abbreviations:125 ppm: Experimental groups containing 125 ppm fluoride, 500 ppm: Experimental groups containing 500 ppm fluoride, 900 ppm: Experimental groups containing 900 ppm fluoride Each row belongs to the same group.

The passive protective layer present on SS archwires (Cr_2O_3) and titanium-containing archwires (TiO_2) resists corrosion and self-healing. Since the TiO_2 layer is stronger than the Cr_2O_3 layer in Ti-

containing alloys, alloys containing titanium are expected to exhibit greater durability compared to stainless steel (Schiff et al., 2002). However, it's important to note that other factors can influence the corrosion rate of titanium-containing alloys. In the current study, the SEM images and Ra results indicated that the surface roughness of SS archwires was lower than that of NiTi or Cu-NiTi archwires. The smoother surface state of SS archwires continued in both artificial saliva alone and artificial saliva containing various concentrations of fluoride. Archwires containing titanium exhibited rougher surfaces compared to SS archwires, which may contribute to the galvanic corrosion of these alloys (Oshida et al., 1992; Jacobs al., 1998). Additionally, manufacturing defects in NiTi archwires may be another factor in exhilarating corrosion (Oshida et al., 1992). Thus, surface roughness should be considered a significant factor contributing to the corrosive behaviour of orthodontic archwires, alongside the composition of protective oxide layers and other environmental factors.

During orthodontic treatment, the corrosion process is multifactorial and is affected by many factors, such as temperature, food acidity, microorganisms, and friction. To understand the corrosion process, it is important to search for the effects of the factors one by one, but the corrosion behaviour of alloys may change with the influence of other factors. For this reason, more comprehensive *in vitro* corrosion studies should be carried out, to understand the corrosion process of alloys considering the environment's temperature change, microbial flora, friction, and pH levels with fluoride.

4. CONCLUSION

This study was carried out to investigate the effect of fluoride on nickel and chromium release in a simulated intraoral environment. We concluded the following.

1. No significant difference was detected in the average amount of chromium ion release among the control groups.
2. Nickel ion was released the most in simulated orthodontic appliances with Cu-NiTi archwires, while the least amount was released in appliances with SS archwires in control groups.
3. In the experimental groups containing 125 ppm fluoride, simulated orthodontic appliances with SS archwires released more chromium ions than those with Cu-NiTi and NiTi archwires.
4. In experimental groups containing 125, 500, and 900 ppm fluoride, simulated orthodontic appliances with Cu-NiTi archwires released more nickel ions than those with SS archwires.
5. Simulated orthodontic appliances with NiTi archwires released more nickel ions than those with SS archwires in experimental groups containing 500 ppm fluoride.
6. No significant difference was observed in chromium and nickel release between simulated orthodontic appliances with CuNiTi or NiTi archwires in experimental groups containing 125, 500 and 900 ppm fluoride.
7. Surface roughness should be considered a significant factor contributing to the corrosive behaviour of orthodontic archwires.
8. The use of materials from different brands and testing with varying methods may reduce the comparability of corrosion studies in the literature.

5. ACKNOWLEDGEMENTS

The authors would like to thank The Scientific and Technological Research Council of Türkiye (TUBİTAK, project number 319S015).

6. CONFLICT OF INTEREST

Authors approve that. to the best of their knowledge. There is no conflict of interest or common interest with an institution/organisation or a person that may affect the paper's review process.

7. AUTHOR CONTRIBUTION

Conceptualisation. Serap Titiz YURDAKAL; Methodology. Serap Titiz YURDAKAL and Safiye Elif KORCAN; Formal analysis Serap Titiz YURDAKAL and Safiye Elif KORCAN. Investigation. Serap Titiz YURDAKAL; Data curation. Serap Titiz YURDAKAL and Elif Esin HAMEŞ; Writing-original draft and review & editing. Serap Titiz YURDAKAL, Elif Esin HAMEŞ, and Atıf KOCA

8. REFERENCES

Baeshen H., Kjellberg H., Birkhed D., Oral fluoride retention in orthodontic patients with and without fixed appliances after using different fluoridated home-care products, Acta Odontologica Scandinavica, 68(4), 185-192, 2010.

Barrett R.D., Bishara S.E., Quinn, J.K., Biodegradation of orthodontic appliances. Part I. Biodegradation of Nickel and chromium *in vitro*, American Journal of Orthodontics and Dentofacial Orthopedics, 103(1), 8-14, 1993.

Brantley W.A., Theodore E., Orthodontic materials: scientific and clinical aspects, American Journal of Orthodontics and dentofacial orthopedics, 119(6), 672-673, 2001.

Campus G., Lallai MR., Carboni R., Fluoride concentration in saliva after use of oral hygiene products. Caries research, 37(1), 66-70, 2003.

Chantarawaratit P.O., Yanisarapan T., Exposure to the oral environment enhances the corrosion of metal orthodontic appliances caused by fluoride-containing products: Cytotoxicity, metal ion release, and surface roughness, American Journal of Orthodontics and Dentofacial Orthopedics, 160(1), 101-112, 2021.

Condò R., Carli E., Cioffi A., Cataldi M.E., Quinzi V., Casaglia, A., ... & Mampieri G., Fluorinated agents effects on orthodontic alloys: a descriptive *in vitro* study, Materials, 15(13), 4612, 2022.

Eliades T., Athanasiou A.E., In vivo aging of orthodontic alloys: Implications for corrosion potential nickel release. and biocompatibility, The Angle Orthodontist, 72(3). 222-237, 2002.

Faccioni F., Franceschetti P., Cerpelloni M., Fracasso M.E., *In vivo* study on metal release from fixed orthodontic appliances and DNA damage in oral mucosa cells, American Journal of Orthodontics and Dentofacial Orthopedics, 124(6), 687-693, discussion 693, 2003.

Genelhu M.C.L.S., Marigo M., Alves O.L.F., Malaquias L.C.C., Gomez R.S., Characterisation of nickel-induced allergic contact stomatitis associated with fixed orthodontic appliances American journal of orthodontics and dentofacial orthopedics, 128(3), 378-381, 2005.

Heravi F., Moayed M.H., Mokhber N., Effect of fluoride on nickel-titanium and stainless steel orthodontic archwires: an in-vitro study, Journal of Dentistry (Tehran. Iran), *12*(1), 49, 2015.

Huang H.H, Effects of fluoride concentration and elastic tensile strain on the corrosion resistance of commercially pure titanium, *Biomaterials*, *23*(1), 59-63, 2002.

Huang H.H, Effect of fluoride and albumin concentration on the corrosion behavior of Ti–6Al–4V alloy, *Biomaterials*, *24*(2). 275-282, 2003.

Huang H.H., Lee T.H., Electrochemical impedance spectroscopy study of Ti–6Al–4V alloy in artificial saliva with fluoride and/or bovine albumin, Dental Materials, *21*(8), 749-755, 2005.

Jacobs J.J., Gilbert J.L., Urban RM., Corrosion of metal orthopaedic implants, The Journal of Bone and Joint Surgery (American Volume), 80(2), 268-282, 1998.

Karnam S.K., Reddy A.N., Manjith C.M., Comparison of metal ion release from different bracket archwire combinations: an in vitro study, J Contemp Dent Pract, 13(3), 376-81, 2012.

Klimek J., Hellwig E., Ahrens G., Fluoride taken up by plaque. by the underlying enamel and by clean enamel from three fluoride compounds in vitro, Caries Research, 16(2), 156-161, 1982

Kuhta M., Pavlin D., Slaj M., Varga S., Lapter V.M., Slaj M., Type of archwire and level of acidity: effects on the release of metal ions from orthodontic appliances, The Angle Orthodontist, 79(1), 102-110, 2009.

Luft S., Keilig L., Jäger A., Bourauel C., In-vitro evaluation of the corrosion behavior of orthodontic brackets. Orthod Craniofac Res, 12(1), 43-51, 2009.

Mikulewicz M., Chojnacka K., Trace metal release from orthodontic appliances by in vivo studies: a systematic literature review, Biological Trace Element Research, 137(2), 127-138, 2010.

Močnik P., Kosec T., Kovač J., Bizjak M., The effect of pH, fluoride and tribocorrosion on the surface properties of dental archwires. Materials Science and Engineering, C, 78, 682-689, 2017.

Nakagawa M., Matsuya S., Udoh K., Effects of fluoride and dissolved oxygen concentrations on the corrosion behavior of pure titanium and titanium alloys, Dental materials journal, *21*(2), 83-92, 2002.

Oshida Y., Sachdeva R.C., Miyazaki S., Microanalytical characterisation and surface modification of TiNi orthodontic archwires. Bio Med Mater Eng. 2(2), 51-69, 1992.

Pulikkottil V.J., Chidambaram S., Bejoy P.U., Femin P.K., Paul P., Rishad M., Corrosion resistance of stainless steel. nickel-titanium. titanium molybdenum alloy. and ion-implanted titanium molybdenum alloy archwires in acidic fluoride-containing artificial saliva: An: *in vitro:* study, Journal of Pharmacy and Bioallied Sciences, *8*(Suppl 1), S96-S99, 2016.

Schiff N., Grosgogeat B., Lissac M., Dalard F., Influence of fluoride content and pH on the corrosion resistance of titanium and its alloys, Biomaterials, 23(9), 1995-2002, 2002.

Ten Cate J.M., Duijsters P.P.E., Influence of fluoride in solution on tooth demineralization: II. Microradiographic data, Caries Research, 17(6), 513-519, 1983.

Titiz S., Erdoğan Z.K., Tuna E.E.H., Aras A., Nickel release and the viability of *Streptococcus mutans* corresponding to low risk of dental caries in artificial saliva containing orthodontic appliances: *In vitro* study, Turkish journal of orthodontics, *35*(3), 157, 2022.

Yanisarapan T., Thunyakitpisal P., Chantarawaratit PO., Corrosion of metal orthodontic brackets and archwires caused by fluoride-containing products: Cytotoxicity, metal ion release and surface roughness, Orthodontic Waves, 77(2), 79-89, 2018.

JOURNAL of
MATERIALS and MECHATRONICS:A

e-ISSN 2717-8811
JournalMM, 2024, 5(1), 195-213
https://doi.org/10.55546/jmm.1498662

Araştırma Makalesi / Research Article

Investigation on Microstructural and Mechanical Properties of $FeNiMnCrCoTi_{0.1}$ High Entropy Alloy with B Addition

Mahmud Cemaleddin YALÇIN[1*], Şükrü TALAŞ[2]

[1*] Afyon Kocatepe University, Faculty of Technology, Department of Metallurgical and Materials Engineering, Afyonkarahisar, Turkey,
ORCID ID: https://orcid.org/0000-0003-1685-7319, mcyalcin@aku.edu.tr
[2] Afyon Kocatepe University, Faculty of Technology, Department of Metallurgical and Materials Engineering, Afyonkarahisar, Turkey,
ORCID ID: https://orcid.org/0000-0002-4721-0844, stalas@aku.edu.tr

Geliş/ Received: 10.06.2024**;** **Revize/Revised:** 25.06.2024 **Kabul / Accepted:** 25.06.2024

ABSTRACT: High-entropy alloys (HEAs) are alloys with high potential for use in defense, aircraft, and aerospace industries due to their properties such as high strength, hardness, wear resistance, corrosion resistance, and ability to operate at high temperatures. Therefore, in this study, $FeNiMnCrCoTi_{0.1}B_X$ (x values in molar ratio, x = 0-1) high entropy alloys were produced by arc melting technique under protective gas atmosphere using a reverse vacuum method. The microstructural properties of the produced HEAs were examined by scanning electron microscopy (SEM), and energy-dispersive X-ray spectroscopy (EDX) analysis was also performed. The crystal lattice structure of the produced HEAs was determined by X-ray diffraction (XRD) analysis. Microhardness and compression tests were conducted to determine the mechanical properties of the produced HEAs. It is observed that the hardness of the $FeNiMnCrCoTi_{0.1}B_X$ high-entropy alloy increases as the boron content increases. The highest microhardness obtained was 593.8 HV in the $FeNiMnCrCoTi_{0.1}B$ alloy. As the boron content increases, the yield stress has also increased in compression testing. The highest yield stress was determined to be 1329 MPa in the $FeNiMnCrCoTi_{0.1}B$ alloy.

Keywords: High Entropy Alloy, Arc Melting, Microhardness, Compression Test, Physical Properties.

*Sorumlu yazar / Corresponding author: mcyalcin@aku.edu.tr
Bu makaleye atıf yapmak için /To cite this article

Yalçın, M.C., Talaş, Ş. (2024). Investigation of Microstructural and Mechanical Properties of $FeNiMnCrCoTi_{0.1}$ High Entropy Alloy with B Addition. Journal of Materials and Mechatronics: A (JournalMM), 5(1), 195-213.

1. INTRODUCTION

High-entropy alloys (HEAs), differ from traditional single-element-based alloys (such as Fe, Cu, Ni, Al, Mg, and Ti, etc.) in that they consist of at least 5 principal elements in equimolar or near-equimolar proportions in their structure, rather than having a single primary element matrix (Yeh et al., 2004; Zhang et al., 2018). These alloys, due to their high mixture entropy, tend to be more stable and often form solid solutions containing complex phases instead of simple ones, including both face-centered cubic (FCC) and body-centered cubic (BCC) crystal structures (Zhou et al., 2007; Yang and Zhang, 2012). In 2006, Yeh (Yeh, 2006) described high-entropy alloys, explaining that the combination of multiple principal elements leads to high entropy, lattice distortion, slow diffusion, and cocktail effects (Yeh, 2006; İçin et al., 2023).

High-entropy alloys, due to their ability to combine superior properties such as high strength, high wear resistance, stability at high temperatures, good corrosion resistance, have broad application potential in various sectors including defense, aerospace, nuclear, automotive industry, superconductors, and healthcare (Zhang et al., 2014; Gao et al., 2018; Murty et al., 2014). Various methods are used to produce HEAs, including mechanical alloying-sintering (solid-state), magnetron sputtering (physical vapor deposition), selective laser melting (additive manufacturing), induction melting (liquid state), and vacuum arc melting (liquid state). Among these, vacuum arc melting is the most commonly used method (Murty et al., 2014; Algan Şimşek et al., 2022). In this method, all elements are melted into a liquid state inside a copper crucible in an inert gas environment by an arc formed by a tungsten electrode tip and then solidified in the copper crucible. To ensure the chemical homogeneity of the alloys, multiple melting and solidification cycles are often performed. The shape of the solidified samples is button-shaped inside a cup-like copper crucible. To facilitate sample preparation processes for analyses such as tension and compression, the button-shaped sample is poured into a pre-machined cylindrical copper mold (Zhou et al., 2007; Gao et al., 2016).

The effects of elemental additions made to high-entropy alloys on the crystal structure and microstructure morphology have been observed to have positive impacts on mechanical properties in many studies (He et al., 2014). The FeNiMnCrCo high-entropy alloy exhibits approximate yield strength of 200 MPa and approximate ultimate tensile strength of 600 MPa at room temperature, depending on grain size (Otto et al., 2013). Due to its relatively low strength, numerous studies have been conducted to establish a good balance between strength and ductility. This alloy possesses excellent work hardening ability, exceptional ductility at both room and cryogenic temperatures, and promising fracture toughness at cryogenic temperatures. These properties make these alloys attractive for industrial applications and encourage researchers to explore the addition of intermediate elements (Shahmir et al., 2023).

In the studies of $Al_{0.5}$CoCrCuFeNiTix (Chen et al., 2006) and CoCrFeNiTix (Shun et al., 2012), it has been observed that the addition of Ti improves the mechanical properties. This observation is attributed to the altered crystal structure due to the addition, and these alloys have either a BCC or a FCC crystal structure, or a mixture of both. Generally, alloys with a body-centered cubic crystal structure exhibit higher strength compared to alloys with a face-centered cubic crystal structure, but they are more difficult to process (Chuang et al., 2011). In the study conducted by Algan Şimşek and colleagues (Algan Şimşek et al., 2021), it is observed that the addition of boron to the FeNiCoCrCu high-entropy alloy has a positive effect on the mechanical properties. Similarly, in the research conducted by Xiaotao and colleagues (Xiaotao et al., 2016), it is observed that boron addition to the $Al_{0.5}$CoCrCuFeNi high-entropy alloy contributes positively to the mechanical properties. Taking all

of these into consideration, we investigated the microstructure and mechanical properties of the $FeNiMnCrCoTi_{0.1}$ high-entropy alloy with the addition of B.

2. MATERIALS AND METHODS

The flowchart of processes employed in this study is provided in Figure 1 and was followed to ensure the experimental activities conducted effectively.

Figure 1. Flowchart of the experimental study

In order to create $FeNiMnCrCoTi_{0.1}Bx$ (x values in molar ratio, x= 0-1) high-entropy alloys, Ni, Mn, Cr, Co, and B powders from Nanografi company with a purity of 99.9% and Fe and Ti granules from Alfa Aesar company with a purity of 99.9% were obtained as raw materials, each with a particle size of 325 mesh.

The general properties of the powders used for alloy making and the alloy composition and are given in Table 1 and Table 2, respectively.

Table 1. General properties of the powders used for alloy making

Material	Commercial References	Molecular Weight (g/mol)	Purity (%)	Density (g/cm^3)	Melting Point (°C)	Boiling Point (°C)
Fe	Alfa Aesar	55.845	99.98	7.8	1535	3000
Ni	Nanografi	58.693	99.99	8.9	1453	2730
Mn	Nanografi	54.938	99.99	7.43	1245	2150
Cr	Nanografi	51.996	99.99	7.19	1857	2672
Co	Nanografi	58.933	99.99	8.92	1495	2900
Ti	Alfa Aesar	47.867	99.99	4.5	1668	3260
B	Nanografi	10.811	99	2.34	2300	2550
Mo	Nanografi	95.95	99.95	10.2	2610	5560

Table 2. . The nominal composition of alloys made in this study based on $FeNiMnCrCoTi_{0.1}B_X$

HEA		Ratio of Elements							Total
		Fe	Ni	Mn	Cr	Co	Ti	B	
$FeNiMnCrCoTi_{0.1}$	R (%)	19.61	19.61	19.61	19.61	19.61	1.96	-	100
$FeNiMnCrCoTi_{0.1}B_{0.2}$	R (%)	18.87	18.87	18.87	18.87	18.87	1.89	3.77	100
$FeNiMnCrCoTi_{0.1}B_{0.4}$	R (%)	18.18	18.18	18.18	18.18	18.18	1.82	7.27	100
$FeNiMnCrCoTi_{0.1}B_{0.6}$	R (%)	17.54	17.54	17.54	17.54	17.54	1.75	10.53	100
$FeNiMnCrCoTi_{0.1}B_{0.8}$	R (%)	16.95	16.95	16.95	16.95	16.95	1.69	13.56	100
$FeNiMnCrCoTi_{0.1}B$	R (%)	16.39	16.39	16.39	16.39	16.39	1.64	16.39	100

The molar weights of the elements were calculated and then weighed using high sensitivity Dikomsan ES410D balance. The weighed powders were mixed for half an hour, and then pressed uniaxially at 250 MPa pressure using 60 ton press (Figure 2 a) in a cylindrical mold with a diameter of 20 mm (Figure 2 b).

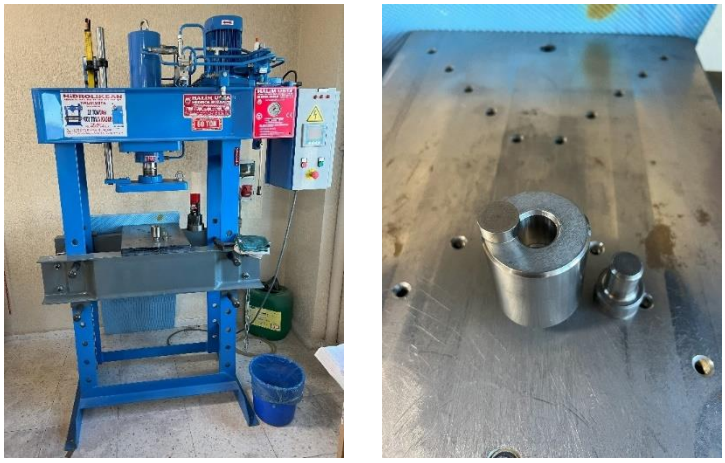

(a) (b)

Figure 2. a) uniaxial press machine b) 20 mm diameter steel mold

For the melting process, the pressed sample was placed in a copper crucible, and melting was performed using a Nuriş DC-TIG/ARC350 welding machine equipped with a tungsten electrode tip, applying a current of 300 Amperes (A) while purging argon onto the sample. To ensure chemical homogeneity, samples were melted four times. Additionally, after each melting, the surface impurities were cleaned by brushing with a wire brush, and then the samples were remelted by turning them upside down.

After the melting process, the samples were poured into a 6 mm diameter copper mold using the reverse vacuum method with a current of 300 A to give them a cylindrical shape. These processes are shown in Figure 3 (a) and (b).

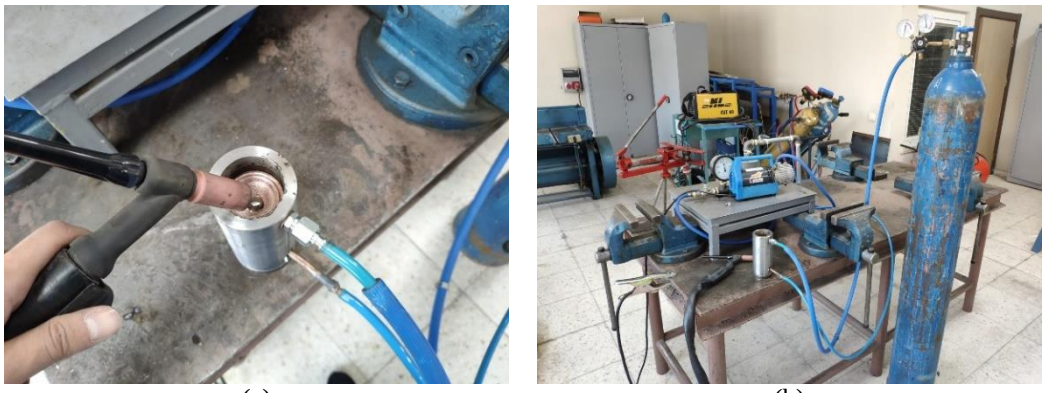

(a) (b)

Figure 3. a) Copper casting mold, b) reverse vacuum casting system

The cylindrical samples obtained after casting were machined on a lathe to flatten their outer surfaces. Subsequently, the machined samples were cut using a precision cutting machine. The cut samples were then reattached to the lathe and sanded with 120, 240, 400, 600, 800, 1000, and 1200 G SiC sandpapers to make the top and bottom surfaces completely parallel. Then, XRD scans were performed using a Bruker D8 Advance X-ray diffractometer with Cu-Kα (λ= 1.542 Å) radiation source in the range of 2θ=20-100°, and XRD peaks were analyzed. Next, the samples were polished using velvet cloth with 1µm alumina (Al_2O_3) suspension in FORCIPOL 2V device for hardness testing and microstructure examination. After polishing, the samples were etched with aqua regia, and their microstructures were examined using a LEO 1430 VP SEM with a backscattered electron detector, and semi-quantitative elemental analysis was performed using an EDX detector. Finally, for the determination of mechanical properties, Vickers microhardness tests were conducted using the MICROBUL microhardness measurement device with a 100g load applied for 10 seconds at 10 different points, and compression tests were performed using the MICROANALIZ UNIVERSAL TEST MACHINE 100kN device.

3. RESULTS AND DISCUSSION

XRD pattern of the $FeNiMnCrCoTi_{0.1}B_X$ high-entropy alloy is given in Figure 4. Upon examination of the XRD pattern, it is observed that $FeNiMnCrCoTi_{0.1}$ exhibits a single-phase FCC crystal structure, and as the addition of B increases, the presence of the FCC crystal structure is maintained. In a study conducted by Mehranpour et al., it is observed that the homogenized $FeNiMnCrCoTi_{0.1}$ alloy exhibits a single-phase FCC crystal structure (Mehranpour et al., 2021). Peaks corresponding to borides were detected, although with very low intensity, in the study conducted by Xiaotao and colleagues (Xiaotao et al., 2016). Similarly, in our XRD analyses, low-intensity peaks resembling borides are also observed.

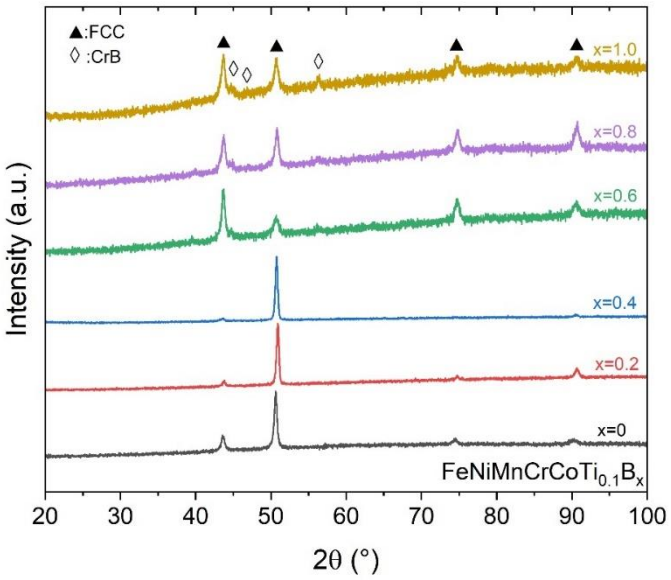

Figure 4. X-ray diffraction patterns of $FeNiMnCrCoTi_{0.1}B_X$ alloys

In Figure 5, the results of microstructural analysis using a SEM with a backscattered electron detector and semi-quantitative elemental analysis using an EDX detector are shown. In the high-magnification EDX point analysis seen in Figure 5 (a-1), it is observed that a segregation with high amount of Ti occurs within the grains or along the phase boundaries. This situation is also observed in the study conducted by İçin (İçin, 2024). In the EDX point analysis in Figure 5 (a-2), it is clearly observed that the matrix is in the form of solid solution of FCC phase (Otto et al., 2016) and contains Cr, Mn, Fe, Co, and Ni in similar proportions. Similar situations are observed in other EDX analyses with boron additions. However, the same study by Otto et.al (Otto et al., 2016) also showed that mainly FCC and in addition many minor phases formed after melting that are FCC + Cr-rich BCC + Ni-Mn rich L10 + Fe-Co rich B2, which were not clearly observed in this study as the specimens in this study was not heat treated following the casting or fell below the detection limit of XRD analysis. Nevertheless, this study was carried out without the addition of Ti and B, which may have had little effect on the matrix solid solution phase but rather may be effective in the formation of precipitation, for example, Ti addition introduces A_3B, A_2B and/or A_2BC (Laves) types of precipitation into the matrix (Chuang et al., 2011; Luan et al., 2019), increasing the matrix hardness significantly. As the amount of Boron addition increases, as was shown in the study by Xiaotao and colleagues (Xiaotao et al., 2016), needle-like boride precipitates were observed. This structure is located beneath the Ti segregation, as seen in Figure 5 (b-1), hence the Ti ratio appears to be lower in atomic ratio in the EDX analysis. Considering XRD and EDX analyses, the likelihood of needle-like precipitates being CrB is very high. As the boron addition increases, it is observed that the needle-like precipitates also increase in size and amount.

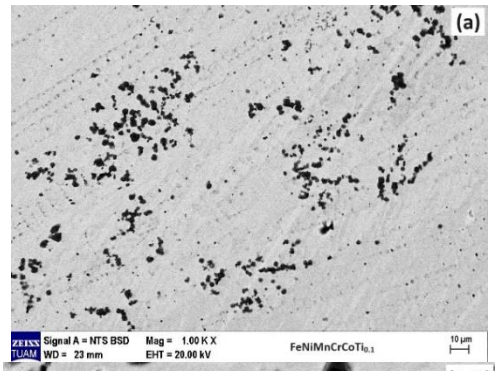

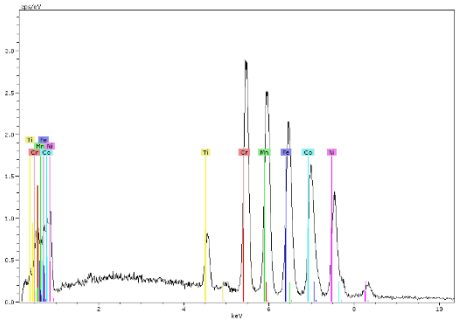

Element	Atomic (%)
Ti	2.89
Cr	21.71
Mn	19.24
Fe	20.48
Co	18.61
Ni	17.07

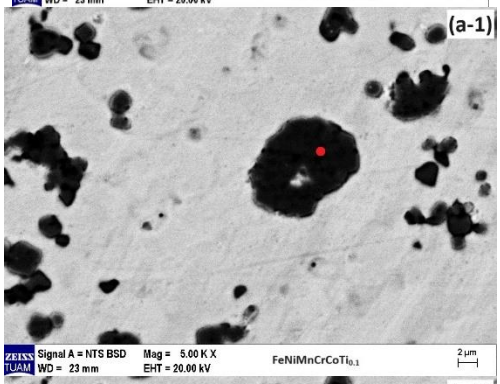

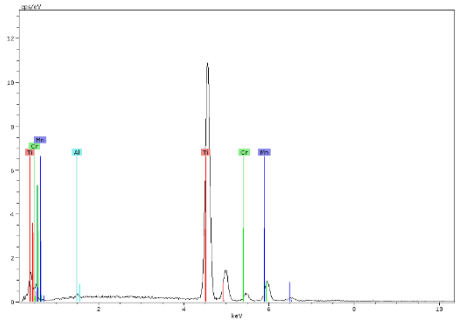

Element	Atomic (%)
Ti	85.39
Cr	4.13
Mn	10.48

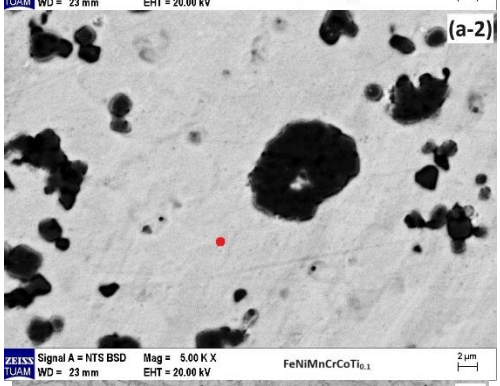

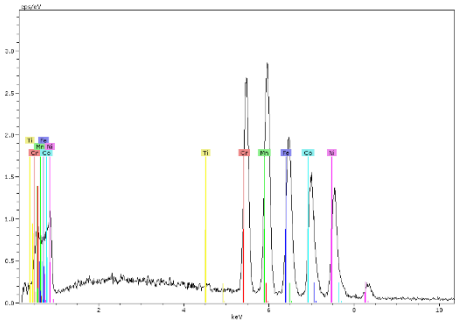

Element	Atomic (%)
Ti	0
Cr	21.25
Mn	22.81
Fe	18.52
Co	18.57
Ni	18.85

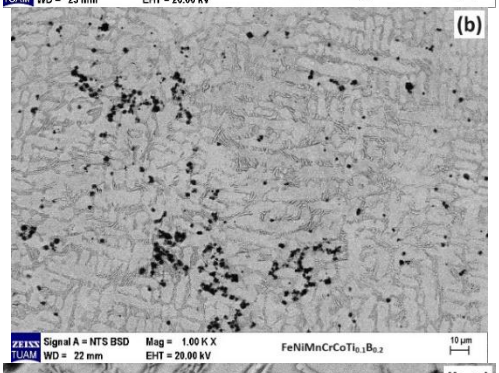

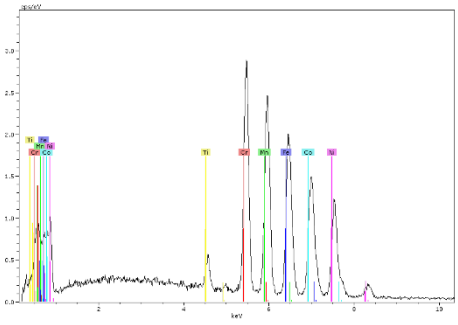

Element	Atomic (%)
Ti	1.45
Cr	23.04
Mn	19.11
Fe	20.48
Co	19.19
Ni	16.74

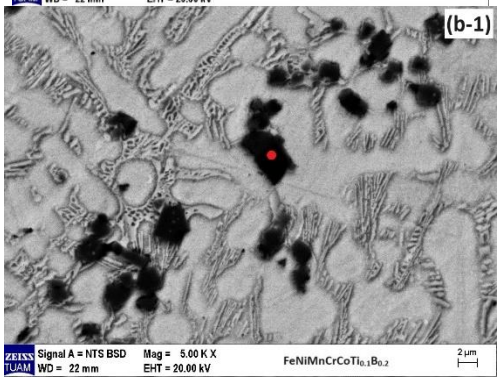

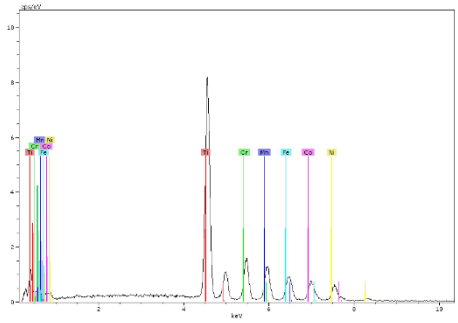

Element	Atomic (%)
Ti	49.29
Cr	13.86
Mn	10.70
Fe	9.70
Co	8.99
Ni	7.47

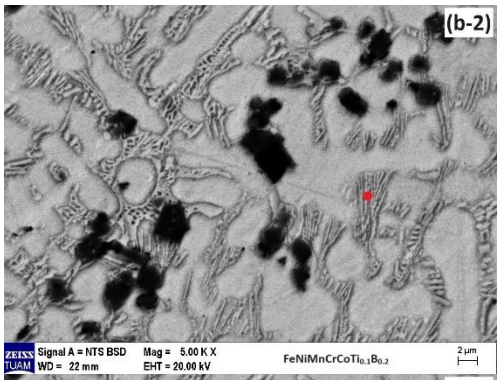

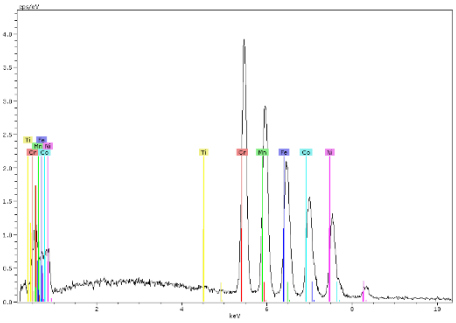

Element	Atomic (%)
Ti	0
Cr	27.73
Mn	20.29
Fe	18.82
Co	17.65
Ni	15.51

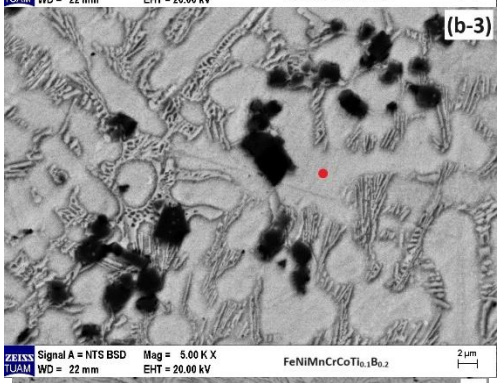

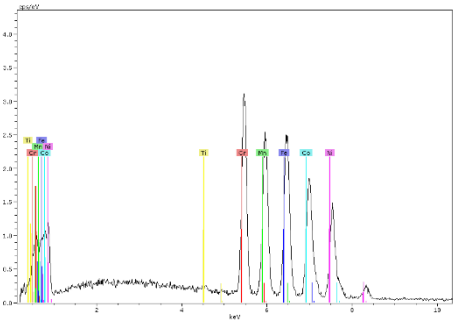

Element	Atomic (%)
Ti	0
Cr	21.55
Mn	16.97
Fe	24.07
Co	20.06
Ni	17.35

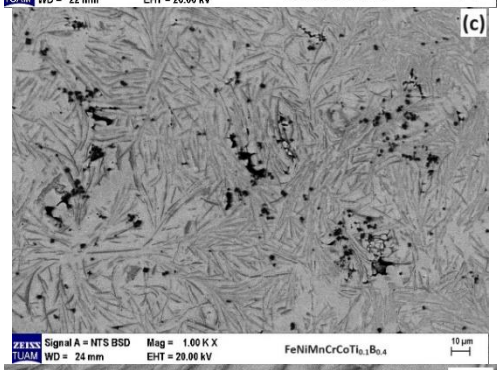

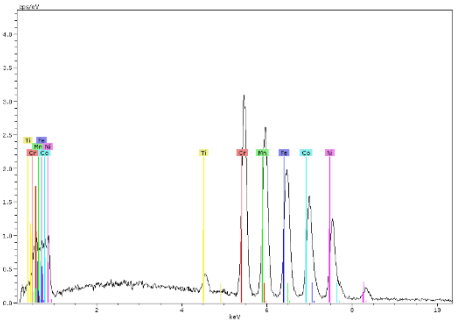

Element	Atomic (%)
Ti	0,76
Cr	23.99
Mn	19.42
Fe	19.84
Co	19.13
Ni	16.86

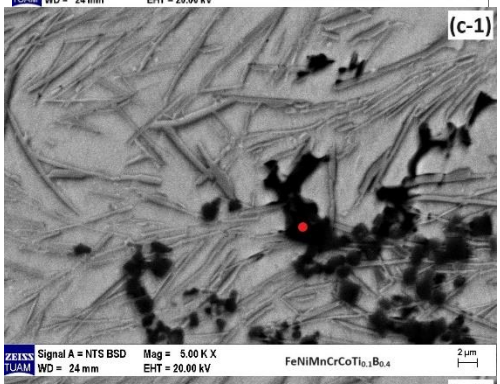

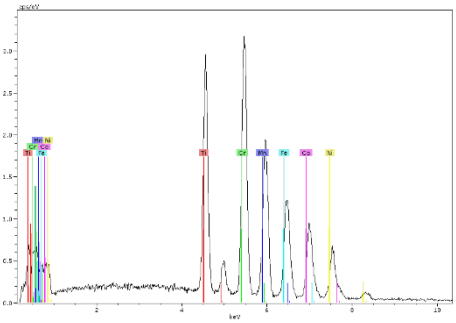

Element	Atomic (%)
Ti	18.10
Cr	31.38
Mn	14.88
Fe	14.45
Co	12.02
Ni	9.16

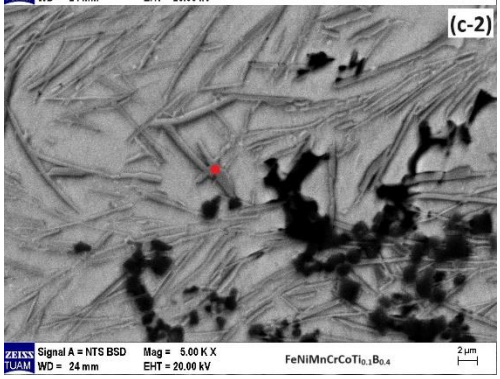

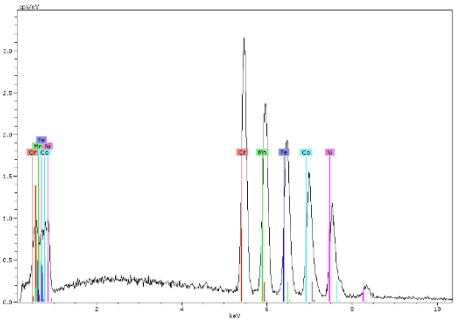

Element	Atomic (%)
Ti	0
Cr	26.00
Mn	18.58
Fe	20.54
Co	19.01
Ni	15.86

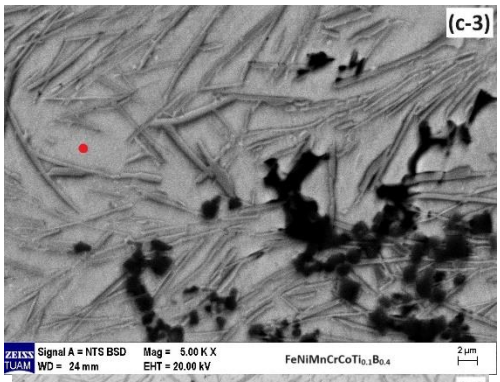

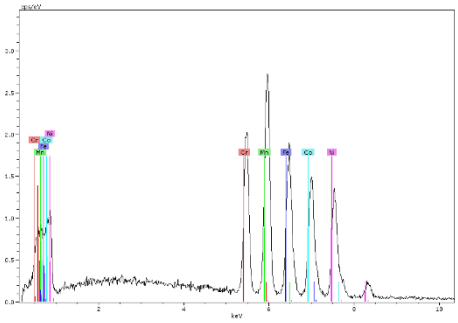

Element	Atomic (%)
Ti	0
Cr	18.17
Mn	24.32
Fe	17.38
Co	21.05
Ni	19.07

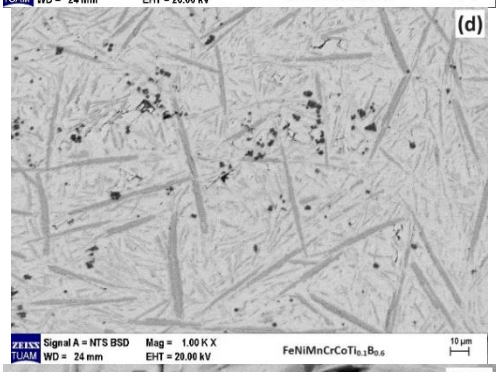

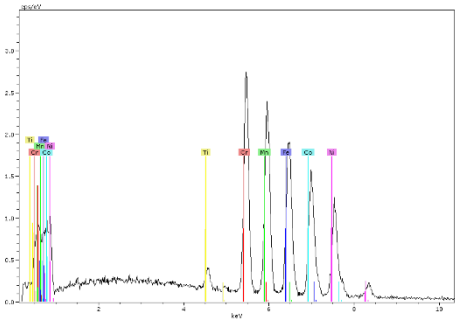

Element	Atomic (%)
Ti	0.90
Cr	23.31
Mn	19.18
Fe	20.59
Co	19.20
Ni	16.83

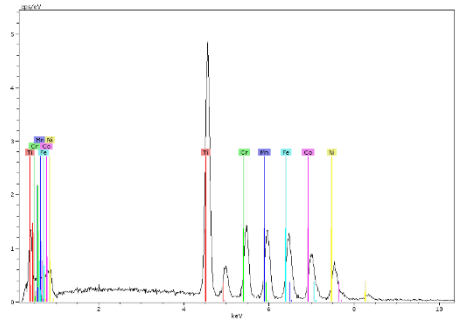

Element	Atomic (%)
Ti	33.80
Cr	14.23
Mn	13.17
Fe	15.12
Co	12.83
Ni	10.84

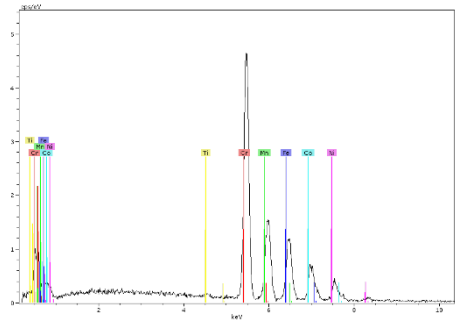

Element	Atomic (%)
Ti	0
Cr	55.24
Mn	10.13
Fe	18.15
Co	10.60
Ni	5.88

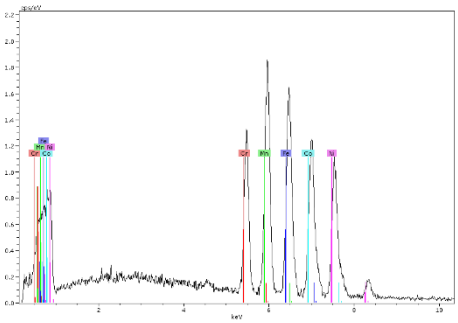

Element	Atomic (%)
Ti	0
Cr	13.11
Mn	21.65
Fe	22.42
Co	21.78
Ni	21.05

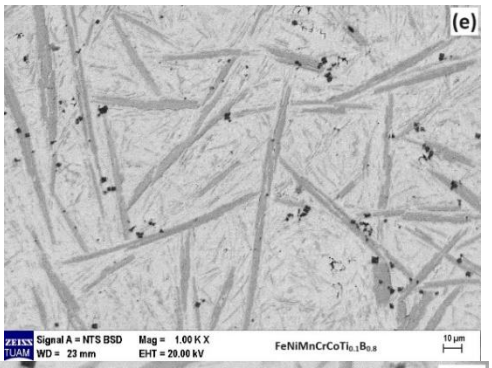

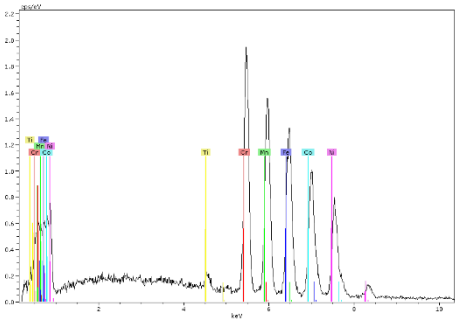

Element	Atomic (%)
Ti	0.29
Cr	24.19
Mn	18.54
Fe	21.68
Co	19.30
Ni	15.98

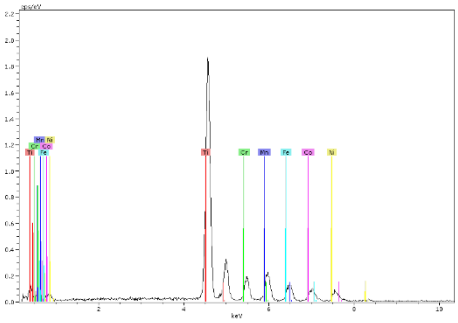

Element	Atomic (%)
Ti	62.41
Cr	9.71
Mn	10.36
Fe	6.72
Co	6.42
Ni	4.37

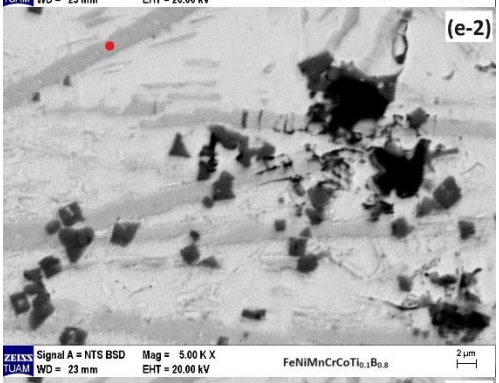

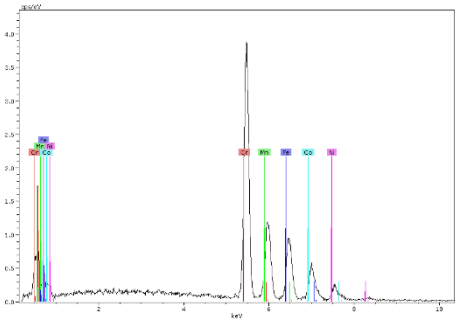

Element	Atomic (%)
Ti	0
Cr	55,72
Mn	10.92
Fe	18.99
Co	9.71
Ni	4.65

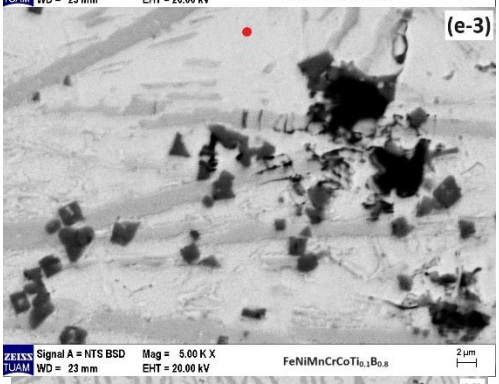

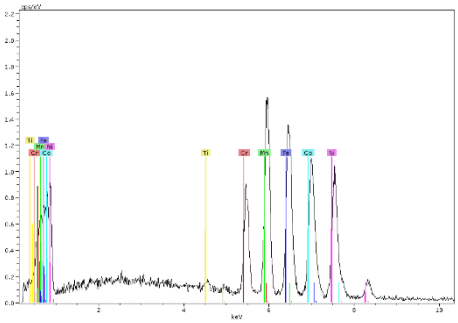

Element	Atomic (%)
Ti	0.05
Cr	10.05
Mn	22.28
Fe	22.23
Co	22.74
Ni	22.55

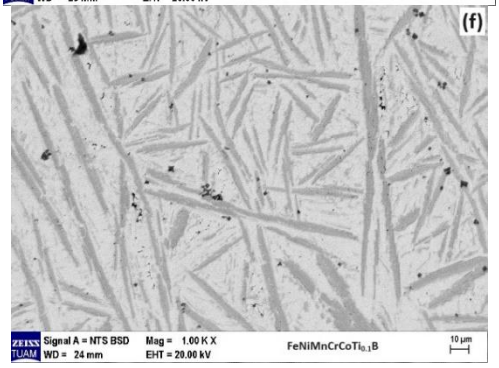

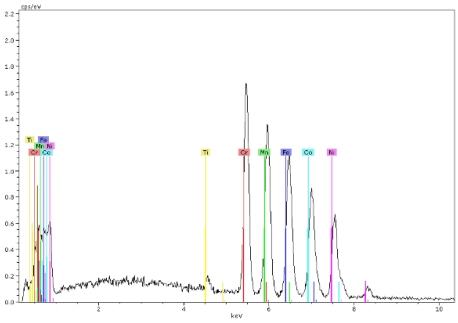

Element	Atomic (%)
Ti	0.15
Cr	24.59
Mn	19.06
Fe	20.76
Co	19.69
Ni	15.74

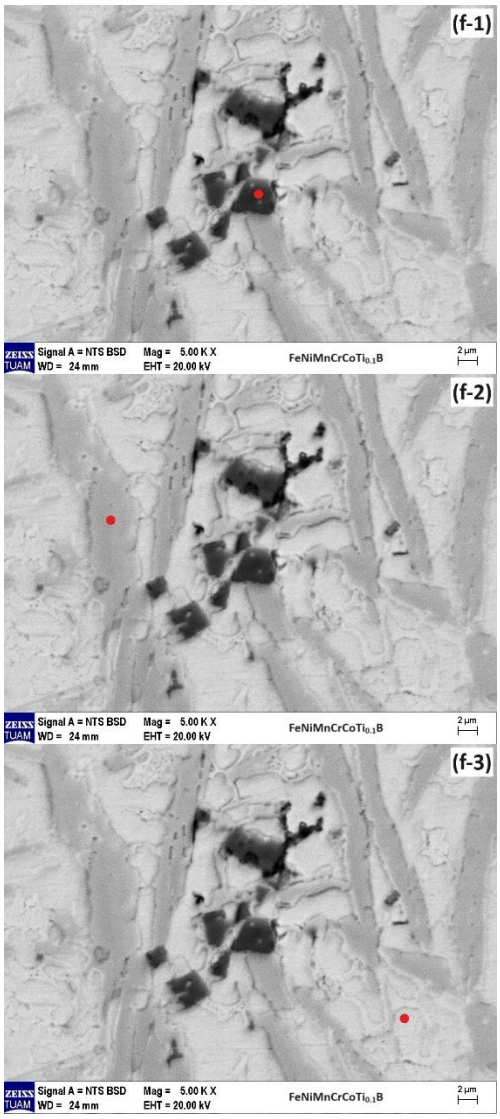

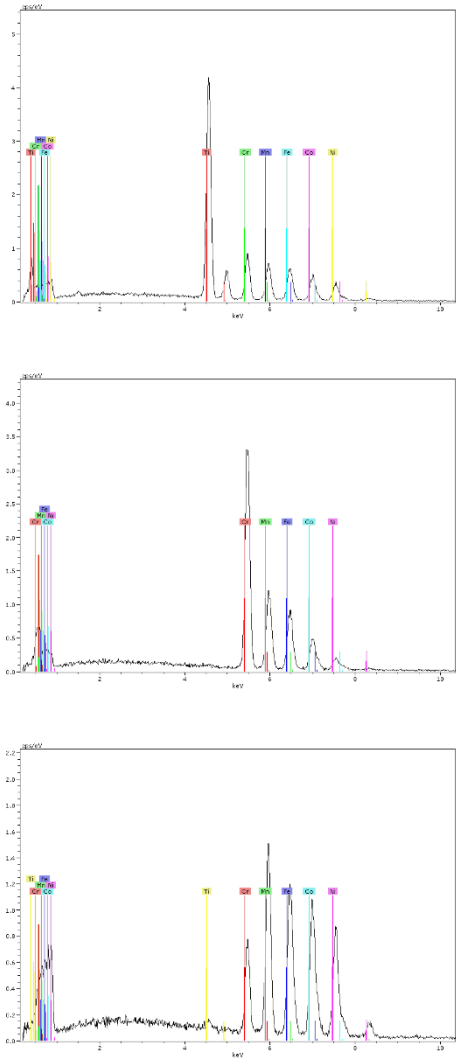

Element	Atomic (%)
Ti	46.10
Cr	14.63
Mn	9.76
Fe	12.06
Co	9.88
Ni	7.56

Element	Atomic (%)
Ti	0
Cr	54.99
Mn	11.42
Fe	19.61
Co	9.76
Ni	4.22

Element	Atomic (%)
Ti	0.20
Cr	9.59
Mn	24.33
Fe	21.30
Co	23.88
Ni	20.70

Figure 5. SEM images and EDX spectra of $FeNiMnCrCoTi_{0.1}B_X$ alloys with various boron (a) x:0 (b) x:0.2 (c) x:0.4 (d) x:0.6 (e) x:0.8 and (f) x:1 mol

As seen in Figure 6, the hardness of the $FeNiMnCrCoTi_{0.1}$ high-entropy alloy was measured to be 200.4 HV as the average of ten measurements. As the ratio of boron addition increases, the hardness of the alloy also increases significantly. In Figure 5(d-f), the average number of needles per 5cmx5cm square appears to be 126 (x: 0.4), 36 (x: 0.6), 31 (x: 0.8) and 29 (x: 1), respectively. However, the aspect ratios of needles are 0.33, 0.28, 0.21 and 0.11, respectively. These results indicate that as the amount of boron increases the needle becomes less in number but elongates and few number of needles become thicker in width. As the number of needles is high in the first series of boron addition, it significantly becomes thick and number decreases in later additions.

The highest hardness value, with an average of ten measurements, was achieved in the $FeNiMnCrCoTi_{0.1}B$ alloy, measuring 593.8 HV. With the addition of boron, the amount of needle-like structures increases and they become elongated in shape and net like appearance of these needle like structures are believed to be increasing the overall hardness of the specimens as shown in Figure 6. As seen Figure 5(e) that it is likely that (Cr, Fe)B constitutes the needle like structures which was also suggested by Xiaotao et al (Xiaotao et al., 2016). It is interesting to note that as seen in Figure 5(b) the needle like phase separation was observed as a eutectic phase separation which suggest that this zone is gradually becoming rich in eutectic making elements however, the EDX analysis was

not able to detect the boron content. A seaweed appearance of second phase in high entropy alloys was observed in FeNiCoCrMnPd eutectic high entropy alloys in addition to FCC+ Mn_7Pd_9 precipitates (Tan et al., 2017); with the addition of Nb into FeNiCrCoMn i.e. FeNiCrCoMnNb (Huo et al., 2015), the phase separation concludes as FCC+laves phase (A_2B or A_2BC) and the appearance becomes lamellar as shown in Figure 5(c). However, the excessive addition of boron transforms seaweed appearance into initially to lamellar and then the appearance becomes needle like and/or lamellar. The addition of Ti also produces the same effect as lamellar structure in addition to FCC+laves phase (Jain et al., 2018). It can be suggested that at the composition of $FeNiMnCrCoTi_{0.1}B_{0.2}$ the alloy shows eutectic high entropy alloy behavior and can be regarded as one.

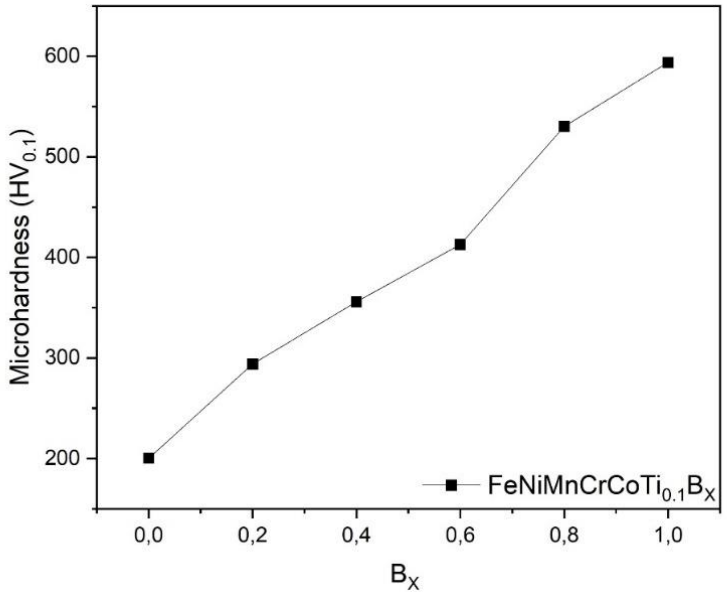

Figure 6. Hardness graph of $FeNiMnCrCoTi_{0.1}B_X$ alloys

In Figure 7, the stress-strain curve of the $FeNiMnCrCoTi_{0.1}B_X$ compression test conducted at room temperature is depicted. As observed in the stack of curves, with the increase in boron addition, the strain percentage decreases significantly for the first two specimens, however, for boron addition of x: 0.4 - x: 1, the strain is less pronounced. Nevertheless, regardless of strain increase rate, yield stress gradually increases and becomes stable after x: 0.4 addition of boron.

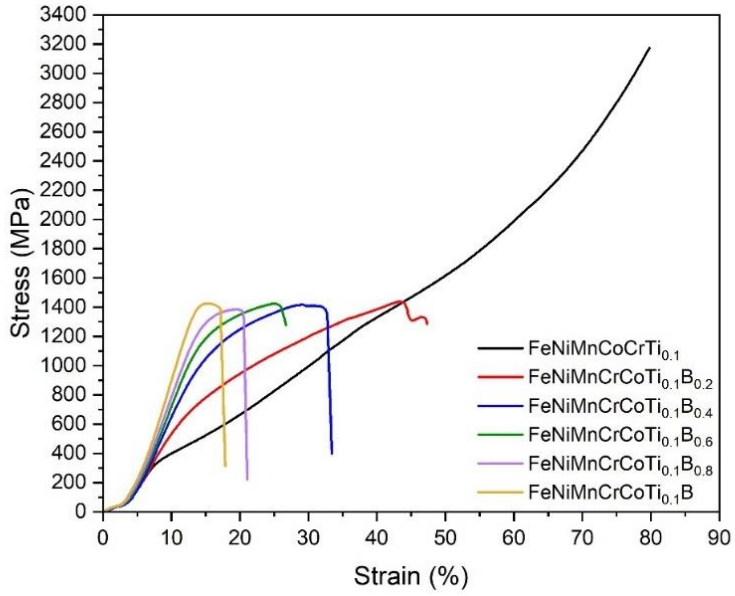

Figure 7. Room-temperature compression stress-strain curves of $FeNiMnCrCoTi_{0.1}B_X$ alloys

In Figure 8, the yield stress graph varying with boron content is shown. As depicted in the graph, the yield stress of the $FeNiMnCrCoTi_{0.1}$ high-entropy alloy is 329 MPa. With increasing boron addition, a gradual increase in the yield stress was observed, which was believed to be due to increasing amount of needle like structures. The highest yield stress, reaching 1329 MPa, was obtained in the $FeNiMnCrCoTi_{0.1}B$ alloy. As was stated that the aspect ratio of needles were proved to be decreasing i.e. becomes elongated with respect to increasing addition of boron. This implies that strength is more affected not by the number of needles but more to do with length of the needles i.e. aspect ratio, as it will affect the deformation capacity if there are larger precipitates and crack formation and advancement are hindered in these specimens.

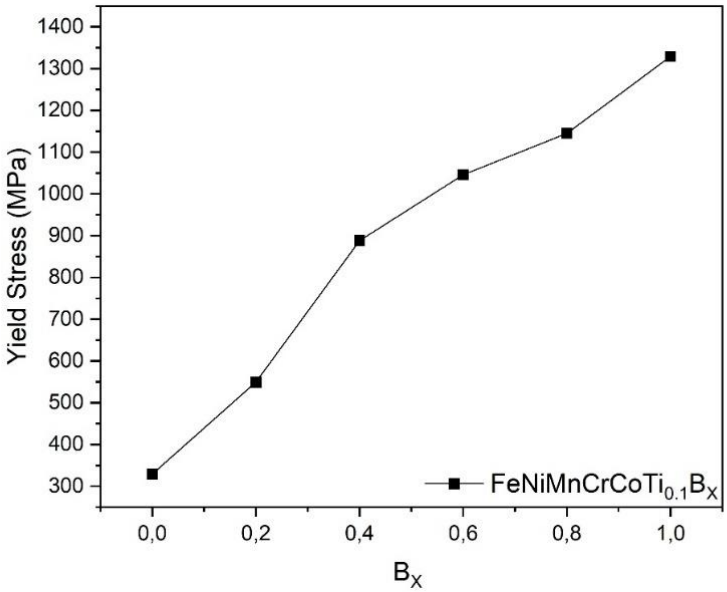

Figure 8. Compression 0.2% offset yield stress graph of $FeNiMnCrCoTi_{0.1}B_X$ alloys

In Figure 9, the maximum compression stress graph varying with boron content is depicted. The maximum compression stress value of the $FeNiMnCrCoTi_{0.1}$ high-entropy alloy is 3167 MPa.

This value was obtained with an applied load of 80 kN, which is the capacity of the compression test machine, and the sample remained unbroken. Depending on the boron addition, the maximum compression stress varies between 1384 MPa and 1438 MPa. The highest compression stress, reaching 1438 MPa, was achieved in the FeNiMnCrCoTi0.1$B_{0.2}$ alloy. However, the aspect ratio of needles have little effect on the maximum compression strength as it may indicate that the matrix phase in addition to the distribution is also a dominant factor in obtaining a high compression rate.

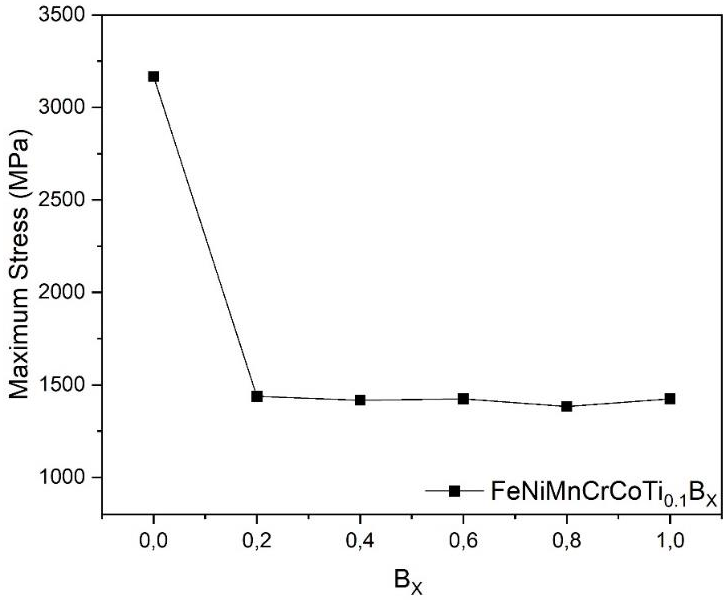

Figure 9. Compression maximum stress graph of FeNiMnCrCoTi$_{0.1}B_X$ alloys

In Figure 10, the percentage elongation graph varying until fracture with respect to boron content is shown. The highest percentage elongation was measured as 79.73% in the FeNiMnCrCoTi$_{0.1}$ high-entropy alloy. The lowest percentage elongation was measured as 17.85% in the FeNiMnCrCoTi$_{0.1}$B alloy. The microstructures given in Figure 9(a and b) is suitable for the defition of bimodal microstructures that is two different morphology exists at the same time where the microstructures given in Figure 5(c-f) are compatible with the definition of bilamellar structures. As the amount of boron increases, similar to hardness variation curves, the strain at maximum compression strength drops dramatically as the the needle morphology transforms from high in number and smaller in size to low in number but elongated in shape form. The deformation capacity of alloys with higher boron content may be affected by thick phase boundaries through which a crack cannot pass whereas thinner sections of needles can easily be broken by the action of crack (propagation) or passed by dislocation movement. It was shown that bilamellar structure is more effective in diverting the crack propagation than bimodal microstructures (Tan et al., 2021; Tan et al., 2017). The apperance of crack features also align with this view because of their height at which the crack occurred.

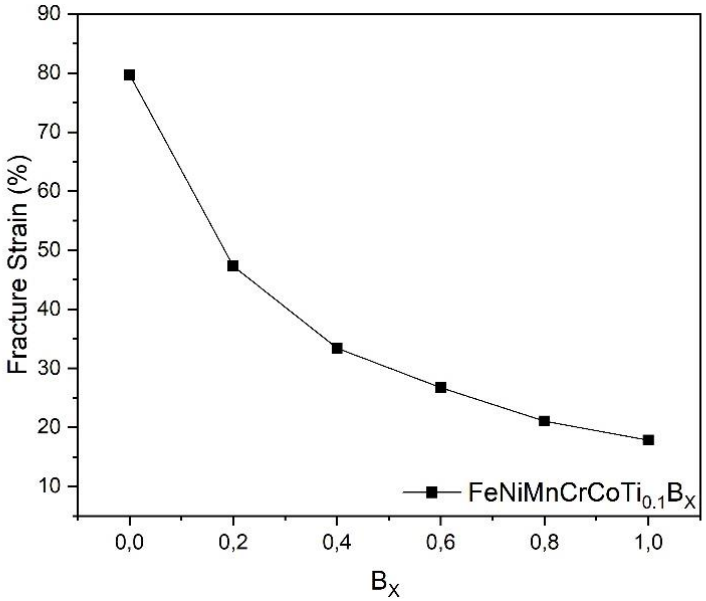

Figure 10. Compression fracture strain graph of $FeNiMnCrCoTi_{0.1}B_X$ alloys

In Figure 11, sample images before and after the compression test are provided. With increasing boron content, the height of compression specimen did not decrease, that is, compared to specimens with boron content of x: 0, x: 0.2, x: 0.4 (Figure 11 (b, d and f)), the specimens shown in Figure 11 (h, I and j) were not affected by the compression force in height. This can also be observed in Table 3, showing the mechanicla properties of alloys tested in this study with respect to their boron additions.

Table 3. Mechanical properties of $FeNiMnCrCoTi_{0.1}B_X$ at room temperature**.**

Alloys	$\sigma_{0.2}$ (MPa)	σ_{max} (MPa)	ε_f (%)	HV
$FeNiMnCrCoTi_{0.1}$	329	--	79.73	200.4
$FeNiMnCrCoTi_{0.1}B_{0.2}$	549	1438	47.33	293.9
$FeNiMnCrCoTi_{0.1}B_{0.4}$	888	1417	33.42	355.8
$FeNiMnCrCoTi_{0.1}B_{0.6}$	1046	1424	26.71	412.8
$FeNiMnCrCoTi_{0.1}B_{0.8}$	1145	1384	21.05	530.1
$FeNiMnCrCoTi_{0.1}B$	1329	1425	17.85	593.8

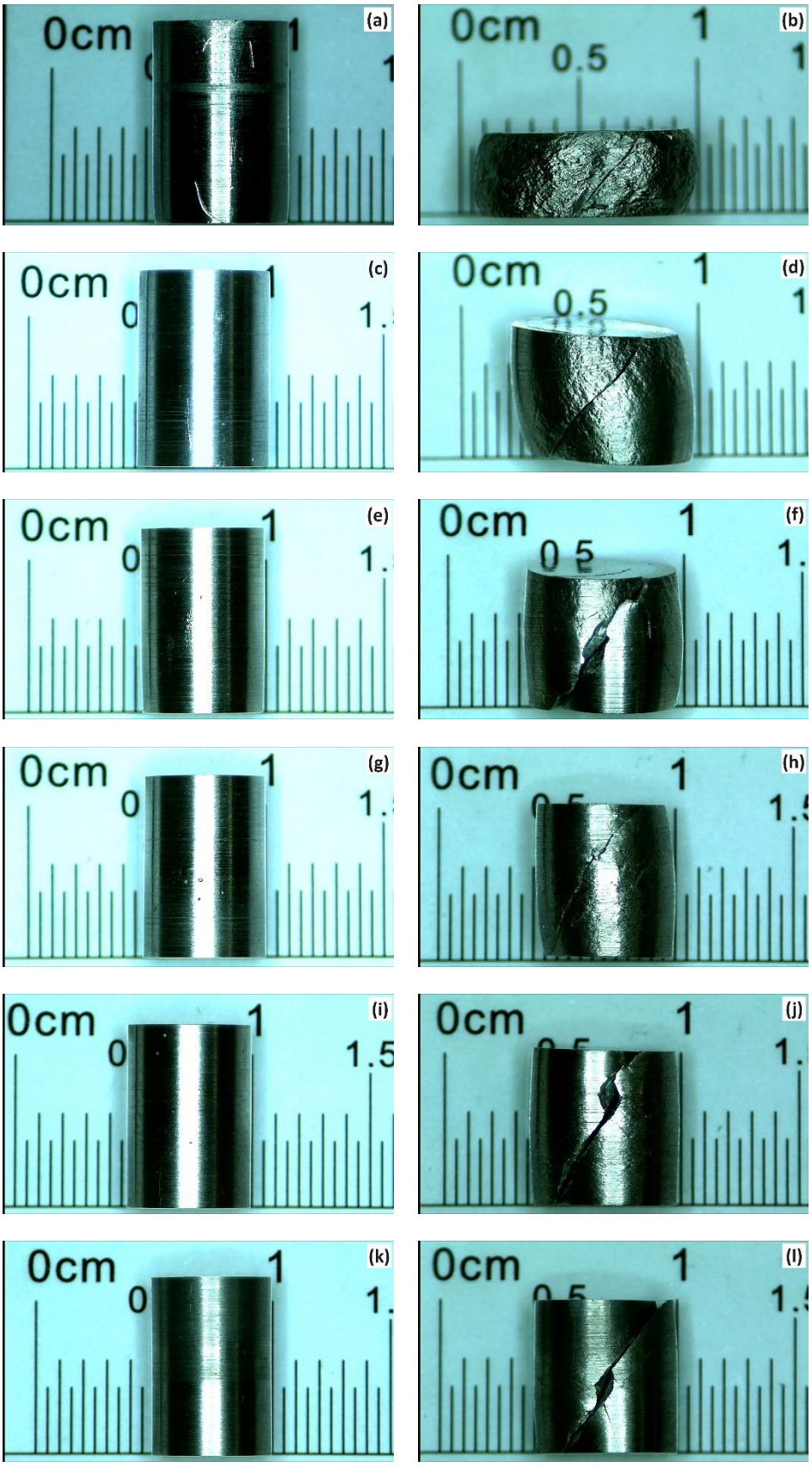

Figure 11. Before (a, c, e, g, i, k) and after (b, d, f, h, j, l) compression test sample images of $FeNiMnCrCoTi_{0.1}B_X$ alloys

4. CONCLUSION

The results obtained by adding B to the $FeNiMnCrCoTi_{0.1}$ high-entropy alloy are provided below.

- Despite the arc melting process being conducted with argon blowing in an open atmosphere, no oxide or nitride compounds were observed in the XRD analysis results. This condition is more favorable for industrial production in terms of process feasibility compared to vacuum arc melting.
- Considering the SEM and EDX analysis results, segregation of Ti element was observed, and concurrently, with the increase in boron addition, needle-like CrB precipitates were observed, taking into account of the XRD results.
- Microhardness tests showed that the hardness of the alloy increased with the increase in boron content.
- Compression tests revealed that the yield stress increased with the increase in boron content, while the percentage elongation decreased.

5. ACKNOWLEDGEMENTS

This study was supported by Afyon Kocatepe University Scientific Research Projects Coordination Unit with Project number of 21.FEN.BİL.11.

6. CONFLICT OF INTEREST

Authors approve that to the best of their knowledge, there is not any conflict of interest or common interest with an institution/organization or a person that may affect the review process of the paper.

7. AUTHOR CONTRIBUTION

Both Mahmud Cemaleddin YALÇIN and Şükrü TALAS contributed to determining the concept and/or design process of the research, managing the concept and/or design process of the research, analyzing data and interpreting the results, preparing the manuscript, critically analyzing the intellectual content, and providing final approval and full responsibility. Additionally, Mahmud Cemaleddin YALÇIN also contributed to data collection.

8. REFERENCES

Algan Şimşek İ., Talaş S., Kurt, A., The evolution of phases in FeNiCoCrCuBx high entropy alloys produced through microwave sintering and vacuum arc melting. Revista de Metalurgia, 58(1), 2022.

Algan Şimşek İ.B., Arık M.N., Talaş Ş., Kurt A., The effect of B addition on the microstructural and mechanical properties of FeNiCoCrCu high entropy alloys. Metallurgical and Materials Transactions A, 52, 1749-1758, 2021.

Chen M.R., Lin S.J., Yeh J.W., Chen S.K., Huang Y.S., Tu C.P., Microstructure and properties of Al0. 5CoCrCuFeNiTix (x= 0–2.0) high-entropy alloys. Materials transactions, 47(5), 1395-1401, 2006.

Chuang M.H., Tsai M.H., Wang W.R., Lin S.J., Yeh J.W., Microstructure and wear behavior of AlxCo1. 5CrFeNi1. 5Tiy high-entropy alloys. Acta Materialia, 59(16), 6308-6317, 2011.

Gao M.C., Miracle D.B., Maurice D., Yan X., Zhang Y., Hawk J.A. High-entropy functional materials. Journal of Materials Research, 33(19), 3138-3155, 2018.

Gao M.C., Yeh J.W., Liaw P.K., Zhang Y., High-entropy alloys: fundamentals and applications. Springer. 2016.

He J.Y., Liu W.H., Wang H., Wu Y., Liu X.J., Nieh T.G., Lu Z.P., Effects of Al addition on structural evolution and tensile properties of the FeCoNiCrMn high-entropy alloy system. Acta Materialia, 62, 105-113, 2014.

He J.Y., Wang H., Huang H.L., Xu X.D., Chen, M.W., Wu Y., Liu X.J., Nieh T.G., An K., Lu Z.P., A precipitation-hardened high-entropy alloy with outstanding tensile properties. Acta Materialia, 102, 187-196, 2016.

Huo W.Y., Shi H.F., Ren X., Zhang J.Y., Microstructure and Wear Behavior of CoCrFeMnNbNi High-Entropy Alloy Coating by TIG Cladding. Advances in Materials Science and Engineering, 2015(1), 647351, 2015.

İçin K., Investigation of phase transformation related magnetic properties of Ti addition to FeCoCuNiMn and FeCoCuNiAl high entropy alloys by vacuum arc melting. Materials Today Communications, 39, 108821, 2024.

İçin K., Sünbül S.E., Yıldız A., Cantor Yüksek Entropili Alaşımına Mn Yerine Cu İkamesinin Yapısal ve Mekanik Özellikler Üzerindeki Etkisinin Araştırılması. Gazi University Journal of Science Part C: Design and Technology, 11(2), 379-387, 2023.

Jain R., Rahul M.R., Jain S., Samal S., Kumar V., Phase evolution and mechanical behaviour of Co–Fe–Mn–Ni–Ti eutectic high entropy alloys. Transactions of the Indian Institute of Metals, 71, 2795-2799, 2018.

Luan H.W., Shao Y., Li J.F., Mao W.L., Han Z.D., Shao C., Yao K.F., Phase stabilities of high entropy alloys. Scripta Materialia, 179, 40-44, 2020.

Mehranpour M.S., Shahmir H., Derakhshandeh A., Nili-Ahmadabadi M., Significance of Ti addition on precipitation in CoCrFeNiMn high-entropy alloy. Journal of Alloys and Compounds, 888, 161530, 2021.

Murty B.S., Yeh J.W., Ranganathan S., High-entropy alloys. Elsevier, 2014.

Otto F., Dlouhý A., Pradeep K.G., Kuběnová M., Raabe D., Eggeler G., George E.P., Decomposition of the single-phase high-entropy alloy CrMnFeCoNi after prolonged anneals at intermediate temperatures. Acta Materialia, 112, 40-52, 2016.

Otto F., Dlouhý A., Somsen C., Bei H., Eggeler G., George E.P. The influences of temperature and microstructure on the tensile properties of a CoCrFeMnNi high-entropy alloy. Acta Materialia, 61(15), 5743-5755, 2013.

Shahmir H., Mehranpour M.S., Shams S.A.A., Langdon T.G., Twenty years of the CoCrFeNiMn high-entropy alloy: Achieving exceptional mechanical properties through microstructure engineering. Journal of Materials Research and Technology, 23, 3362-3423, 2023.

Shun T.T., Chang L.Y., Shiu M.H., Microstructures and mechanical properties of multiprincipal component CoCrFeNiTix alloys. Materials Science and Engineering: A, 556, 170-174, 2012.

Tan C., Sun Q., Xiao L., Zhao, Y., Sun J., Slip transmission behavior across α/β interface and strength prediction with a modified rule of mixtures in TC21 titanium alloy. Journal of Alloys and Compounds, 724, 112-120, 2017.

Tan C., Sun Q., Zhang G., Role of microstructure in plastic deformation and crack propagation behaviour of an α/β titanium alloy. Vacuum, 183, 109848, 2021.

Xiaotao L., Wenbin L., Lijuan M., Jinling L., Jing L., Jianzhong C., Effect of boron on the microstructure, phase assemblage and wear properties of Al0. 5CoCrCuFeNi high-entropy alloy. Rare Metal Materials and Engineering, 45(9), 2201-2207, 2016.

Yang X., Zhang Y., Prediction of high-entropy stabilized solid-solution in multi-component alloys. Materials Chemistry and Physics, 132(2-3), 233-238, 2012.

Yeh J.W., Chen S.K., Lin S.J., Gan J.Y., Chin T.S., Shun T.T., Tsau C.H., Chang S.Y., Nanostructured high-entropy alloys with multiple principal elements: novel alloy design concepts and outcomes. Advanced engineering materials, 6(5), 299-303, 2004.

Yeh J.W., Recent progress in high entropy alloys. Annales De Chimie Science des Materiaux, 31(6), 633-648, 2006.

Zhang W., Liaw P.K., Zhang Y., Science and technology in high-entropy alloys. Sci. China Mater, 61(1), 2-22, 2018.

Zhang Y., Zuo T.T., Tang Z., Gao M.C., Dahmen K.A., Liaw P.K., Lu Z.P., Microstructures and properties of high-entropy alloys. Progress in materials science, 61, 1-93, 2014.

Zhou Y.J., Zhang Y., Wang Y.L., Chen G.L., Solid solution alloys of AlCoCrFeNiTix with excellent room-temperature mechanical properties. Applied physics letters, 90(18), 2007.

Zhou Y.J., Zhang Y., Wang Y.L., Chen, G.L., Microstructure and compressive properties of multicomponent Alx (TiVCrMnFeCoNiCu) 100− x high-entropy alloys. Materials Science and Engineering: A, 454, 260-265, 2007.